UNIVERSITY OF LONDON THESIS

Degree PhD Year 2008 Name of Author NORTH, MATTHEW, W, M

UNIVERSITY COLLEGE LONDON

Faculty of Mathematics and Physical Sciences

Department of Physics & Astronomy

Rapid Rotation in Be Stars

(Testing the Null Hypothesis: Be stars are all 'Near-Critical' Rotators)

Thesis submitted for the Degree of Doctor of Philosophy of the University of London

by

Matthew W M North

Supervisors:

Prof. Ian D. Howarth

Prof. Raman Prinja

Examiners:

Prof. Iain Steele

Prof. Allan Willis

September 3, 2008

ProQuest LLC
789 East Eisenhower Parkway
P.O. Box 1346
Ann Arbor, MI 48106-1346

This thesis is dedicated to Coral Abby North

Abstract

The purpose of this thesis is to test the null hypothesis that all Be stars rotate close to their critical velocities. To do this, a grid of synthetic Be–star spectra is constructed, for $V_{\rm eq}/V_{\rm crit} = 0.95$, accounting for gravity darkening, limb darkening and viewing angle. This grid explores the full parameter space of the B star domain, subject to a minimum equatorial temperature constraint ($T_{\rm Local} > 6000K$), for a range of equatorial rotational velocities. The models are compared to 95 of the 116 Be stars in the Chauville et al. (2001) atlas. Of the stars modelled, 79 are fit acceptably, 12 show minor mismatches, the general cause of which is attributed to the presence of emission in the spectra. The four remaining fits are unacceptable, three due to a high degree of shell spectrum contamination, another as a result of a binary companion.

In essence, the null hypothesis is believed to survive. One important implication of this is that velocities on the order of the sound speed are sufficient to promote the formation of Be–star circumstellar disks.

Acknowledgements

I would like to acknowledge and thank Professor Ian Howarth for the opportunity he has given me. His wealth of knowledge, experience and scientific excellence has been invaluable throughout this work.

I would like to thank my wonderful wife, her constant belief and support throughout the last eight years has culminated in this thesis. I am forever in her debt.

I would also like to thank Professor Raman Prinja, his willingness to help, encourage and stimulate my research has been inspiring.

I also wish to thank my closest colleagues, Fabrizio, Jo, Sam, Simon, Dugan, Sam, Nutan and Jamie. It has been a great joy to have worked alongside you all.

Declaration

I, Matthew W. M. North, confirm that the work presented in this thesis is my own. Where information has been derived from other sources, I confirm that this has been indicated in the thesis.

"Many a short path is found by many a long wandering"

Roger Ascham

Contents

List of Figures

List of Tables

Chapter 1

Introduction

1.1 B stars

B stars are amongst the most massive stars. Their mass range extends from just a few solar masses up to around 25 solar masses, with photospheric temperatures from around 12kK up to approximately 30kK, and radii ranging from a few solar radii up to around $20R_{\odot}$, whilst on the main sequence.

The spectroscopic definition of a B star is that neutral helium is present, but no ionised helium is observed in classification–quality spectra (Jaschek & Jaschek 1990). The Yerkes (or Morgan–Keenan, MK) system for the classification of stars uses absorption–line strength ratios to determine classes and subclasses. Each major class (i.e., O, B, A, F, G, K and M) is uniquely defined by the presence of particular lines. In the case of B stars, the key lines are He I, Si II/Si III and Mg II. Indeed the blend of either He I with Si II/Si III or He I with Mg II provides an excellent temperature (or subclass) diagnostic as their respective line strengths vary in opposition to each other (Jaschek & Jaschek 1990, Underhill & Doazan 1982). The presence of Mg II or Si II/Si III is acceptable as their behaviours throughout the B–star temperature regime are comparable. In the case of the silicon lines it is evident from Figure 1.1 that Si II peaks at low temperatures while Si III peaks at high temperatures. Equivalently, the Mg II lines peak at the low temperature end and tail off to the high temperature end. In contrast though, the He I lines increase in strength with increasing temperature (from late to early subclass). Similar to the Mg II lines, hydrogen

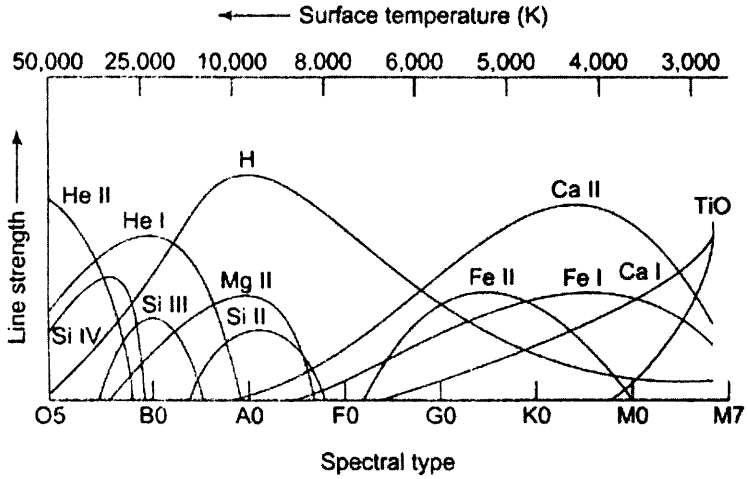

Figure 1.1. Diagram illustrating the change in line strengths versus temperature and spectral type.

lines decrease in strength over this same range but their additional sensitivity to pressure (surface gravity) necessitates the combination of at least three species to classify these stars accurately. In fact, the sensitivity of hydrogen lines to pressure enables accurate classification of luminosity class (Underhill & Doazan 1982). Thus, if we combine the temperature subclass information obtained from a helium–magnesium (or helium–silicon) line ratio with a hydrogen–line–strength ratio we have a measure of both temperature and luminosity. This in turn is calibrated to a mass–radius relation.

1.2 Be stars

A subset of the B stars is the Be stars, so categorised as their spectra show or have shown emission components in the Balmer transitions. Such emission lines are commonly associated with the presence of circumstellar disks or extended envelopes.

Since the discovery of these 'bright line' stars by A. Secchi in 1866 [discussed in the paper Secchi (1867)], Be stars have still not been comprehensively explained (Porter & Rivinius 2003). Indeed, despite the initial efforts of Struve (1931) and, more recently, Slettebak (1979) and Slettebak & Kusma (1979) [amongst many others], these objects have caused continuing debate in the massive–star community and form one of the longest standing challenges in modern astronomy. In particular, the transient nature of the Balmer emission, in conjunction with other observables, implies that these stars decrete matter to form disks which eventually dissipate, typically on scales of years (e.g., Slettebak 1988, Hirata 1995). Much of the contention has arisen from the combination of noting that the

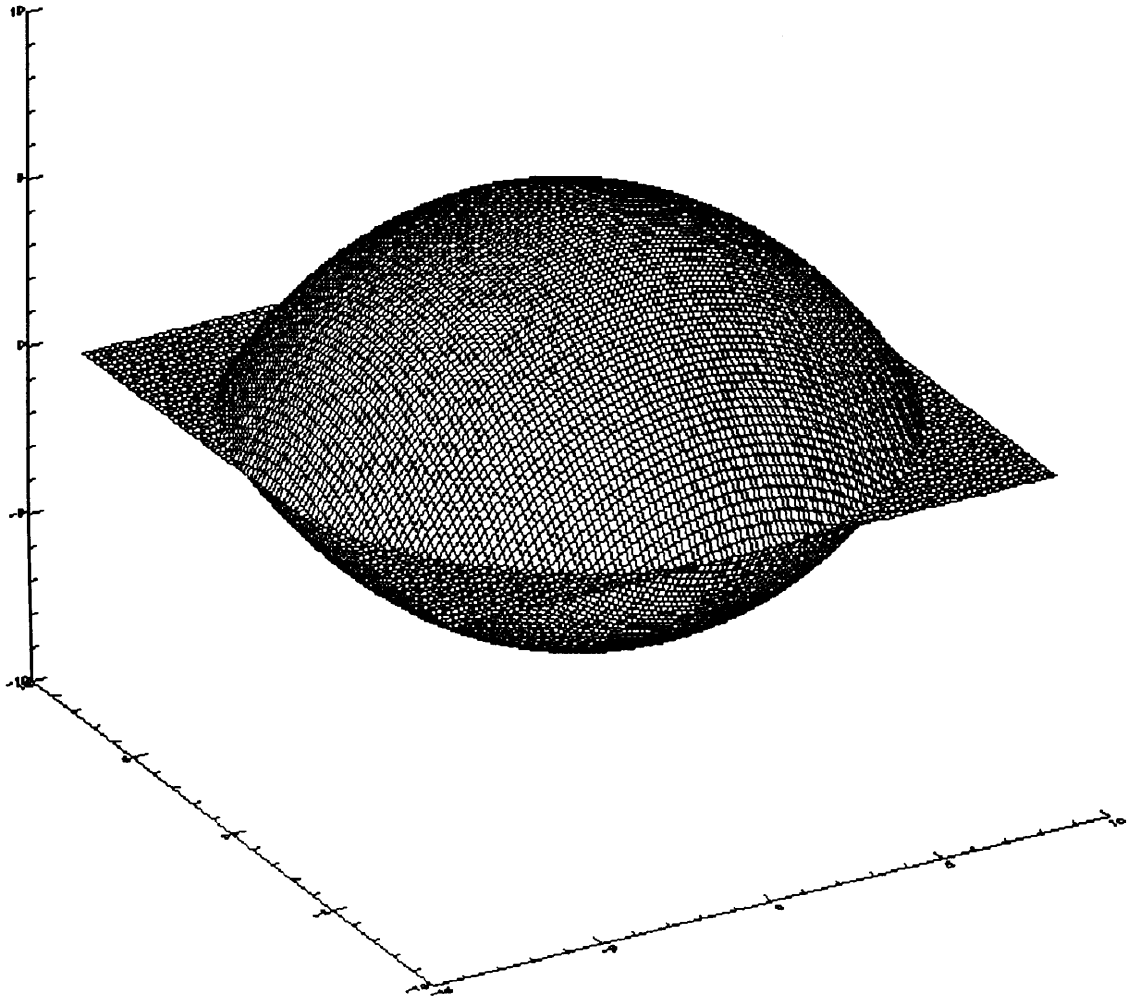

Figure 1.2. 3D representation of a near–critically rotating star. Note: The plane cutting through the equator is an artifact of the plotting.

Be star population as a whole forms the most rapidly rotating normal stellar population known (Slettebak 1949, Struve 1931), and that the disks are likely to form from the star outward (Struve 1931). These two points readily combine to promote the hypothesis that the rotation itself significantly reduces the surface gravity at the stellar equator to allow weak processes, such as acoustic waves, to eject matter into Keplarian orbits and thereby form a disk. However, herein lies the debate; to allow weak processes to form these disks the stars themselves would have to rotate on the order of 95% of their critical[1] velocity, but this has not been proven to be the case.

Figure 1.2 displays a rotationally distorted star rotating at a near–critical velocity.

[1]Critical, here, is defined to mean the velocity at which effective gravity at the stellar surface becomes zero.

Clearly evident is the sharp edge that appears at the equator which naturally lends itself to the decretion of a disk structure. This *lens–shape* geometry was first proposed by Jeans (1928) and referenced by Struve (1931) when he noted that, in general, the Be star spectra were characterised by double–peaked emission and broad, flattened absorption features. He suggested that a rapidly rotating star could be so destabilised such that matter could be ejected from the equator and form into a ring about the star. He justified this hypothesis by presenting a simplified theoretical description of the emission component from such a ring.

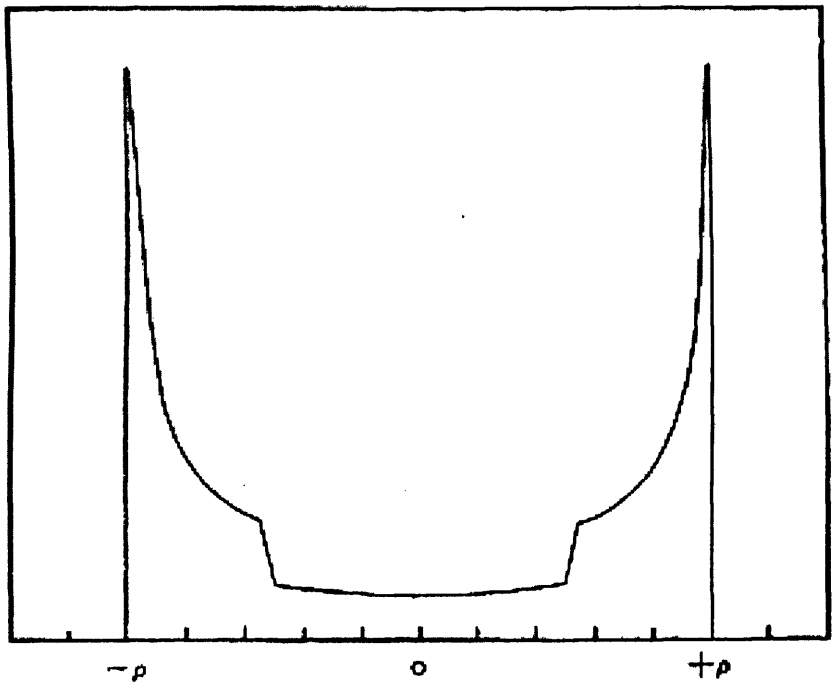

Figure 1.3. Struve's simplified theoretical contour of the emission components observed in Be stars, extracted from the Be star review paper of Slettebak (1988).

Figure 1.3 displays the theoretical emission component, generated by Struve's circumstellar ring. Struve also noted that the inclination of the star's rotational axis relative to the observer would naturally give rise to a range of emission–line widths, from broad double–peaked lines to single–peaked narrow ones. A schematic of this is displayed in figure 1.4.

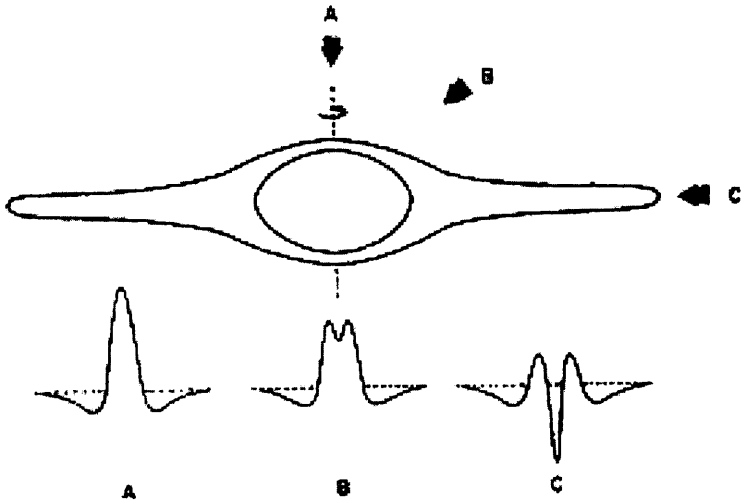

Figure 1.4. Slettebak's schematic of Struve's rapidly rotating star+ring emission at varying viewing angles.

1.2.1 $v \sin i$

Implicit to the above discussion, and at the heart of this research as a whole, is the $v \sin i$ debate. Whilst it is undoubtedly true that the profiles of absorption lines in the spectra of these stars encode the rotational velocities, this information is convolved with the angle of the rotational axis to the line of sight. Hence, should the absorption lines contain doppler broadened components from the equators of these stars (the most rapidly rotating regions, assuming solid body rotation), then one needs to know this viewing angle, i, to correctly identify the equatorial velocity from absorption line widths.

Their have been many attempts to deconvolve these values, however the general result has been to conclude that these stars do not rotate with near–critical velocity (e.g., Chen & Huang 1987, Porter 1996). Indeed, whether the approach taken is one of absorption–line synthesis (e.g., Slettebak 1949, Chauville et al. 2001) or population statistics (e.g., Chen & Huang 1987), the highest estimates of the equatorial velocities of the most rapidly rotating members of this population, essentially obtained from these measurements of absorption lines widths, are only of the order of about 80% of critical (Chauville et al. (2001)). The difference in energy required between ejecting matter into orbit from 80% to 95% of critical is enormous (Townsend et al. 2004); thus, if this *substantially sub–critical*[2] viewpoint is true, a *new* physical mechanism to generate these disks is required. Many such theories

[2]Here and throughout this thesis the term *"substantially sub–critical"* refers to any $V_{\rm eq}$ which implies a $V_{\rm eq}/V_{\rm crit} \lesssim 0.85$.

have been presented to accommodate substantially sub–critical rotation (e.g., Lee et al. 1991, Bjorkman & Cassinelli 1993, Cassinelli et al. 2002) but none have achieved general acceptance.

1.2.2 Sub–critical rotation disk models

Amongst the most promising of theories that was thought could describe Be–star disk formation with a substantially sub–critical rotational velocity, built on the theory of winds from rotating, magnetic, hot stars, developed by Friend & MacGregor (1984). They combined the line-driven wind theory of Castor et al. (1975) [CAK–theory] with the rotating, magnetic–wind model of Weber & Davis (1967) to derive a set of solutions that drove the terminal velocity of winds up with increased magnetic field strength and also drove mass loss up with increased rotation.

This point–source theory was then modified by Poe & Friend (1986) [hereafter PF86] to account for the finite disk of the stellar surface[3]. This modification had the effect of reducing the magnetic–field enhancement of terminal velocity. Indeed, with a low enough magnetic field this theory describes a slower, denser, wind at the equator than at the pole. However, whilst this theory produces promising results with $V_{\rm eq}$ on the order of 85% of critical, it still suffers a few key draw–backs. Specifically, though this scenario produces a sufficiently dense, slow flow at the equator and close to the star, it also provides for a substantially higher mass loss rate and terminal velocity (away from the star), in conflict with independent observational evidence (Madura et al. 2007).

Another promising approach was the Wind Compressed Disk (WCD) model of Bjorkman & Cassinelli (1993). This model viewed the Be star disk phenomena as resulting from a 'ballistic' orbit. The combination of angular momentum, gravity and the line–driving radiation force results in particles ejected from intermediate latitudes entering into orbits that intersect at the equatorial plane. Thus, when summing over all latitudes and a continuous mass flux these particles inevitably collide. These collisions ultimately flatten these orbits until they settle down into the equatorial plane to form a disk. However, Cranmer & Owocki (1995) and Owocki et al. (1996) showed that accounting for the rotational distortion of the stellar surface and gravity darkening (see § 4.1 for details) generates non–radial line–force components in both azimuth and latitude which act to inhibit the formation

[3]This *modification* of CAK–theory is commonly referred to as m–CAK which was formally presented simultaneously and independently by Friend & Abbott (1986) and Pauldrach et al. (1986)

of the WCD. Moreover, these line forces are so effective that they lead to a significantly reduced density of outflow material in the equatorial region relative to all other latitudes, in total opposition to the decretion–disk scenario.

Despite these failures, attempts to describe the decretion–disk phenomenon with sub–critical rotational velocities have persisted. The sub–sonic equatorial flow model presented by Curé (2004) appears to provide a plausible explanation. This paper presented a re-analysis of the m-CAK theory for a rotating star in which, by a change of variables, a semi–analytic solution is derived which enables numerical solutions for rotational velocities in excess of $V_{\rm eq}/V_{\rm crit} \gtrsim 0.85$ (the maximum value attained in previous solutions). Curé showed that his new solutions for $V_{\rm eq}/V_{\rm crit} \sim 0.7-0.8$, have a critical point[4] located well away from the stellar surface and delivers a very low terminal velocity and consequently higher density. This solution goes significantly further than the earlier work of PF86 in that it provides a substantially lower estimate of the terminal velocity for the equatorial flow and hence is closer to describing the disk structure believed to transiently form about stars. Nevertheless, despite these promising results, Madura et al. (2007) point out that for the classical Be stars, the now substantial observational evidence all but confirms these disks to be Keplerian in nature (e.g., Meilland et al. 2007, Quirrenbach et al. 1997 and papers in Ignace & Gayley 2005). Thus, despite the low estimates for the terminal equatorial–velocity, they still imply a steady outflow of material, in conflict with the Keplerian–disk paradigm. Madura et al. (2007) also point out that non–radial line–force components and the reduced equatorial mass flux resulting from gravity darkening are not accounted for by Curé.

Prior to any of these theories, Stoeckley (1968) laid down what he perceived to be the five key physics components which one should have to include for in any attempt to synthesise the photospheric spectra of these stars. Essentially these are:

(i) Limb darkening;

(ii) differential rotation;

(iii) deformation of the star;

(iv) gravity darkening

[4] A critical point is defined as the location at which an outflow becomes supersonic.

(v) variation of absorption–line strength with local latitude temperature/gravity and angular distance from the limb

In particular, Stoeckley noted that gravity darkening, first presented by von Zeipel (1924), had not been adequately accounted for at that time.

Consequently, one key focus of this research has been to account for von Zeipel's law in constructing a grid of synthetic spectra to compare to observations. Moreover, by constructing these model spectra under the assumption that these stars do indeed rotate with a near critical velocity, the subsequent comparison of synthetic to real spectra tests the near–critical rotation hypothesis.

1.2.3 von Zeipel's Law

In 1924 H. von Zeipel published two papers which considered the problem of radiative equilibrium in rotating systems. In these papers he derived and calculated the effect of rotation on the surface brightness (and effective temperature, amongst other parameters) of a star. He ultimately deduced that "the net flux of energy per second in cm^2 through a level surface anywhere within the partial body is proportional to the gravity". In effect, the introduction of rotation tends to alter the net flux emitted from a part of a star proportionally to the resulting change in effective gravity, i.e., $g_{\rm eff} \propto T_{\rm eff}^4$. This is gravity darkening, point (iv) of Stoeckley's requisites.

1.2.4 Be star geometry

To establish the geometry of a rotating star requires the mass distribution within the star. With the mass distribution known, the internal pressures are equated with the gravitational and centrifugal forces and thus a geometry determined. However, the mass distribution itself is dependent upon the internal pressure structure of the star and thus the process is iterative. Nonetheless, by considering that gases, in general, are highly compressive, and that the masses of these stars are extremely large, it is not unreasonable to assume that *most* of the stars mass will be concentrated at its centre. Hence, to ascertain a rotating star's geometry it is assumed that the mass of the star is concentrated at the centre. This is the Roche approximation.

1.3 Modelling Stellar Spectra

In the context of this thesis the modelling undertaken seeks to recreate the visible spectrum we observe from Be stars using three basic steps. First, a grid of local thermal equilibrium (LTE) model atmospheres is generated using ATLAS9 (see § 3.2). Secondly, each model atmosphere then provides the structural input into the spectrum synthesis program SYNSPEC which calculates a grid of angle–dependent spectra, embodying limb–darkening [Stoeckley, point (i)]. Thirdly, this grid provides the input to a Roche model code which ultimately produces the final grid of synthesised spectra [Stoeckley, points (iii), (iv) and (v)]. Stoeckley point (ii) is considered in 8.

1.4 A Null Hypothesis

Whilst the debate surrounding Be stars has been summarised and a method for synthesising their spectra identified, a clear direction for this research has yet to be established.

In this regard a null hypothesis is stated that motivates this research in a singular direction. Specifically, the following hypothesis is adopted:

> Be stars are near–critical rotators such that 'weak' processes alone can naturally give rise to the Be disk.

Consequently, a grid of Be–star spectra is synthesised on the basis that their rotational velocities are close to 95% of critical. These models are subsequently compared to observation and the hypothesis examined for failure.

1.5 Thesis Structure

This thesis is structured in the following way:

- Chapter 2 provides a brief introduction to the observational data.
- Chapter 3 discusses the generation of the static–star atmospheres.
- Chapter 4 further discusses the Roche approximation and von Zeipel's theorem before describing how the rotating star model is generated by the BUSH code.
- Chapter 5 is the first results chapter. A selection of fits is presented and discussed in detail.

- Chapter 6 uses a χ^2 approximation to help establish the extent of degeneracy in the grid for any given fit. In so doing, the selections of chapter 5 are then revisited and improved fits, where needed, are found.
- Chapter 7 summarises the results for the full data set, having followed the process of best–fit selection presented in chapter 5, and discusses their significance.
- Chapter 8 discusses unexpected results from the previous two chapters that are suggestive of differential rotation.
- Chapter 9 presents the overall conclusions and presents a view of future work to build on this foundation.

Chapter 2

Observations

2.1 Chauville's Be-Star Altas

For the purpose of testing the null hypothesis the spectra of Chauville et al. (2001) were used. These data were obtained via three ground based telescopes, namely, Complejo Astronòmico El Leoncito (CASLEO, 2.15m) in Argentina, ESO–La Silla (1.52m) in Chile and Haute–Provence Observatory (OHP, 1.52m) in France.

The CASLEO observations were taken with an èchelle spectrograph providing high–resolution dispersion spectra of approximately $R = 27000$ at 4900Å, with a wavelength coverage of λ3900 to λ6400 Å. The ESO–La Silla observations were taken with an èchelle spectrograph also providing high–resolution dispersion spectra with $R = 35000$ at 4473Å and a wavelength range of λ4255 to λ4630 Å. The OHP observations were taken with the AURELIE èchelle spectrometer providing intermediate dispersion spectra with the two independent arrays delivering $R = 16200$ and 8000 at 4340Å and 4470Å, respectively. All of these observations provided a $S/N \simeq 100$

These data were reduced using custom written software by J. Chauville. This software essentially delimits each order of the èchelle–dispersed spectrum before applying a second or third order polynomial fit[1] to each order for extraction. All spectra are flat–field and bias subtracted before each order, of the individual spectra, are linked to form the individual spectra. All spectra were subsequently normalised.

[1]The 'polynomial fits' referred to here seek to trace out the curvature intrinsic to each order as they arc across the CCD's

Table 2.1. Absorption line–list for 4300-4500Å spectra

Wavelength	Ion	Transition	Wavelength	Ion	Transition
4318	S II	4Po-4D	4319	O II	4P-4Po & 2Po-2S
4340	Hγ	2-5	4367	O II	4P-4Po & 4P-4So
4372	Fe III	5Fo-5G	4388	He I	1Po-1D
4396	O II	2Do-2D	4411	O IV	2P-2Po
4411	S II	2Po-2P	4416	O II	2P-2Do & 2P-2Do
4417	S V	3Po-3D	4437	He I	1Po-1S
4438	S II	2Po-2P	4448	O II	2Fo-2F
4471	He I	3Po-3D	4481	Mg II	2D-2Fo

2.1.1 Example spectra from the Chauville Be–star atlas

Figures 2.1, 2.2 and 2.3 display six spectra selected from the Chauville Be–star atlas. Figure 2.1 displays HD 149757 and HD 164284, late O and early B dwarf stars respectively. Figure 2.2 displays HD 202904 and HD 22780, these two are B3 and, late–type, B7 dwarf stars respectively. Figure 2.3 displays the "near main–sequence", subgiant and giant, stars HD 212076 and HD 23302.

The first five spectra displayed are all formed from multiple exposures, evident in these plots is the high quality signal–to–noise this provides. The final plot, HD 23302, is a single exposure, again of excellent quality, and indicative of the overall quality of all the individual spectra used in this research.

The spectra of HD 164284, HD 202904 and HD 212076 all clearly display typical Balmer emission components, characteristic of the Be stars, with each Hγ emission being double peaked (see § 1.2 for discussion).

Marked on each plot are the main absorption lines present in these stars which contribute to the overall profiles of the spectra. Whilst the 'minor' transitions are generally weak in these examples, HD 212076 (figure 2.3) clearly shows the presence of all of these lines. A line–list is provided in table 2.1.1.

2.1.2 Selection effects

The Chauville et al. (2001) Be–star atlas is subject to the obvious selection effect of a bias toward the 'brightest', hence early–type, stars. One possible impact of this could be a failure to identify an evolutionary preference for 'near–critical rotation'.

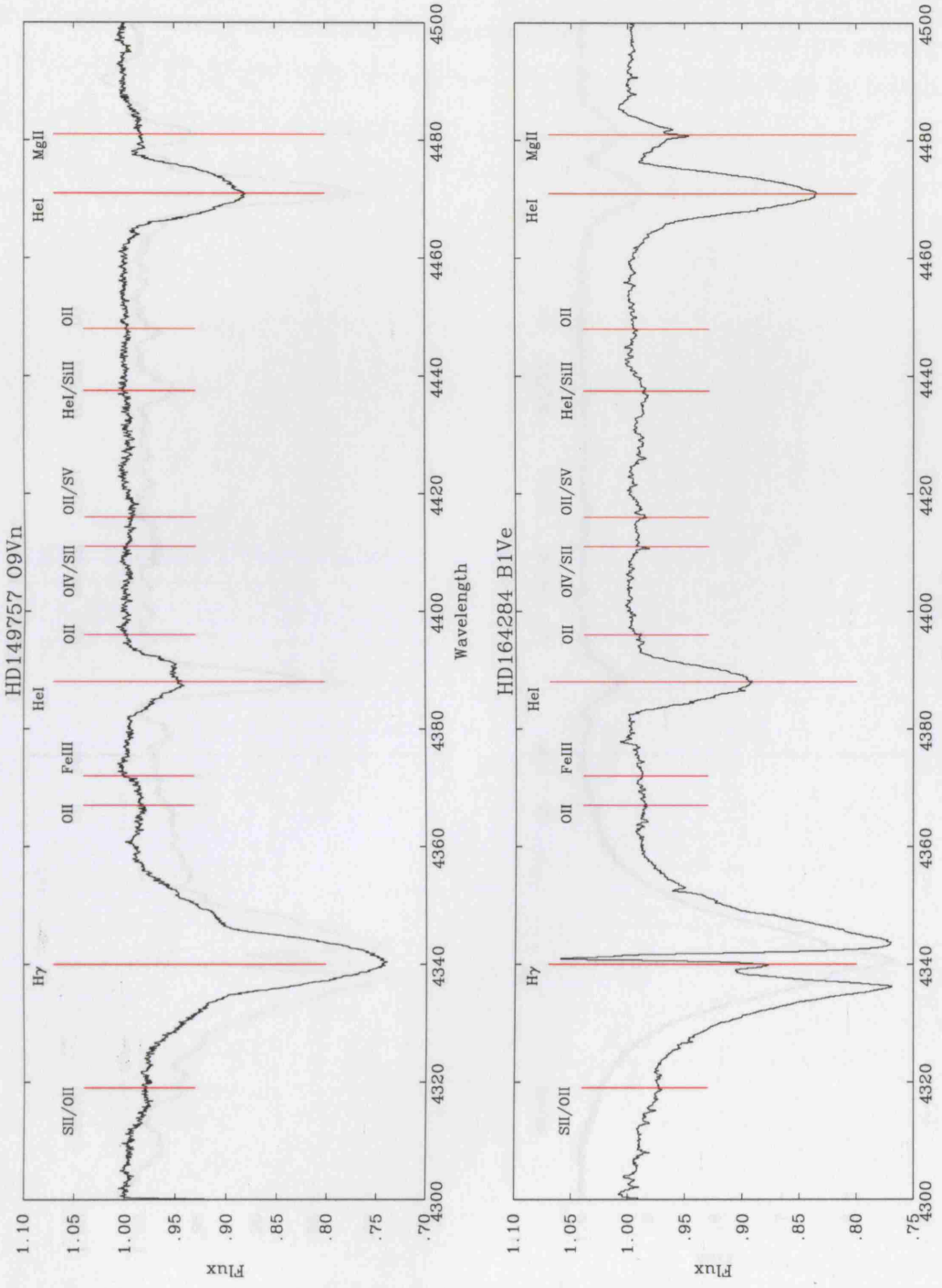

Figure 2.1. Two plots displaying Chauville's spectra for HD 149757 and HD 164284, classified as O9Vn and B1Ve (upper and lower panels) respectively.

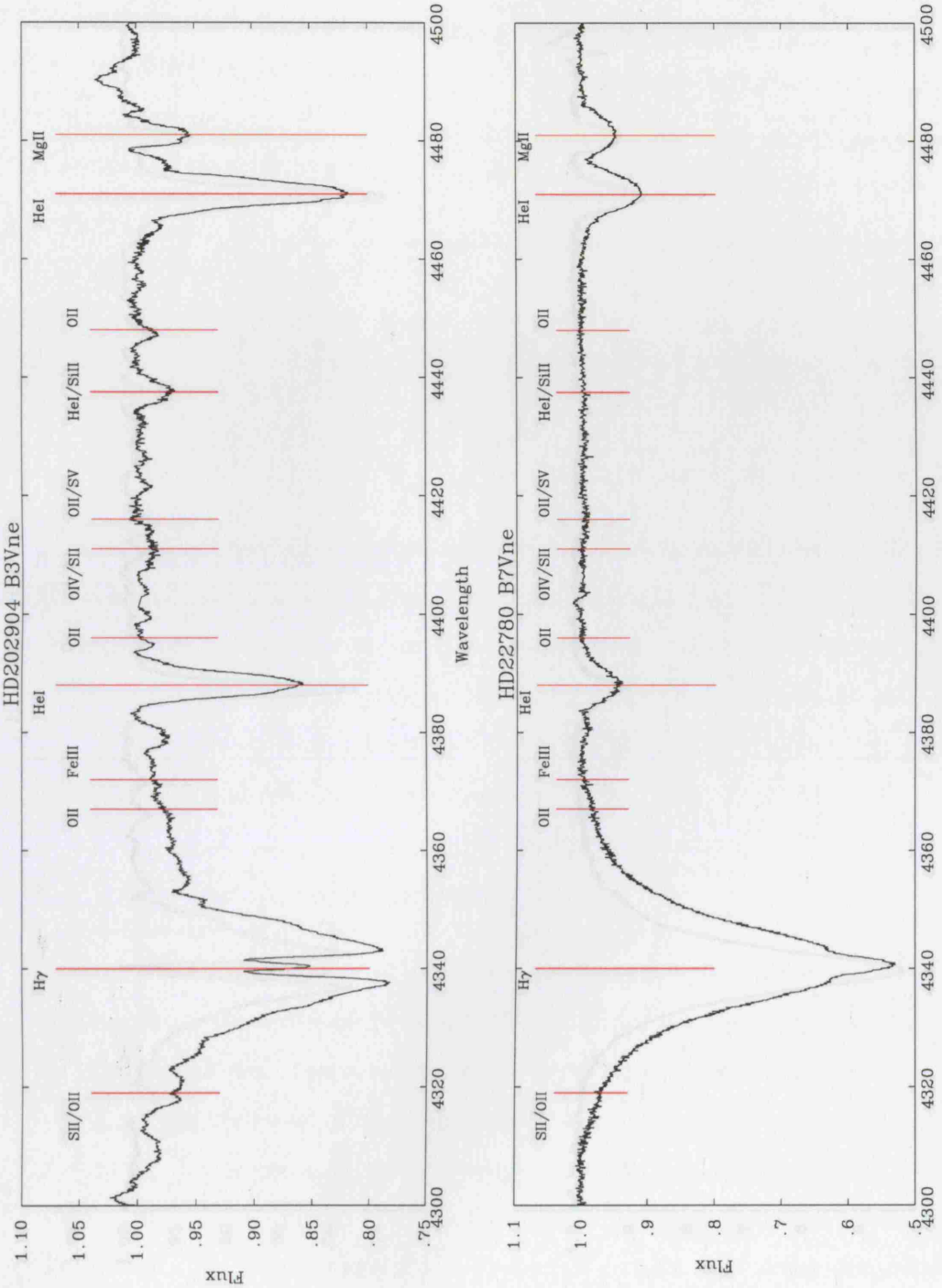

Figure 2.2. Two plots displaying Chauville's spectra for HD 202904 and HD 22780, classified as B3Vne and B7Vne (upper and lower panels) respectively.

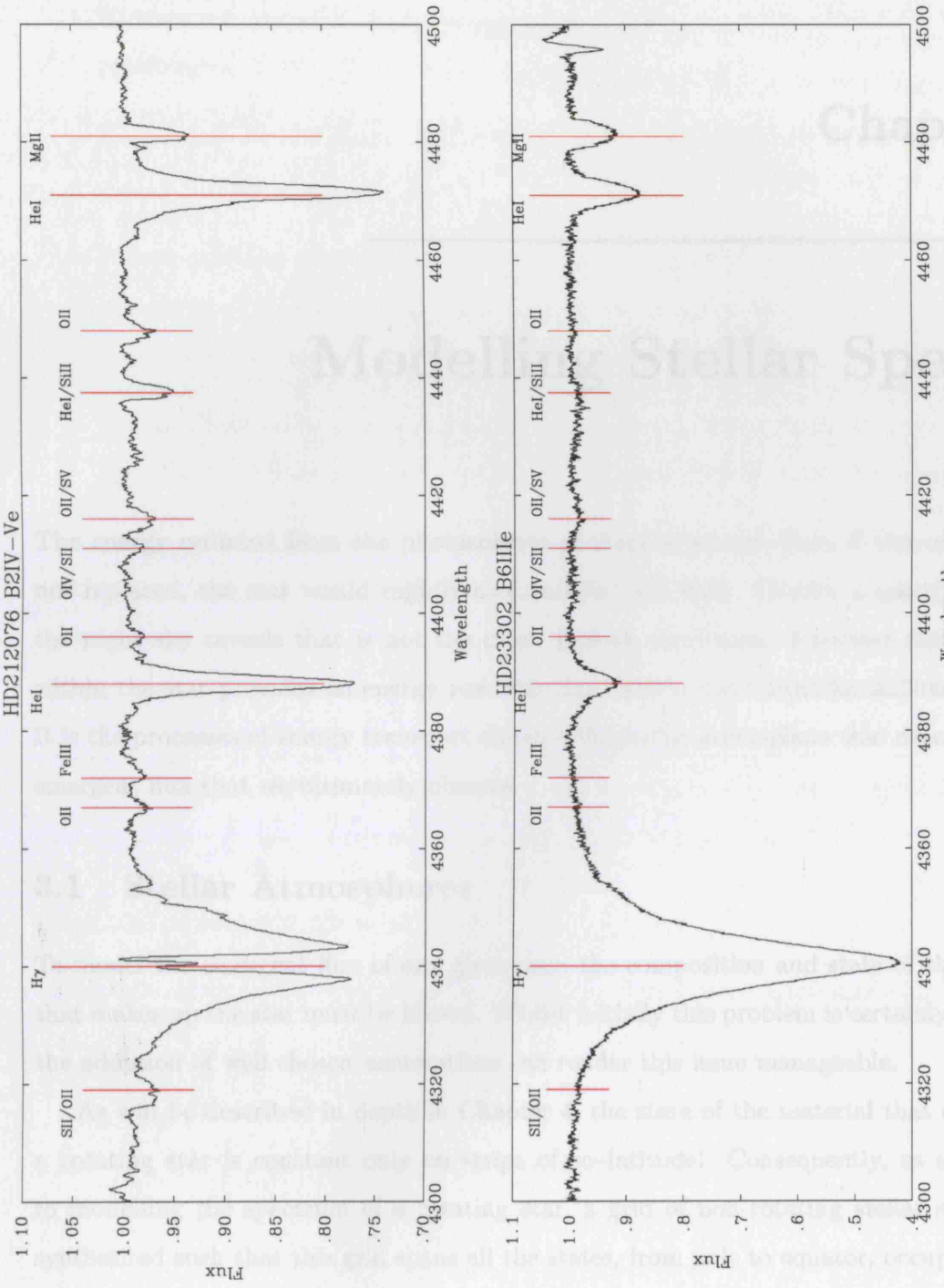

Figure 2.3. Two plots displaying Chauville's spectra for HD 212076 and HD 23302, classified as B2IV-Ve and B6IIIe (upper and lower panels) respectively.

Chapter 3

Modelling Stellar Spectra

The energy radiated from the photospheres of stars is so vast that, if this energy were not replaced, the star would rapidly cool and its light fade. Clearly, a quick glimpse of the night sky reveals that is not the case. Indeed, the fusion of nuclear material deep within the star provides an energy reservoir that fuels a star's light for millions of years. It is the processes of energy transport through the stellar atmosphere that determines the emergent flux that we ultimately observe.

3.1 Stellar Atmospheres

To model the emergent flux of any given star, the composition and state of the material that makes up the star must be known. Whilst initially this problem is certainly daunting, the adoption of well chosen assumptions can render this issue manageable.

As will be described in depth in Chapter 4, the state of the material that constitutes a rotating star is constant only on strips of co-latitude. Consequently, as a first step to modelling the spectrum of a rotating star, a grid of non-rotating stellar spectra are synthesised such that this grid spans all the states, from pole to equator, occupied by the rotating case.

The assumptions employed for the purposes of modelling a non–rotating B star spectrum, within the context of this research are detailed below.

- **Steady state:** no time dependencies exist.

- **Chemical homogeneity:** assumes the photosphere to have a chemically homogeneous make–up.
- **Hydrostatic equilibrium:** enforces the equality of gravitational force to internal pressures.
- **Radiative equilibrium:** imposes the restriction that only radiation transports energy through the photosphere.
- **Plane–parallel geometry:** assumes that the atmosphere of a star approximates to a series of plane–parallel, adjoining, layers, whereby each layer is idealised by a single state. Hence a 3–d problem reduces to a 1–d problem.
- **Local Thermodynamic Equilibrium:** assumes that collisional processes dominate the local level populations, i.e., the radiation field is locally isotropic.

These assumptions combine to distill the general problem of *radiative transport* to one of 1–d, time and state invariance. In other words, under these assumptions, a stellar spectrum can be synthesised from the specification of chemical abundances (metalicity) and the temperature and pressure structure down to a suitably high optical depth at which the transport becomes diffusive. To illustrate this more completely, the remainder of this section summarises the relevant physics and discusses how these assumptions lead to the method by which the grid of non-rotating–star spectra is generated.

3.1.1 Hydrostatic Equilibrium

The density structure in an atmosphere is described by hydrostatic equilibrium, given by,

$$\frac{dP_r}{d\tau_\nu} + \frac{dP_T}{d\tau_\nu} = \frac{g}{\kappa_\nu} \tag{3.1}$$

where P_r is the radiation pressure, τ_ν is the optical depth at a chosen frequency, κ_ν is the opacity at that same frequency, P_T is the thermal pressure and g the surface gravity. The definition of optical depth, here, is given by the equation[1]:

$$d\tau_\nu = \kappa_\nu \rho dr \tag{3.2}$$

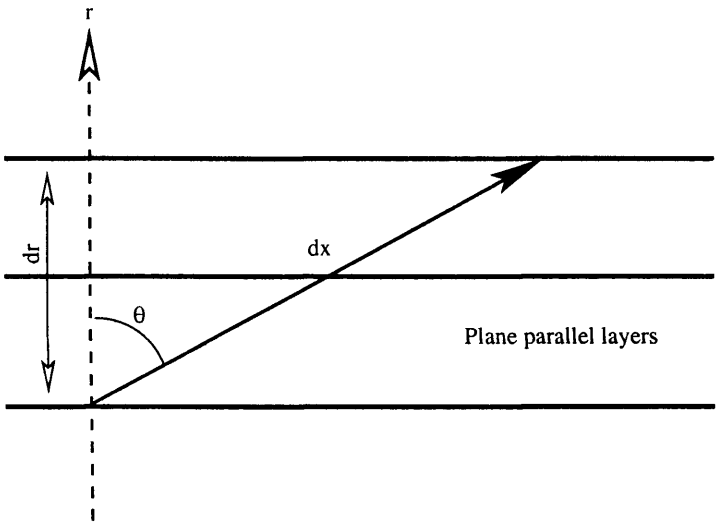

Figure 3.1. Schematic of a ray, at angle θ to the radial direction, passing from one homogeneous layer to the next.

3.1.2 Radiative Transfer

Returning briefly to the assumption that the stellar atmosphere being modelled is in a steady state, it is a natural consequence that the radiation transfer is also in a steady state. Clearly, if this were not the case the atmosphere would be heating or cooling. Consequently, the rate of change of the intensity spectrum with respect to some path length $\mathrm{d}x$ can be related to the difference between absorption and emission, over that path, with no time dependency. Thus a basic equation of radiative transfer is given by,

$$\frac{\mathrm{d}I_\nu}{\kappa\rho\mathrm{d}x} = I_\nu - S_\nu \equiv \frac{\mathrm{d}I_\nu}{\mathrm{d}\tau_\nu} \tag{3.3}$$

where I_ν is the intensity spectrum and S_ν is the source function, given by,

$$S_\nu = \frac{j_\nu}{\kappa_\nu} \tag{3.4}$$

where j_ν is the emission coefficient per unit mass and κ_ν is the absorption coefficient per unit mass.

Clearly, though, the path, $\mathrm{d}x$, here is arbitrary and, for the plane–parallel case, I_ν is a function of height $[I_\nu(r)]$. Hence, review of figure 3.1 implies that $\mathrm{d}r = \cos\theta\mathrm{d}x$, and thus a more general equation of radiative transfer is given by,

[1]Here, and throughout this thesis, the subscript ν implies a frequency dependence.

$$\mu \frac{\delta I_\nu}{\delta \tau_\nu} = I_\nu - S_\nu \tag{3.5}$$

where $\mu = \cos\theta$ and θ is the angle at which the intensity spectrum is considered. The intensity spectrum, $I_\nu(\tau)$, now has the formal solution given by:

$$I_\nu(\tau_\nu, \mu) = \frac{e^{\frac{\tau_\nu}{\mu}}}{\mu} \int S_\nu(\tau_\nu) e^{-\frac{\tau_\nu}{\mu}} d\tau_\nu \tag{3.6}$$

To solve both equations 3.1 and 3.5 requires a knowledge of the frequency dependent opacities through the stellar atmosphere. To know these demands a knowledge of the ionisation and population levels within the atmosphere. To calculate opacities, a knowledge of the temperature and pressure structure is required. Clearly, the interdependence here is problematic. However, this problem is simplified by assuming local thermodynamic equilibrium (LTE), alluded to in the opening paragraph of this chapter.

It is noted here however, that use of this simplification is not always appropriate for a whole host of reasons, not least of which is the science one is seeking to glean, however as explained in more detail at the end of this chapter, § 3.4, for the purposes of the research herein this assumption provides an adequate first order approximation.

3.1.3 Local Thermodynamic Equilibrium

The LTE approximation assumes that on a small enough scale we can approximate the local conditions of a gas to those of thermodynamic equilibrium. This in turn implies that the state of the gas is dominated by local processes – in practice, collisional processes (unless the mean free path for photons is not much greater than the mean free path for particles). A Maxwell–Boltzmann distribution is adopted and, as such, the local conditions can be characterised by temperature alone. Consequently the ionisation state of the gas is described by Saha's Equation:

$$\frac{N_{i+1} N_e}{N_i} = \left(\frac{2\pi m_e kT}{h^3}\right)^{3/2} \frac{2U_{i+1}}{U_i} e^{-I/kT} \tag{3.7}$$

where N_i is the number of ions in ionisation state i, N_e is the number of free electrons (essentially liberated by the ionisation itself), m_e is the electron mass, U_i is the partition

function for state i, I is the ionisation potential and all other variables have their usual meanings.

The excitation level populations for each ion are described by the Boltzmann Equation:

$$\frac{N_n}{N} = \frac{g_n}{U} e^{-E_n/kT} \tag{3.8}$$

where N_n is the number of ions in excitation state n, N is the total number of ions, g_n is the probability of excitation to state n, U again is the partition function of the ionisation state, E_n is the excitation energy and the remaining constants again have their usual meanings.

And finally, by assuming LTE, it is also possible to approximate the radiation field locally, i.e., approximate the source function S_ν, by Planck's Equation:

$$S_\nu = B_\nu(T) = \frac{2h\nu^3}{c^2} \frac{1}{e^{h\nu/kT} - 1} \tag{3.9}$$

where all variables have their usual meanings.

So, by use of equations 3.1, 3.5, 3.7, 3.8 and 3.9 there is the basis to begin an iterative process through which the detailed structure of the atmosphere, and hence emergent spectrum, can be determined.

3.1.4 An LTE solution for stellar atmospheres

The $T - \tau$ relation

As alluded to above, to synthesise an emergent spectrum requires an iterative process that converges to a solution. To achieve convergence generally requires that the start point is sufficiently close to the actual solution. To provide that start point one common approach is to make the 'grey atmosphere approximation'. Essentially the grey atmosphere assumes that opacity, hence also optical depth, is independent of frequency. Subsequently, by asserting LTE and radiative equilibrium, the effective temperature of the emergent flux is related to the temperature at a given optical depth by,

$$T^4(\overline{\tau}) = \frac{3}{4} T_{\rm eff}^4 [\overline{\tau} + q(\overline{\tau})] \tag{3.10}$$

where $\overline{\tau}$ is independent of frequency and $q(\overline{\tau})$ is known as the Hopf function which essentially allows the variation of temperature with optical depth to take on a non–linear form[2].

The iterative procedure

With a $T - \tau$ relation approximated, a calculation of the corresponding pressures, at these depths, is required. This can be achieved by, again, utilising the grey atmosphere approximation to assign a mean opacity with which to begin an iterative process. Hence, starting at the stellar surface (where the pressure and temperature are assigned), a starting opacity is assumed and consequently the equation of hydrostatic equilibrium (eqn., 3.1) is solved for the pressure change over the first step in optical depth,

$$P(\tau + \Delta\tau) \;=\; P(\tau) + (g/\kappa_0)\Delta\tau \tag{3.11}$$

With a temperature and pressure estimate for the first step in optical depth, the ideal gas equation can be utilised,

$$P_g \;=\; NkT \tag{3.12}$$

[where P_g is the gas pressure, N is the number of particles and k is Boltzmann's constant], and hence calculate the ionisation and level populations from equations 3.7 and 3.8. The opacities can now be calculated directly and consequently, the pressure can be recalculated, over this first step, with the improved opacities. This pressure–opacity cycle is repeated until a convergence is achieved. This process can now be repeated for the next optical–depth step – and so on until a set of converged pressures and opacities are calculated at all depths. Finally, a revised $T - \tau$ relation is calculated (via e.g., a perturbation method[3]) for this new set of opacities before returning to the top of the atmosphere and repeating this entire process until a convergence in both temperature and pressure is attained.

[2]A common form of this general equation is the Eddington approximation which derives the Hopf function to be a constant.

[3]See Mihalas 1978 for a detailed discussion.

3.2 ATLAS9

Provided with an effective temperature and surface gravity, $\log g$, of a star, the ATLAS9 code (Kurucz 1993) solves the equations of hydrostatic equilibrium, eqn 3.1, and radiative transfer, eqn 3.5, via a similar method to that described above, § 3.1.3. It utilises a method for solving the equation of radiative transfer that bins the frequency such that it averages continuum and line opacities over relatively broad regions and thus saves considerably on processing time. The consequence of this, however, is that it does not produce a detailed emergent spectrum for the given input parameters but rather produces a converged line–blanketed – LTE – plane parallel structure for the stellar atmosphere: the, so called, Kurucz structure. Kurucz structures essentially embody the key information that describes a stars atmosphere, namely the temperature and pressure profile as it changes with optical depth through the atmosphere. Thus, with a converged temperature and pressure profile for an atmosphere (of a given $T_{\rm eff}$, surface gravity and metalicity) the equation of radiative transfer is solved directly and an emergent spectrum obtained. This research used the spectrum synthesis code known as SYNSPEC for this purpose.

3.3 SYNSPEC

SYNSPEC is a spectrum synthesis program (described briefly by Hubeny et al. 1985). It takes as input a model atmosphere (in this case, a Kurucz structure) and a line list and, by dynamically selecting all the lines that contribute to the total opacity, it then solves the Radiative Transfer Equation, 3.5, over a user specified wavelength range and resolution.

The output from SYNSPEC can be provided in several different formats. For the purposes of the research described herein the output generated was continuum plus line blanketed, angle dependent (implicitly, limb darkened) intensity spectra over the wavelength range 4300Å - 4700Å (See § 4.2).

3.4 Summary

As discussed in this chapter, there are several approximations made in the production of the synthetic stellar spectra used for this research. However, whilst most of these assumptions adequately represent conditions deep within a star, they do will, generally, break down in the outer regions of the photosphere. A more rigorous treatment comes in the

form of a non–local thermal equilibrium (NLTE) solution. However, the complications that arise from NLTE require computing resources and time which may not always pay dividends. Comparisons between LTE and NLTE constructed spectra for B star fundamental parameter space have been shown to produce little by way of differences (Lanz & Hubeny 2007). The differences that do arise tend to be confined to the line cores of the major transitions (e.g., Balmer, He I, Mg II, Si II and Si III lines in particular). It is further noted that the wings of H–Balmer lines can be understated in the LTE case, thus a marginal overstatement of the surface gravity can result. To illustrate these points, a comparison of LTE–vs–NLTE synthetic spectra is presented in figures 3.2, 3.3, 3.4 and 3.5. These figures display different $T_{\rm eff}$–log$g$ combinations, with each plotting the respective LTE and NLTE spectra with their difference spectrum over–plotted. The LTE models were custom constructed using the ATLAS9 and SYNSPEC code described within this chapter. The NLTE spectra were obtained from the BSTAR2006 grid courtesy of the TLUSTY website (ref. Lanz & Hubeny 2007) Review of these four plots highlights several key issues, listed below.

- In general, discrepancies are confined to the line cores and at most are of just a few percent. The exceptions to this are the Hγ and He I lines in the high $T_{\rm eff}$ – low log$g$ case and the He Iλ4471 in the low $T_{\rm eff}$ – low log$g$ case.

- Keeping $T_{\rm eff}$ constant and varying log$g$ from a low to high value reduces the weak transitions throughout the spectrum whilst marginally broadening, and strengthening the discrepancy in the Hγ line, only.

- Keeping log$g$ constant and varying $T_{\rm eff}$ from a low to high value increases the strengths of the weak lines but makes very little difference to the discrepancies[4]

Of particular interest resulting from these comparisons is the low $T_{\rm eff}$ – low log$g$ and high $T_{\rm eff}$ – high log$g$ cases. These two cases (figs., 3.2 and 3.5) are the most representative of the equator to pole relation, of $T_{\rm eff}$ and log$g$, intrinsic to the rapidly rotating star problem. In both cases two of the three key diagnostic lines (Hγ and Mg II) have all the discrepancies confined to less than $\sim$2%. In respect of He Iλ4471, it is only the equatorial emission component that leads to a more significant discrepancy. However, this difference is clearly confined to a very narrow region of the line core. What this illustrates is that, use of

[4]With the clear exception already noted.

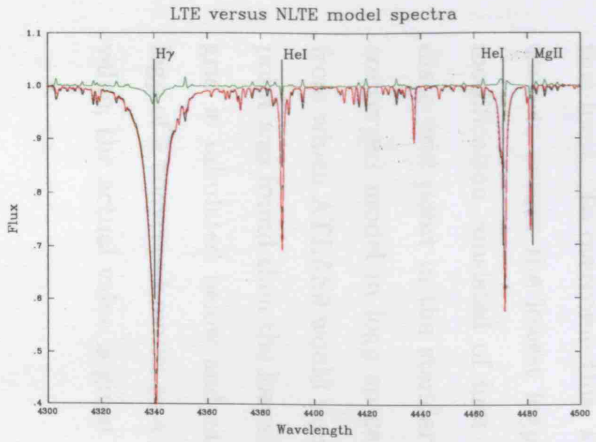

Figure 3.2. LTE vs NLTE for $T_{\rm eff}$ = 16kK and log$g$ = 3.0. The black line is the LTE spectrum, the red line is the NLTE spectrum and the green line is the difference spectrum.

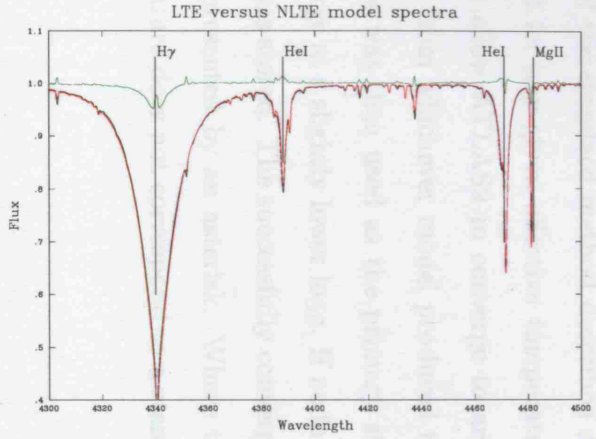

Figure 3.3. LTE vs NLTE for $T_{\rm eff}$ = 16kK and log$g$ = 4.5. The black line is the LTE spectrum, the red line is the NLTE spectrum and the green line is the difference spectrum.

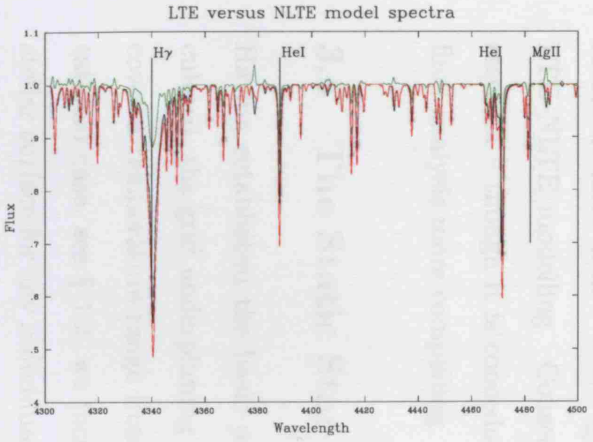

Figure 3.4. LTE vs NLTE for $T_{\rm eff}$ = 24kK and log$g$ = 3.0. The black line is the LTE spectrum, the red line is the NLTE spectrum and the green line is the difference spectrum.

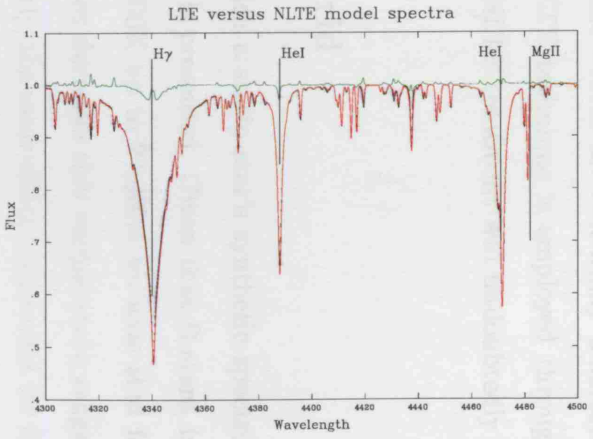

Figure 3.5. LTE vs NLTE for $T_{\rm eff}$ = 24kK and log$g$ = 4.5, The black line is the LTE spectrum, the red line is the NLTE spectrum and the green line is the difference spectrum.

the LTE approximation is acceptable provided the line cores are not key to the analysis. In the context of the null hypothesis this proves convenient, i.e., it is a measurement of the width of these absorption lines that leads to the conclusion that these stars do not rotate at more than $\sim$0.80 $V_{\rm eq}/V_{\rm crit}$ – The line widths are essentially unaffected by the LTE–NLTE modelling. Consequently, the LTE technique is employed throughout this research – though it is conceded that a full NLTE treatment will undoubtedly make the final analysis more compelling.

3.5 The Static Star Model Grid

Having established the basic process by which a static star's synthetic spectrum is calculated, the grid underpinning this research is presented. Given that B stars, in general, cover a temperature range from around 12,000K up to 27,000K we note that for the rotational case, see § 1.2, we increase as well as decrease this temperature range over the stellar surface for any individual case. Similarly, the same effect is apparent for the surface gravity. Indeed, by the definition of Von Zeipel's law already presented, see § 1.2.3, the effective temperature and surface gravity are intrinsically linked. Thus the static star grid generated spans a $T_{\rm eff}$ range 6,000K–50,000K, in steps of 2,000K, and a range in log$g$ from 1.2–6.0, in steps of 0.3dex. Where the selected model parameters start to approach the Eddington limit[5] ATLAS9 would often fail to converge, despite being somewhat short of this limit. To overcome this, an alteration of the standard method described above was used to ensure the lowest log$g$ was obtained for any given effective temperature. This modification consisted of first attempting to allow ATLAS9 to converge to an intermediate grid point in the standard way. Then, from whichever model produced the lowest converged model in log$g$ space, the structure was then used as the primary start point from which ATLAS9 would then try to converge at a slightly lower log$g$. If no further grid point was found then the lowest log$g$ model was stored. The successfully converged model grid is tabulated below and each success represented by an asterisk. Where the lowest log$g$ of a converged model at a given temperature does not correspond to a standard grid value, the actual value is given in the table.

[5]The Eddington limit, or luminosity, is the limit at which radiation pressure equals gravity.

Table 3.1. ATLAS9 and SYNSPEC generated model grid of static star case - Table showing where models successfully converged for a given Mass, log$g$, and effective temperature $T_{\rm eff}$.

	log$g$												
	1.2	1.5	1.8	2.1	2.4	2.7	3.0	3.3	3.6	3.9	4.2	4.5	4.8
$T_{\rm eff}$ (kK)													
6.0	*	*	*	*	*	*	*	*	*	*	*	*	*
8.0	-	-	-	*	*	*	*	*	*	*	*	*	*
10.0	-	-	-	-	2.6	*	*	*	*	*	*	*	*
12.0	-	-	-	-	-	*	*	*	*	*	*	*	*
14.0	-	-	-	-	-	*	*	*	*	*	*	*	*
16.0	-	-	-	-	-	*	*	*	*	*	*	*	*
18.0	-	-	-	-	-	*	*	*	*	*	*	*	*
20.0	-	-	-	-	-	*	*	*	*	*	*	*	*
22.0	-	-	-	-	-	*	*	*	*	*	*	*	*
24.0	-	-	-	-	-	2.8	*	*	*	*	*	*	*
26.0	-	-	-	-	-	-	3.1	*	*	*	*	*	*
28.0	-	-	-	-	-	-	3.2	*	*	*	*	*	*
30.0	-	-	-	-	-	-	-	3.4	*	*	*	*	*
32.0	-	-	-	-	-	-	-	-	*	*	*	*	*
34.0	-	-	-	-	-	-	-	-	3.8	*	*	*	*
36.0	-	-	-	-	-	-	-	-	-	4.0	*	*	*
38.0	-	-	-	-	-	-	-	-	-	-	*	*	*
40.0	-	-	-	-	-	-	-	-	-	-	4.3	*	*
42.0	-	-	-	-	-	-	-	-	-	-	4.4	*	*
44.0	-	-	-	-	-	-	-	-	-	-	-	*	*
46.0	-	-	-	-	-	-	-	-	-	-	-	*	*
48.0	-	-	-	-	-	-	-	-	-	-	-	4.6	*
50.0	-	-	-	-	-	-	-	-	-	-	-	4.7	*

Chapter 4

Be-Star Model Grid

Depending on what observational data are available for any given star, failure to consider the physical effects of rotation (beyond the simple doppler broadening of spectral lines) can result in an over or under-estimation of all the remaining physical parameters one is trying to determine. As has already been indicated in § 1.2 the effect of rotation is to distort the star's geometry to one approximated by an oblate spheroid, and to introduce pole–to–equator gradients in surface temperature and gravity. Hence, depending on the specific angle at which one views a given star, physical parameters such as mass, luminosity, radius and hence even the stars location upon the evolutionary track of main–sequence life are likely to be distorted. Thus, characterising a rapidly rotating star with a single effective temperature without independently obtaining an accurate measure of the rotational velocity, mass and viewing angle clearly can lead to a gross miss-classification.

It is therefore the method of this research to generate a detailed multi-parameter grid of rotating–star models which are then simply compared to Be star spectra through RMS fitting of key diagnostic lines, subsequently checked by eye.

This chapter details the Roche approximation for the geometry of rotating stars' photospheres and specifically presents the method by which the BUSH code[1] employs this geometry to generate the model Be star spectra.

[1]The BUSH code was developed by Prof. I. Howarth. It was originally employed and briefly described in the paper Howarth & Smith (2001)

4.1 The Rotating Case

The gravitational potential energy of a mass can be expressed in a general form by the following equation:

$$\Phi = \int \frac{G}{r^2} \left(\int \rho(r, \theta, \phi) dV \right) dr \tag{4.1}$$

As is clear from this, attempting to model a stars gravitational potential energy (G.P.E.) for an arbitrary mass distribution is non trivial. However, simple modelling of a star's density profile quickly identifies the almost asymptotic decline in density as one goes from centre to surface. The implication is that one can simplify the above equation by assuming the G.P.E. approximates to a central mass solution. This approximation is known as the Roche approximation and expresses the net of gravitational and rotational energies in terms of a single potential.

4.1.1 The Roche Model

The Roche approximation for the total potential, Ψ, at some distance, r, from a central mass, M, is given by:

$$\Psi = \Phi + V = -\frac{GM}{r} - \frac{s^2\omega^2}{2}, \tag{4.2}$$

where s is the perpendicular distance from the axis of rotation, r is the displacement from the central mass, Φ is the gravitational potential, V the rotational energy and ω the rotational velocity.

A solution for r which is in steady state must be coincident with an equipotential solution to this equation, i.e., Ψ is a constant. Hence the potential which describes the surface geometry can be written as:

$$-\Psi = \frac{GM}{r} + \frac{s^2\omega^2}{2} = \frac{GM}{r_p}, \tag{4.3}$$

where r_p is the polar radius.

4.1.2 Gravity Darkening

Hydrostatic equilibrium - for rotating stars

To establish an equation that expresses the effect of gravity darkening, it is helpful to rewrite the equation of hydrostatic equilibrium (ref. equation 3.1) in its simpler, more general, form:

$$\nabla P = -\rho \nabla \Psi \tag{4.4}$$

In words, this says that any surface of constant pressure must coincide with a surface of constant potential, i.e., $P = P(\Psi)$. If the gas is assumed to behave as an ideal gas then temperature also must be a function of the potential, leading to:

$$T = T(\Psi). \tag{4.5}$$

(for a chemically homogeneous gas in hydrostatic equilibrium.)

Radiative transport

The process of radiative transport in a stellar interior is diffusive. The diffusive flux, j, between regions of differing densities, n, may be written as:

$$j = -D \nabla n \tag{4.6}$$

where D is the coefficient of diffusion; for the radiative case:

$$F = -D_{\rm ph} \nabla u \tag{4.7}$$

where $D_{\rm ph}$ now represents some photon diffusion coefficient and u is the energy density of radiation, itself given by:

$$u = aT^4 \tag{4.8}$$

where a is the radiation–density constant ($\frac{4\sigma}{c}$). Hence the diffusive flux of radiative energy, F, may be written as:

$$F = -D_{\rm ph} a \nabla(T^4). \tag{4.9}$$

Using equation 4.5, the diffusive flux of radiative energy becomes:

$$F = -4D_{\rm ph} a T^3 \nabla T = 4DaT^3 \frac{dT}{d\Psi} \nabla\Psi \tag{4.10}$$

Hence, noting that $\nabla\Psi = g$, this is rewritten as:

$$F = k(\Psi) g \tag{4.11}$$

This is, in essence, gravity darkening. As the effective gravity drops due to increasing centrifugal forces from pole to equator, so does the diffusive (hence emergent) flux. Of course, the emergent flux is not diffusive – but the lower boundary of the atmosphere reflects the diffusive flux, provided the energy transport is radiative. Consequently, the equatorial regions of rapid rotators can be significantly cooler than their respective poles.

4.2 Wavelength Range Selection

The standard temperature–sequence diagnostic for B stars is the He Iλ4471/Mg IIλ4481 ratio (He I decreasing in strength to cooler temperatures, Mg II increasing), while the Balmer lines are the standard luminosity–class (i.e. gravity) discriminant, because of the pressure sensitivity of the line wings. These diagnostics conveniently transfer to rapidly rotating stars, although the additional model parameter of viewing angle (for a given $v/v_{\rm crit}$ and $v\sin i$) means that one has to consider profile information, not just line strength. We therefore synthesise the 4300 – 4700Åwavelength range, encompassing these features.

4.3 The Model Grid

Synthesising the spectrum

The *effective temperature* of a star is the temperature of a blackbody characteristic of the emergent flux. However, equation 4.11 implies that the emergent flux of a rotating star

consists of components emitted from regions of differing *local "effective temperatures"*. These local temperatures, though, are identical for identical $g_{\rm eff}$'s, i.e., on strips of constant co–latitude, with symmetry about the equator. Consequently, and in tandem with equation 4.3, by specifying: polar gravity, polar temperature, rotational velocity and the fraction of critical rotation, it is possible to deduce the stellar mass, radii, and spread of temperatures and gravities from pole to equator. With this description, the rotating stars surface is then divided into these constant–latitudinal strips, with each strip assigned its respective effective gravity and temperature. Subsequently, each strip is divided into individual facets for which a projected velocity, projected area and specific intensity spectrum are allocated. Hence, by specifying a viewing angle, the emergent flux from each facet is extracted by angle, scaled relative to the facet's projected area and doppler shifted relative to its projected velocity. Finally, all of these individual fluxes are summed and the synthesised spectrum is complete.

The model grid

The previous method details how the BUSH code, employed for this research, synthesises a spectrum for a rapidly rotating star. For the purposes of this research, this code is supplied with the polar gravity (log $g_{\rm pole}$), effective temperature ($T_{\rm eff}$)[2], equatorial velocity ($V_{\rm eq}$), inclination (i) and the ratio of equatorial to critical velocity ($V_{\rm eq}/V_{\rm crit}$, fixed at 0.95)[3]. A grid of near–critically–rotating B–star spectra is synthesised through varying these fundamental parameters ($T_{\rm eff}$, *log* $g_{\rm pole}$, $V_{\rm eq}$, i). To span the entire range of B star possibilities, the following parameter space is explored: $T_{\rm eff}$ from 12000–30000K in 2000K steps; log $g_{\rm pole}$ from 2.7dex–4.8dex in 0.3dex steps; $V_{\rm eq}$ from 250–500km/s in 50km/s steps; i from $0 - 90°$ in 15° steps. For each grid point a line blanketed spectrum and a continuum model is produced. Consequently, a simple division provides a normalised spectrum output for every grid point.

This entire process is executed via a shell script which explores the full grid space. The production of both a spectrum and continuum for a given grid point takes approximately 4 minutes using a 1.8GHz, 64bit, processor with 1GB RAM and 333MHz FSB.

[2]In the case of the rotating star, $T_{\rm eff}$ refers to the temperature of the blackbody characteristic of the total emitted flux from the entire star

[3]The BUSH code will accept parameters in a variety of combinations provided all fundamental parameters are represented in some fashion, e.g., mass, temperature, radius, rotation.

Selection criteria - too cool

The grid of Kurucz/SYNSPEC models was truncated at a cool limit of 6000K due to the growing importance of molecules at lower temperatures[4]. Thus, allowing for uncertainties in classification and potential viewing-angle effects, for $V_{\rm eq}/V_{\rm crit} = 0.95$, this limits the spectral–type temperatures that can be satisfactorily modelled to > 11750K. We therefore remove from consideration the 18 stars in the Chauville et al. (2001) data–set classified B8 or later.

4.4 The Model fitting procedure

With a complete grid of normalised, rapidly–rotating, model spectra and the normalised Be star spectra of Chauville et al. (2001) a formal comparison is performed. In the light of the science goals of this thesis, a simple mean square of residuals calculation is performed over the key areas to be fit. Specifically, the wings of the Hγ line, He Iλ4471 and the complete Mg II line profile are extracted from both model and observation. This 'extraction' is performed by re–griding the data onto common wavelength grids whilst also taking a select number of data points from each region to provide an intrinsic weighting. Then the mean square of the residuals is calculated for each observation versus every model spectrum.

[4]No molecular line lists are readily available for SYNSPEC

Chapter 5

Results

Determining whether any given model is an acceptable reproduction of a real spectrum, and hence inferring that its parameters are representative of the star's fundamental parameters, is non-trivial, and it will always be the case that some level of subjectivity is a prerequisite for 'acceptance' to occur. However, in the context of this research, no model–atmosphere calculation ever matches an observed spectrum to within the formal statistical uncertainties, and that (unfortunately) it's necessary to make recourse to other criteria (for the plausibility of inferred parameters). Thus though the determination of a mean square of residuals provides the starting point to this analysis, the secondary focus is on the Hertzsprung-Russell diagram and the relation of model–fit parameters to those which are empirically derived. This not only acts as a useful independent test of whether the model fits are indeed appropriate, but it also provides some interesting insight into the natural subdivisions that exist in Be star spectra and the susceptibility of model fitting procedures to unacceptable results. Beyond this, these results provide the impetus for a 're-think' of Be star astrophysics, discussed in Chapter 8.

The model grid is compared to 95[1] of the 116 stars published by Chauville et al. (2001)[2], by determining the mean square of residuals (models to spectra) over the red and blue wings of the Hγ absorption line, the blue wing of the He I λ4471Å absorption line, as

[1] 18 of the 116 Chauville stars are excluded as per §4.3, another 3 are excluded as they do not have complete coverage of the Hγ, He I and Mg II lines key to this analysis.

[2] They present 271 individual spectra; Eighty–eight stars have multiple spectra which were co–added, producing 116 spectra used for this analysis.

well as the red wing of the He I λ4471Å blended with the Mg II λ4481Å absorption line. As noted in §4.2, these 3 lines provide sensitivities to surface gravity, high temperature and low temperature respectively. Thus the ability to fit well all 3 lines provides a high degree of confidence as to the overall 'fit' of the model fundamental parameters, i.e., inclination of rotation axis (i), equatorial rotational velocity ($v_{\rm eq}$), polar surface gravity ($\log g$) and effective temperature ($T_{\rm eff}$). Clearly this necessitates coverage of all three lines and as a consequence 3 of the 116 Chauville spectra lacking complete wavelength coverage are excluded from the analysis.

5.1 Chapter outline

It would be excessive to detail the analysis of each of the 95 Chauville spectra analysed in testing the model grid. Consequently, this chapter presents a selection 19 of the 95 spectra, chosen on the basis of their locations on key correlation plots (described below, §5.3). This hopefully provides insight into the processes employed. To this end, the remainder of this section introduces the two main tools utilised throughout this chapter; the Hertzsprung–Russell diagrams and the temperature correlation plots.

5.1.1 The Hertzsprung–Russell diagram

Hertzsprung–Russell (H–R) diagrams essentially plot luminosities against effective temperature. Throughout this chapter, and the remainder of this thesis, the H–R diagrams displayed plot absolute magnitude against effective temperature. On each diagram, model derived values are over–plotted along with spectral–type derived values. In respect of the models, these parameters are absolute in that the modelling process provides all the relevant data to locate a precise point in the diagram. In respect of the observational data, this is not the case; the observational data are drawn from different sources that have employed differing methods to arrive at values for the individual stars. First of all, the spectral types are derived from two different methods:

- *The BCD classification scheme*, detailed in the definitive paper of Chalonge & Divan (1952) is a spectrophotometric method. In this scheme, the parameters used to classify B stars are D, a measure of the Balmer jump ($D = \log F_R - \log F_B$, where F is the flux redward, R, and blueward, B, of the Balmer jump), and λ_1 which gives the effective wavelength at which the jump occurs. These two parameters are

used as indicators of spectral subtype (equivalently, temperature) and luminosity, respectively, where the BCD spectral types have been calibrated to match those of the MK system.

- *The MK system*, by comparison, is a purely spectroscopic method and assigns a spectral type by the presence of absorption lines and their respective line strength ratios; this was discussed in §1.2.

Allocating a spectral type by one of these two methods, Chauville et al. 2001 applied the BCD calibration of effective temperature. This assumes that the BCD–to–MK calibration of spectral type is unaffected by rotation and hence a one–to–one relationship remains. This assumption has not been substantiated. Consequently, those stars which are primarily classified by the BCD method alone (hereafter, BCD) are treated here as a separate population to those classified, and subsequently assigned fundamental parameters, by the MK and BCD method combined (hereafter, MK+BCD).

Chauville et al. 2001 used, where possible, a fully BCD derived spectral type and temperature. However, where the relevant data were lacking they used previously published MK spectral types[3], which were then employed to read off a BCD temperature.

With a temperature assigned to each star, an absolute magnitude is required to locate its place on the H–R diagram. The apparent magnitude and parallax of each object considered here is obtained from the revised Hipparcos Catalogue [van Leeuwen (2007), by Astrogrid]. These data then enable an absolute magnitude, with Hipparcos error, to be calculated. In addition, visual extinction values have been calculated from the Hipparcos $(B-V)$–magnitudes in conjunction with the intrinsic colour versus spectral–type values $[(B-V)_0]$ of Underhill & Doazan (1982); $E_{\mathrm{B-V}} = (B-V)-(B-V)_0$. These extinction values were combined with the Hipparcos–derived absolute magnitudes, $M(V)_{\mathrm{Hip}}$. These total errors are displayed an all of the H–R diagrams plotted and the upper and lower $M(V)_{\mathrm{Hip}}$ bounds are tabulated in appendix B and D. It is noted here that reddening due to the circumstellar excess is not accounted for in this calculation. It is further noted that the technique presented by Howells et al. (2001) (which utilises photometry from 3 infrared (IR) bands [J, H, K] to establish this excess) would be ideal. Given the variable nature of these disks, one should ideally obtain these IR data as close to the date of the

[3]Review of all the related sources from which Chauville et al. (2001) drew their data [in particular Ballereau et al. 1995, Moujtahid et al. 1998 and Zorec & Briot 1991] reveals that seven stars, claimed to be BCD sources, in fact belong to the MK+BCD.

optical spectroscopy as possible to enable an accurate measure of this excess as it relates to the observations used herein. No IR photometry is known to have been observed for the Chauville data and consequently this technique has not been applied here. However, according to the results of Howells et al. (2001), the maximum impact on E(B-V) was no more than a few tenths of a magnitude which, in conjunction with the Hipparcos uncertainties, should have a minimal effect to the results presented here.

5.2 Effective–temperature correlation plots

In conjunction with the H–R diagrams, two additional plots of the model–to–spectral type temperatures are employed here. One plot displays the spectral–type–assigned versus model–effective temperatures, the other displays the spectral–type–assigned versus model–apparent temperatures. These plots provide an additional aid to help identify which models are apparently well correlated to spectral types and which are not.

For clarity, the following terms, and abbreviations are defined:

- The spectral–type–assigned effective temperatures, $T_{\rm sp}$, are defined to include either/or the BCD–only and MK+BCD derived effective temperatures.
- The model–assigned effective temperatures, $T_{\rm mod}$, are the 'true' effective temperature of the model fits. It is important to recognise that these are not angle dependent.
- The model–assigned apparent temperatures,$T_{\rm app}$, account for the viewing angle dependency of 'measuring' an effective temperature. This is the value expected to correlated most closely with $T_{\rm sp}$.

5.3 Chapter structure

The presentation of the initial results is split into 4 sections, as follows:

- §*5.4* begins with a brief discussion of the H–R diagram and temperature–correlation plots for the entire population of 95 spectra and MS–model fits.
- §*5.5.* From the population of 95 spectra, 29 spectra that do not show Balmer emission are split out; the H–R and temperature plots recreated; and the results discussed. From this population, 3 outliers and 3 close–correlated Be stars are selected

(identified from the temperature correlation plots); for each sub–set, 2 BCD and 1 MK+BCD objects are discussed in detail.

- §*5.6* From the population of 95 spectra, 66 spectra that *do* show Balmer emission are split out; the H–R and temperature plots recreated; and the results discussed. From this population, a further 9 Be stars are singled out from the temperature correlation plots, 4 outliers and 5 close–correlated; for the outlier sub–set, 3 are drawn from the MK+BCD population and 1 from the BCD; for the correlated sub–set, 3 are drawn from the MK+BCD population and 2 from the BCD. These are all discussed in detail.

- §*5.7* From the population of 66 spectra that show some level of Balmer emission, 44 that show *clear*, pronounced Balmer emission in the Hγ line are separated out. Again, the H–R and temperature correlation plots are displayed and the implications discussed. From this population, 4 outliers are selected from the temperature correlations, plotted and discussed in detail.

- §*5.8* concludes this chapter with a brief summary.

5.4 Be-star model fits to all spectra

Figure 5.1 displays an H–R diagram with $T_{\rm app}$ versus model–derived absolute magnitudes, $M(V)_{\rm Mod}$, and $T_{\rm sp}$ versus Hipparcos derived absolute magnitudes, $M(V)_{\rm Hip}$. The first point to note is that the model results loosely span the same parameter space as that of the spectral type and Hipparcos data. If they did not do so significant doubt would be cast on the plausibility of these model fits. Despite this, there is a general lack of overlap with model–to–empirical data, with ~30% of the model fits sitting well above the main sequence.

The bottom two panels of figure 5.1 examine the correlation between model–derived temperatures and spectral–type–derived temperatures. These two plots show similar distributions approximately correlated to the 1:1 line with a standard deviation of $\sim$ 20%. However, there is a distinct asymmetry exhibited in both panels which is suggestive of underestimation of model effective temperatures

Whilst it is possible that the method by which the BCD parameters are calibrated to MK spectral types holds for all rotational velocities, it is clearly also possible that this

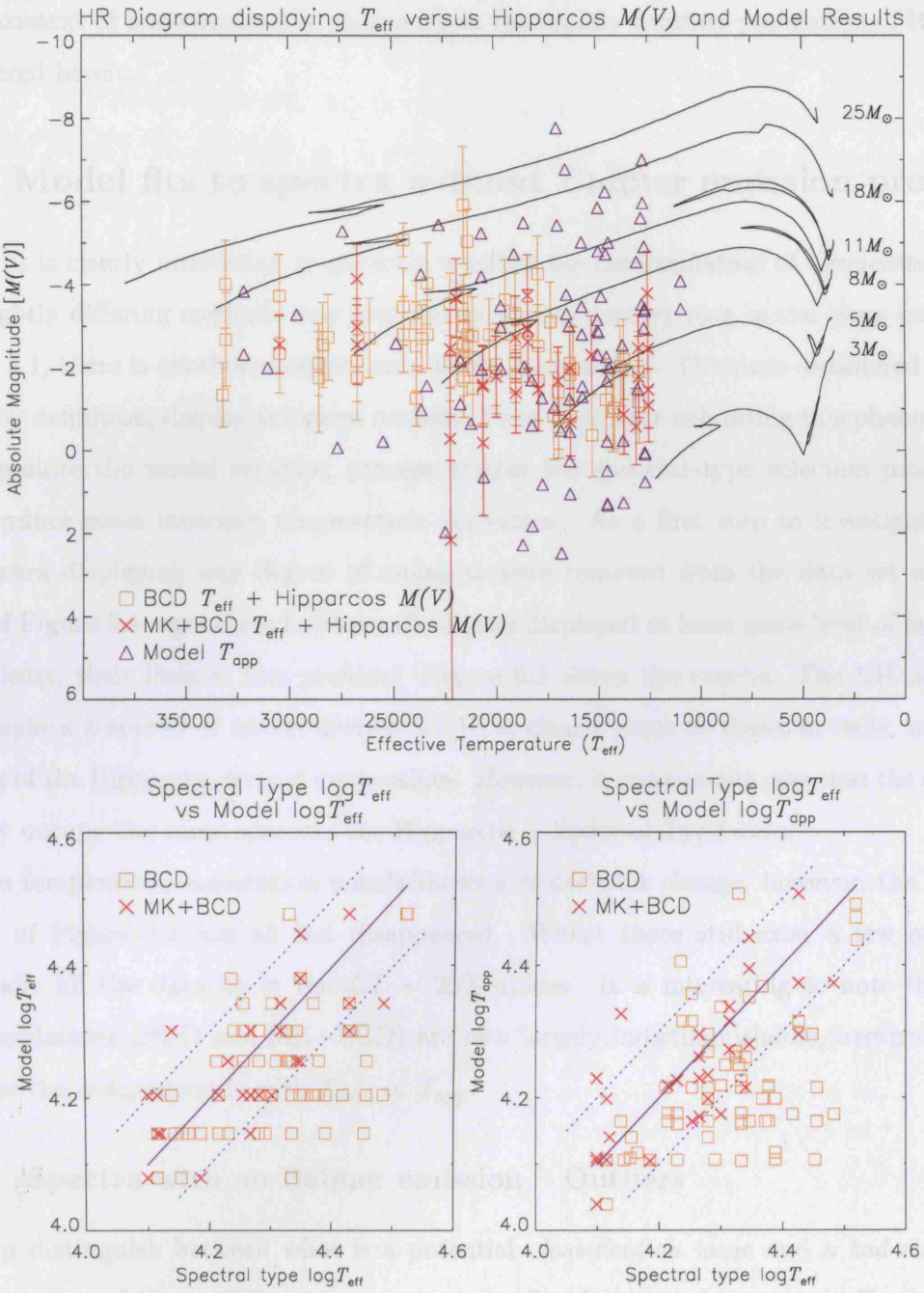

Figure 5.1. *The top panel* displays an H–R diagram for each of Chauville's stars: T_{sp} vs $M(V)_{Hip}$ (orange square and red cross for BCD and MK+BCD respectively) with the BUSH models' apparent temperature vs model $M(V)$'s over-plotted (blue triangles). The error bars reflect the Hipparcos uncertainties. *The bottom two panels* display the log$T$ of Spectral type vs BUSH models' effective and apparent temperatures, from left to right respectively. The key for these two plots defines the 3 methods by which the published spectral–type temperatures are calculated, see §5.4 for details.

relation may break down. Hence, caution is required when employing such a correlation in the context of non-standard B stars, such as the rapidly rotating population of Be stars considered herein.

5.5 Model fits to spectra *without* Balmer emission present

Whilst it is clearly interesting to question whether the determination of temperatures by two slightly differing methods may give rise to the asymmetry seen in the lower panels of Figure 5.1, there is another possible, even likely, explanation. The stars considered in this work, by definition, display transient emission lines. Any star exhibiting this phenomenon could pollute the model selection process and/or the spectral–type selection process so as to induce some incorrect temperature derivation. As a first step to investigate this, all spectra displaying *any* degree of emission were removed from the data set and the plots of Figure 5.1 regenerated. [Some 66 objects displayed at least some level of emission in, at least, their Balmer line profiles.] Figure 5.2 shows the results. The HR diagram still displays a spread of model derived $M(V)$'s; clearly some of these, at least, must lie outside of the Hipparcos derived error values. However, it remains the case that the models broadly occupy the same space as the Hipparcos + Spectral Type data.

The temperature–correlation panels shows a remarkable change, however; the 'asymmetry' of Figure 5.1 has all but disappeared. Whilst there still exist a few outliers, essentially all the data lie in the $\Delta T \sim 20\%$ guides. It is interesting to note that the two populations (BCD and MK+BCD) are now largely indistinguishable, irrespective of whether the comparison is with $T_{\rm mod}$ or $T_{\rm app}$.

5.5.1 Spectra with no Balmer emission – Outliers

To help distinguish between what is a potential *classification* issue and a *bad model fit* some scrutiny of the models with respect to the fitted spectra is required. To this end, the three most prominent outliers in Figure 5.2 are considered in detail. HD 183656, an MK+BCD–classified object, where the model predicts a higher $T_{\rm eff}$ and $T_{\rm app}$, is plotted in Figure 5.3. The two BCD–classified objects which sit clear of the lower guide (i.e., the model fits provide for a lower $T_{\rm eff}$ and $T_{\rm app}$ than the spectral types) are HD 57219 and HD 174237, plotted in Figures 5.4 and 5.5 respectively.

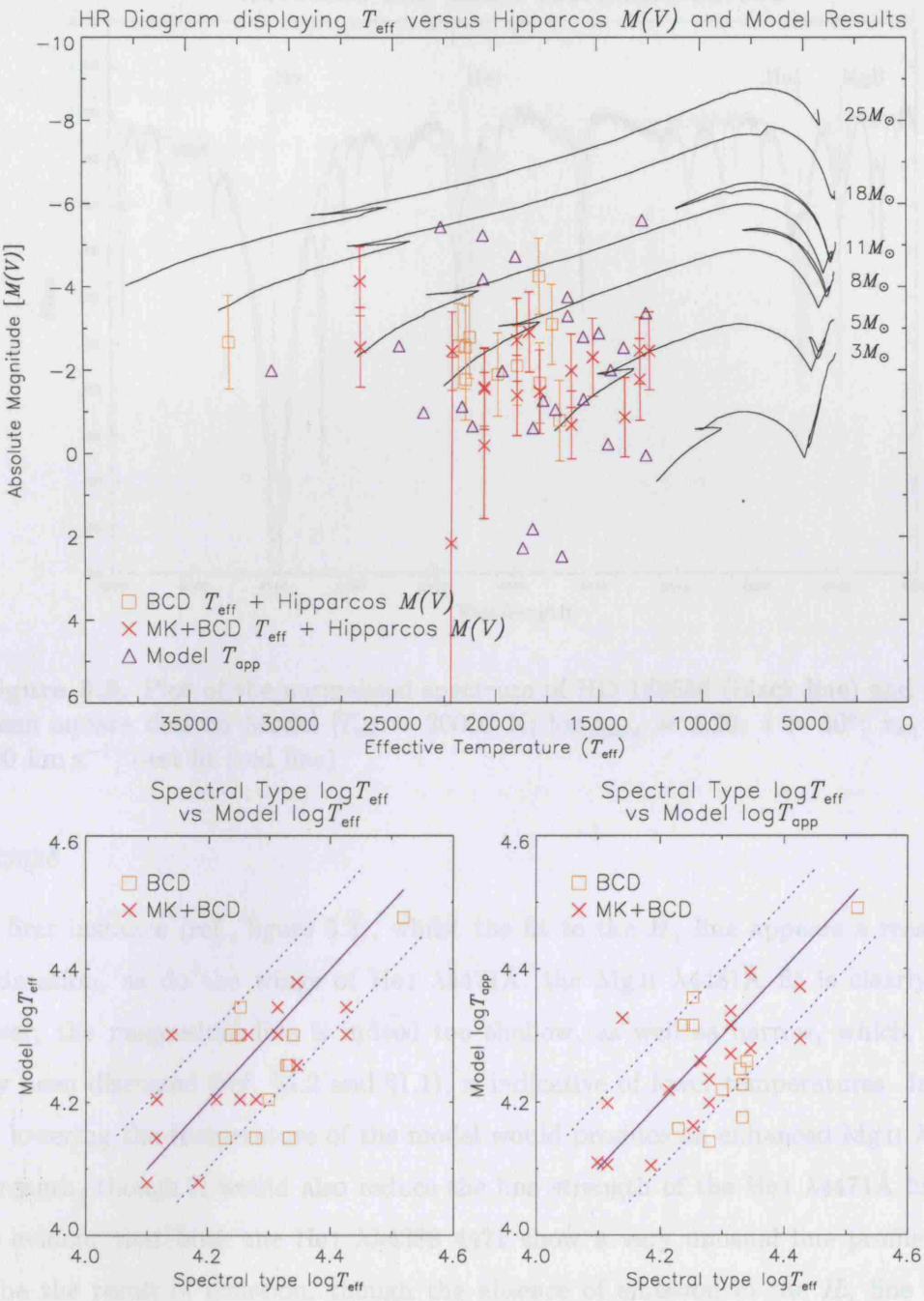

Figure 5.2. *The top panel* displays an H–R diagram for each of Chauville's stars that do not show Balmer emission: T_{sp} vs $M(V)_{Hip}$ (orange square and red cross for BCD and MK+BCD respectively) with the BUSH models' apparent temperature vs model $M(V)$'s over-plotted (blue triangles). The error bars reflect the Hipparcos uncertainties. *The bottom two panels* display the log$T$ of Spectral type vs BUSH models' effective and apparent temperatures, from left to right respectively. The key for these two plots defines the 3 methods by which the published spectral type temperatures are calculated, see §5.4 for details.

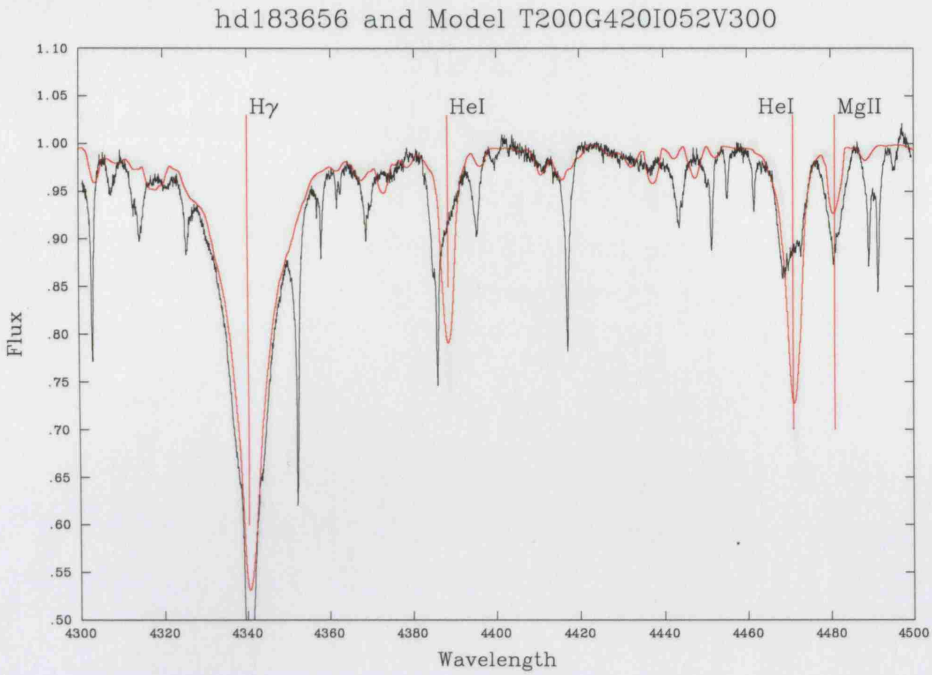

Figure 5.3. Plot of the normalised spectrum of HD 183656 (black line) and its mean square derived Model [$T_{\rm eff}$ = 20000 K; $\log g_{\rm pole}$ = 4.20; i = 30°; $v_{\rm eq}$ = 300 km s^{-1}] best fit (red line).

HD 183656

In the first instance (ref., figure 5.3), whilst the fit to the H_γ line appears a reasonable approximation, as do the wings of He I λ4471Å, the Mg II λ4481Å fit is clearly poor. Moreover, the magnesium line is indeed too shallow, as well as narrow, which, as has already been discussed (ref. §4.2 and §1.1), is indicative of lower temperatures. In other words, lowering the temperature of the model would produce an enhanced Mg II λ4481Å line strength, though it would also reduce the line strength of the He I λ4471Å line[4]. It is also evident that both the He I $\lambda\lambda$4388 4471 show a very unusual line profile which could be the result of emission, though the absence of emission in the H_γ line core is inconsistent with this. Nevertheless, whatever the physical nature of these features, the impact of classifying this star by the MK process using these two lines is to deduce this object to be a low $T_{\rm eff}$ B star (e.g., B9–B6). Thus, with no mechanism in the modelling procedure to replicate the line cores precisely (which might require nLTE+Disk emission) even with a reasonable fit to the Mg II line it is highly unlikely that a 1:1 correlation of

[4]Clearly, model degeneracies and fundamental parameter inter-dependencies come into effect here but a detailed discussion of these issues is deferred to until chapter 6

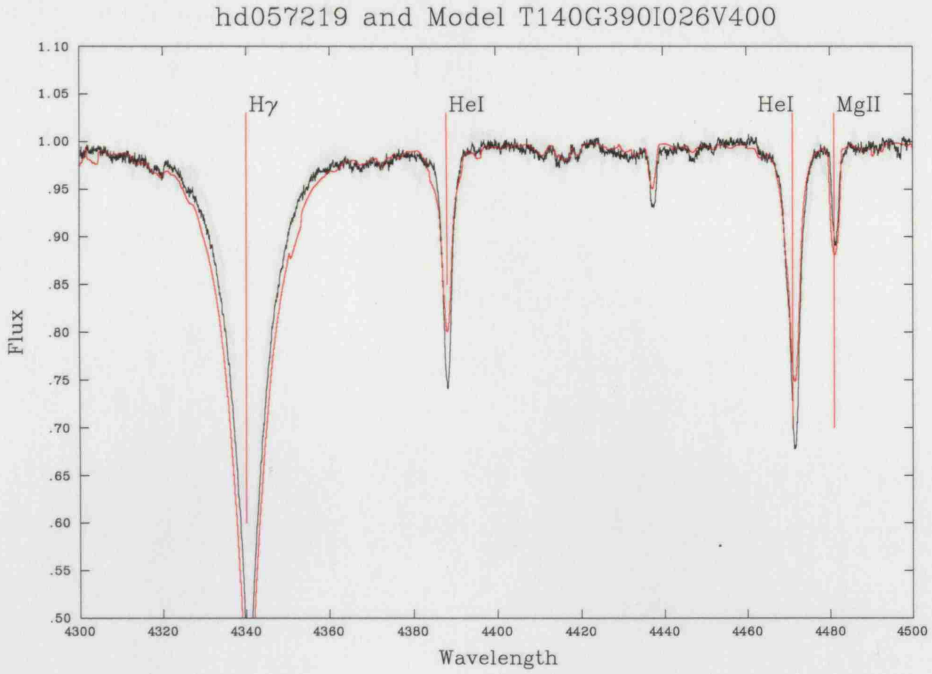

Figure 5.4. Plot of the normalised spectrum of HD 57219 (black line) and its mean square derived Model [$T_{\rm eff}$ = 14000 K; $\log g_{\rm pole}$ = 3.90; i = 15°; $v_{\rm eq}$ = 400 km s^{-1}] best fit (red line).

$T_{\rm mod}$, or $T_{\rm app}$, to $T_{\rm sp}$ would be produced. As a final remark on this model fit, though an LTE line blanketed approach has been taken, the failure to mimic any of the other ionic species transitions present throughout this spectrum ultimately drives the conclusion that this is indeed a poor model fit and as such little stock can be placed on the fundamental parameters assigned by the model.

HD 57219

The second outlier selected here, Figure 5.4, is HD 57219; a B2IV star. As noted above, the $T_{\rm sp}$ ($\sim$ 21500K) assigned to this object is significantly hotter than the model $T_{\rm mod}$ of 14000K, though $T_{\rm app}$ is marginally closer at $\sim$15000K. However, whilst the Mg II λ4481 line is marginally overstated and both the He I $\lambda\lambda$4388 4471 lines are marginally understated, the general trend of this spectrum is well matched. The wings of all the modelled lines (H_γ, He I λ4471 and Mg II λ4481) are well matched. The slightly discrepant fit to the extreme red and blue regions of both the H_γ and Mg II λ4481 lines can not be distinguished from a minor continuum–fit issue. In the case of the Mg II line, correcting the continuum fit would push the line core deeper toward a more compelling match to the model. Thus

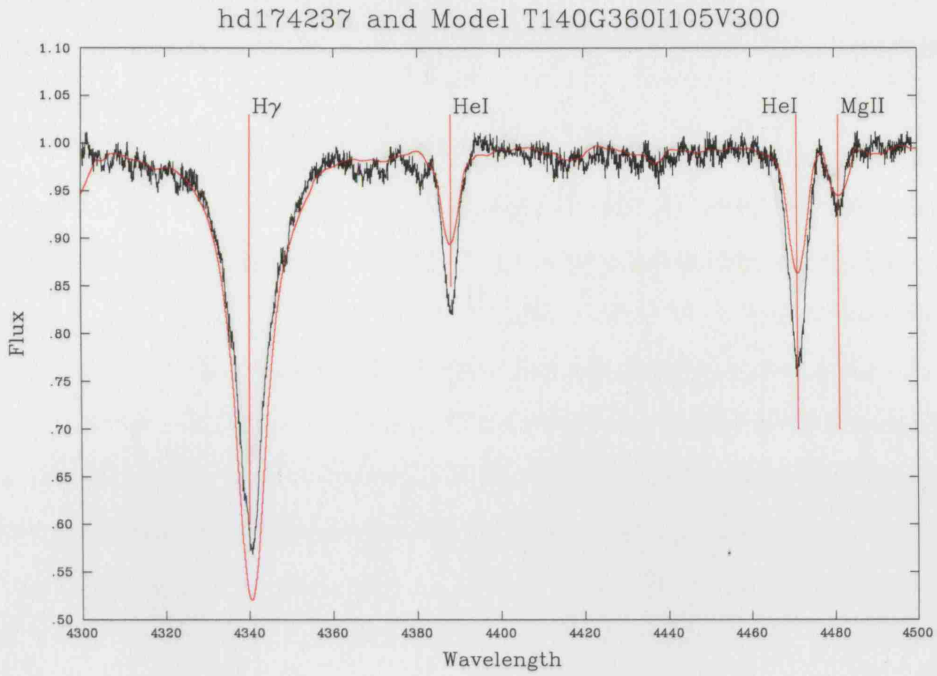

Figure 5.5. Plot of the normalised spectrum of HD 174237 (black line) and its mean square derived Model [$T_{\rm eff}$ = 14000 K; $\log g_{\rm pole}$ = 3.60; i = 60°; $v_{\rm eq}$ = 300 km s^{-1}] best fit (red line).

given the susceptibility of the He I (but also the H Balmer lines) to nLTE effects coupled with the clearly, near precise, matching of the other minor features along the length of this spectrum it is difficult to discount this model.

HD 174237

The third outlier selected, displayed in Figure 5.5, is HD 174237. Both $T_{\rm mod}$ and $T_{\rm app}$ are cooler than expected from the spectral type. This is BCD classified as B3Ve and has a $T_{\rm sp}$ of 19010K; $T_{\rm mod}$ is 14000K which, combined with the angle dependence, yields a $T_{\rm app}$ of 13810K. Figure 5.5 shows that whilst the H_γ wings are well fit and the Mg II λ4481 line is not too discrepant, the He I lines are narrow and significantly understated. Any improvement to the model fits would have to drive the He I line–cores deeper, which could only be achieved by increasing the $T_{\rm eff}$ substantially. Consequently, the good fit to the wings of the Hγ line does not lead to any confidence in the model log$g$; pushing to higher temperatures will demand a potentially significant revision of log$g$. Note the very pronounced 'V' shape of the Mg II line profile; close scrutiny of the overall spectrum suggests this 'V' like profile is mimicked in all the metal lines, weak though they are.

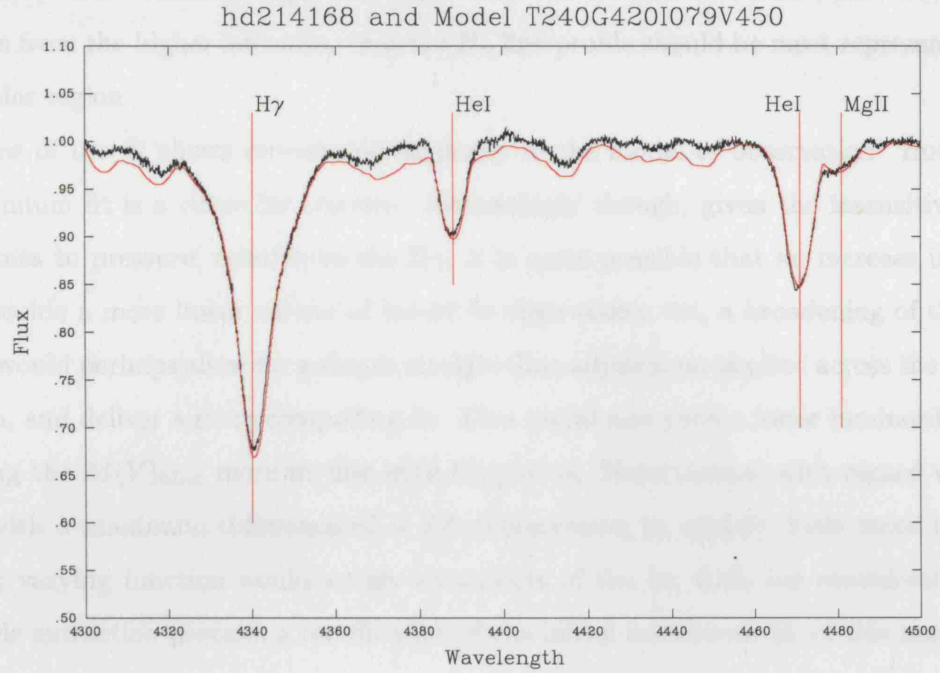

Figure 5.6. Plot of the normalised spectrum of HD214168 (black line) and its mean square derived Model [$T_{\rm eff}$ = 24000 K; $\log g_{\rm pole}$ = 4.20; i = 45°; $v_{\rm eq}$ = 450 km s^{-1}] best fit (red line).

Further comment on this *saw–tooth effect* is reserved for Chapter 8.

5.5.2 Spectra with no Balmer emission – well correlated temperatures

We now examine a sample of those objects in this 'no Balmer emission' group whose $T_{\rm sp}$'s *and* $T_{\rm app}$'s appear to be in reasonable agreement. A further three objects are randomly selected, displayed and discussed below.

HD 214168

Figure 5.6 displays the spectrum of the, MK+BCD, B2Ve star HD 214168. The $T_{\rm sp}$ is 22182K with a $\log g$ of 3.98. The model–derived parameters are $T_{\rm mod}$ 24000K; $T_{\rm app}$ 24790K; and polar $\log g$ 4.20. $M(V)_{\rm Hip}$ is $\sim 2.0^{+1.1}_{-2.8}$, which contains one of the largest Hipparcos errors in the Chauville sample; $M(V)_{\rm Mod}$ is -2.59. Whilst the absolute magnitudes appear to be substantially different, the extremely large Hipparcos error ($\sim$72%) casts doubt on the reliability of this as a guide. In contrast, the temperature correlations and gravity correlations, of model to spectral type, are far more comparable. In particular, bearing

in mind that a 45° viewing angle, combined with Von Zeipels law, infers that most flux originates from the higher latitudes, thus the H_γ line profile should be most representative of the polar region.

Review of the fit shows remarkable similarity in the model to observation. However, the continuum fit is a cause for concern. Interestingly though, given the insensitivity of weaker lines to pressure, relative to the Hγ, it is quite possible that an increase in log$g$ would provide a more linear off–set of model to observation, i.e., a broadening of the Hγ line also would perhaps allow for a simple straight–line adjustment applied across the entire spectrum, and deliver a more compelling fit. This would also yield a lower luminosity and thus bring the $M(V)_{\rm Mod}$ more in–line with Hipparcos. Nevertheless, with regard to this model, with a maximum difference of $\sim$ 3% (observation to model), little more than a smoothly varying function would satisfy all aspects of the fit; with due consideration of the echelle extraction process, a rectification of the initial continuum fit, of this nature, is acceptable.

HD 33328

Figure 5.7 displays the normalised spectrum of HD 33328 with a model fit over–plotted. This star is BCD classified as B2III-IVne, $T_{\rm sp}$ 21330K, log$g$ of 3.70 and Hipparcos derived absolute magnitude of $-2.9^{+0.2}_{-0.2}$. The corresponding model derived values are $T_{\rm eff}$ = 18000K, $T_{\rm app}$ = 17750K, a polar log$g$ of 4.20 and $M(V)_{\rm Hip}$ −1.28. Thus, as before, the absolute magnitude is quite different, but in this case the Hipparcos error is far smaller so more weight is given to this discrepancy. Also, whilst the temperatures are not hugely discrepant, they are clearly pushing toward a questionable difference. With regard to the fit itself, some of the continuum undulations are repeated in the model, whilst others are not. In particular, the region between the H_γ and He I λ4388 is far more 'flattened' in the model. In addition, the line blends at around 4015Å are almost non-existent in the model. However, the wings of the H_γ line are well fitted, with only the core deviating (perhaps a nLTE effect?), whilst the He I–Mg II blend is very well fitted, with only the extreme red wing (Mg II) being mildly discrepant. It is at least clear that, insofar as a mean square fitting process is employed (ref. §4.4), one is unlikely to improve significantly on this fit.

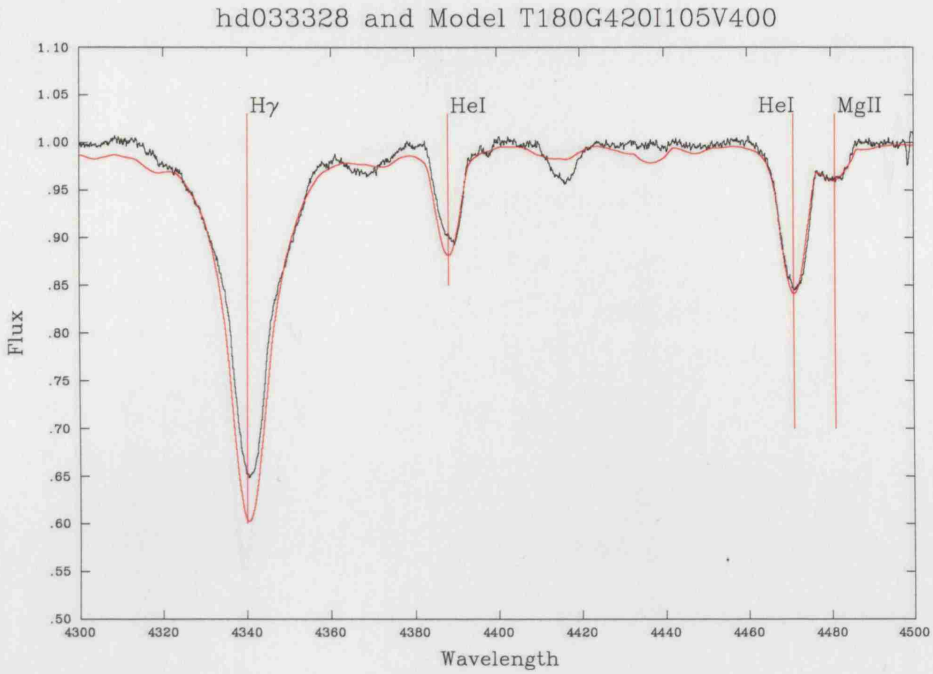

Figure 5.7. Plot of the normalised spectrum of HD 33328 (black line) and its mean square derived Model [$T_{\rm eff}$ = 18000 K; $\log g_{\rm pole}$ = 4.20; i = 60°; $v_{\rm eq}$ = 400 km s^{-1}] best fit (red line).

HD 209522

Figure 5.8 displays the spectrum of HD 209522. This is an MK–classified BIV4ne with $T_{\rm sp}$ 16368K; log$g$ 3.81; and $M(V)_{\rm Hip}$ $-2.0^{+0.3}_{-0.3}$. The model–fit yields $T_{\rm mod}$ 16000K; $T_{\rm app}$ 16530K; log$g_{\rm pole}$ 3.90; and $M(V)_{\rm Mod}$ -3.31. Once again the $M(V)$'s are not in agreement and, with the relatively small $M(V)_{\rm Hip}$ error, some doubts result. The $T_{\rm mod}$ and $T_{\rm app}$ actually straddle $T_{\rm sp}$ and sit within just a few hundred degrees of each other, which is encouraging. The BCD surface gravity value sits between the model polar to equatorial values with the expected skew to the polar value, resulting from the 45° viewing angle and dominant polar spectrum. This effect is described in some detail by Slettebak et al. (1980).

Comparison of the spectrum to model fit is also very promising. Whilst, as previously, one can argue for a small adjustment of the continuum fit the overall profile throughout the length of the spectrum is very well mimicked by the model. The H_γ line is a near perfect fit as are both the He I lines with only a slight mismatch occurring in the core of the Mg II λ4471 line as well as the shoulder of the He I–Mg II blend.

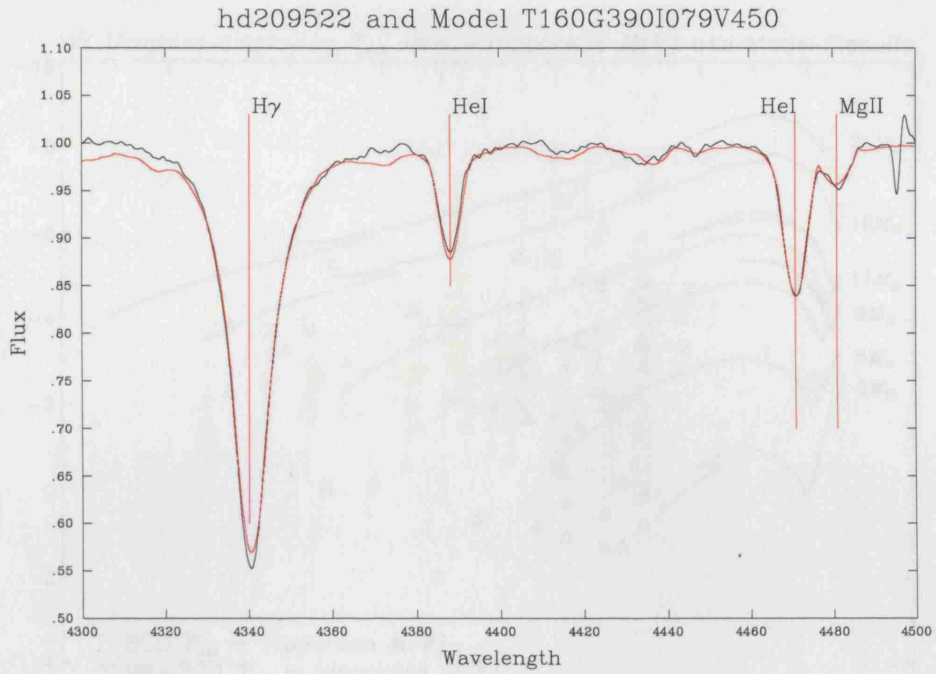

Figure 5.8. Plot of the normalised spectrum of HD 209522 (black line) and its mean square derived Model [$T_{\rm eff}$ = 16000 K; $log\ g_{pole}$ = 3.90; i = 45°; $v_{\rm eq}$ = 450 km s^{-1}] best fit (red line).

5.6 Model fits to Spectra *with* Balmer emission present

In contrast to the previous section that focused on those spectra which did not exhibit any *obvious* Balmer emission, this section focuses on those that do. Figure 5.9 shows results these stars. Essentially all the original outliers (in figure 5.1) are present in this plot. Some 43% of this population clearly express a bias to a higher $T_{\rm eff}$ when derived by a purely BCD–based classification and temperature derivation method, whilst for the remainder, derived by an MK+BCD method, just three from twelve repeat this trend (and they all sit on the border of the $\Delta T \sim 20\%$ guides). As a consequence, before seeking any 'physical' explanation for this skew, it is of interest to examine the three outliers classified by the MK+BCD method: HD 184279, HD 66194 and HD 212076. The three spectra, along with their model fits, are displayed in Figures 5.10, 5.11 and 5.12, respectively.

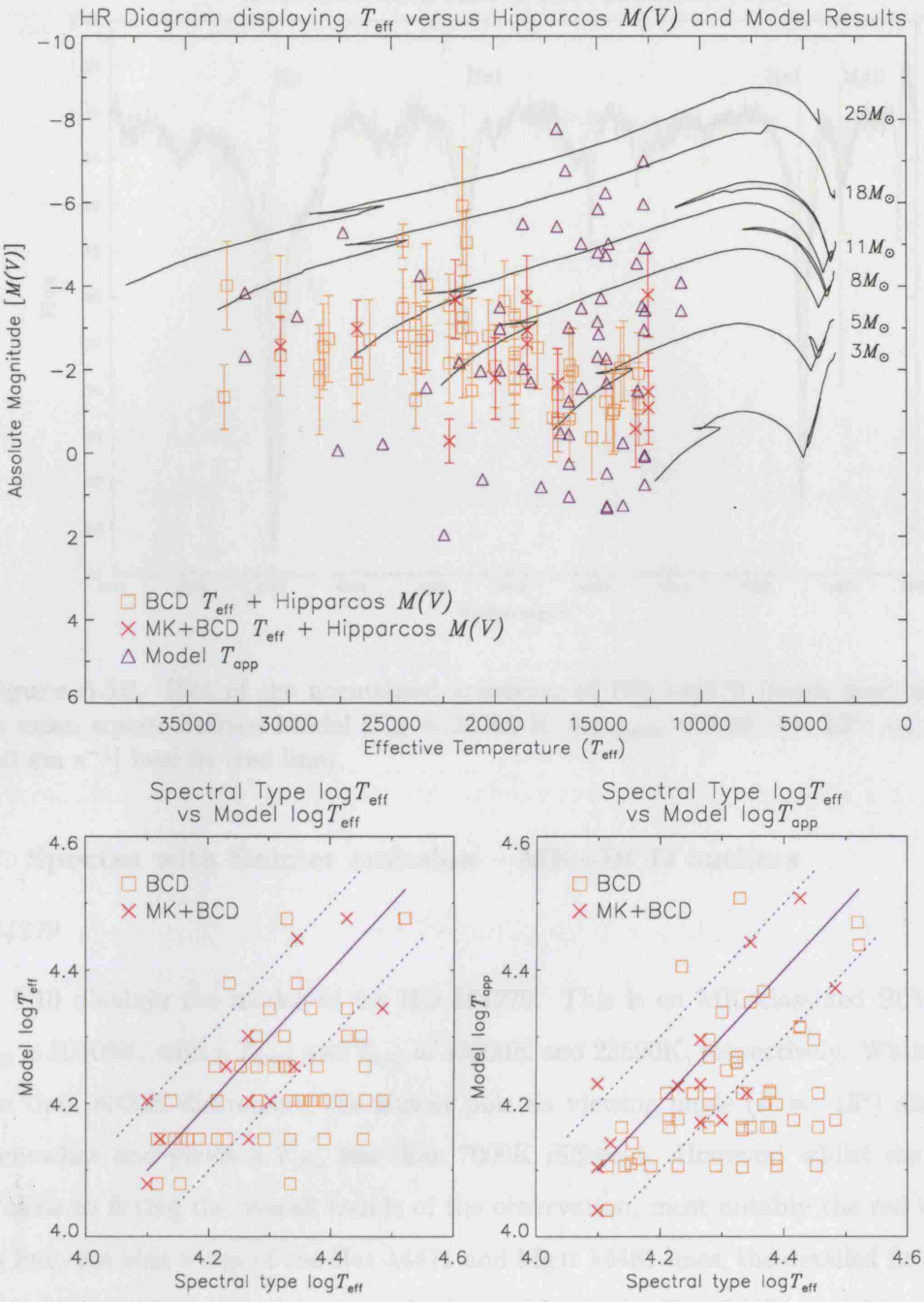

Figure 5.9. *The top panel* displays an H–R diagram for each of Chauville's stars that show Balmer emission: T_{sp} vs $M(V)_{Hip}$ (orange square and red cross for BCD and MK+BCD respectively) with the BUSH models' apparent temperature vs model $M(V)$'s over-plotted (blue triangles). The error bars reflect the Hipparcos uncertainties. *The bottom two panels* display the log$T$ of Spectral type vs BUSH models' effective and apparent temperatures, from left to right respectively. The key for these two plots defines the 3 methods by which the published spectral type temperatures are calculated, see §5.4 for details.

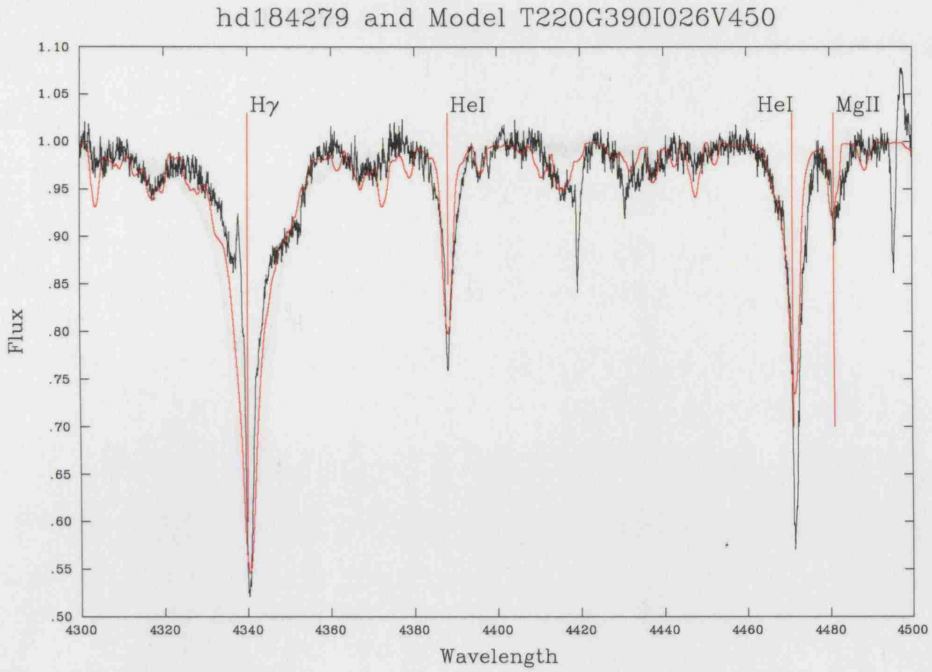

Figure 5.10. Plot of the normalised spectrum of HD 184279 (black line) and its mean square derived Model [$T_{\rm eff}$ = 22000 K; $\log g_{\rm pole} = 3.90$; $i = 15°$; $v_{\rm eq}$ = 450 km s^{-1}] best fit (red line).

5.6.1 Spectra with Balmer emission – MK+BCD outliers

HD 184279

Figure 5.10 displays the model–fit for HD 184279. This is an MK–classified B0Ve star. The $T_{\rm sp}$ is 30409K, with a $T_{\rm mod}$ and $T_{\rm app}$ of 22000K and 23590K, respectively. Whilst $T_{\rm mod}$ is more than 8000K discrepant, the almost pole on viewing angle (i = 15°) alleviates this somewhat and yields a $T_{\rm app}$ less than 7000K different. However, whilst the model comes close to fitting the overall trends of the observation, most notably the red wing of the Hγ line, the blue wings of the He I λ4471 and Mg II λ4481 lines, the detailed fit is most definitely lacking; in particular, the red wings of both the He I λ4471 and Mg II λ4481 lines, the line core of the He I λ4471 (though not He I λ4388) and also the blue wing of the Hγ line. However, in the case of the Hγ line, emission is clearly present so one should not expect a good fit here. Attention is drawn to the 'V-shape' line profile seen in the Mg II line and also, apparently, other lines. This is quite reminiscent of the 'saw–tooth effect' noted in §5.5.1 when discussing HD 174237, though in this case (HD 184279) it is far more pronounced.

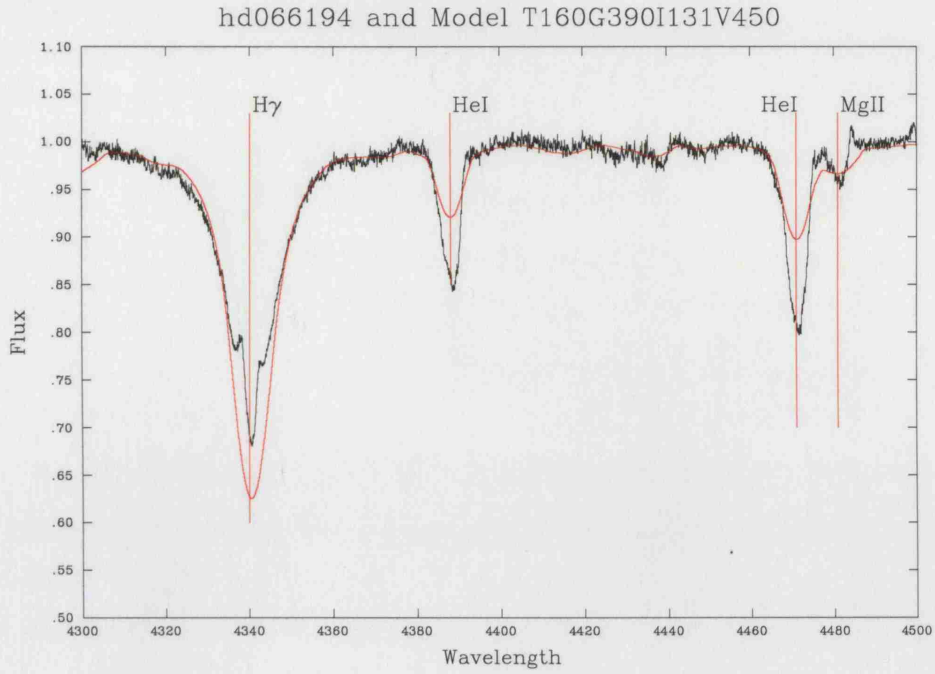

Figure 5.11. Plot of the normalised spectrum of HD 66194 (black line) and its mean square derived Model [$T_{\rm eff}$ = 16000 K; $\log g_{\rm pole}$ = 3.90; i = 75°; $v_{\rm eq}$ = 450 km s^{-1}] best fit (red line).

HD 66194

Figure 5.11 displays results for HD 66194. This star is MK classified as B2.5IVe, with $T_{\rm sp}$ 19953K. $T_{\rm mod}$ is 16000K and an inclination dependent $T_{\rm app}$ of 14960K (at i = 75°). The $T_{\rm sp}$ and $T_{\rm app}$ values are clearly disparate. This star's BCD $\log g$ is 3.82, with the model yielding log $g_{\rm pole}$ 3.90. Again, taking account of the inclination dependence, one might reasonably expect an observationally derived value to be somewhat lower than 3.82. This is not the case and the displayed fit is obviously poor. Whilst the Hγ fit is good, emission component aside, the He I and Mg II lines reveal substantial mismatches. Though the blue wings of both He I lines are good matches, the line cores and red wings are not. To produce an improved fit here, one would require an increased $T_{\rm eff}$ and decreased $v_{\rm eq}$ with a consequent change in $\log g$ and perhaps also i. Again the model fails to reproduce the apparent saw–tooth effect, though in this case the effect is not pronounced; again, the distinctive 'V-shape' is particularly apparent in the Mg II λ4481 line.

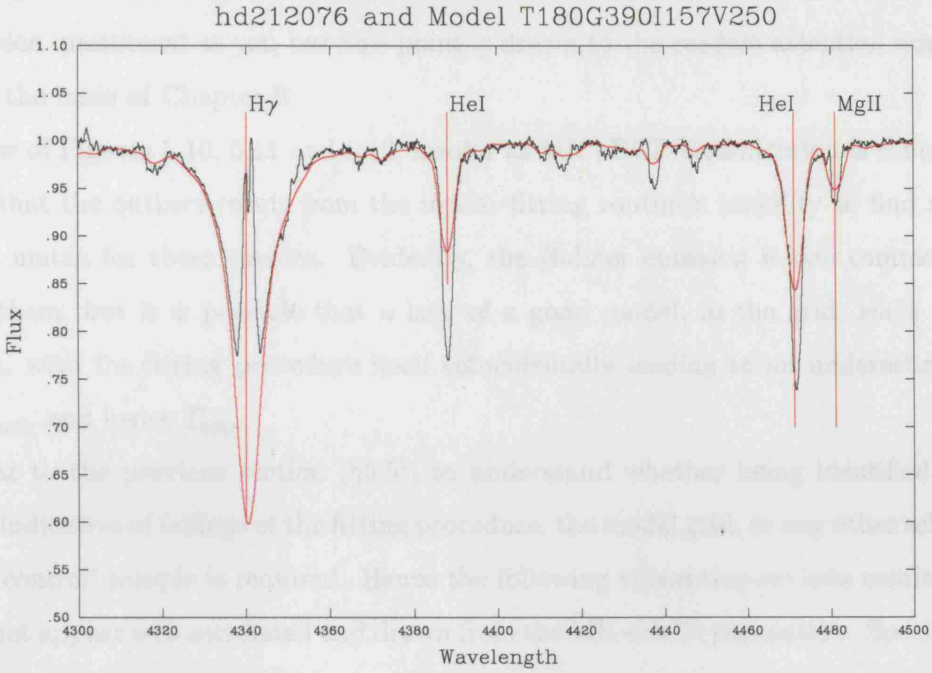

Figure 5.12. Plot of the normalised spectrum of HD 212076 (black line) and its mean square derived Model [$T_{\rm eff}$ = 18000 K; $\log g_{\rm pole}$ = 3.90; $i = 90°$; $v_{\rm eq}$ = 250 km s^{-1}] best fit (red line).

HD 212076

Figure 5.12 displays the results for, and spectrum of, HD 212076. This star has an MK type of B2IV–Ve with $T_{\rm sp}$ 21878K and $\log g$ 3.90. The model parameters are $T_{\rm mod}$ and $T_{\rm app}$ 18000K and 16410K, respectively. Whilst these temperatures sit just within the $\Delta T \sim 20\%$ guides of the $T_{\rm sp}$–$T_{\rm mod}$ plot (ref., figure 5.9), the inclination angle of $i = 90°$ leads to a $T_{\rm sp}$–$T_{\rm app}$ that clearly does not. Despite the polar surface gravity being in 'precise' agreement (i.e., 3.90), the inclination angle should drive any apparent gravity to a lower value, i.e., toward that of the equatorial value - $\log g = 2.73$. Interestingly, the *reasonable* fits at various points throughout the spectrum hint toward the degeneracy of the model grid discussed in depth in the following chapter, §6. Many of the failings of the previous two fits are again present here. Whilst the Hγ line is apparently well matched, the model He I line cores are substantially discrepant. The red and blue wings of the model He I lines are actually fairly good matches to the data but the Mg II line is not. Also, though the trends of the observation are in essence replicated, the detail of each *minor* feature is not. However, *apparently*, unlike the previous examples, the saw–tooth effect and distinctive

'V-shape' is not seen. Whether or not these features are linked to the Balmer emission has not been questioned as yet, but this point is drawn to the readers attention now as it will form the basis of Chapter 8.

Review of Figures 5.10, 5.11 and 5.12, insofar as MK+BCD classification is concerned, suggests that the outliers result from the model–fitting routine's inability to find an appropriate match for these spectra. Evidently, the Balmer emission is one commonality between them, but it is possible that a lack of a good model, in the grid, leads to the mismatch, with the fitting procedure itself coincidentally leading to an underestimation of the $T_{\rm mod}$, and hence $T_{\rm app}$.

Similar to the previous section (§5.5), to understand whether being identified as an outlier is indicative of failings of the fitting procedure, the model grid, or any other selection effect, a 'control' sample is required. Hence the following subsection reviews results for a sample that appear well correlated and drawn from the MK+BCD population. Specifically, HD 210129 ,HD 224559 and HD 203467, displayed, along with their model fits, in Figures 5.13, 5.14 and 5.15 respectively.

5.6.2 Spectra with Balmer emission – MK+BCD correlated

HD 210129

Figure 5.13 displays HD 210129, MK classified as B6-7Vne. The $T_{\rm sp}$ is 13183K, with the model yielding $T_{\rm mod}$ and $T_{\rm app}$ 14000K and 13810K, respectively. The model log $g_{\rm pole}$ is 4.20 with a viewing angle $i = 60^{\circ}$ relative to the rotational axis. In general, the model appears to be a good match for the observation; in particular, the Hγ line and the relative strengths of the He I λ4471 - Mg II λ4481 line blend. The unusual kink in the He I λ4388 line is also well mimicked (this is likely due to Fe III *lambda*4383), though the marginally over-stated continuum throughout the entire observed spectrum detracts from this somewhat. Indeed, this also impacts on the wings of the He I λ4471 line, though clearly any adjustment in this region will affect the line core also. So, as this is a fairly well–matched spectrum it is of no surprise that the temperatures correlate so well. However, the He I–Mg II blend clearly needs improvement if a model fit is to be compelling. Achieving this would probably only entail a minor alteration of the model parameters as well as a 'tweak' to the continuum, but nevertheless, an adjustment is required.

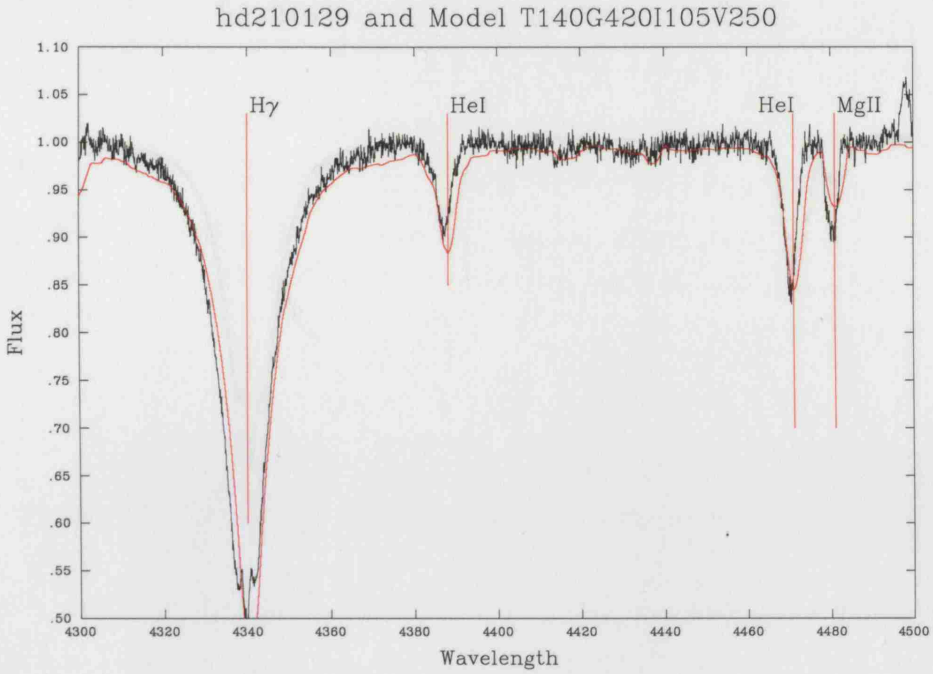

Figure 5.13. Plot of the normalised spectrum of HD 210129 (black line) and its mean square derived Model [$T_{\rm eff}$ = 14000 K; $\log g_{\rm pole} = 4.20$; $i = 60°$; $v_{\rm eq}$ = 250 km s^{-1}] best fit (red line).

HD 224559

Figure 5.14 displays the result for HD 224559. This star is MK classified as B4Ven with a $T_{\rm sp}$ of 16943K. The model yields $T_{\rm mod}$ and $T_{\rm app}$ 18000K and 16829K, respectively. The implied, and published, apparent $\log g$ is 4.01 with the model log $g_{\rm pole}$ 4.20. The inclination, i, of the model is 75° which, as previously mentioned, one might expect to correlate with a lower spectral-type derived value. $M(V)_{\rm Mod}$ is -0.49 with $M(V)_{\rm Hip} = -1.7^{+0.4}_{-0.6}$. Nevertheless, the near match of $T_{\rm app}$ with $T_{\rm sp}$ is clearly encouraging and review of the model fit adds confidence to the success of the model fit. The Hγ profile is an excellent match; though the emission in the Hγ core and the emergence of the wings into what is, evidently, an overstated continuum detract from the fit slightly. This overstatement of the continuum is present throughout the spectrum and though the normalisation has gone some way to smoothing out the minor features one can clearly see the various undulations repeated in both model and observation. Finally, the wings of the He I–Mg II blend are also an excellent match with just the line cores slightly askew. However, the shape of the magnesium line is neatly reproduced and the He I line cores may well be elevated by

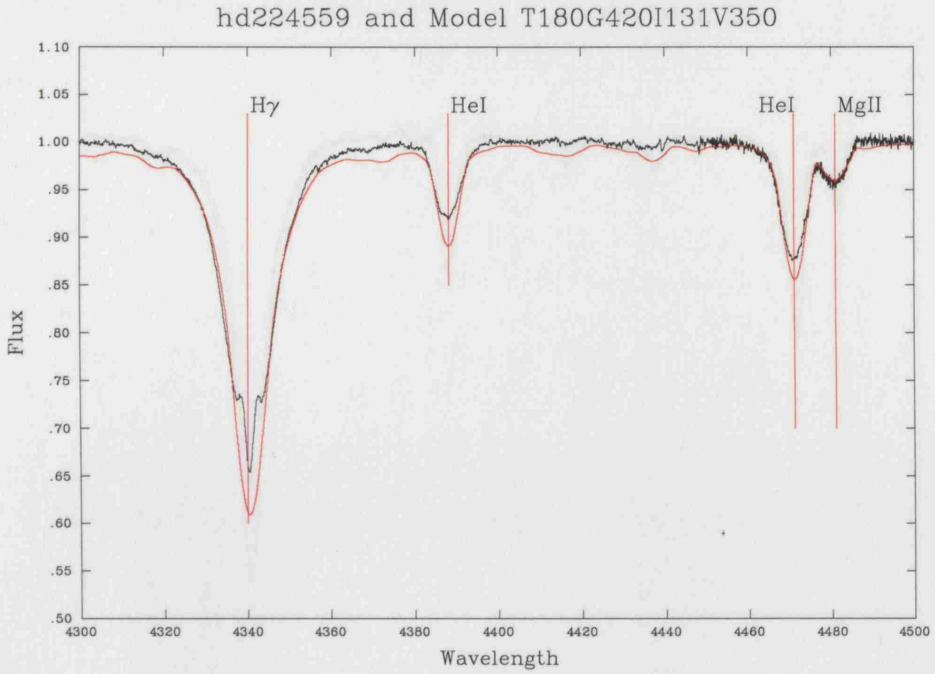

Figure 5.14. Plot of the normalised spectrum of HD 224559 (black line) and its mean square derived Model [$T_{\rm eff}$ = 18000 K; $\log g_{\rm pole}$ = 4.20; $i = 75°$; $v_{\rm eq}$ = 350 km s^{-1}] best fit (red line).

some slight emission. No obvious saw–tooth effect nor 'V-shape' profiles are seen in this observation.

HD 203467

HD 203467, displayed in Figure 5.15, is MK classified as B3IVe. The $T_{\rm sp}$ is 18408K with the model yielding $T_{\rm mod}$ and $T_{\rm app}$ as 16000K and 16950K, respectively. A $\log g$ of 3.82 is published, whereas the model $\log g_{\rm pole}$ is 3.30. Also, $M(V)_{\rm Hip}$ is $-3.8^{+0.2}_{-0.3}$, with $M(V)_{\rm Mod}$ -5.44, so, as in previous cases, these are significantly different. Whilst the $\log g$ and $M(V)$ values are discrepant, $T_{\rm app}$ and $T_{\rm sp}$ are not and, significantly, neither is the spectrum fit. Indeed, review of Figure 5.15 is suggestive of a more reliable fit than one might conclude from the above. The He I–Mg II blend is a near perfect match with only the line core of He I λ4471 marginally different. But once again, the fact that this object exhibits emission, this should not be a surprise. Also, significantly, in this fit, the weak lines, of which there are many, are all excellently matched. Though the continuum either side of the Hγ line is slightly overstated, these 'minor' features are still clearly well mimicked. The only exception to this is the small region around 4410-4420Å[most likely an O II λ4417–

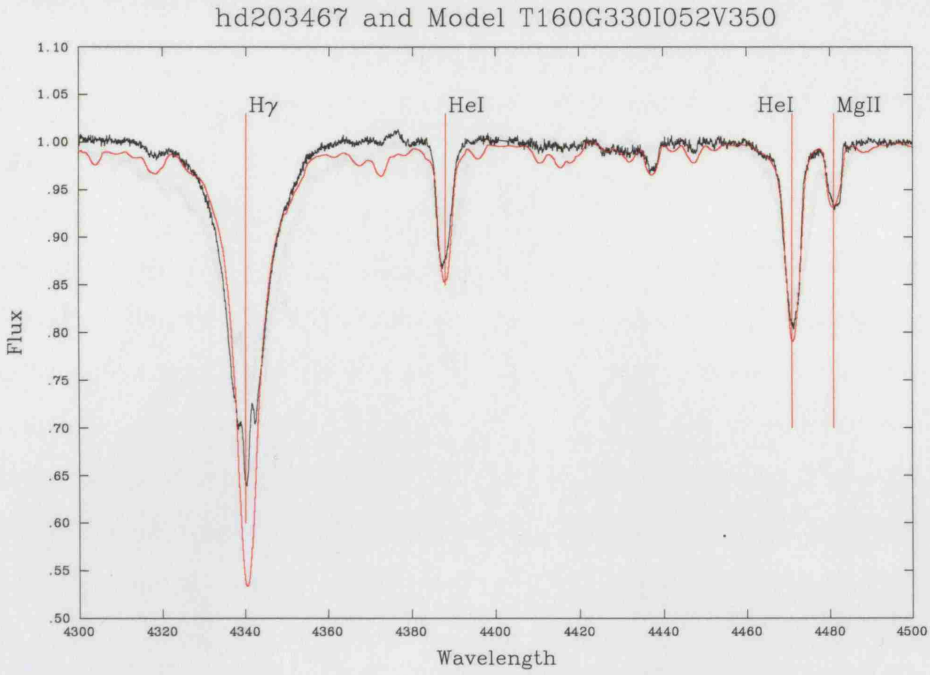

Figure 5.15. Plot of the normalised spectrum of HD 203467 (black line) and its mean square derived Model [$T_{\rm eff}$ = 16000 K; $\log g_{\rm pole} = 3.90$; $i = 30°$; $v_{\rm eq}$ = 350 km s^{-1}] best fit (red line).

N II λ4418 blend]. This aside, the one real concern of this fit comes from the blue-wing of the Hγ line where the model does appear to be slightly narrower, the obvious correction to this is an increase in $\log g$ which would likely encourage a step change in $T_{\rm mod}$ and i. It may also be that this could be rectified by an increase in model grid resolution so as to minimise this knock on effect on the other variables, and in turn minimise the overall impact on what is otherwise an excellent model fit. However, once again it is stressed that exploration of the model–grid degeneracy, alluded to repeatedly throughout this section, may also remedy this issue with minimal sacrifice elsewhere in the spectrum. Despite this though, the overall impression delivered by this fit is very promising.

5.6.3 Spectra with Balmer emission – BCD–correlated

This section has so far focused on the MK+BCD subset. Thus, to complete this review, the remainder of this section discusses three results from the BCD subset only. HD 20336 and HD 173948 [Figures 5.16 and 5.17, respectively] are selected on the basis that their spectral $T_{\rm eff}$'s and model $T_{\rm app}$'s are apparently well correlated, §5.6.3. The third result presented is for HD 28497 [Figure 5.18], this is selected as it sits in the centre of the *bias*

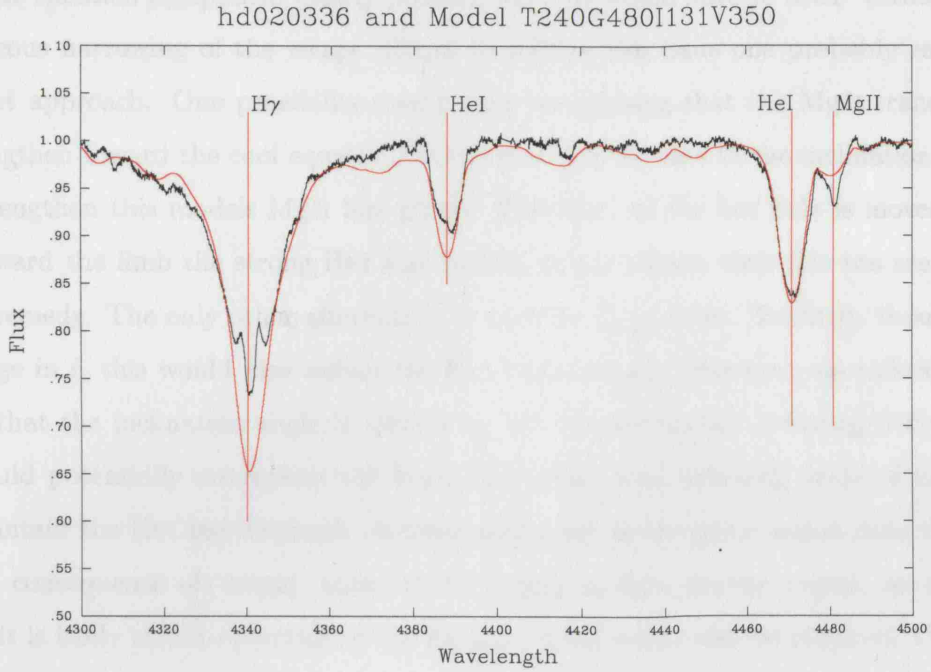

Figure 5.16. Plot of the normalised spectrum of HD 20336 (black line) and its mean square derived Model [$T_{\rm eff}$ = 24000 K; $\log g_{\rm pole}$ = 4.80; i = 75°; $v_{\rm eq}$ = 350 km s^{-1}] best fit (red line).

sample with relatively low model derived temperatures. All three were also subject to the criterion that they do not show a *strong* Balmer emission component as that population is the subject of the final analysis of this chapter, §5.7.

HD 20336

HD 20336, displayed in Figure 5.16, is BCD classified as B2Ve. The corresponding $T_{\rm sp}$ is 22182K with the model–fit yielding $T_{\rm mod}$ and $T_{\rm app}$ 24000K and 22450K, respectively. The BCD $\log g$ is 3.98 with the model fit yielding $\log g_{\rm pole}$ 4.80, with an inclination angle, i, of 75°. These data all appear to be well correlated. However, on viewing the fit itself, one is struck by two obvious details. The first is the good fit of both the Hγ wings as well as the overall fit of the He I λ4471 line. The second point, in contrast, is the very poor fit to the Mg II line. With the realisation that *all* rotationally broadened lines are weakened at their cores one might be tempted to think that reducing the rotational velocity would improve the Mg II line fit. However, the additional *cost* would be to simultaneously degrade the He I λ4471 fit by reducing the broadening in the wings whilst also deepening the core. It should be stressed that a deepening of the He I core is in itself not necessarily an issue in

view of the emission component clearly present, but this would have to occur without the simultaneous narrowing of the wings. Hence to resolve this issue one probably requires a different approach. One possibility comes from recognising that the Mg II transitions will strengthen toward the cool equator, thus perhaps an increase in the inclination angle could strengthen this models Mg II line profile. However, as the hot pole is moved ever closer toward the limb the strong He I absorptions would reduce, thus this too seems an unlikely remedy. The only other alternative, is to drive $T_{\rm mod}$ down. Similarly, though, to the change in i, this would also reduce the He I line strength. However, on reflection of the fact that the inclination angle is already at 75°, simultaneously reducing both $T_{\rm mod}$ and i could potentially strengthen the Mg II line whilst also, exposing more of the hot pole, maintain the He I line–strength. Exposure of more of the polar region does though have the consequence of 'seeing' more of the higher surface gravity region, so in this scenario it is likely that a reduction of the $\log g_{\rm pole}$ value would also be required. Clearly, without actually quantifying this as yet, the very likely impact would be to disrupt what initially seems to be well correlated model to observationally established $T_{\rm eff}$'s. This point is interesting though in the context of apparent *bias* that the temperature plots illustrate, as remedying this model fit would potentially add to the bias population. As a closing comment on this star, the readers attention is drawn again to the 'V-shaped' Mg II λ4481 line profile which is again apparent.

HD 173948

HD 173948, displayed in figure 5.17, is BCD classified as B1.5IIIe with $T_{\rm sp}$ 23281K. The model yields a $T_{\rm mod}$ and $T_{\rm app}$ 22000K and 23310K, respectively. The BCD $\log g$ is 3.62 with a model $\log g_{\rm pole}$ 3.90. With an inclination angle of 30° off axis these data initially appear promising. $M(V)_{\rm Mod}$ is -1.57 whilst $M(V)_{\rm Hip}$ is $-4.1^{+0.2}_{-0.2}$, this is clearly discouraging. However, review of Figure 5.17 perhaps alleviates this somewhat as, across the spectrum, almost every feature is replicated in the model fit. Though there are some minor mismatches in normalised flux strength, this is easily rectified by just a nominal continuum adjustment. Dealing with the key lines in turn; the Hγ line profile is extremely well matched, the two small kinks on the blue wing as well as the single kink in the red wing is well matched. It is in fact only the small emission component that significantly upsets the fit here. The He I lines are both very well fitted and in particular the blue wing of the He I λ4471 which also exhibits a kink which is mimicked in the model. Once again

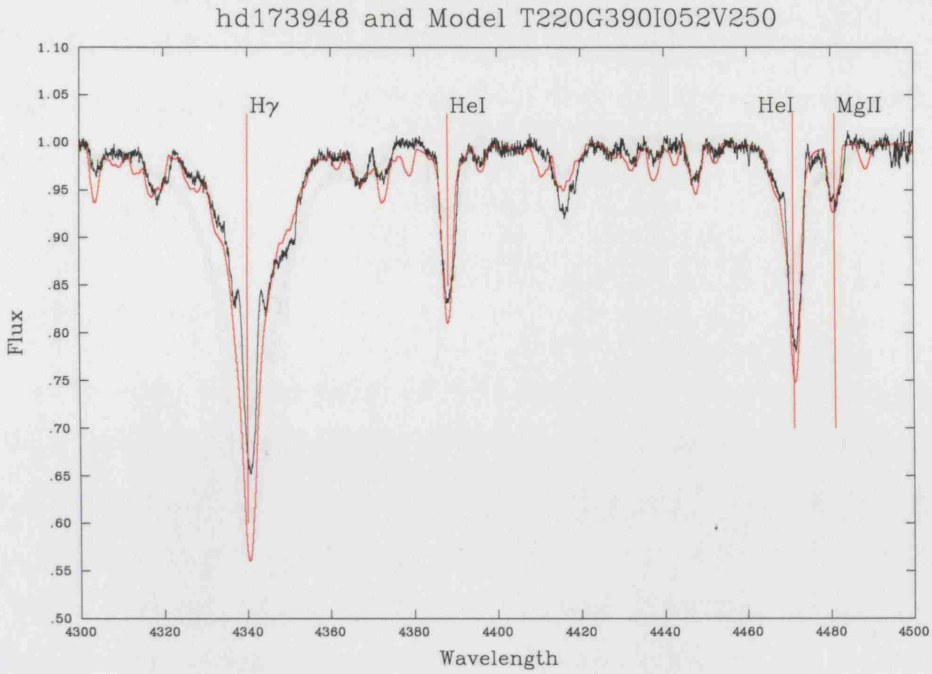

Figure 5.17. Plot of the normalised spectrum of HD 173948 (black line) and its mean square derived Model [$T_{\rm eff}$ = 22000 K; $\log g_{\rm pole} = 3.90$; $i = 30°$; $v_{\rm eq}$ = 250 km s^{-1}] best fit (red line).

though, the line core is marginally deeper but the small emission may well account for this (nLTE effects notwithstanding). Finally, the Mg II λ4481 line is also a good fit. The line core again is just a fraction off but the line width and shape in the wings is an excellent match. In conclusion then, though the $M(V)$ values appear significantly discrepant almost every other detail is in very good agreement and it is certainly difficult to envisage a significantly better correlation of model to observation.

5.6.4 Spectra with Balmer emission – BCD outlier

HD 28497

HD 28497, displayed in Figure 5.18, is the final of these three BCD–classified stars considered in this section. This has a BCD classification of B1.5Vne. The $T_{\rm sp}$ is 24434K whereas $T_{\rm mod}$ and $T_{\rm app}$ are 16000K and 15780K, respectively. The BCD $\log g$ is 3.97; the model log $g_{\rm pole}$ is 4.20. The model–derived inclination angle of 60° suggests that the surface gravities of model to observation are not quite in sink. However, it is the temperature correlations that are of most concern. $M(V)_{\rm Mod}$ is −1.56 with $M(V)_{\rm Hip} = -2.8^{+0.3}_{-0.5}$;

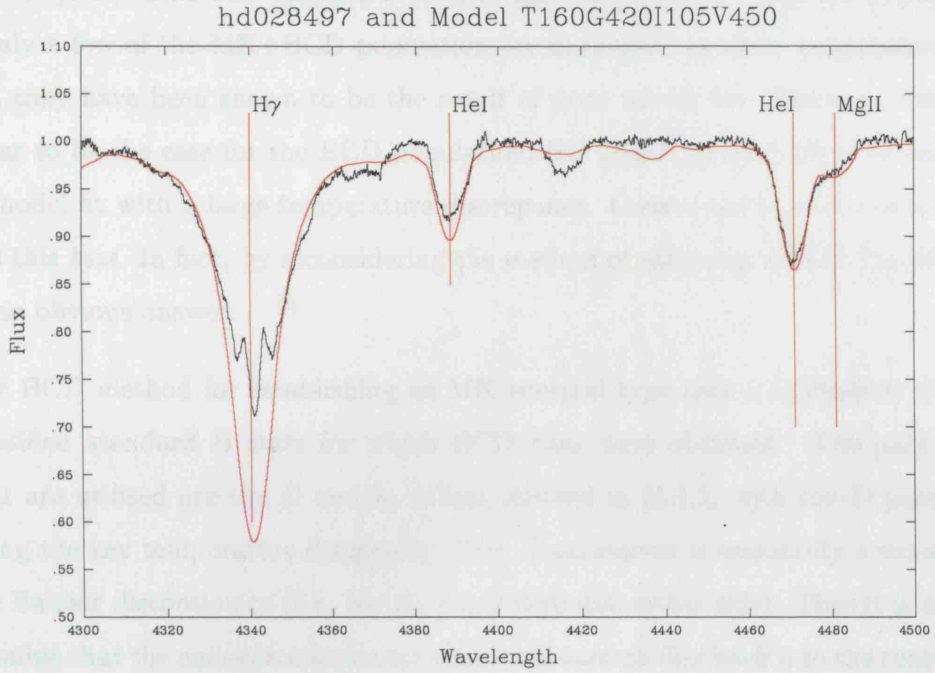

Figure 5.18. Plot of the normalised spectrum of HD 28497 (black line) and its mean square derived Model [$T_{\rm eff}$ = 16000 K; $\log g_{\rm pole}$ = 4.20; i = 60°; $v_{\rm eq}$ = 450 km s^{-1}] best fit (red line).

again these are not in agreement, though this result is the closest thus far and hence a little unusual in the light of the large temperature disparity. Inspection of Figure 5.18 is somewhat surprising; there is clearly a need for some slight continuum adjustment but all the key lines are striking in their similarity. The Hγ emission obviously pollutes the line core but the wings are a good fit and well within the dispersion present in the individual observations which make up this average. The He I–Mg II line blend clearly makes this fit compelling; though the Mg II λ4481 line fit sits marginally below the observation, a slight continuum adjustment will rectify this whilst benefiting the He I core also; this is illustrated by figure A.15. It is also noted that the region around 4410Å - 4420Å is clearly not reproduced, similar to HD 203467 [ref. Figure 5.15]. Though a slight drop in intensity is present in the model, over this region, no *reasonable* continuum adjustment will align the observation to the model over this feature.

5.6.5 Section summary

The Be star spectra that have Balmer emission present appear to show $T_{\rm mod}$ and $T_{\rm app}$ values that are systematically lower than those attributed to the spectral types of the

individual objects. This bias appears to be strongest in the BCD classified population. Whilst only a few of the MK+BCD population are discrepant in these temperature correlations, they have been shown to be the result of poor model fits. However, this does not appear to be the case for the BCD population; HD 28497 [figure 5.18] is an example of good model fit with a large temperature discrepancy. Consequently, one cannot easily disregard this *bias*. In fact, by reconsidering the method of assigning a BCD $T_{\rm eff}$, there is perhaps an obvious answer:

- The BCD method for establishing an MK spectral type uses a calibration of MK–classified standard B stars for which BCD data were obtained. The parameters that are utilised are the D and λ_1 values, defined in §5.1.1, with the D parameter being the key temperature diagnostic. This D parameter is essentially a measure of the Balmer discontinuity (i.e., by the flux differential either side). Thus it is at least possible that the emission component could add enough flux back into the continuum short of the discontinuity so as to imply a higher temperature. Consequently, it is now interesting to select all those stars whose spectra exhibit clear and substantial emission and check to see whether this population remains.

5.7 Model fits to Spectra with clear Balmer emission present

Figure 5.19 displays an H–R diagram, plus $T_{\rm eff}$ vs $T_{\rm app}$ plots, for all the Be–star observations that exhibit a distinct, pronounced, Balmer emission in their Hγ absorption line profiles. The bulk of the model fits for this population occupies a quite distinct region in the HR diagram, toward the low temperature end. However, the magnitude spread is quite pronounced and, in general, appears to exceed the spread of the Hipparcos data. With a mind to the closing comments of §5.6, a selection of stars and their model fits is displayed below [Figures 5.20, 5.21, 5.22 & 5.23] and their merits discussed. All of these stars are drawn from the BCD population and, unsurprisingly, they are all drawn from the outlier subset. Conclusions are drawn at the end of this section.

HD 56139

Figure 5.20 displays results for HD 56139. This star is BCD classified as B2IVe. The $T_{\rm sp}$ is 21528K with the model–fit yielding $T_{\rm mod}$ and $T_{\rm app}$ 12000K and 12710K, respectively. The BCD $\log g$ for this star is 3.81; the model $\log g_{\rm pole}$ is 3.00. All of these parameters

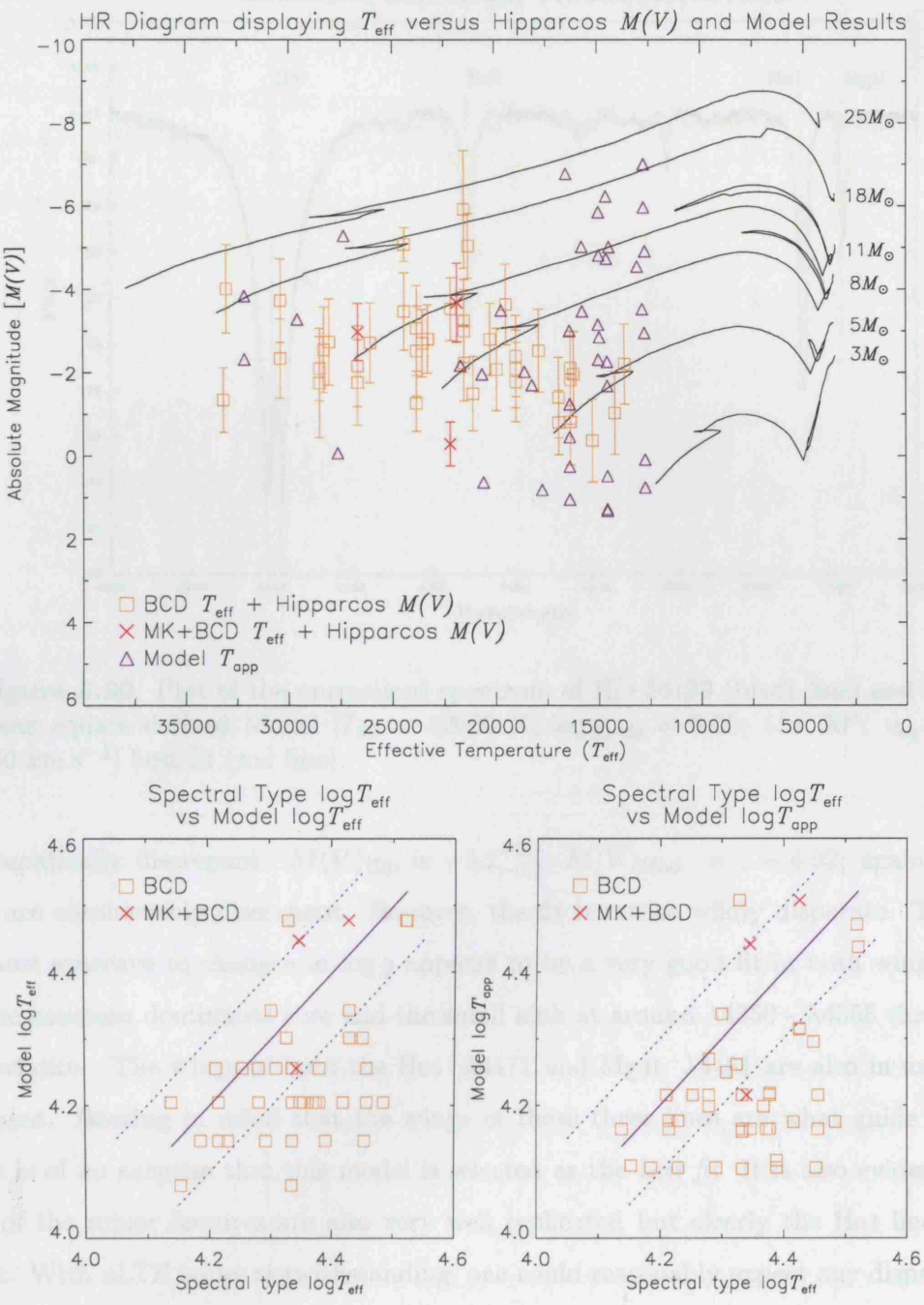

Figure 5.19. *The top panel* displays an H–R diagram for each of Chauville's stars that have strong Balmer emission in their spectra: T_{sp} vs $M(V)_{Hip}$ (orange square and red cross for BCD and MK+BCD respectively) with the BUSH models' apparent temperature vs model $M(V)$'s over-plotted (blue triangles). The error bars reflect the Hipparcos uncertainties. *The bottom two panels* display the log$T$ of Spectral type vs BUSH models' effective and apparent temperatures, from left to right respectively. The key for these two plots defines the 3 methods by which the published spectral type temperatures are calculated, see §5.4 for details.

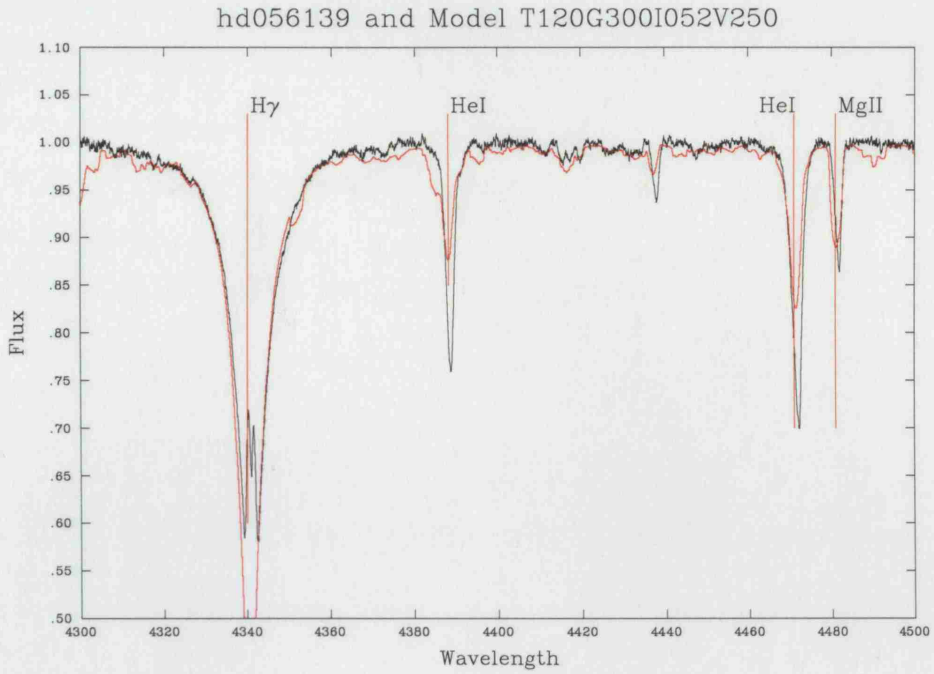

Figure 5.20. Plot of the normalised spectrum of HD 56139 (black line) and its mean square derived Model [$T_{\rm eff}$ = 12000 K; $\log g_{\rm pole}$ = 3.00; i = 30°; $v_{\rm eq}$ = 250 km s^{-1}] best fit (red line).

are dramatically discrepant. $M(V)_{\rm Hip}$ is $-3.2^{+0.1}_{-0.2}$; $M(V)_{\rm Mod}$ = − 4.92; again, these values are considerably discrepant. However, the fit is not so wildly disparate. The Hγ line, most sensitive to changes in $\log g$ appears to be a very good fit in both wings; it is only the emission dominated core and the small kink at around λ4350 - λ4355 that show any deviation. The wings of both the He I λ4471 and Mg II λ4481 are also in excellent agreement. Bearing in mind that the wings of these three lines are what guide the fit then it is of no surprise that this model is selected as the *best fit*. It is also evident that many of the minor features are also very well replicated but clearly the He I line cores are not. With nLTE issues notwithstanding, one could reasonably expect any disparity in these lines to show a shallower observation with respect to the model, due to the potential for emission, and not the reverse. To rectify the He I line cores one would undoubtedly have to push the $T_{\rm mod}$ upward. This would in turn demand an increase in $\log g$ to offset the impact of increased temperature on the Hγ line width. It is also likely that such a process would demand a reduction in viewing angle to offset the resulting broadening the He I lines; clearly it is only their depths that are at odds with the observation. As a consequence, though no quantification has been placed on these steps here, it is likely

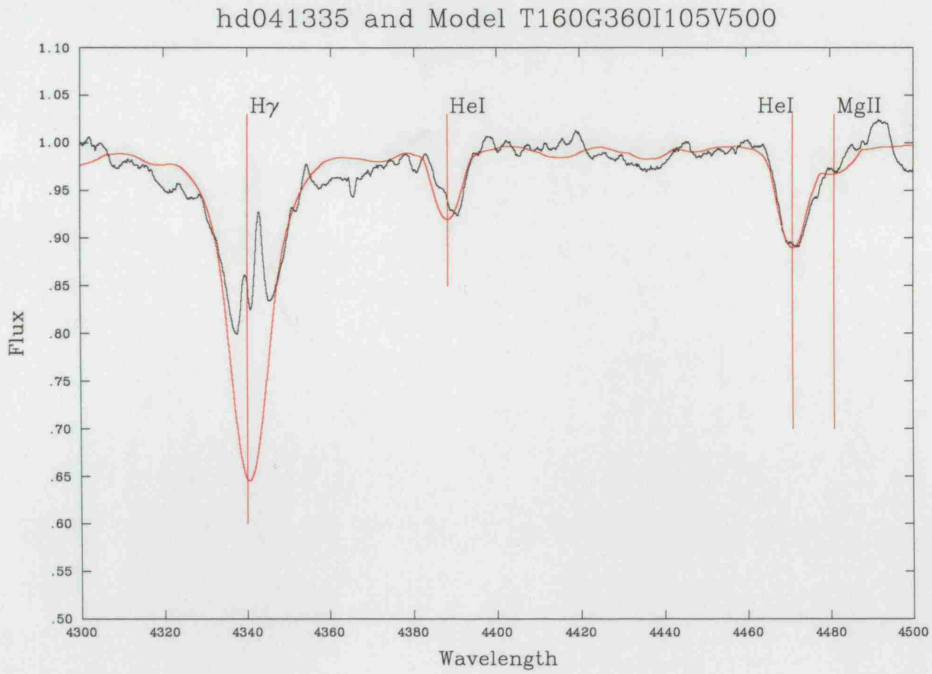

Figure 5.21. Plot of the normalised spectrum of HD 41335 (black line) and its mean square derived Model [$T_{\rm eff}$ = 16000 K; $\log g_{\rm pole}$ = 3.60; i = 60°; $v_{\rm eq}$ = 500 km s^{-1}] best fit (red line).

that the significant disparity in fundamental parameters between model and observations, would be, at least in part, alleviated by these actions.

HD 41335

Figure 5.21, displays results for HD 41335. This star is BCD classified as B1.5IIIen with $T_{\rm sp}$ 23281K. The corresponding model parameters are $T_{\rm mod}$ and $T_{\rm app}$ 16000K and 15780K, respectively. The published $\log g$ is 3.62 and the model $\log g_{\rm pole}$ is 3.60 with inclination, i, 90°. $M(V)_{\rm Hip}$ is $-2.9^{+0.5}_{-0.9}$, which despite the large Hipparcos error is still someway short of $M(V)_{\rm Mod}$ = −5.03. In respect of the fit itself, there is a mixture of successes and failures. On the success side, the red and blue wings of the Hγ line are reasonable fits; the He I lines are apparently a very good representation, in particular the He I λ4471 line. The general trends of the observed spectrum between the two He I lines are also reasonably matched. A final positive is the absence of the Mg II lines blue-wing, it has become completely blended with the He I line in both model and observation. However, throughout the entire spectrum, none of the minor features present in the observation are reproduced in the model. This is clearly a concern, though it is not clear what impact

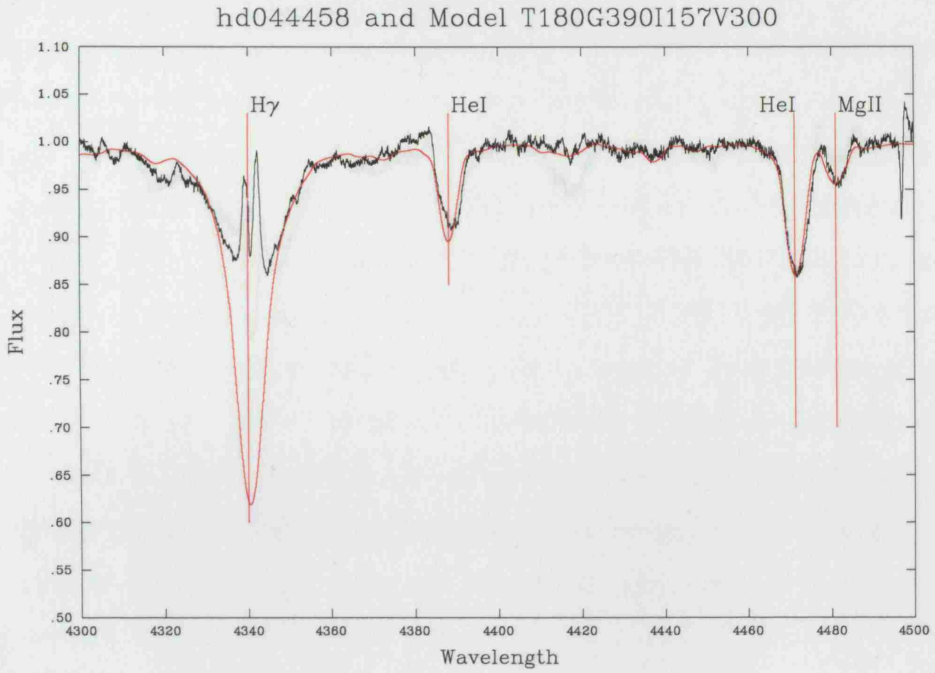

Figure 5.22. Plot of the normalised spectrum of HD 44458 (black line) and its mean square derived Model [$T_{\rm eff}$ = 18000 K; $\log g_{\rm pole}$ = 3.90; i = 90°; $v_{\rm eq}$ = 300 km s^{-1}] best fit (red line).

drawing out such features would have on the diagnostics. Shifting to any off–90° viewing angle would reduce the amount of blending of these minor features, in effect removing the smooth undulations, and perhaps recover some of this detail. Despite this, insofar as the model–fitting algorithm is concerned, the fundamental parameters, as modelled for this observation, should not be excluded without a more thorough investigation of the model degeneracy space (ref. chapter 6).

HD 44458

Figure 5.22 displays the results for HD 44458. The BCD derived spectral type is B0.5Vpe, with a corresponding $T_{\rm eff}$ of 28511K. The model–derived $T_{\rm eff}$ and $T_{\rm app}$ are 18000K and 16410K respectively. These are hugely discrepant, but interestingly, though, the Hipparcos derived $M(V)$ is $-2.3^{+1.0}_{-0.7}$, with the model value of -1.3 relatively close. The published $\log g$ is 3.94; the model $\log g_{\rm pole}$ and $\log g_{\rm eq}$ 3.90 and 2.73, respectively. These surface gravities appear to be discrepant, particularly when one considers the viewing angle of 90°; this would suggest an apparent $\log g$ somewhat lower than the model $\log g_{\rm pole}$. Review of the model fit though implies a largely different story; though the $T_{\rm eff}$ versus $T_{\rm app}$ are

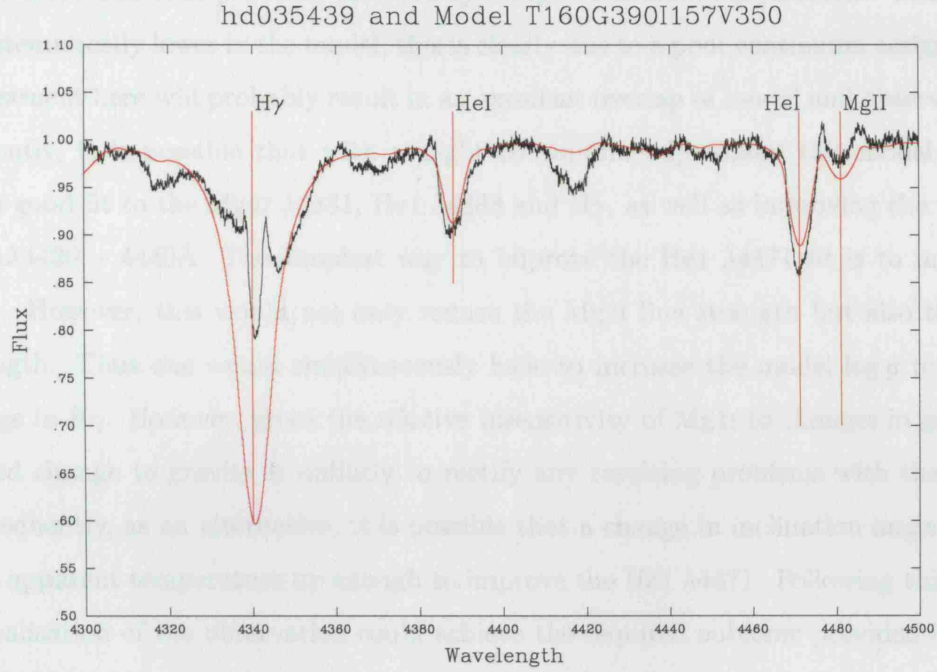

Figure 5.23. Plot of the normalised spectrum of HD 35439 (black line) and its mean square derived Model [$T_{\rm eff}$ = 16000 K; $\log g_{\rm pole}$ = 3.90; i = 90°; $v_{\rm eq}$ = 350 km s^{-1}] best fit (red line).

considerably discrepant, the key temperature diagnostics (He I & Mg II) are an almost perfect match. The Hγ line profile is consistent in the wings but slightly undermined by the emission in the core and the minor feature in the blue wing. Consequently, one must regard this model as a good fit.

HD 35439

Figure 5.23 displays the results for HD 35439. This star is BCD–classified as B1.5III-IVpe with $T_{\rm sp}$ 23550K. $T_{\rm mod}$ and $T_{\rm app}$ are 16000K and 14590K, respectively. The published $\log g$ is 3.72, the model yields a $\log g_{\rm pole}$ 3.90 with viewing angle i = 90°, thus the $\log g$ values are not unreasonable. Review of the model fit though is a little discouraging. The wings of the Hγ line are not vastly different, particularly when one considers the apparent asymmetry in the emission component. However, the depressions present either side of the Hγ wings are not replicated in the model; though as previously mentioned, it is unclear just how much emphasis should be placed on the ability to fit the regions outside of the key diagnostic lines. The wings of the He I λ4471 are a good fit, though the line core is shallower in the model; this trend is repeated in the He I λ4388 line, though is obviously

less pronounced and thus probably rectified by a slight continuum adjustment. The Mg II line is systematically lower in the model; this is clearly due to a poor continuum assignment and adjustment here will probably result in an excellent overlap of model and observation. Consequently, it is possible that with a slight continuum adjustment this model could provide a good fit to the Mg II λ4481, He I λ4388 and Hγ, as well as improving the region around $\lambda\lambda 4420 - 4440$Å. The simplest way to improve the He I λ4471 fit is to increase the $T_{\rm mod}$. However, this would not only reduce the Mg II line strength but also the Hγ line strength. Thus one would simultaneously have to increase the model $\log g$ to offset the change in Hγ. However, given the relative insensitivity of Mg II to changes in gravity, this forced change to gravity is unlikely to rectify any resulting problems with the Mg II fit. Consequently, as an alternative, it is possible that a change in inclination angle could push the apparent temperature up enough to improve the He I λ4471. Following this with a renormalisation of the observation could achieve the required outcome provided it does not substantially decrease the strength of the Mg II line. It is further possible that the competition between $T_{\rm eff}$ and $\log g$ in respect of the Hγ line would minimise the change here also; though the apparent log$g$ effect, mentioned throughout this chapter may prove dominant.

Figure 5.24 is included here to help illustrate these points. This plot shows the original composite spectrum from Chauville et al. (2001) data in black, the, 'marginally', continuum adjusted composite spectrum in green and the inclination–angle adjusted model fit. The inclination angle has been altered from 90° to 60°. This figure clearly shows the He I λ4471 line is now a fairly good fit throughout its profile. The Mg II λ4481 line has been minimally altered by the change in viewing angle and, in conjunction with a renormalisation, it also displays a fairly good fit. The He I λ4388 line has arguably been improved; the core of the observation now apparently shows a hint of emission, relative to the model. As a slight drawback though, the blue wing of the Hγ line is now too broad[5] and consequently casts a different doubt on the model fit. However, as already mentioned above, this could be due to the asymmetric Balmer emission. In any event, insofar as the model fitting procedure is concerned, it seems probable that the resulting $T_{\rm mod}$ is not far from reality. Hence, once again, it does appear that the BCD classification and subsequent determination of $T_{\rm eff}$ is at odds with the model grid.

[5]Interestingly, this does provide some direct evidence for the viewing–angle dependency of the (*apparent*) $\log g$, mentioned repeatedly throughout this chapter.

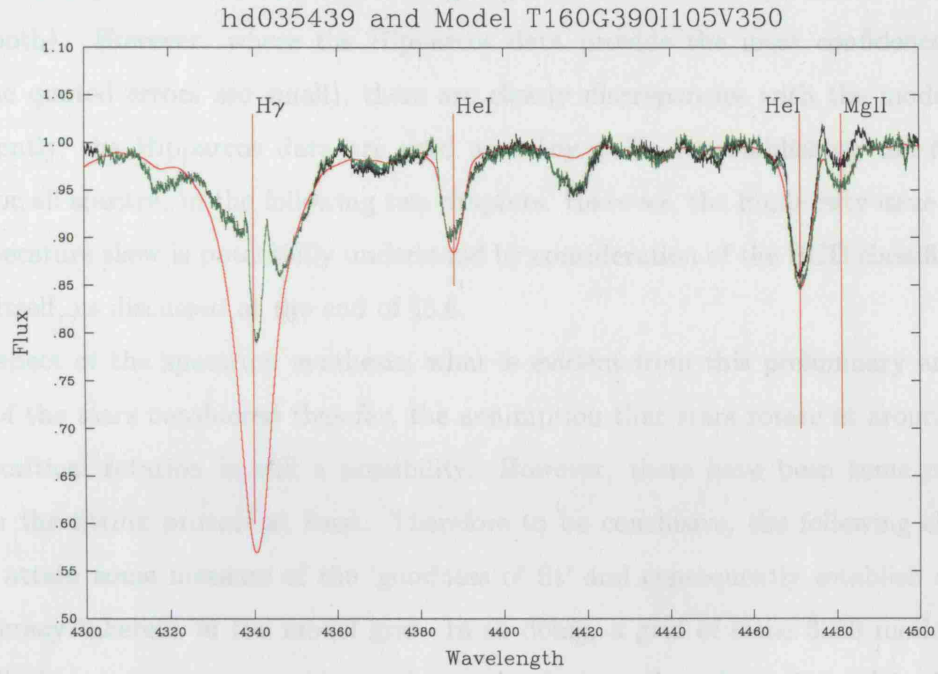

Figure 5.24. Plot of the normalised spectrum of HD 35439 (black line), a re-normalised spectrum of HD 35439 (green line) and an adjusted model [$T_{\rm eff}$ = 16000 K; $\log g_{\rm pole} = 3.90$; $i = 60°$; $v_{\rm eq} = 350$ km s^{-1}] fit (red line).

This observation bears some striking resemblances to previous examples. This spectrum has a quite distinctive saw–tooth effect appearance, it also displays the significant depression at around 4410Å - 4420Å, though it lacks the distinctive 'V-shaped' line profile, previously noted in the Mg II line.

5.8 Summary

In summary of this section, there is evidently a distinction between those stars which show *pronounced* Balmer emission and those that do not, in respect of the assignment of fundamental parameters. The H–R plots differentiate between these two subgroups such that the model-fits prefer a cooler solution than those assigned by the BCD classification method. In addition, the luminosities attributed to the star derived from Hipparcos data (in conjunction with BCD temperatures), result in ∼20% of these stars sitting below the main–sequence. Though the preliminary model–fits show the same percentage below the main–sequence, they also show a slightly higher fraction to be more evolved along the main–sequence. It thus appears inconclusive, at this stage, which method (i.e., model–

fitting or BCD spectral classification) of assigning these fundamental parameters is flawed (if not both). However, where the Hipparcos data provide the most confidence (i.e., where the quoted errors are small), there are clearly discrepancies with the model–fits. Consequently, the Hipparcos data are used as a key guide to establishing the *best–fit* models for all spectra, in the following two chapters. However, the luminosity issue aside, the temperature skew is potentially understood by consideration of the BCD classification method itself, as discussed at the end of §5.6.

In respect of the spectrum synthesis, what is evident from this preliminary analysis is that, of the stars considered thus far, the assumption that stars rotate at around 0.95 of their critical rotation is still a possibility. However, there have been some notable issues, in the fitting process at least. Therefore to be conclusive, the following chapter seeks to attain some measure of the 'goodness of fit' and consequently establish a level of degeneracy inherent in the model grid. In so doing, a grid of some 3360 models can potentially be cut to a manageable number and subsequently, a best–fit model selected. This will then feed back into the temperature and luminosity issues and provide a more conclusive outcome.

Chapter 6

Analysis of the Model–Grid Degeneracy

6.1 The χ^2 statistic

As previously stated, to obtain some feel for the level of degeneracy present in the model grid, whilst also ascertaining some degree of goodness of fit, a chi-square test is employed. The χ^2 statistic is given by equation 6.1.

$$\chi^2 = \sum_{i=1}^{N} \frac{(Observation_i - Model_i)^2}{\sigma_i^2} \tag{6.1}$$

where σ_i^2 denotes the error in the i^{th} data point in the observation. However, whilst it is possible to define the statistical errors in the observational data, no model ever fits the data to within these tiny errors. Thus a strict application of the χ^2 statistic is unlikely to prove useful. Hence, for the analysis carried out here, an assumption that the best fit model is indeed the 'true' fit for each observation is invoked. Consequently the following must hold,

$$\chi^2_{\nu_{BF}} \simeq \frac{\chi^2_{BF}}{(N-P)} = 1, \tag{6.2}$$

where $\chi^2_{\nu_{BF}}$ is the reduced χ^2 statistic, the BF subscript denotes best–fit, N is the number of data points and P is the degrees of freedom. Thus, noting that,

$$\sigma^2 = \frac{1}{(N-P)} \sum_{i=1}^{N} (O_i - M_i)^2, \tag{6.3}$$

in turn implies,

$$\chi^2_{BF} \simeq (N-P) = \frac{1}{\sigma^2_{BF}} \sum_{i=1}^{N} (O_i - M_i)^2. \tag{6.4}$$

Thus, recognising that the mean square of the residuals (MS) is simply,

$$MS = \frac{1}{(N)} \sum_{i=1}^{N} (O_i - M_i)^2, \tag{6.5}$$

equation 6.4 can be rewritten as,

$$\sigma^2_{BF} = \frac{N}{(N-P)} MS_{BF}. \tag{6.6}$$

Hence, finally, a set of chi–square values can be generated to enable all model fits to be compared to the best model fit via equation 6.7,

$$\chi^2 = \frac{(N-P)}{MS_{BF}} MS. \tag{6.7}$$

Whilst this is clearly not a *strict* definition of χ^2, it is, within this context, an appropriate and pragmatic one.

This form of the χ^2 statistic is applied to N=28 data points extracted from the mean square of the residuals resulting from the best–fit algorithm described in § 4.4; 7 data points are taken from the Hγ blue–wing (4329-4332Å), 7 from the Hγ red–wing (4348-4351Å), 7 from the He I blue–wing (4466-4469Å), 7 from the He I–Mg II line blend (4473-4484Å).

As previously stated, all χ^2 values calculated via this method are subject to the assumption that the best fit is indeed a *good* fit. Thus, as a consequence, should the best

fit in fact be a poor fit, χ^2_ν is still guaranteed to be unity and hence the goodness of fit, in effect, becomes a relative *poorness* of fit. Consequently, review of this chi-square space must be performed in conjunction with a 'by-eye' inspection of the best fit, as performed in the previous section [§5.4]. To this end, the individual cases discussed previously are reviewed in the context of their respective set of six, 2-d, contour plots of the chi-square space generated, i.e. each of the four parameters are plotted against each other. Hence, in the following subsections [§§6.2.1, 6.2.2 and 6.2.3] all of the examples explored thus far in section, §5.4, are separated into three subsets. Specifically, those that constitute a good 'by-eye' fit, those that are an intermediate good/poor fit (i.e. some, but not all, of the key diagnostics are an *adequate* fit) and those which are obviously a 'poor' fit. Further to this, in the context of reviewing the contour plots, the following analysis focuses upon the *apparent* degeneracy formed within the regions generated where the one to three sigma levels are in concordance. The reason for this is that it is not uncommon for the three sigma level to appear as more than one distinct region, thus to infer some additional level of significance to such a region it is required that a one sigma level region coincides.

6.2 The contour maps

6.2.1 Chi-Square contour maps for *Good* Model fits

HD 57219

Contour plots for HD 57219 are shown in figure 6.1. Figure 5.4 shows this to be an excellent model fit. The contour plots here reveal an uncertainty in temperature of no more than 2000K, an uncertainty in log$g$ of 0.3, an uncertainty in inclination of 15° and a $v_{\rm eq}$ uncertainty of around 100km s^{-1}. As is the case in general, the algorithm selected *best fit* model is discrepant in absolute magnitude from the Hipparcos derived value. Indeed, in this case, the Hipparcos upper limit for $M(V)$ is -2.0 whereas the model yields a value of -2.90. However, by exploring the model fits within the error space, defined by the above quoted uncertainties, a lower $M(V)_{\rm Mod}$ of -1.1 whilst maintaining an excellent *by-eye* fit. Evidently, this change in the model parameters also results in a change in $T_{\rm pole}$ to 19790K with a corresponding $T_{\rm app}$ of 17150K which is also in a much better agreement with the published $T_{\rm eff}$ of 21500K. However, further comment on this is reserved until the next chapter wherein the model–degeneracy space is explored in an attempt to simultaneously

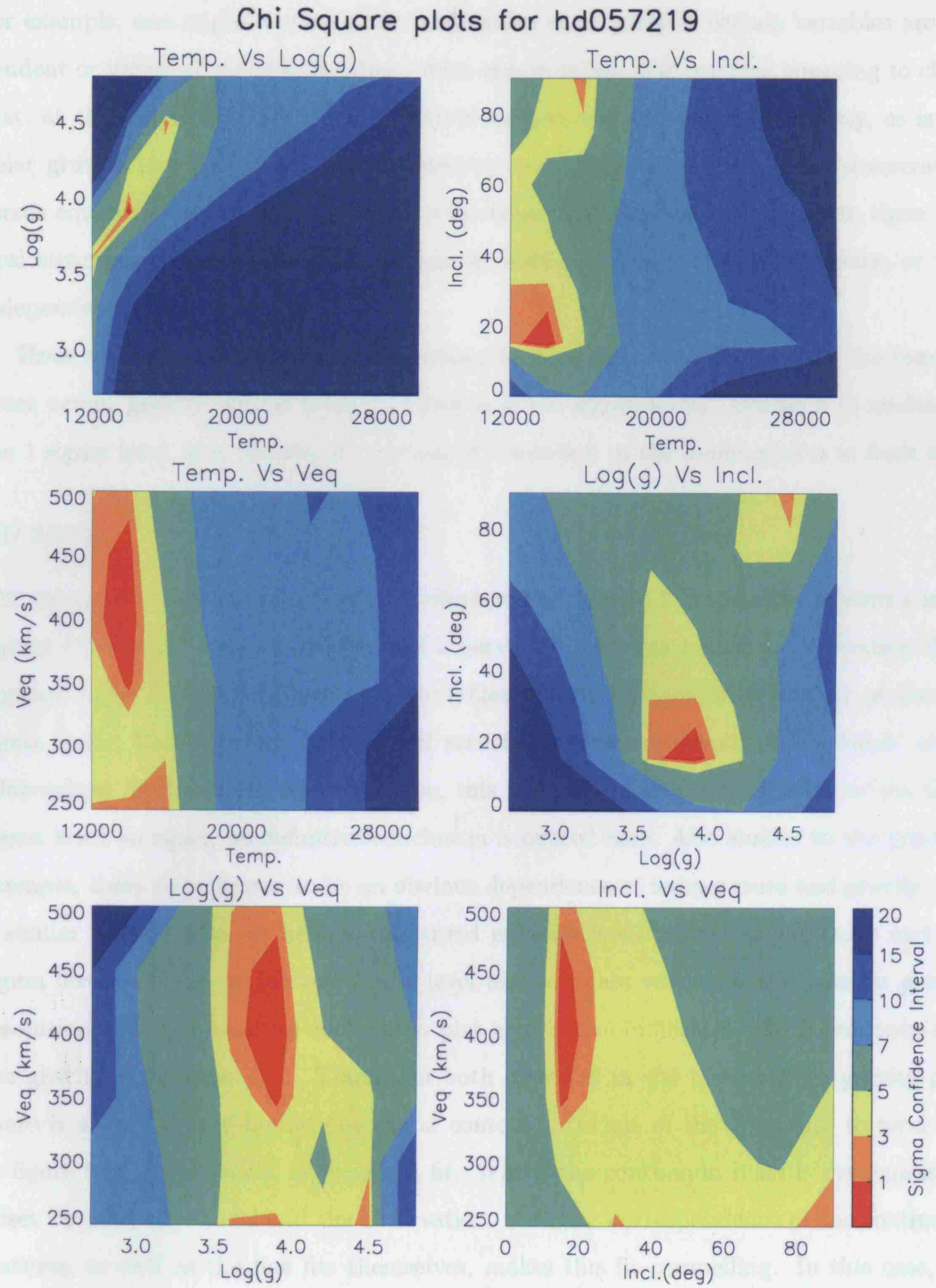

Figure 6.1. The six χ^2 plots for HD 57219; all of the four fundamental model parameters ($T_{\rm eff}$, $\log g_{\rm pol}$, i and $v_{\rm eq}$) are plotted against one another.

fit the observed spectra as well as the Hipparcos data.

At first glance it is not obvious if any greater detail can be gleaned from these plots. For example, one might wish to draw conclusions as to whether certain variables are dependent or independent of each other. With this in mind, it is perhaps tempting to claim that; at the one sigma level, temperature is independent of equatorial velocity, as is the polar gravity and also inclination. However, there does exist in both the temperature versus equatorial velocity and gravity versus equatorial velocity a thickness to these vertical structures which spans two grid points, thus it is non–trivial to attribute, or not, independence.

However, where there does indeed appear to be a clear dependency is in the temperature versus gravity plot at both the three and five sigma levels. Whilst it is unclear at the 1 sigma level, it is possible that a lack of resolution in the model grid is at fault here.

HD 214168

The second contour plot of HD 214168, displayed in figure 6.2, appears to present a much tighter correlation between models and observation. As was hinted at previously, there appears to be an independence of all variables relative to equatorial velocity at the one sigma level. Unlike before, the vertical structures here are devoid of 'thickness' which adds weight to this conclusion. However, this independence is not apparent at the three sigma level, so again, no definitive conclusion is offered here. Also similar to the previous example, there does appear to be an obvious dependence of temperature and gravity with a similar trend. Also, as before, this trend exhibits itself clearly at the three and five sigma levels but not at the one sigma level and so again reiterates the case for greater resolution. The temperature–inclination plot here is also indicative of a dependency as is the gravity–inclination plot. Though in both cases, as in the temperature–gravity plot, there is a very tightly bound one sigma contour. Review of the spectrum to model fit in figure 5.6, reveals again an excellent fit. Whilst the continuum itself is systematically offset between the model and the observation, the clear correspondence of the continuum features, as well as the line fits themselves, makes this fit compelling. In this case, the observational data implies, as a maximum, an absolute magnitude of -0.8, compared with the model derived value of -2.59. Clearly this is discrepant. Thus returning to the contour plot to try to attain some level of degeneracy, there is little alternative but to drop to the three sigma level to provide some reasonable parameter space to explore. With this in

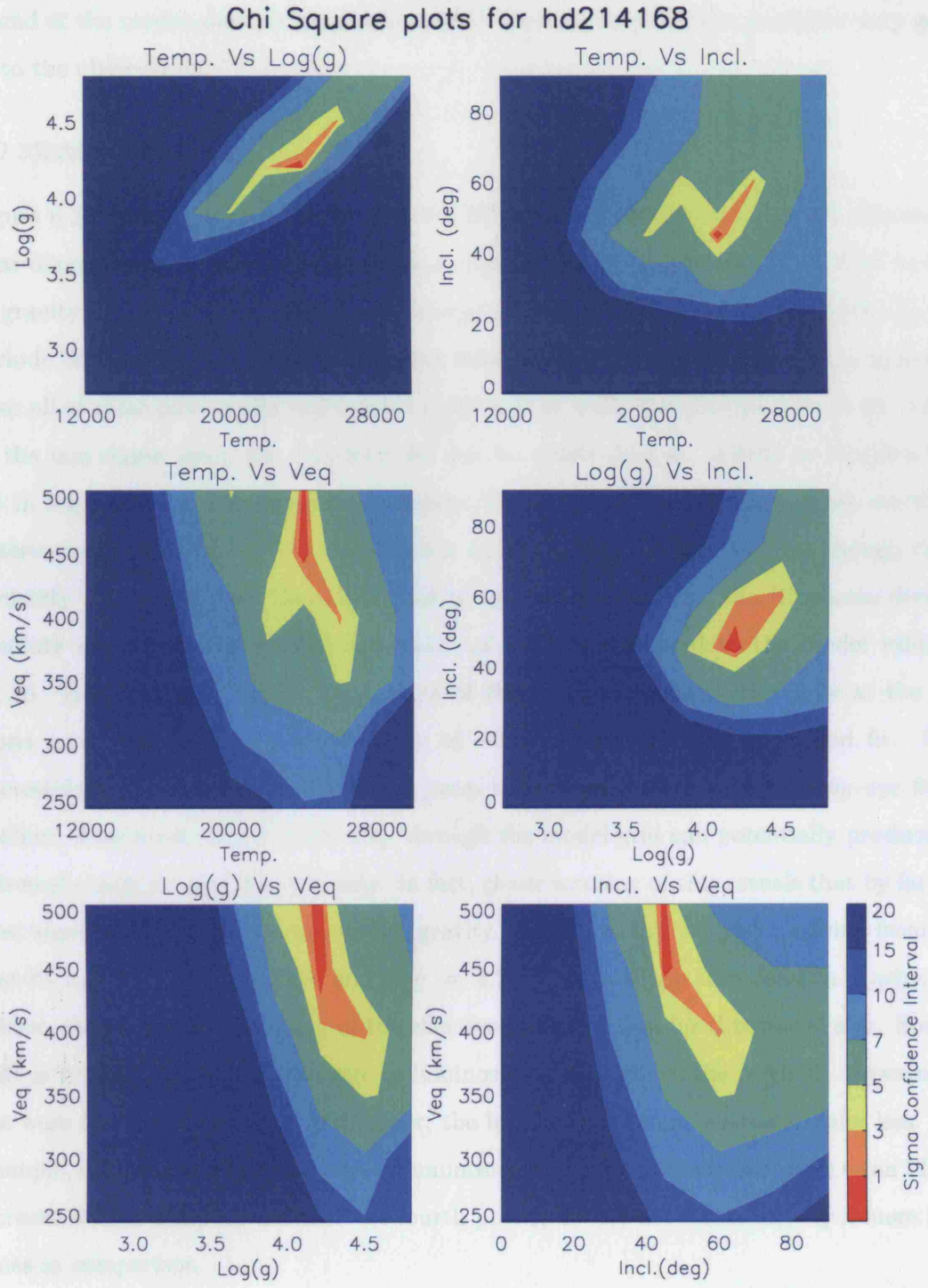

Figure 6.2. The six χ^2 plots for HD 214168; all of the four fundamental model parameters ($T_{\rm eff}$, $\log g_{\rm pol}$, i and $v_{\rm eq}$) are plotted against one another.

mind, the following uncertainties are allowed for: 2000K in temperature; 0.3 in log$g$; 15° in inclination; 100km s^{-1} in equatorial velocity. Exploration of this space reveals a lower bound of the model absolute magnitude of 0.0. This model does also provide a very good fit to the observation.

HD 33328

Figure 6.3 displays the six contour plots for HD 33328. Similarly to figure 6.2, this shows clear dependency's between temperature and gravity, temperature and inclination as well as gravity and inclination, all at the one sigma level. Whilst the remaining plots do not exclude dependency, they do preclude any inference of trend. However, what is apparent from all of these plots is the well defined space within which the *good–fit* models sit. Thus, at the one sigma level, the uncertainties can be established as: 4000K in temperature; 0.6 in log$g$; 50km s^{-1} in equatorial velocity; 30° in inclination. Review of the model to observation plot in figure 5.7 reveals what is, in general, an excellent fit, though there is clearly some issue with the finer detail of this fit. In this case, the Hipparcos derived absolute magnitude has a minimum value of -2.70 as opposed to the model value of -1.28. However, once again, exploration of the degenerate space, this time at the one sigma level, can lead to a model value of -3.99 whilst maintaining a good fit. It is interesting to note here the significant jump in luminosity from one good *by–eye* fit to another. Essentially just a single step through the model grid can potentially produce an extremely large change in luminosity. In fact, closer scrutiny of this reveals that by far the most significant impactor is the surface gravity. Indeed, in this example, moving from the best–fit model of $T = 18000$K and log$g = 4.2$ by just a single step down in gravity, i.e. 0.3dex, causes a, near, doubling of the effective radius of area for this model star. Such a shift is readily equated to a change in luminosity of four times the original. However, if one were to change any other parameter, the luminosity change is substantially less. For example, despite the T^4 dependence of luminosity, a 2000K increase associates to an 11.1% increase which, compounded over the fourth power, boosts the luminosity by a mere 1.52 times in comparison.

HD 209522

Figure 6.4 displays the contour plots for HD 209522. It is again the case that, at the one sigma level, there is clear dependency's between temperature and gravity, temperature

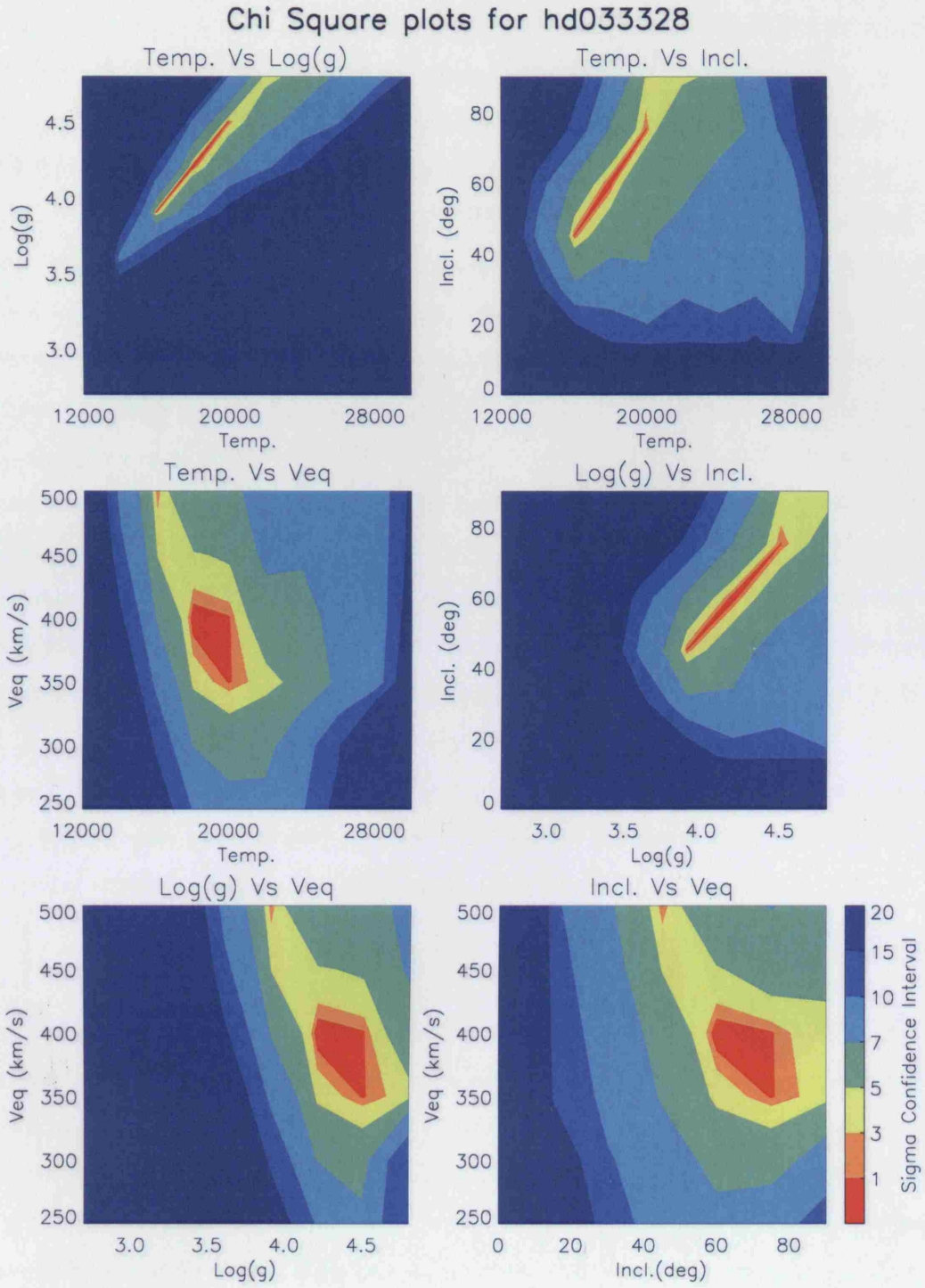

Figure 6.3. The six χ^2 plots for HD 33328; all of the four fundamental model parameters ($T_{\rm eff}$, $\log g_{\rm pol}$, i and $v_{\rm eq}$) are plotted against one another.

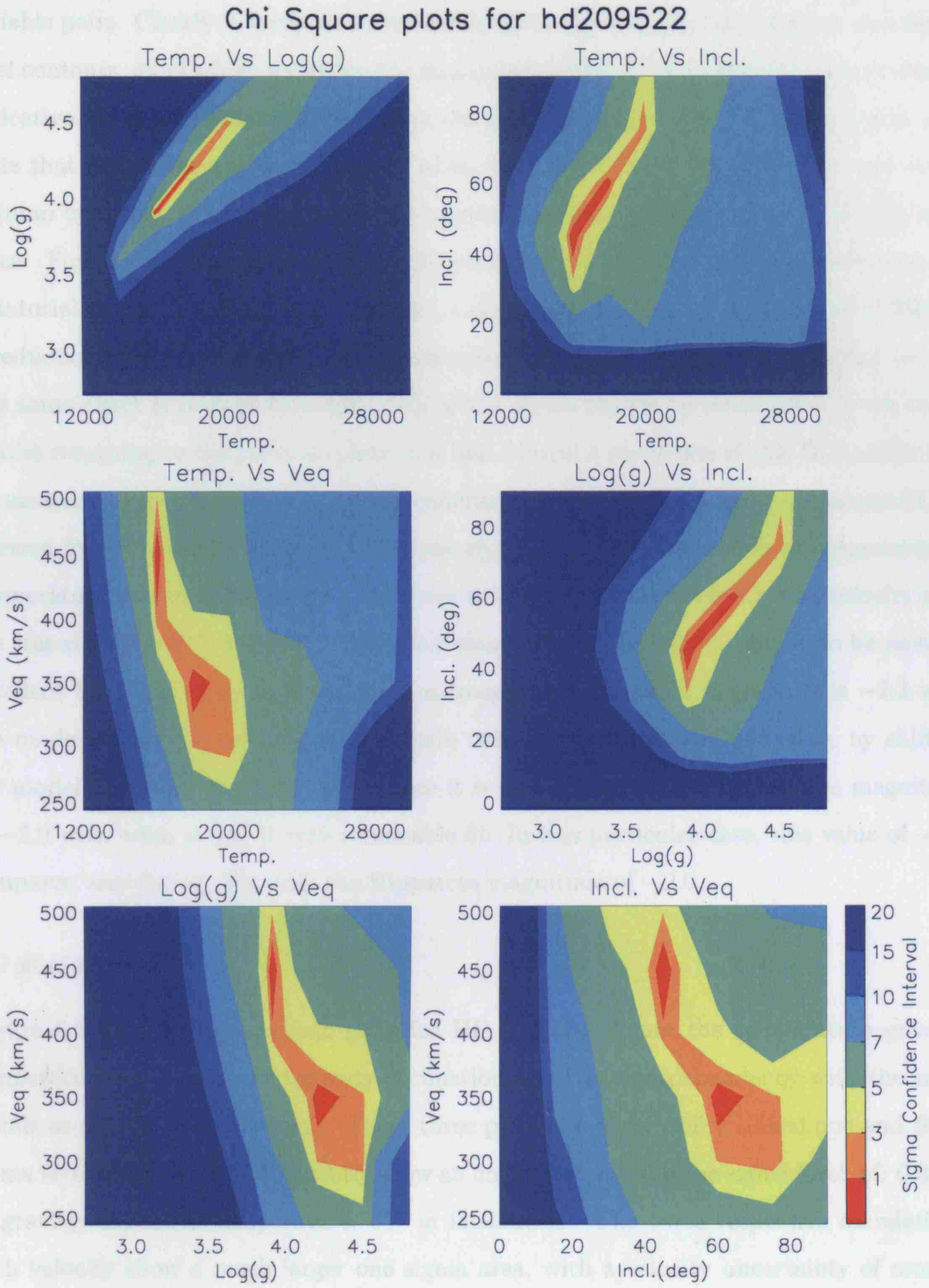

Figure 6.4. The six χ^2 plots for HD 209522; all of the four fundamental model parameters ($T_{\rm eff}$, $\log g_{\rm pol}$, i and $v_{\rm eq}$) are plotted against one another.

and inclination as well as gravity and inclination. However, what was not clear from the previous examples was whether there existed any dependency's between the remaining variable pairs. Clearly in these three remaining plots there is seen two, distinct, one sigma level contours, all of which sit within the single three sigma level contour. This is evidently indicative of an interdependence between the remaining components and essentially suggests that to recover a good–fit model, when stepping through velocity space, one needs to jump by 100km s^{-1} before simultaneously re–establishing values of the remaining variables. Further to this, the trends are the same for all relationships, i.e. increasing the equatorial velocity by 100km s^{-1} drives: a reduction in temperature of around 2000K; a reduction in log$g$ of 0.3dex; and a reduction in inclination of 15°. Whether or not this same effect is present throughout all of the fits of models to observation is not clear. Whilst returning to the previous plots may hint toward a repetition of this Bi–location the parameter space explored prevents any conclusive judgement. However, the uncertainties inferred from these data suggests, at the one sigma level, that the models are degenerate in temperature over a 4000K spread, log$g$ over 0.6dex, inclination over 30° and velocity over the stated 100km s^{-1}. Review of figure 5.8 clearly shows the best–fit model to be another excellent fit. The upper limit of the Hipparcos derived absolute magnitude is -2.3 with the model yielding a value of -3.3. Again this is discrepant, but as before, by shifting the model fit within the degenerate space it is possible to recover an absolute magnitude of -2.0 with what is still a very reasonable fit. In this particular case, this value of -2.0 compares very favourably with the Hipparcos magnitude of -2.0.

HD 224559

Figure 6.5 displays the contour plots for HD 224559. Again the temperature–gravity, temperature–inclination and gravity–inclination show an interdependency with the same trends as commented previously. These three plots also show well confined one and three sigma level contours. They evidently show an uncertainty, at the one sigma level, of: 0.3dex in gravity; 2000K in temperature; 30° in inclination. The three respective correlations with velocity show a much larger one sigma area, with a velocity uncertainty of around 50km s^{-1}. Review of figure 5.14 reveals yet another excellent model fit to observation. The correlation of absolute magnitudes is, again, disparate with an Hipparcos minimum of -1.30 and a model value of -0.5. As has been briefly discussed in the previous section, and in view of a model $\log g_{pole} = 4.20$, it is evident that a step change in gravity

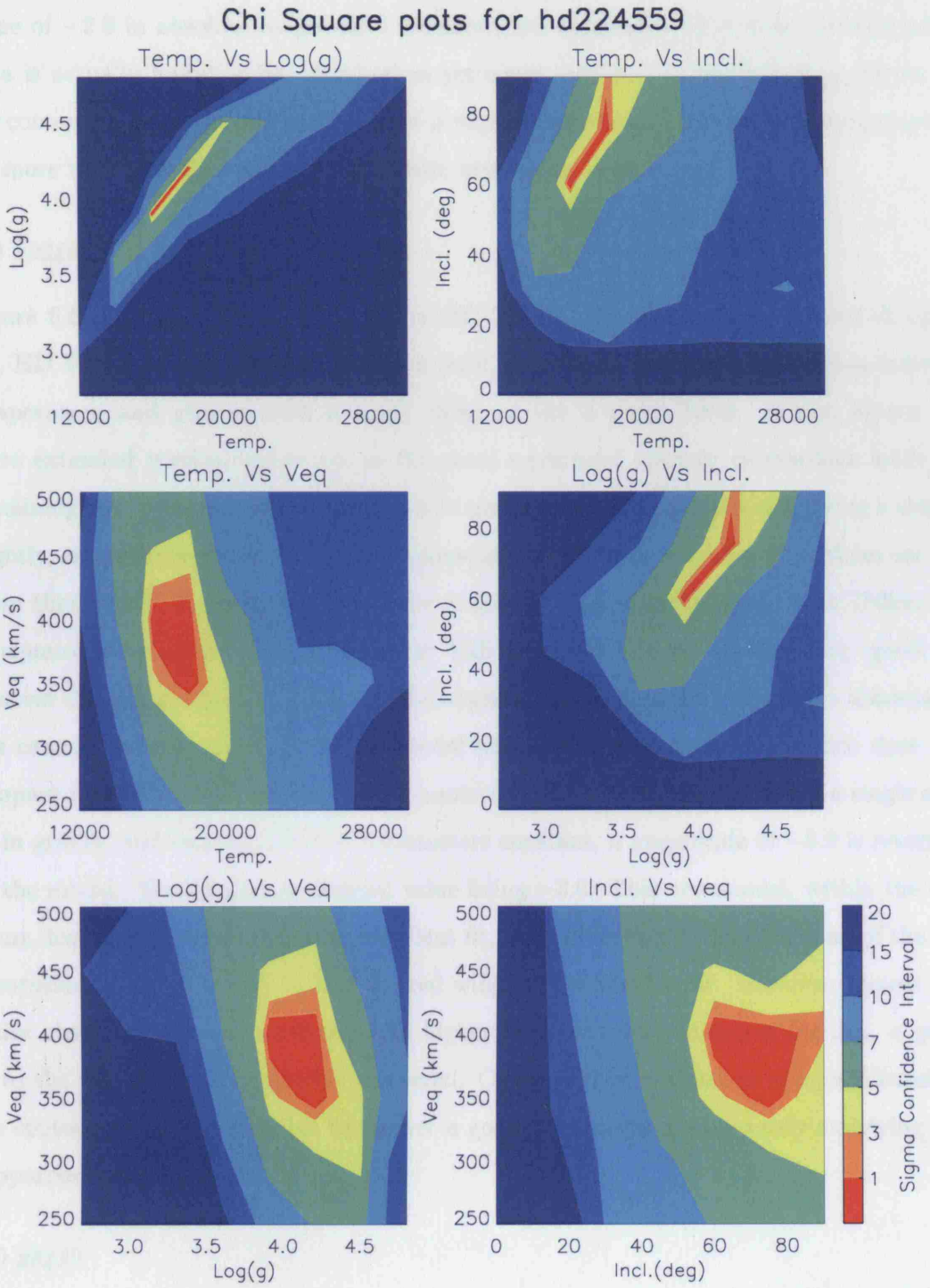

Figure 6.5. The six χ^2 plots for HD 224559; all of the four fundamental model parameters ($T_{\rm eff}$, $\log g_{\rm pol}$, i and $v_{\rm eq}$) are plotted against one another.

would more than reconcile this difference. In fact, with a single step change in gravity, temperature and inclination another excellent model fit is obtained. This though has a value of -2.0 in absolute magnitude. However, the maximum value from the Hipparcos data is actually found to be -2.2 and so yet again, within the degeneracy presented by the contour plots, it is possible to recover a physically appropriate model when accounting for more than just the three key diagnostic absorption lines.

HD 203467

Figure 6.6 displays the contour plots for HD 203467. This plot is reminiscent of figure 6.1, HD 57219, in that, at the one sigma level, it shows a very tight correlation between temperature and gravity with a slight trend at the 3 sigma level. It also shares the more extended vertical structures in the three equatorial velocity correlations with the remaining two, temperature–inclination and gravity–inclination, plots displaying a single, slightly, extended one sigma zone. The apparent uncertainties one infers from these are: no more than 2000K in temperature; 0.3dex in gravity; 30° in inclination; up to 150km s^{-1} in equatorial velocity. Reviewing figure 5.15 shows this to be another very good fit, however the slight offset, of model to observation, in the blue wing of the Hγ absorption line cannot be ignored. The best–fit model absolute magnitude is -5.4 which does not compare favourably with the Hipparcos maximum of -4.1. However, moving a single step up in gravity and keeping all other parameters constant, a magnitude of -3.9 is returned by the model. The Hipparcos derived value being -3.6. This new model, within the one sigma degeneracy level is again an excellent fit, but interestingly, the blue wing of the Hγ absorption line is now well fit but the red wing is now slightly off. However, almost the entire observation has a systematically higher flux and thus, adjusting for this, a good fit to the red wing can be quickly recovered. Consequently, within the bounds offered by the contour plots, it is possible to recover a good fit whilst simultaneously satisfying the Hipparcos data.

HD 28497

The final set of contour plots in this subsection are displayed in figure 6.7 and are for the star HD028497. These plots return to the clear interdependency seen in three out of the six plots reviewed thus far. The temperature–gravity, temperature–inclination and gravity–inclination plots all show a well defined, one sigma level, correlation with a positive

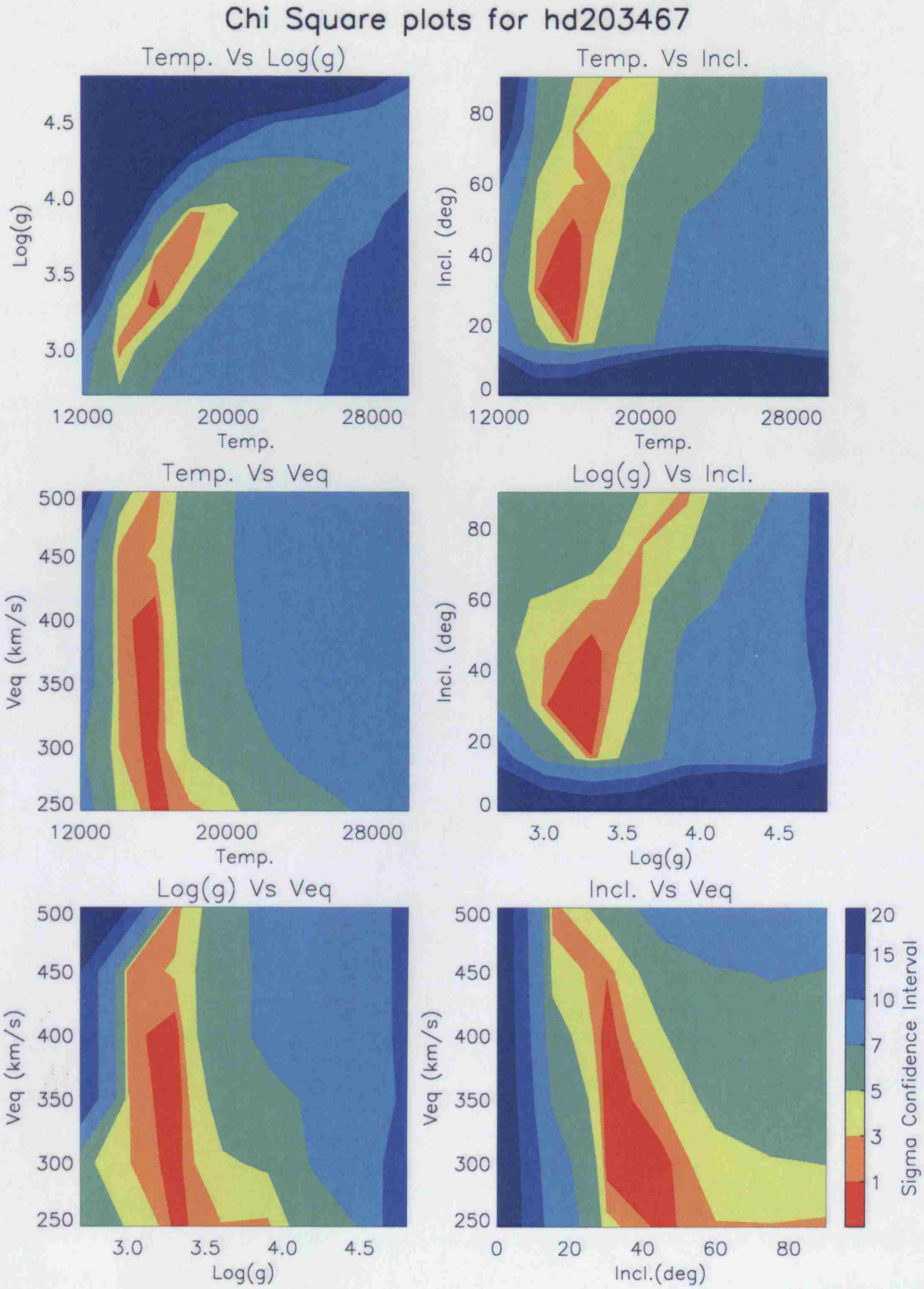

Figure 6.6. The six χ^2 plots for HD 203467; all of the four fundamental model parameters ($T_{\rm eff}$, $\log g_{\rm pol}$, i and $v_{\rm eq}$) are plotted against one another.

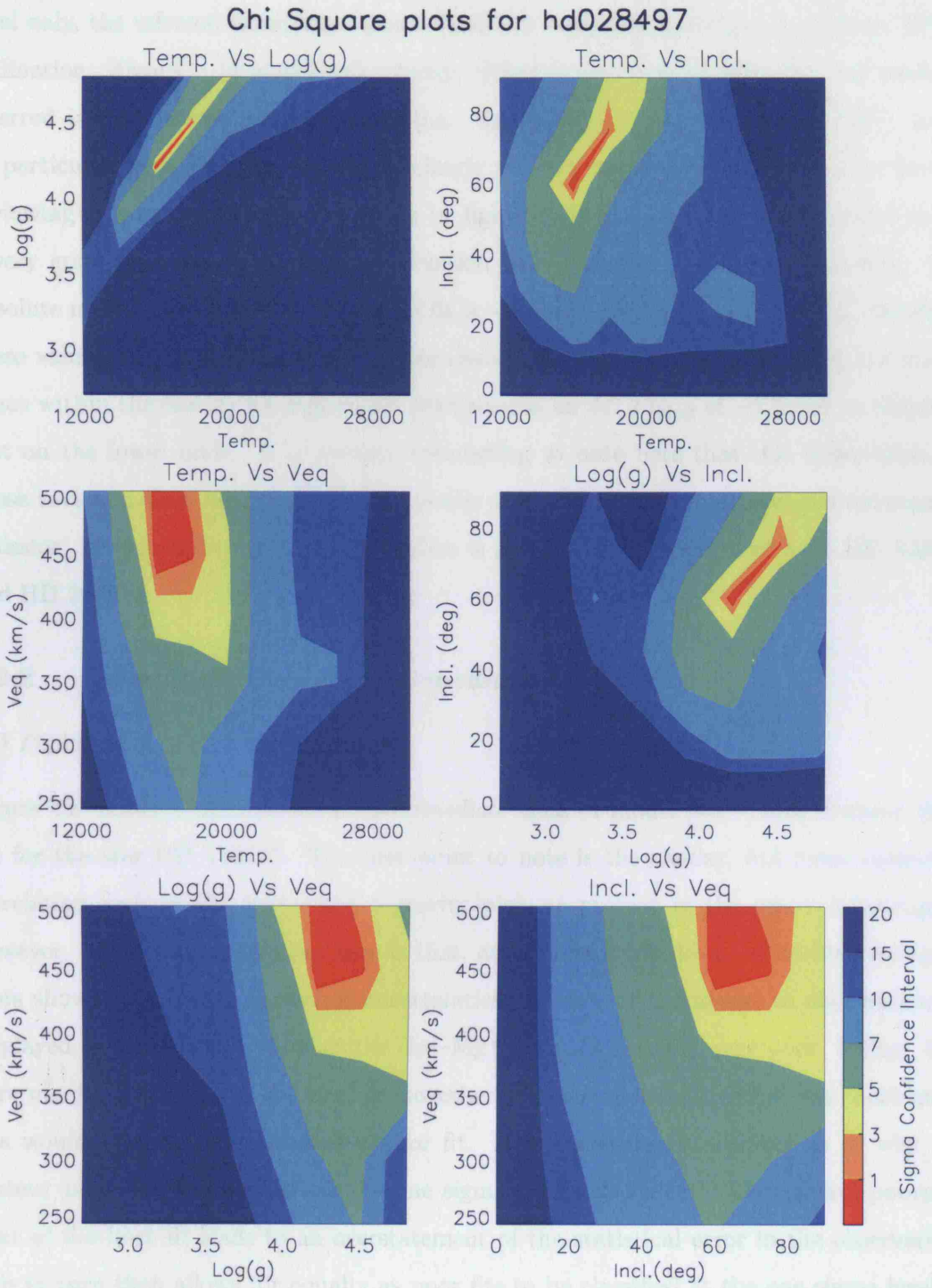

Figure 6.7. The six χ^2 plots for HD 28497; all of the four fundamental model parameters ($T_{\rm eff}$, $\log g_{\rm pol}$, i and $v_{\rm eq}$) are plotted against one another.

gradient. The remaining three plots, again, show a more blurred correlation with a zone, rather than a curve, marking out the one sigma level degeneracy. Using the one sigma level only, the inferred uncertainties are: 2000K in temperature; 0.3dex in gravity; 15° in inclination; 50km s^{-1} in equatorial velocity. What is clearly apparent here, and perhaps inferred in two of the previous plots (i.e. figures 6.2, 6.6) is that the velocity space in particular may need expanding to clearly confine these uncertainties. Nonetheless, reviewing the model to observation fit in figure 5.18 reveals the best–fit model to be a very good representation of the observation with a couple of issues outstanding. The absolute magnitude offered by the model fit is -1.6 with $M(V)_{\rm Hip} = -2.8^{+0.3}_{-0.5}$. So whilst these values are again disparate, they are clearly the closest so far. Searching the model space within the one sigma degeneracy level reveals an $M(V)_{\rm Mod}$ of -2.5 can be obtained just on the lower limit. It is perhaps interesting to note here that this observation, of those reviewed thus far in this section, is the only one to exhibit a clear and substantial emission, though some very slight emission is present in the spectra of both HD 203467 and HD 209522.

6.2.2 χ^2 contour maps for *Intermediate* Model fits

HD 174237

Figure 6.8 displays the first of the *intermediate* class of model fits. These contour plots are for the star HD 174237. The first point to note is the similar, but more extended, correlation seen in the temperature–gravity plot, as present in the previous examples. However, what is most striking here is that, at the one sigma level, all of the remaining plots show a significant spread of uncertainties. Review of the model to observation fit displayed in figure 5.5 shows that the He I–Mg II blend is actually very poor. In fact, if it were not for the wings of the Hγ line, together with the general trend of the continuum, this would have to be classed as a poor fit. It is consequently obvious as to why the contour plots are so extended at the one sigma level. Specifically, the general poorness of fit of the best–fit leads to an overstatement of the statistical error in the observation. This in turn then allows for equally as poor fits to be classified at the one sigma level of degeneracy. It is still interesting though that this extended degeneracy is less apparent in the temperature–gravity correlation. As a consequence, and given that all of the classified *good–fit* models showed degeneracies in equatorial velocity and inclination similar to each

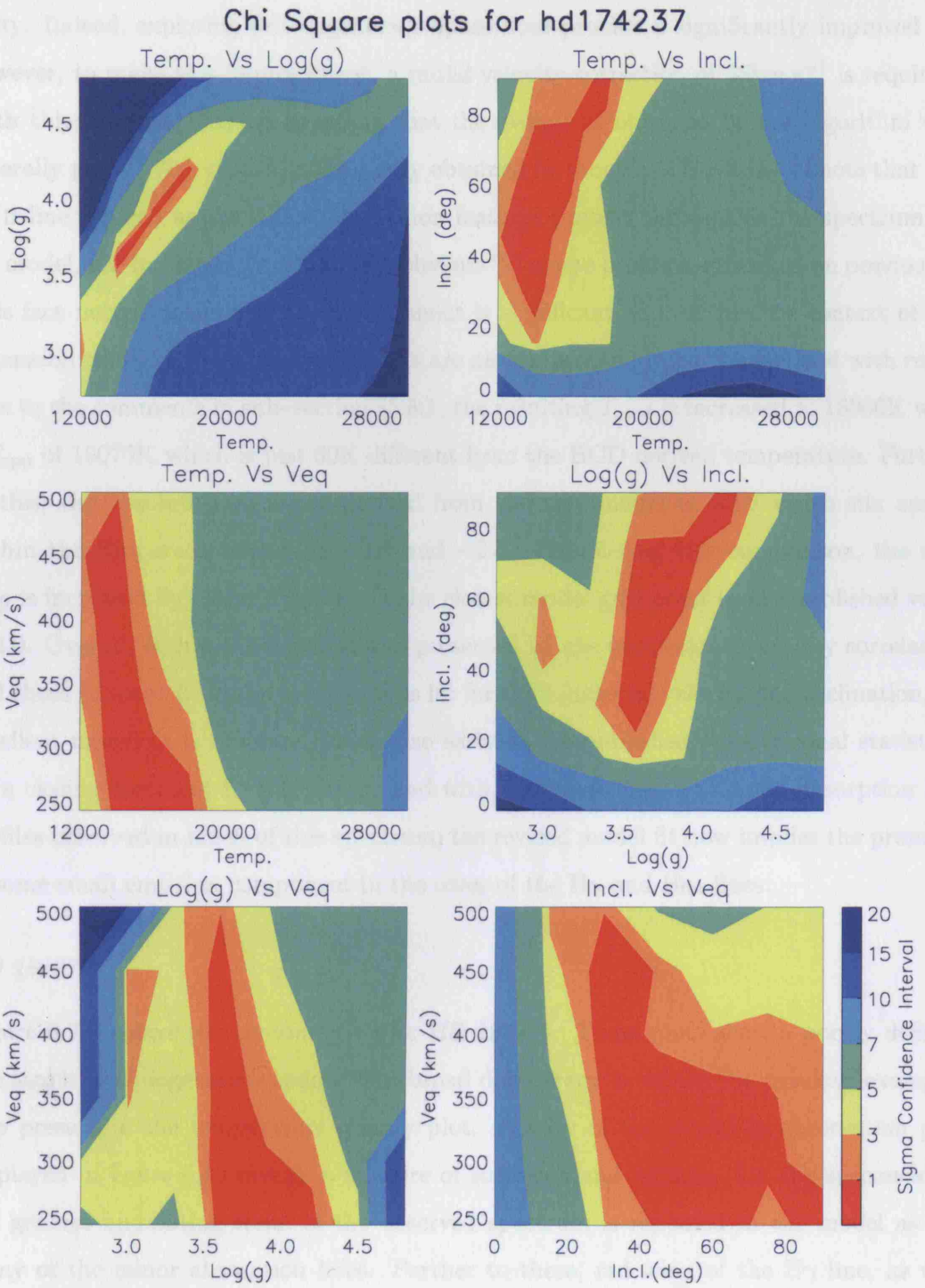

Figure 6.8. The six χ^2 plots for HD 174237; all of the four fundamental model parameters ($T_{\rm eff}$, $\log g_{\rm pol}$, i and $v_{\rm eq}$) are plotted against one another.

other, the following are adopted and explored to see if an improved fit can be obtained: 4000K in temperature; 0.6dex in gravity; 30° in inclination; 100km s^{-1} in equatorial velocity. Indeed, exploring this degeneracy space does provide a significantly improved fit. However, to make this improvement, a radial velocity correction of 35km s^{-1} is required. With this in mind, it is unsurprising that the overall fit obtained by the algorithm was generally poor. With regard to the newly obtained fit though, it is worthy of note that the Mg II line, as well as the minor absorption features present throughout the spectrum, in the model, fail to precisely recreate the obvious 'V' shape profile commented on previously. This fact notwithstanding, the improvement is significant and, within the context of the discussion thus far, the peripheral results are also improved. In particular, and with reference to the comments in sub–section §5.5.1, the resulting $T_{\rm mod}$ is increased to 18000K with a $T_{\rm app}$ of 19070K which is just 60K different from the BCD derived temperature. Further to this, the absolute magnitude derived from the new model is -2.0 which sits neatly within the Hipparcos bounds of -1.9 and -2.5. Completing this comparison, the new log$g$ is increased by 0.3 to 3.9 which is the closest model grid point to the published value of 4.0. Overall, within the uncertainties presented by the temperature–gravity correlation and those adopted from the analysis thus far for the equatorial velocity and inclination, an excellent model fit is obtained which also satisfies the published observational statistics. As a closing comment to this object, and with a mind to the 'V' shaped absorption line profiles observed in much of this spectrum, the revised model fit now implies the presence of some small emission component in the cores of the Hγ and He I lines.

HD 184279

Figure 6.9 displays the contour plots for HD 184279. These plots show a poorly defined one sigma level degeneracy space. This broad degeneracy is, unlike the previous example, also present in the temperature–gravity plot. Review of the model to observation plot displayed in figure 5.10 reveals a mixture of successes and failures. On the success side, the general undulating trend of the observed spectrum is repeated in the model as are many of the minor absorption lines. Further to these, red wing of the Hγ line, as well as the blue wings of both the He Iλ4471 and Mg II lines, relatively well fit. Conversely though, the emission component in the blue wing of the Hγ line notwithstanding, the He I line cores are significantly awry as are the red wings of these lines. The Mg II line, also suffers this same defect which in turn renders this line far too narrow. Evidently, as in

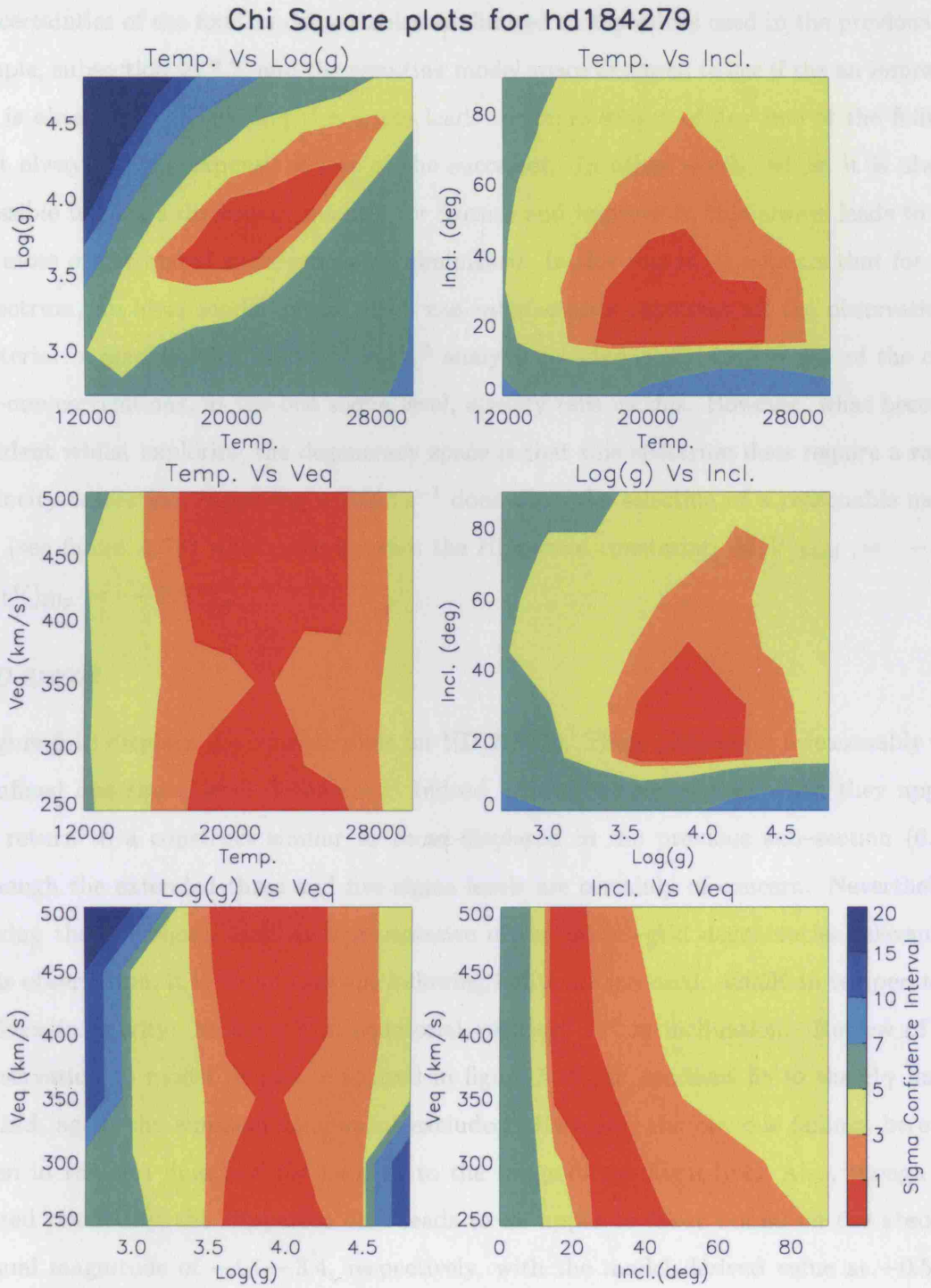

Figure 6.9. The six χ^2 plots for HD 184279; all of the four fundamental model parameters ($T_{\rm eff}$, $\log g_{\rm pol}$, i and $v_{\rm eq}$) are plotted against one another.

the previous discussion, this model fit is sufficiently poor so as to lead the χ^2 analysis to employ a significantly overstated statistical error in the observation. For this reason the uncertainties of the four model variables are limited to the values used in the previous example, subsection §6.2.2, and the resulting model space explored to see if the an improved fit is obtainable. Exploring this space leads to improvement of any one of the failures but always at the expense of one of the successes. In other words, whilst it is always possible to pick a discrepant quantity or feature and improve it, this always leads to one or more of the stated successes being diminished. In this regard, it appears that for this spectrum, no ideal model exists which can satisfactorily represent all the observational criteria. Arguably, the failure of the χ^2 analysis to adequately confine any of the one–to–one correlations, at the one sigma level, already tells us this. However, what becomes evident whilst exploring the degeneracy space is that this spectrum does require a radial velocity correction. Applying a 70km s^{-1} does allow the selection of a reasonable model fit (see figure A.73) which also satisfies the Hipparcos constraint; $M(V)_{\rm Mod} = -4.3$; $M(V)_{\rm Hip} = -2.9^{+1.0}_{-1.4}$.

HD 212076

Figure 6.10 displays the contour plots for HD 212076. These plots show a reasonably well confined one sigma level degeneracy. Indeed, at the one sigma level only, they appear to return to a construct similar to those displayed in the previous sub–section (6.2.1. Though the extended three and five sigma levels are certainly of concern. Nevertheless, taking the one sigma level as representative of the model–grid degeneracies relevant to this observation, it is found that the following limits are imposed: 4000K in temperature; 0.3dex in gravity; 100km s^{-1} in equatorial velocity; 15° in inclination. Review of the observation to model fit plot, displayed in figure 5.12, an excellent fit to the Hγ line is found, again the emission component excluded. However, the obvious failings here are seen in the He I lines and the poor fit to the wings of the Mg II line. Also, though not noted previously, the Hipparcos data leads to an upper to lower bound on the absolute visual magnitude of -4.1–-3.4, respectively, with the model derived value at -0.5; in luminosity terms, this is a massive discrepancy. Exploration of the degenerate model space can maintain as good a fit to the Hγ line, even improve much of the correlation to the minor absorption features along the spectrum, but does not significantly alter the He I and Mg II anti correlations. It is also the case that whilst the absolute magnitude

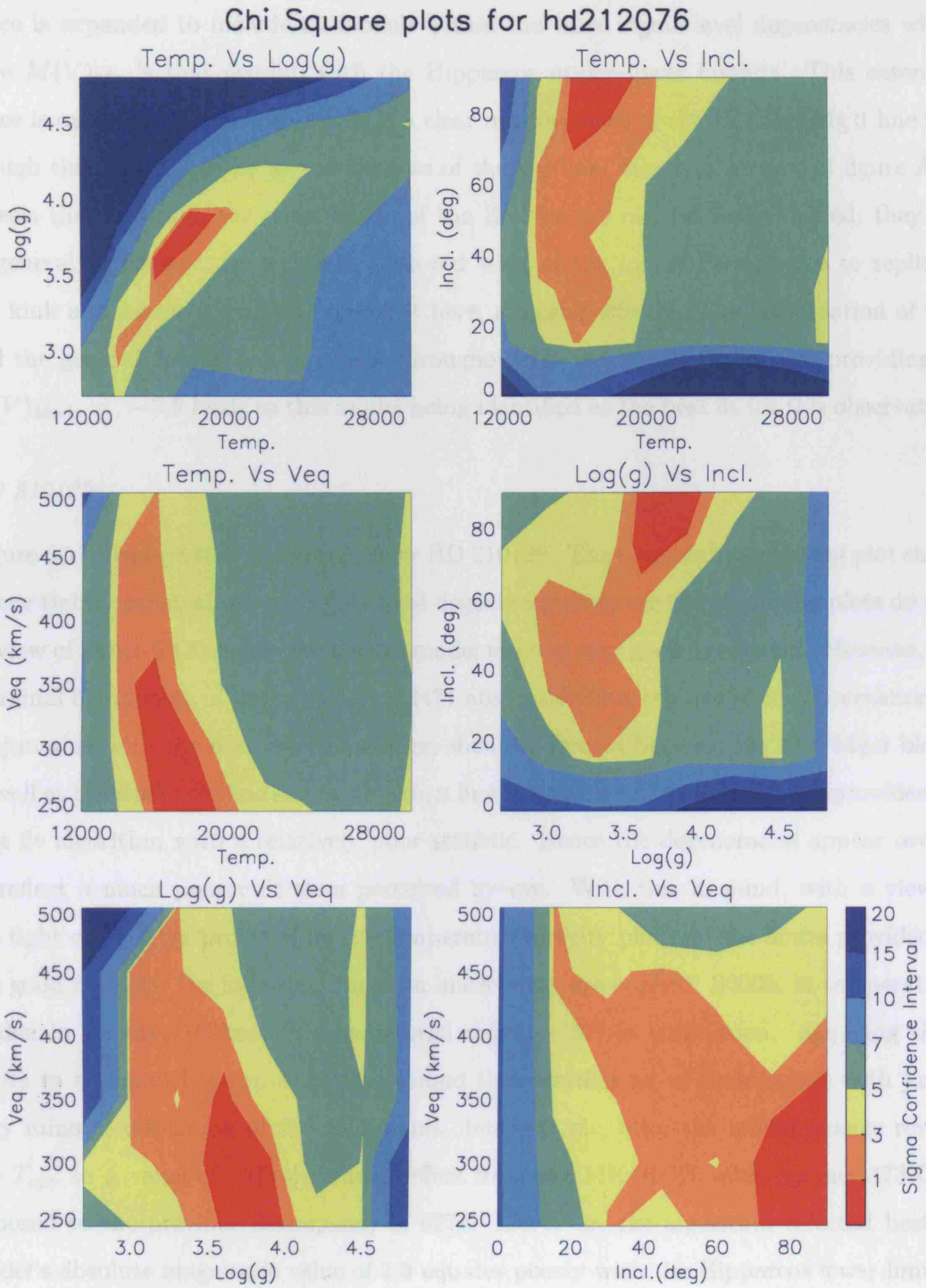

Figure 6.10. The six χ^2 plots for HD 212076; all of the four fundamental model parameters ($T_{\rm eff}$, $\log g_{\rm pol}$, i and $v_{\rm eq}$) are plotted against one another.

is significantly increased, it still falls short of the Hipparcos lower limit. As these signs were encouraging though, a sanity check is employed. Specifically, the degenerate model–space is expanded to include all models within the three sigma level degeneracies which have $M(V)_{\rm Mod}$'s that overlap with the Hipparcos upper–lower bounds. This extended space is explored. The result of this is a clear improvement of the He I and Mg II line fits, though this appears to be at the expense of the Hγ line. However, review of figure A.89 reveals that although the outer wings of the Hγ line are not perfectly aligned, they are in general agreement; in particular, the red wing of the model Hγ appears to replicate the kink and minor transition, apparent here, almost perfectly. The combination of this and the general duplication of trends throughout the weak lines whilst also providing an $M(V)_{\rm Mod} = -3.8$ leads to this model being identified as the best fit for this observation.

HD 210129

Figure 6.11 displays the contour plots for HD 210129. The temperature–gravity plot shows a very tightly constrained one sigma level degeneracy, however the remaining plots do not. Review of figure 5.13 reveals the best fit model to be in very good agreement. However, the marginal broadening of the model He Iλ4471 absorption line, relative to the observation, in conjunction with the narrower, blue edge, shoulder formed between the He I–Mg II blend, as well as the shallower line core in the Mg II line (again model to observation), provides the best fit algorithm with a relatively poor statistic. Hence the degeneracies appear overall to reflect a much poorer fit than perceived by–eye. With this in mind, with a view to the tight correlation provided by the temperature–gravity plot and the limits provided by the good fit plots, the following limits on uncertainty are applied: 2000K in temperature; 0.3dex in gravity; 100km s^{-1} in equatorial velocity; 30° in inclination. Applying these limits to the model space, a model is found that rectifies all of these issues with just a very minor rectification of the continuum. Interestingly, also, the model change revises the T_{app} to a value of 12710K which differs from the MK–BCD value by just 473K, as apposed to the previous discrepancy of 627K. Moreover, the algorithm–selected best–fit model's absolute magnitude value of 1.3 equates poorly with the Hipparcos lower limit of -0.4, whereas the revised model provides a value of -0.4 which is just on the boarder.

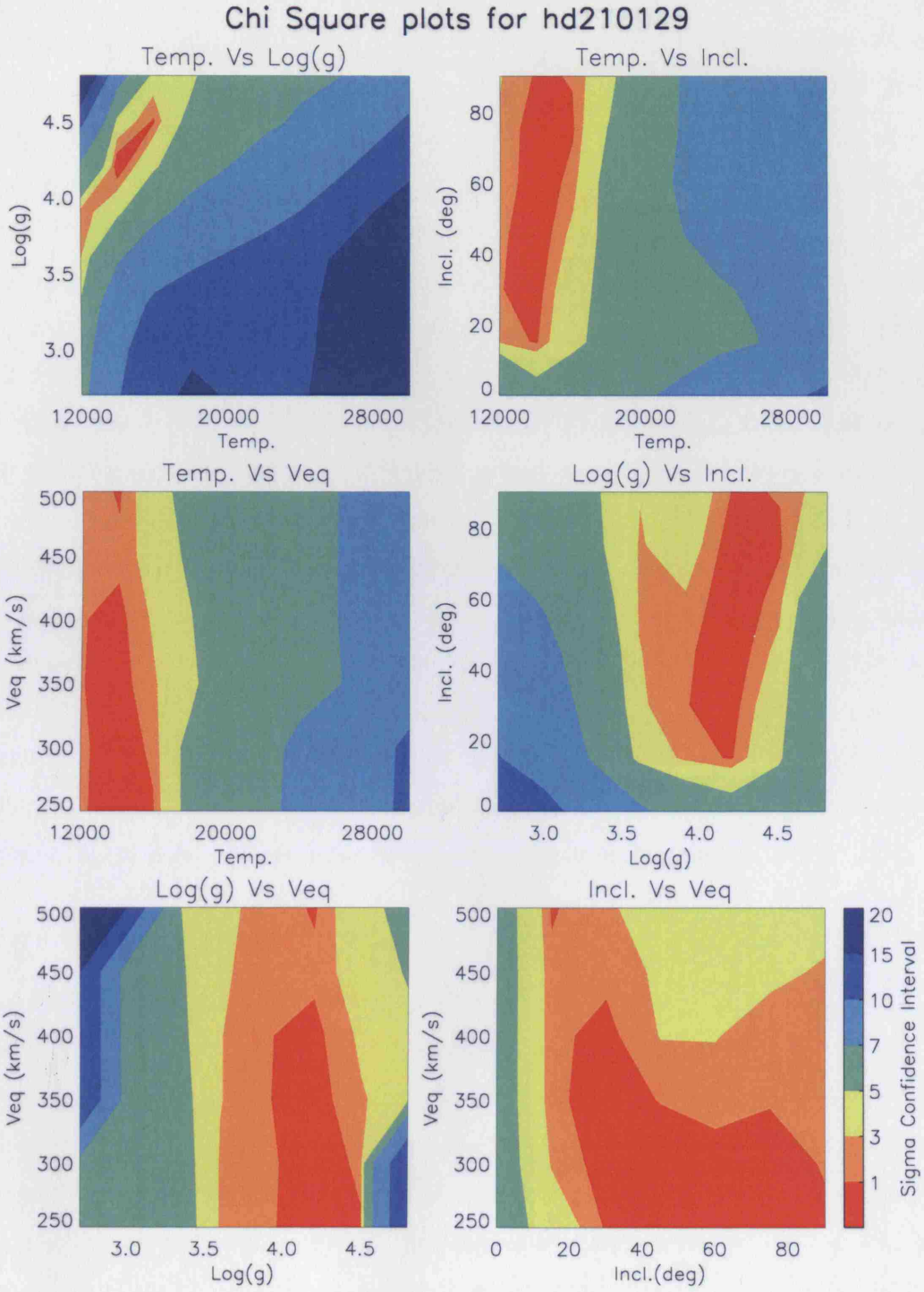

Figure 6.11. The six χ^2 plots for HD 210129; all of the four fundamental model parameters ($T_{\rm eff}$, $\log g_{\rm pol}$, i and $v_{\rm eq}$) are plotted against one another.

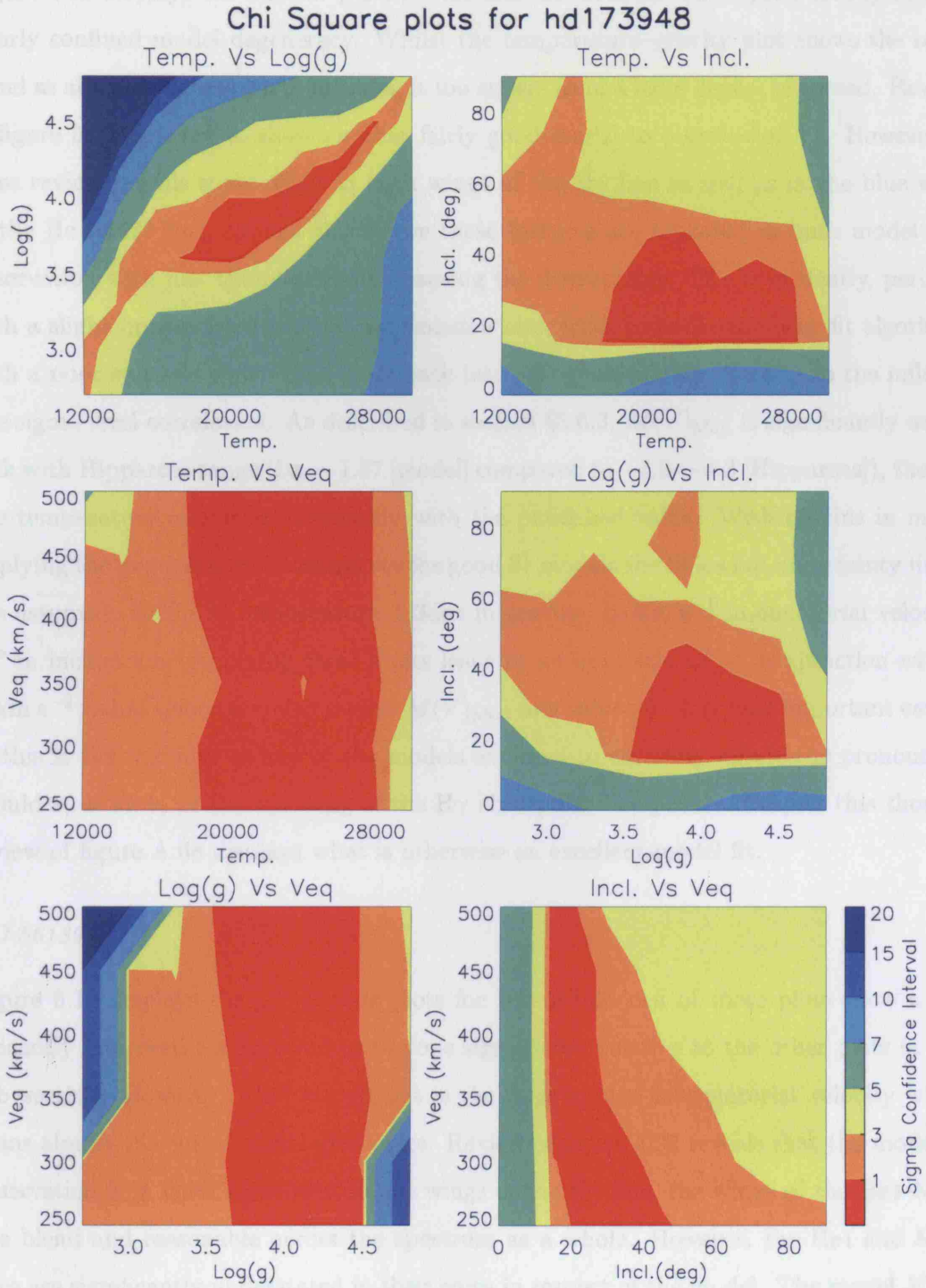

Figure 6.12. The six χ^2 plots for HD 173948; all of the four fundamental model parameters ($T_{\rm eff}$, $\log g_{\rm pol}$, i and $v_{\rm eq}$) are plotted against one another.

HD 173948

Figure 6.12 displays the contour plots for the star HD 173948. These plots clearly show a poorly confined model degeneracy. Whilst the temperature–gravity plot shows the same trend as all the previous good–fit plots, it too suffers from a large degree of spread. Review of figure 5.17 appears to show another fairly good model to observation fit. However, a close review reveals some offset in both wings of the Hγ line as well as in the blue wing of the He Iλ4471 line, though to the eye these features are repeated in both model and observation with just the relative flux causing the discrepancy. This is evidently, perhaps with a slight impact from the Balmer emission also, what provides the best–fit algorithm with a poor statistic which then feeds back into the χ^2 calculation leading to the inflated one sigma level correlation. As described in section §5.6.3, $M(V)_{\rm Mod}$ is significantly out of sink with Hipparcos range (i.e. -1.57 [model] compared to -3.9–-4.3 [Hipparcos]), though the temperature correlates favourably with the published value. With all this in mind, applying the degeneracies obtained via the good fit models the following uncertainty limits are assumed: 4000K in temperature; 0.3dex in gravity; 100km s^{-1} in equatorial velocity; 30° in inclination. Applying these limits leads to an improved fit, in conjunction with a 10km s^{-1} radial velocity, which revises $M(V)_{\rm Mod}$ to a value of -4.2. One important caveat to this is the inability of any of the models explored to correctly mimic the pronounced shoulder, or kink, in the red wing of the Hγ absorption line profile. Despite this though, review of figure A.68 displays what is otherwise an excellent model fit.

HD 56139

Figure 6.13 displays the χ^2 contour plots for HD 56139. All of these plots show a significantly improved confinement at the one sigma level, relative to the other plots in this sub–section. However, what stands out is the large spread in equatorial velocity which spans almost the entire model grid space. Review of figure 5.20 reveals that the model to observation is in good agreement in the wings of the Hγ line, the wings of the He I–Mg II line blend and reasonable across the spectrum as a whole. However, the He I and Mg II lines are significantly understated in their cores in respect of the model. The model $M(V)$ is also discrepant to the Hipparcos data providing a much larger value. Consequently, and in view of the fairly tight confinement at the one sigma level, the uncertainty limits explored for this star relate specifically to figure 6.13. These are as follows: 2000K in

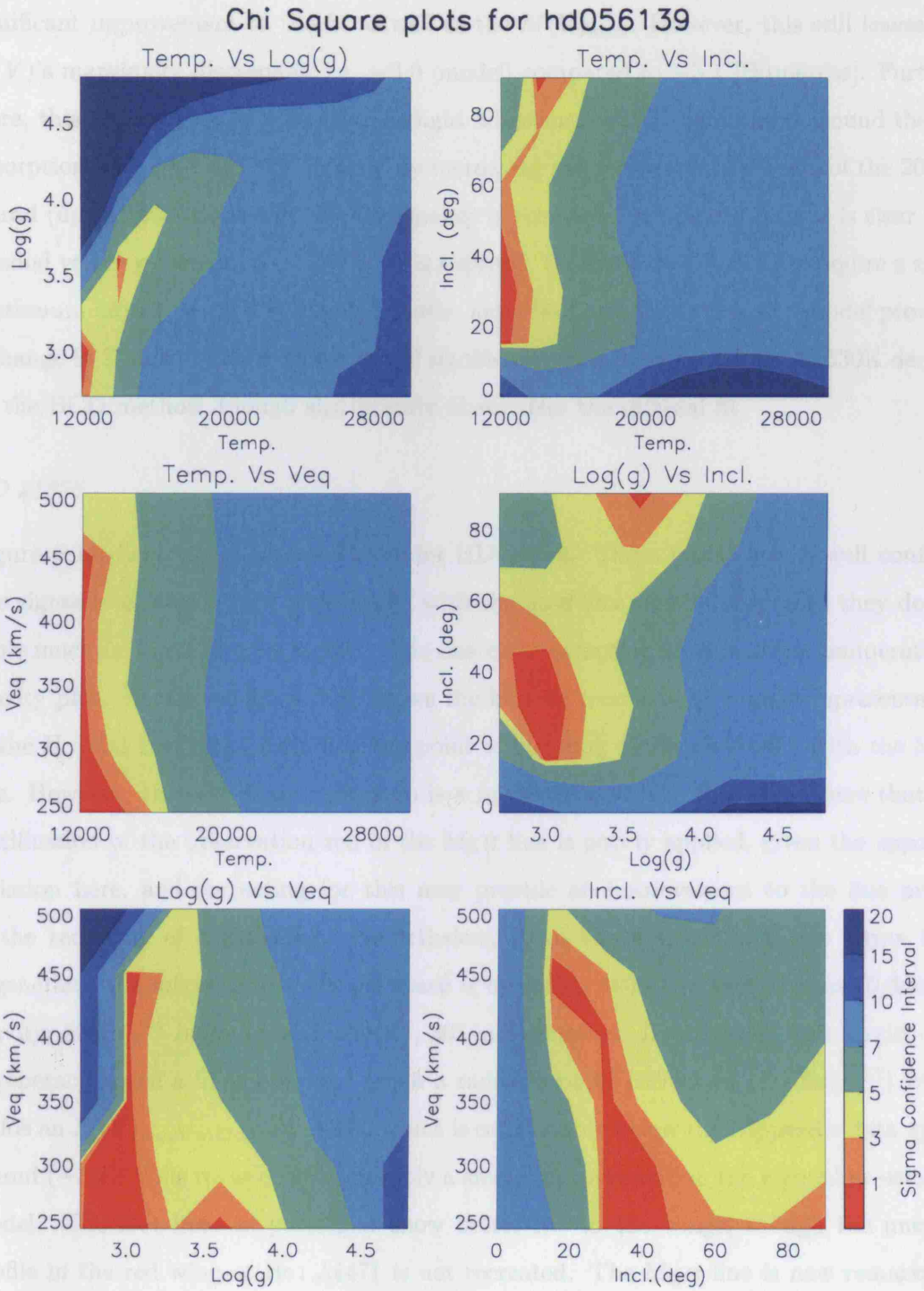

Figure 6.13. The six χ^2 plots for HD 56139; all of the four fundamental model parameters ($T_{\rm eff}$, $\log g_{\rm pol}$, i and $v_{\rm eq}$) are plotted against one another.

temperature; 0.6dex in gravity; 200km s^{-1} in equatorial velocity (essentially, in this example, the entire velocity space); 30° in inclination. Exploring this space does provide a significant improvement to the fit as well as the $M(V)_{\rm Mod}$. However, this still leaves the $M(V)$'s marginally discrepant, i.e. -3.0 [model] compared to -3.1 [Hipparcos]. Furthermore, this improved fit also requires a slight adjustment of the continuum around the Hγ absorption line; Interestingly though, by increasing the temperature outside of the 2000K bound (up to 16000K) the $M(V)$ discrepancy is removed. In this instance, it is clear that a radial velocity correction of 30km s^{-1} is required, though this fit too does require a small continuum adjustment. It is worthy of note, here, that this final change in model provides a change in T_{app} to 17150K which is still significantly out of step with the 21530K derived by the BCD method, though significantly closer than the original fit.

HD 41335

Figure 6.14 displays the contour plots for HD 41335. These plots show a well confined one sigma level degeneracy comparable with the *good–fits*, but differ in that they do not show much in the 20 sigma regime. The one clear exception to this is the temperature–gravity plot. Review of figure 5.21 shows the best–fit model to be a good representation in the Hγ and He I lines, including the point of blending of the He Iλ4471 with the Mg II line. However, the rest of the spectrum is a relatively poor fit. It is noted here that the rectification of the observation red of the Mg II line is poorly applied, given the *apparent* emission here, and correcting for this may provide an improvement to the line profile of the red–wing of Mg IIλ4482. Nevertheless, given the well confined one sigma level degeneracy, the following degenerate space is explored: 4000K in temperature; 0.6dex in gravity; 50km s^{-1} in equatorial velocity; 30° in inclination. By exploring this model–grid degeneracy space a fit is obtained (with a radial velocity correction of 10km s^{-1}) which yields an $M(V)_{mathrmMod} = -3.30$ which is comfortably below the Hipparcos data upper bound (-3.8). This revised fit is arguably a small improvement on the algorithm–selected model. The He I lines in particular show better fits to the wings, though the unusual profile in the red wing of He I λ4471 is not recreated. The Mg II line is now remarkably close, though similar to the afore mentioned helium line, it too fails to recreate the red wing profile in detail. Review of this revised model fit in figure A.25 also shows that the model fails to recreate the detail in the weak lines throughout the spectrum.

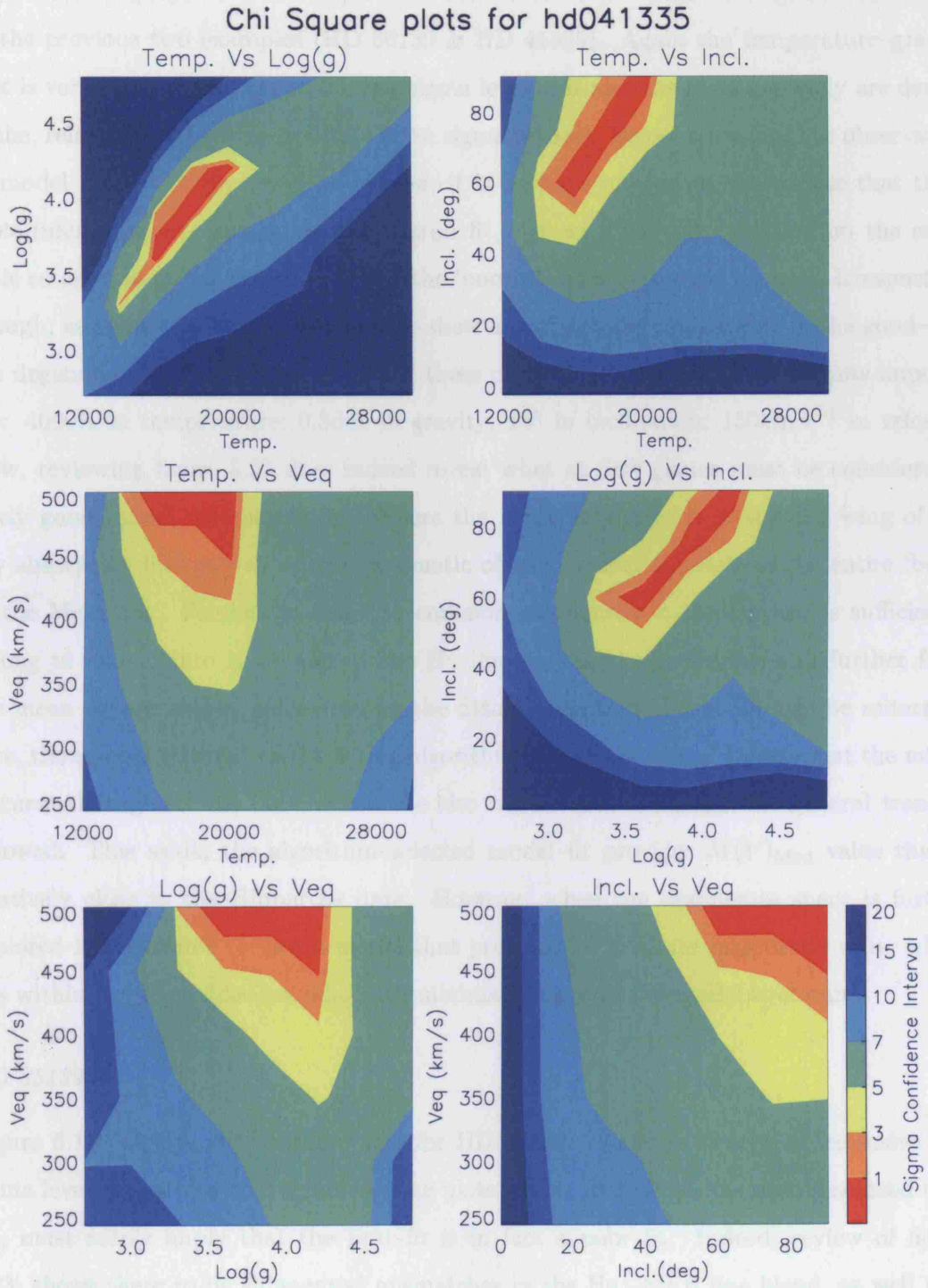

Figure 6.14. The six χ^2 plots for HD 41335; all of the four fundamental model parameters ($T_{\rm eff}$, $\log g_{\rm pol}$, i and $v_{\rm eq}$) are plotted against one another.

HD 44458

Figure 6.15 displays the contour plots for HD 44458. These plots are, again, very similar to the previous two examples (HD 56139 & HD 41335). Again the temperature–gravity plot is very tightly confined at the one sigma level, but also the plots generally are devoid of the, relatively, extremely poor fits (20+ sigma values). Before reviewing the observation to model fit plot of the previous section, it is perhaps interesting to surmise that these plots infer a general success to the overall fit, but with enough deviation on the small scale so as to limit the extent to which the 'poorest' fit is quantified as such. Irrespective, though, as these one sigma degeneracies show a confinement comparable to the good–fits, the degenerate space explored is set via these plots alone. Specifically the limits imposed are: 4000K in temperature; 0.3dex in gravity; 15° in inclination; 150km s^{-1} in velocity. Now, reviewing figure 5.22 does indeed reveal what at first glance must be considered a fairly good model representation. Where the model struggles is in the red–wing of the Hγ absorption line as well as the systematic off–set present throughout the entire 'bowl' of the Mg II line. Further to this, the emission component in the Hγ line is sufficiently strong to extend into the wings of the Hγ line and no doubt detract still further from the mean square values, calculated by the fitting algorithm. It should also be reiterated here, though not relevant to the fitting algorithm (hence also the χ^2 plots), that the minor features throughout the observation are also not recreated, though the general trend is followed. This aside, the algorithm–selected model–fit provides $M(V)_{\rm Mod}$ value that is relatively close to the Hipparcos data. However, when the degenerate space is further explored it is possible to find a model that provides an absolute magnitude value which sits within the Hipparcos bounds, with minimal change to the model spectrum.

HD 35439

Figure 6.16 displays the contour plots for HD 35439. There is clearly an extensive one sigma level degeneracy throughout all the plots which, from what has been discussed thus far, must surely imply that the best–fit is in fact a poor fit. Indeed, review of figure 5.23, shows there to be substantial mismatches in the He I–Mg II line blend, as well as a less than perfect fit to the wings of the Hγ absorption line. However, this observation to model–fit is placed in the intermediate section as, demonstrated in figure 5.24, much of this discrepant fit is alleviated by the renormalisation of this Chauville et al. (2001) spectrum.

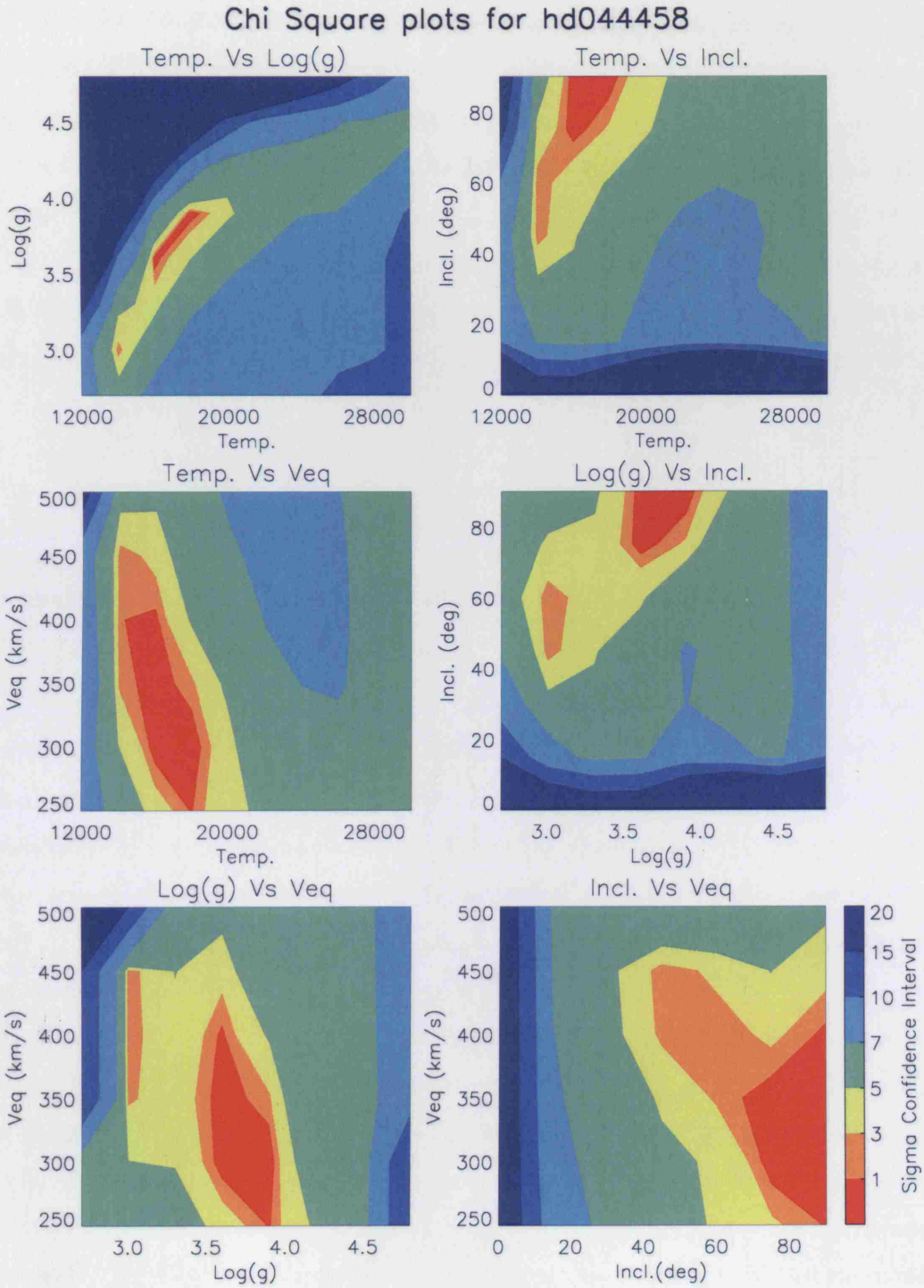

Figure 6.15. The six χ^2 plots for HD 44458; all of the four fundamental model parameters ($T_{\rm eff}$, $\log g_{\rm pol}$, i and $v_{\rm eq}$) are plotted against one another.

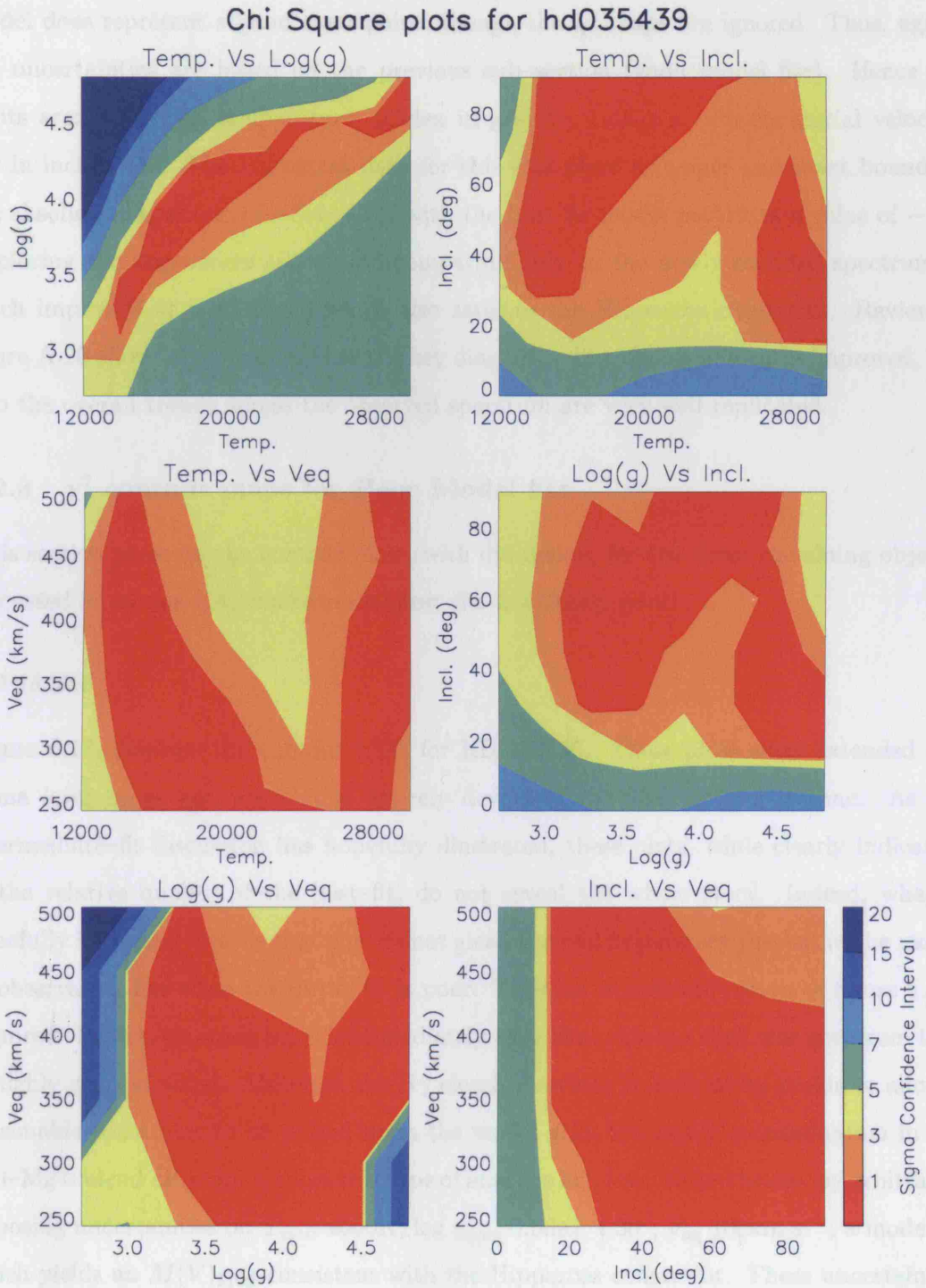

Figure 6.16. The six χ^2 plots for HD 35439; all of the four fundamental model parameters ($T_{\rm eff}$, $\log g_{\rm pol}$, i and $v_{\rm eq}$) are plotted against one another.

What is still discordant, though, is the Hγ line, but here, the strong emission component may possibly be the contaminating factor. Consequently, it is assumed that this best–fit model does represent a good start point, though the χ^2 maps are ignored. Thus, again, the uncertainties are based on the previous sub–section (good model fits). Hence the limits are: 4000K in temperature; 0.3dex in gravity; 100km s^{-1} in equatorial velocity; 30° in inclination. The Hipparcos data for this star place an upper and lower bound on the absolute magnitude of -3.4–-2.1, with the best–fit model providing a value of -1.7. Exploring the degenerate space, and comparing only to the newly rectified spectrum, a much improved fit is obtained which also satisfies the Hipparcos constraint. Review of figure A.20 shows that not only are the key diagnostic line–fits significantly improved, but also the overall trends across the observed spectrum are very well replicated.

6.2.3 χ^2 contour maps for *Poor* Model fits

This section presents the contour plots, with discussion, for the three remaining objects, discussed in section 5.4, whose model best–fits are clearly poor.

HD 183656

Figure 6.17, displays the contour plots for HD 183656. These plots show extended one sigma level zones and are almost entirely devoid of the 20+ contoured zone. As the intermediate–fit discussion has hopefully illustrated, these plots, while clearly indicative of the relative quality of the best–fit, do not reveal the whole story. Indeed, what is hopefully becoming clear is that one cannot glean the *real* degeneracy present in the model to observation fits when the initial fit is poor. Thus, an immediate review of figure 5.3 is required. In fact, on doing so, it is immediately clear that this is a shell star spectrum that is highly contaminated. Although the Hγ clearly provides enough of its profile to allow a reasonable constraint to be placed upon the model grid, the heavy contamination in the He I–Mg II blend ultimate renders this type of analysis helpless. Nevertheless, by arbitrarily imposing uncertainties of: $T_{\rm inod}$ 4000K; log $g_{\rm pole}$ 0.6dex; i 30°; $V_{\rm eq}$ 100km s^{-1}; a model fit which yields an $M(V)_{\rm Mod}$ consistent with the Hipparcos constraint. These uncertainties are justified on the basis of the reasonable fit to the Hγ provided by the algorithm–selected model; given the consistent degeneracy observed throughout this discussion between $T_{\rm eff}$ and log$g$ this is not unreasonable. Interestingly , this revised model fit (see figure A.72) apparently provides an excellent fit to the Hγ line as well as the He Iλ4471 and also a good

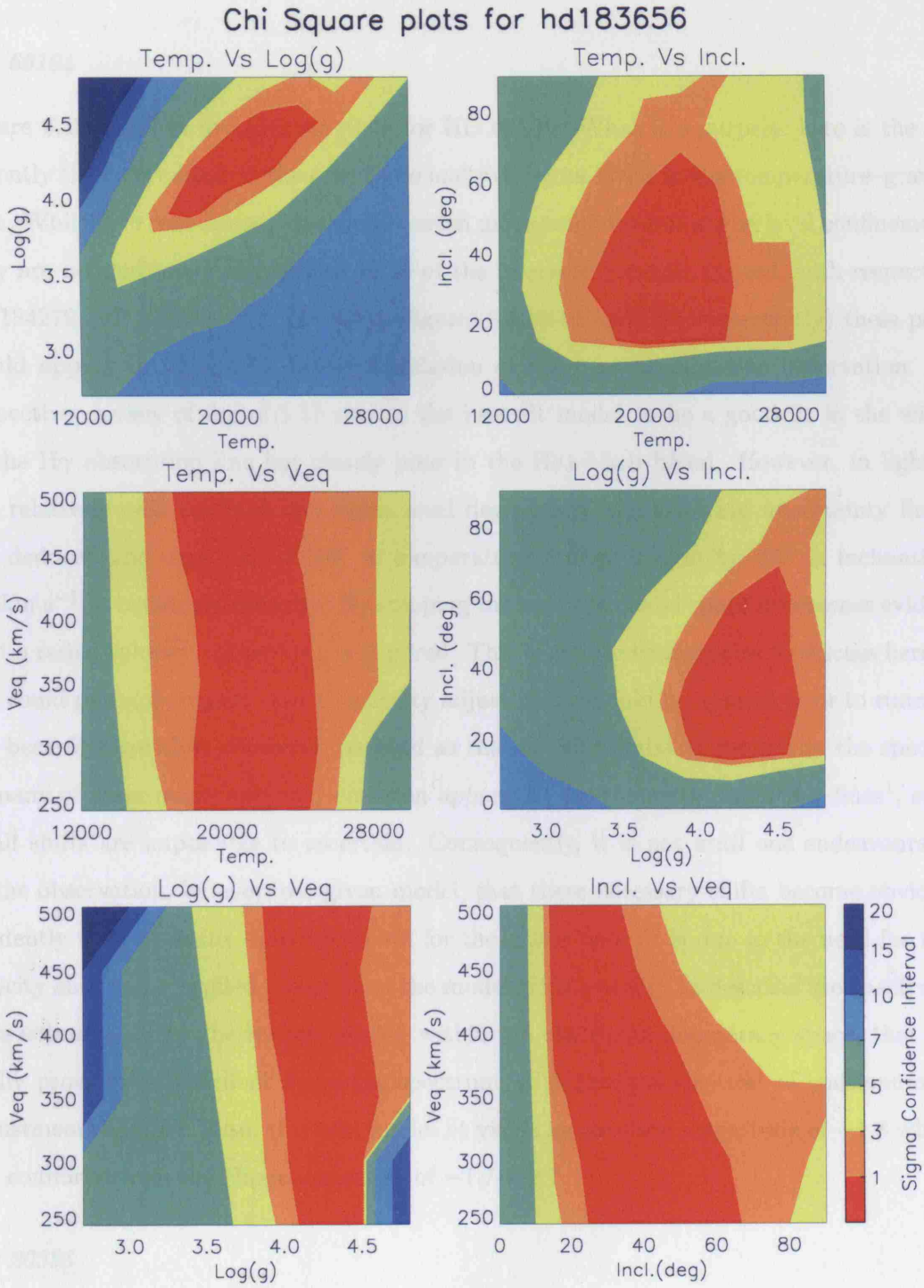

Figure 6.17. The six χ^2 plots for HD 183656; all of the four fundamental model parameters ($T_{\rm eff}$, $\log g_{\rm pol}$, i and $v_{\rm eq}$) are plotted against one another.

fit to the Mg II line wings. However, the Mg II line core is clearly discrepant though the overall trends of the spectrum are well matched.

HD 66194

Figure 6.18 displays the contour plots for HD 66194. What is a surprise here is the apparently tight definition at the one, three and five sigma levels in the temperature–gravity plot. Whilst the remaining plots show a much more extended one sigma level confinement, they are not obviously worse than those of the intermediate–fits. Indeed, with respect to HD184279, HD 173948 and HD 35439 (figures 6.9, 6.12 and 6.16 respectively) these plots would appear to indicate a better correlation of the best–fit model to observation. Irrespective, review of figure 5.11 reveals the best–fit model to be a good fit in the wings of the Hγ absorption line but clearly poor in the He I–Mg II blend. However, in light of the relatively well confined one sigma level degeneracy, the following uncertainty limits are deduced and explored: 4000K in temperature; 0.6dex in gravity; 45° in inclination; 150km s^{-1} in equatorial velocity. By stepping through the model space it becomes evident that a radial velocity adjustment is required. This is an interesting point to discuss here as one could perhaps suggest that all velocity adjustments should be applied prior to running the best–fit algorithm. However, as *ideal* as that is, with emission present in the spectra of many of these stars, and that emission apparently contaminating multiple lines[1], such small shifts are impossible to ascertain. Consequently, it is not until one endeavours to fit the observation, by eye, to a given model, that these necessary shifts become obvious. Evidently then, it seems that the reason for the initial poor fit is due to the need for this velocity shift to be applied rather than the model grids inability to describe the spectrum. This is borne out by the revised model, within the one sigma degeneracy space, that actually provides an excellent fit to the spectrum, with just the slightest of continuum fit adjustments applied. Also, this new model fit yields an absolute magnitude of -1.8 which sits comfortably in the Hipparcos range of -1.7–-2.1.

HD 20336

The final contour plots displayed in figure 6.19 are for HD 20336. These plots show a more extended one sigma level confinement, relative to the previous example, except

[1]This is inferred by the presence of repeated asymmetries in the cores of the other lines, e.g. He Iλ4388, He Iλ4471 and Mg IIλ4481.

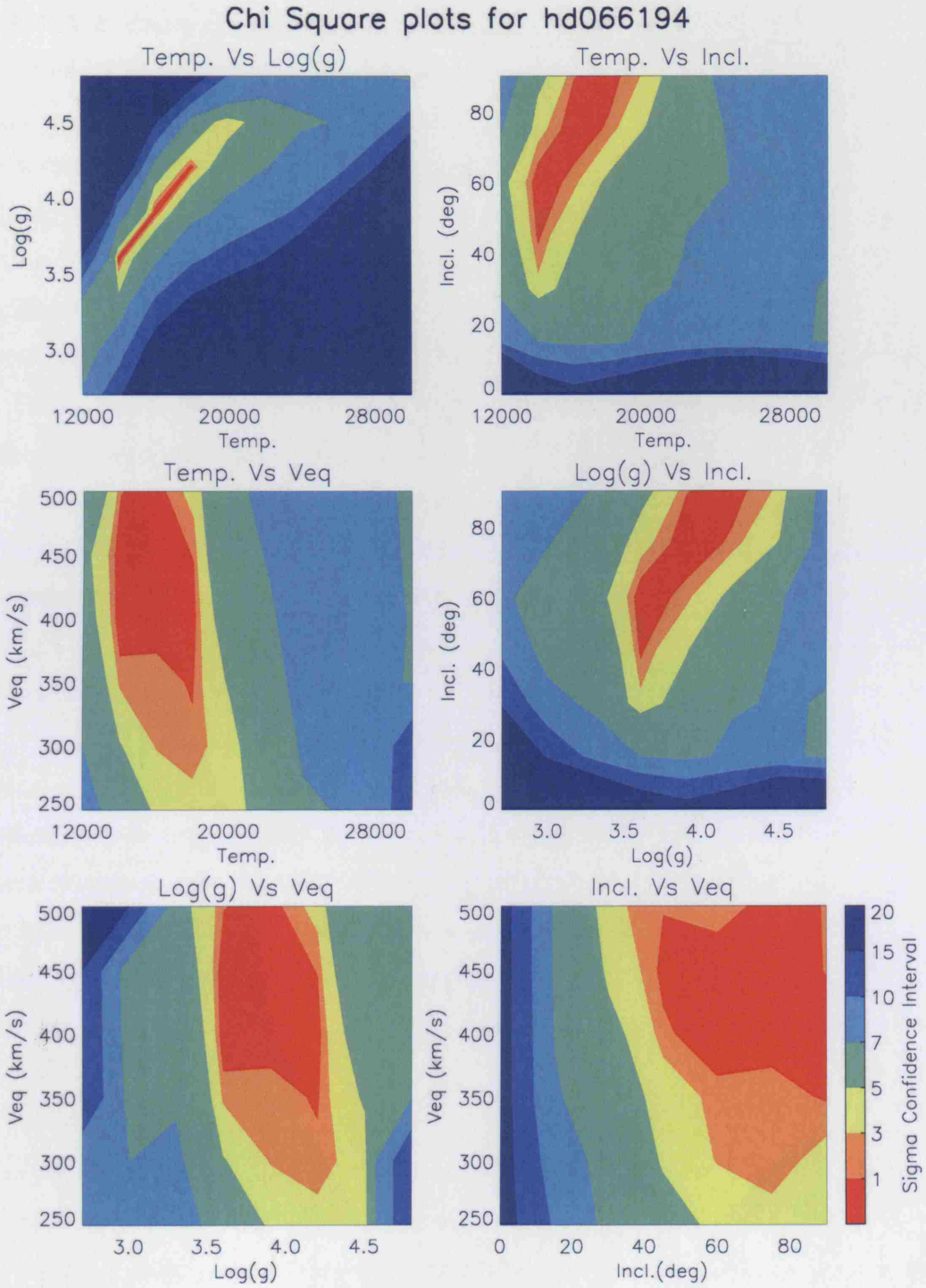

Figure 6.18. The six χ^2 plots for HD 66194; all of the four fundamental model parameters ($T_{\rm eff}$, $\log g_{\rm pol}$, i and $v_{\rm eq}$) are plotted against one another.

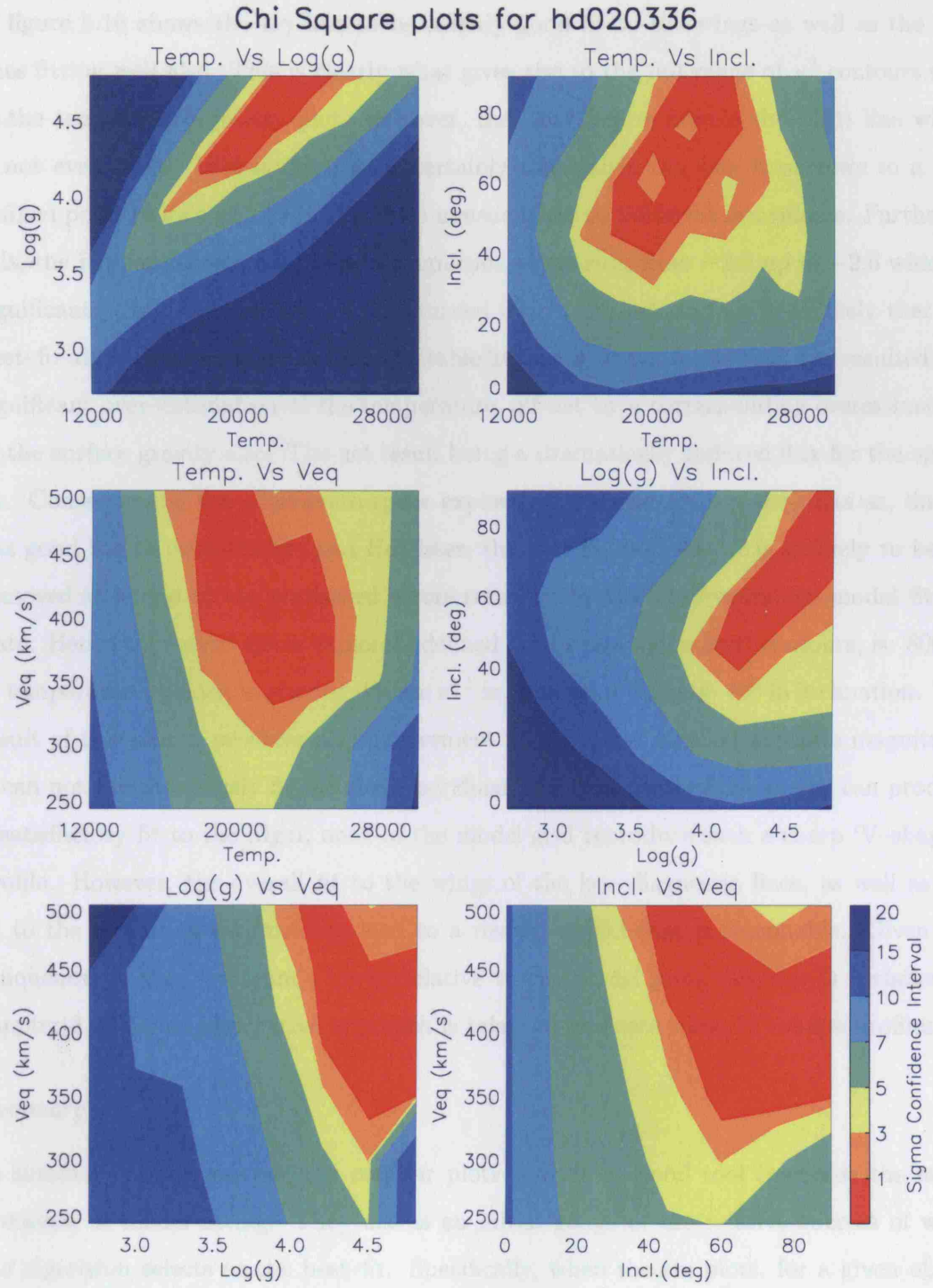

Figure 6.19. The six χ^2 plots for HD 20336; all of the four fundamental model parameters ($T_{\rm eff}$, $\log g_{\rm pol}$, i and $v_{\rm eq}$) are plotted against one another.

for the three equatorial velocity plots. Though the temperature–gravity plot shows a significant amount of 20+ level space, the rest are almost devoid of this feature. Review of figure 5.16 shows the Hγ line to be a fairly good fit to the wings as well as the He I lines fitting well also. This is clearly what gives rise to the full range of χ^2 contours seen in the temperature–gravity plot. However, the clear failure here is the Mg II line which is not even close. Whilst this line is certainly unusual in the way it narrows to a well defined point in its core, it is still a little unusual that no better fit is available. Further to this, the Hipparcos derived absolute magnitude range runs from -2.0 up to -2.6 which is significantly brighter that the $+1.96$ returned for this model. In fact, it is likely that the best–fit algorithms inability to find a suitable fit for the Mg II line as well, has resulted in a significant over–estimation of the temperature, off–set by a corresponding overestimation of the surface gravity also. The net result being a dramatically reduced flux for the model fit. Consequently, the degenerate space explored is that offered by the plots as, due to the good fits to both the Hγ and He I lines, the best fit model itself is unlikely to be far removed in terms of the statistical errors returned by the observation–to–model fitting data. Hence the model space explored, defined by the one sigma level contours, is: 8000K in temperature; 0.6dex in gravity; 150km s^{-1} in equatorial velocity; 45° in inclination. The result of this search provides an improvement to the model derived absolute magnitude, it can not simultaneously fit the three key diagnostic lines. In fact, no model can produce a satisfactory fit to the Mg II, none of the model grid reproduce such a sharp 'V–shaped' profile. However, the overall fit to the wings of the key–diagnostic lines, as well as the fit to the overall spectrum, does lead to a revised model that is reasonable. Given the uniqueness of this spectrum's Mg II, relative to the model grid, this star is revisited in chapter 8 where an alternative approach is taken to replicate these 'V'–shape profiles.

Summary

In summary of this section, the contour plots provide a useful tool that aids the interpretation of model fitting. They act as an initial gauge of the relative success of what the algorithm selects as the best–fit. Specifically, when the six plots, for a given observation, all show a tight correlation (particularly in respect of the temperature–gravity, temperature–inclination and gravity–inclination) and a substantive area of 7, 10 and 20+ sigma levels, then this immediately states that the bulk of the models are considerably different from the best–fit. In this event, the guides (or errors) one can place on the

best fit model are drawn directly from the one (on occasion three) sigma level contours. Exploring the model grid space defined by these errors consistently yields results that, by–eye, improvement of the fit and also alleviates the magnitude discrepancies present in the HR–diagrams of section §5.4. In the event that the six plots all show a broad confinement of the one, three and five sigma levels, and are all but devoid of the 20+ level, unsurprisingly this indicates a poor fit of model to observation. When this is the case, the model grid is found to be lacking an appropriate model to fit the observation. In the cases where all but temperature–gravity plot show the poor–fit signature, just described, then actually some significant improvement can of model to observation fit can be obtained by exploring within the limits defined by the good–fit contour plots in conjunction with the plot that suggests some correlation exists. In general, to obtain a good–fit from this scenario some additional manipulation of the observation is required. Either some slight continuum–fit adjustment or radial velocity shift, or both, is employed. However, the one exception to these rules apparently occurs when the observation is of a star in emission which simultaneously displays a well defined 'V–shape' for the Mg II absorption line.

Chapter 7

Summary of Results

The previous chapter has looked in detail at particular cases of model fits to observations. These cases were selected on the basis of their locations relative to the one–to–one correlation of model temperature to spectral–type temperature, as well as their spectral classification scheme. With their location on the Hertzsprung–Russell diagram providing an additional measure of the successes or failures, the individual model fits were reviewed with particular attention to the key line fits. Subsequently, a by–eye goodness of fit (from within the χ^2 goodness of fit degeneracy space) for each individual case was explored to see if the model grid does provide an acceptable fit to the spectrum whilst simultaneously satisfying other independent constraints. This process of review and exploration of degeneracy space was followed for every star used for this research (i.e., 95 Be stars). The results of this full analysis are summarised in this chapter.

7.1 The Best Fit Models to Observations

Figure 7.1 displays the HR diagram for the full sample of 95 Be stars analysed, with published data and model fit data all over–plotted. What is apparent is that the best fit models are, as a population, significantly shifted from their initial locations (compare to figure 5.1). Evidently, the shifts applied result in all of the best–fit models repositioned on the main–sequence which, compared to the Geneva isochrones, are suggestive of a mass range of 3–18$M_{\odot}$ for these stars. In fact, compared to the published data, in particular

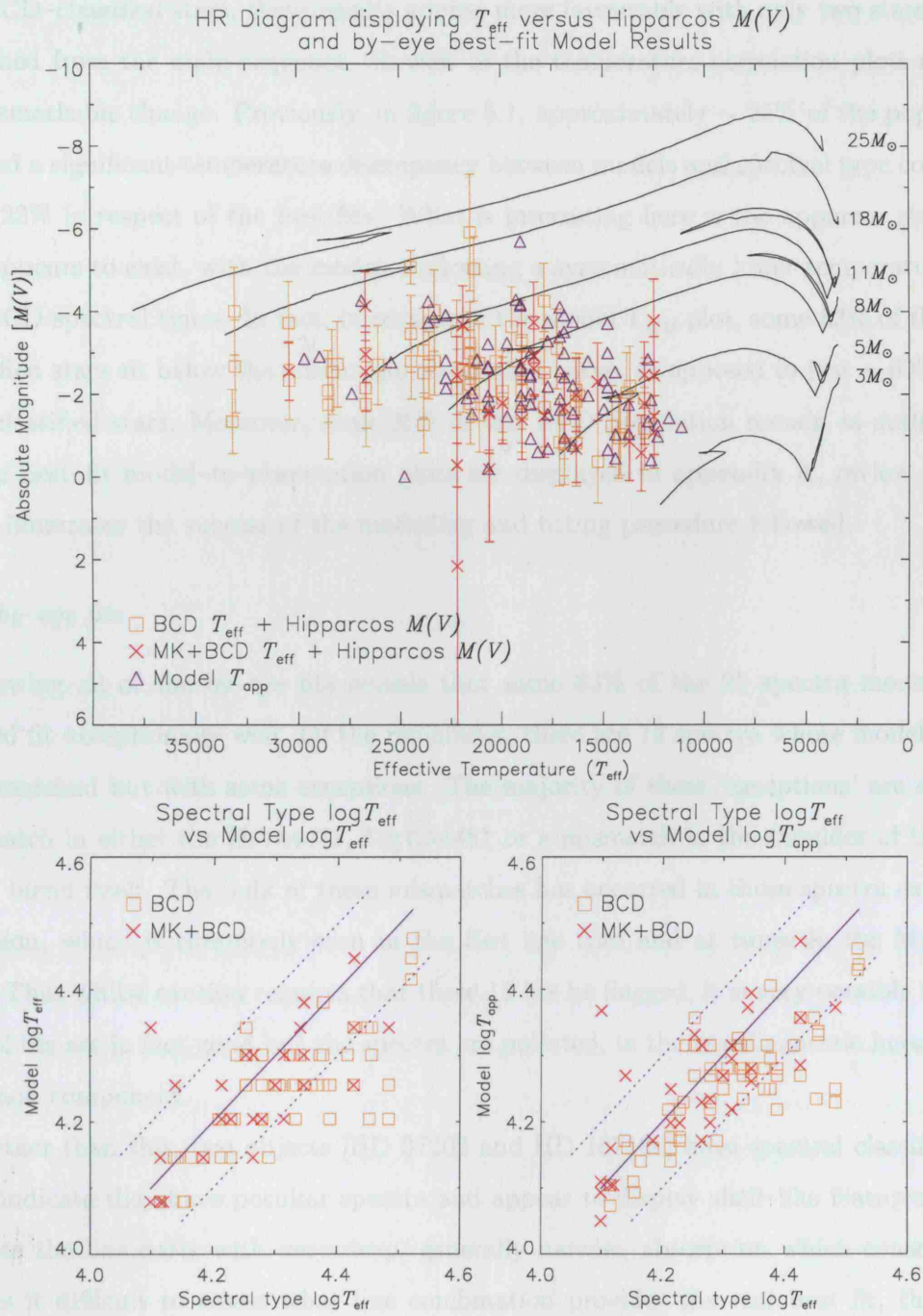

Figure 7.1. *The top panel* displays an HR diagram for each of Chauville's stars', spectral type, effective temperatures vs Hipparcos derived $M(V)$'s (orange square and red cross for BCD and MK+BCD respectively) with the BUSH best–fit models' apparent temperature vs best–fit model $M(V)$'s over-plotted (blue triangles). The error bars reflect the Hipparcos uncertainties. *The bottom two panels* display the log$T$'s of Spectral type vs BUSH models' effective and apparent temperatures, from left to right respectively. The key for these two plots defines the 3 methods by which the published spectral type temperatures are calculated, see § 5.4 for details.

the BCD–classified stars, these results appear more favourable with only two stars clearly detached from the main sequence. Review of the temperature correlation plots shows a less remarkable change. Previously, in figure 5.1, approximately $\sim 25\%$ of the population showed a significant temperature discrepancy between models and spectral type compared to $\sim 22\%$ in respect of the best fits. What is interesting here is the apparent skew that still appears to exist, with the models indicating a systematically lower temperature than the BCD spectral types. In fact, in respect of the model $T_{\rm app}$ plot, some 83% of the BCD classified stars sit below the one to one correlation curve, as opposed to just $\sim 60\%$ of the MK classified stars. Moreover, some 25% of this BCD population remain as outliers. All of the best–fit model–to–observation plots are displayed in appendix A, review of these plots illustrates the success of the modelling and fitting procedure followed.

The by–eye fits

Reviewing all of the by–eye fits reveals that some 83% of the 95 spectra modelled are indeed fit exceptionally well. Of the remainder, there are 12 spectra whose model fits are well matched but with some exceptions. The majority of these 'exceptions' are due to a mismatch in either the He Iλ4471, Mg IIλ4481 or a mismatch in the shoulder of the He I–Mg II blend itself. The bulk of these mismatches has occurred in those spectra exhibiting emission, which is commonly seen in the He I line core and at times in the Mg II core also. Thus whilst caution requires that these 12 fits be flagged, it is very possible that the model fits are in fact good but the spectra are polluted, in the key diagnostic lines, by the emission component.

Other than this, two objects [HD 37202 and HD 167128] have spectral classifications that indicate they have peculiar spectra and appear to display shell–like features. These pollute the line cores with very deep, generally narrow, absorption which consequently makes it difficult to assess what line combination provides the *real* best fit, though in these two cases the fits show significant successes despite the potential contamination.

The remaining issues are confined, again, to the emission–line spectra though in these cases it is the saw–tooth effect and/or the 'V'–profile of the line cores (specifically Mg II).

Finally, there are just four model fits which, despite the exploration of the degeneracy space, are just poor fits. In three cases there is, again, the profile of a shell star spectrum [HD 217050, HD 183656 and HD 142983]. However, unlike the cases mentioned above, these two spectra are highly contaminated, thus distinguishing the photospheric spectrum

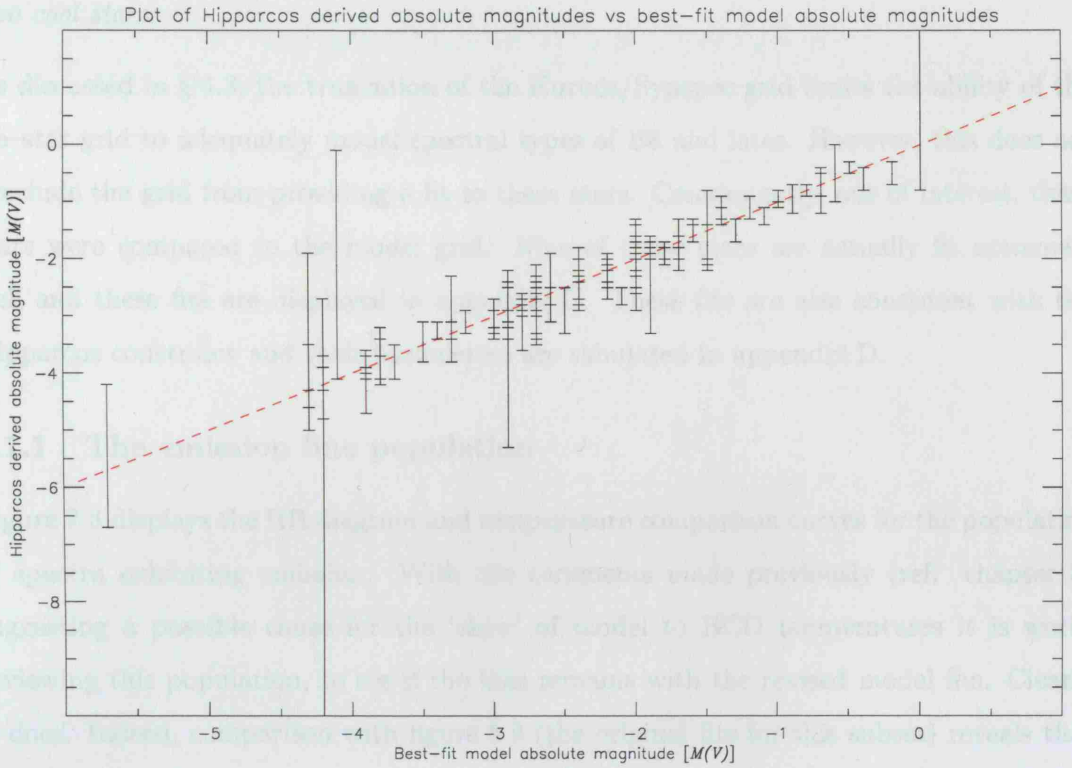

Figure 7.2. Plot of the Hipparcos derived $M(V)$'s (with uncertainties) versus the best–fit model $M(V)$'s. Over-plotted (the red dashed line) is the one–to–one correlation curve.

from the intervening absorbers is extremely difficult. Another case that has clearly failed is that of HD 174638; this is an eclipsing binary and review of figure A.70 appears to indicate that the observation must have been taken close to, or during, an eclipsing event. This seems to be confirmed by utilising the Harmanec and Scholz ephemeris (Harmanec & Scholz 1993) and relating to the time of observation; HJD 2448872.395.

Correlation of the Hipparcos derived absolute magnitudes to the best–fit–model absolute magnitudes

Figure 7.2 displays the correlation of Hipparcos derived absolute magnitudes versus the best–fit model values. Whilst the process of selecting the best–fit models, by definition, pushes this correlation toward the one–to–one relationship, it is clear from this plot the level to which the best–fit models succeed in matching these independently derived values.

Too cool stars

As discussed in § 4.3, the truncation of the Kurucz/Synspec grid limits the ability of the Be–star grid to adequately model spectral types of B8 and later. However, this does not preclude the grid from providing a fit to these stars. Consequently, out of interest, these stars were compared to the model grid. Nine of these stars are actually fit extremely well and these fits are displayed in appendix C. These fits are also consistent with the Hipparcos constraint and their parameters are tabulated in appendix D.

7.1.1 The emission line population

Figure 7.3 displays the HR diagram and temperature comparison curves for the population of spectra exhibiting emission. With the comments made previously (ref. chapter 5) suggesting a possible cause for the 'skew' of model to BCD temperatures it is worth reviewing this population, to see if the bias remains with the revised model fits. Clearly it does. Indeed, comparison with figure 5.9 (the original fits for this subset) reveals that this bias is now even more pronounced. While the outlier population has reduced slightly in size, and has become more tightly correlated, the population as a whole now almost entirely occupies the lower right corner of the plot, where the model fits provide for a lower temperature than that established by the BCD method. The three remaining MK–classified stars do not obviously show any bias, particularly when considered in both the model $T_{\rm eff}$ and model $T_{\rm app}$ correlations. Thus despite the low population size preventing a clear picture of the MK–classified stars being formed, it does seem evident that there exists a systematic offset between the model–derived temperatures and the BCD–derived ones. The fact that the emission–line population gives rise to this bias makes the suggested reasoning provided in chapter 5 now quite compelling. To reiterate, the presence of the Balmer emission components may serve to inflate the Balmer discontinuity so as to imply a 'reduced' hydrogen–ion presence, which in turn implies a higher temperature. The MK system would not suffer this problem as the line–strength ratios of the He I, Mg II and Si II, whilst altered by rotation, and perhaps also emission, will probably change by similar degrees and hence retain their ratios in a reasonably constant fashion.

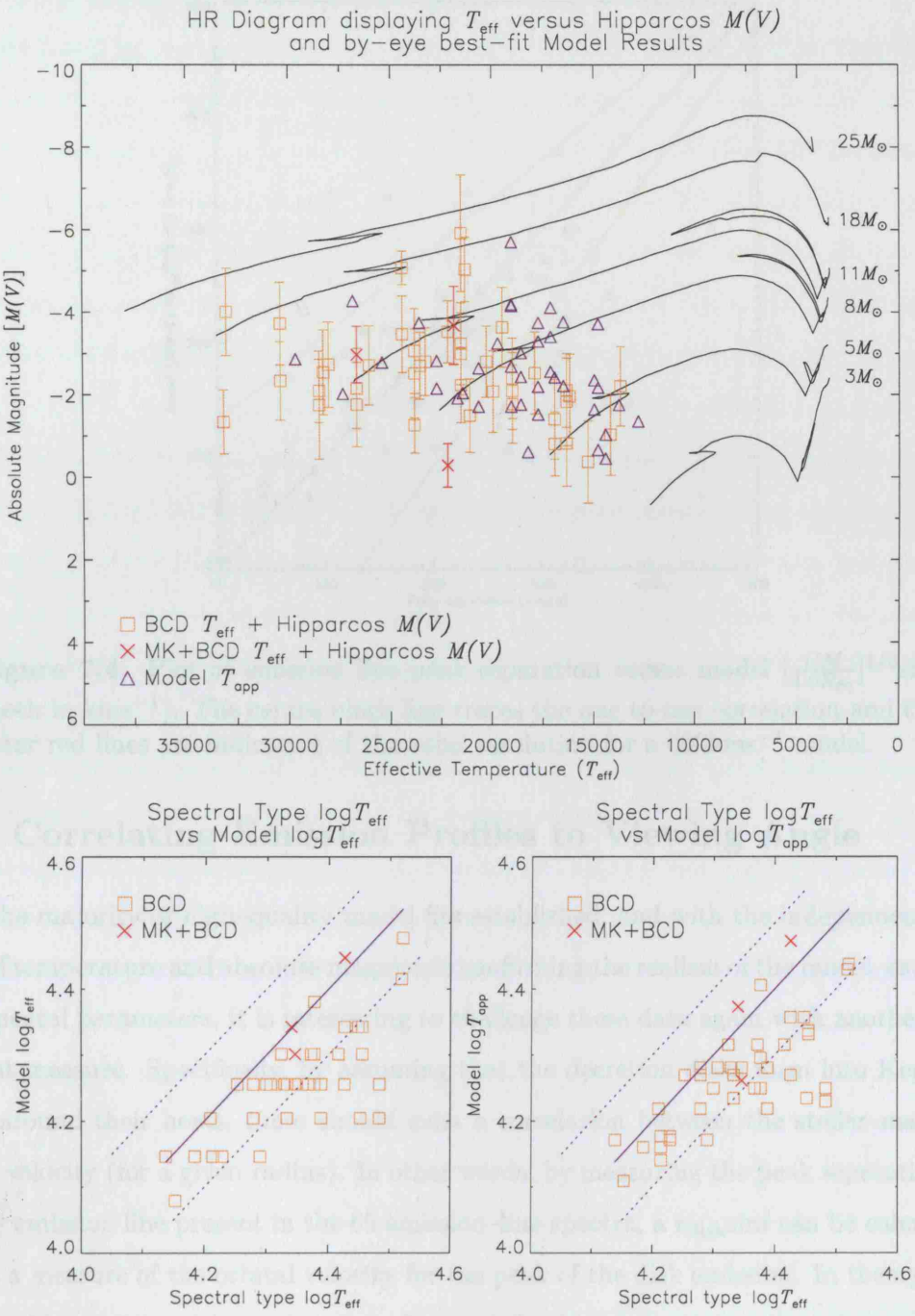

Figure 7.3. *The top panel* displays an HR diagram for each of Chauville's stars', spectral type, effective temperatures vs Hipparcos derived $M(V)$'s (orange square and red cross for BCD and MK+BCD respectively) with the BUSH models' apparent temperature vs model $M(V)$'s over-plotted (blue triangles). The error bars reflect the Hipparcos uncertainties. *The bottom two panels* display the log$T$'s of Spectral type vs BUSH models' effective and apparent temperatures, from left to right respectively. The key for these two plots defines the 3 methods by which the published spectral type temperatures are calculated, see § 5.4 for details.

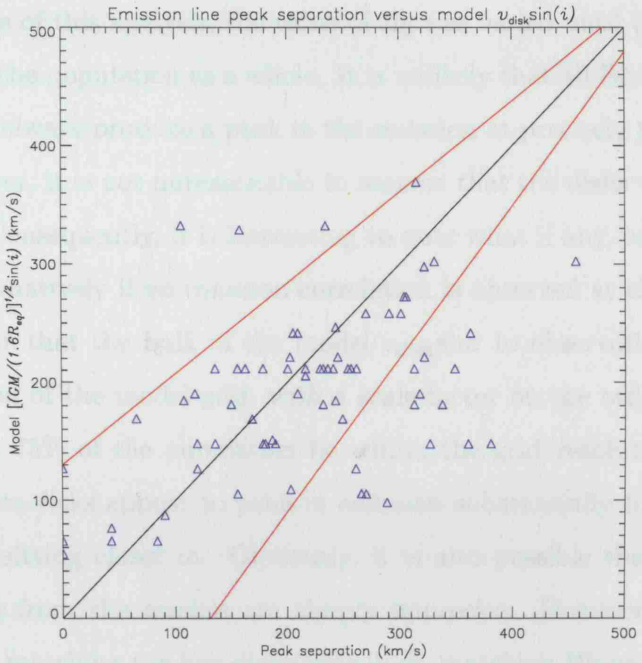

Figure 7.4. Plot of emission line peak separation versus model $[\frac{GM}{1.6R_{\rm eq}}]^{1/2}{\rm sin}i$ (both in kms^{-1}). The centre black line traces the one to one correlation and the outer red lines are indicative of the $v{\rm sin}i$ resolution for a 500kms^{-1} model.

7.2 Correlating Emission Profiles to Viewing Angle

With the majority of high–quality model fits established, and with the independent measures of temperature and absolute magnitude confirming the realism of the model–established fundamental parameters, it is interesting to challenge these data again with another independent measure. Specifically, by assuming that the decretion disks form into Keplerian orbits around their hosts, there should exist a correlation between the stellar mass and orbital velocity (for a given radius). In other words, by measuring the peak separations, of any Hγ emission line present in the 69 emission–line spectra, a $v_{\rm disk}{\rm sin}i$ can be calculated. This is a measure of the orbital velocity for the peak of the disk emission. In theory then, this should correlate with a value given by the following:

$$v_{\rm disk}{\rm sin}i \;=\; \sqrt[2]{\frac{GM_{\rm model}}{A_0 R_{\rm eq}}}{\rm sin}i \qquad (7.1)$$

where A_0 is some scale factor indicative of where the peak of the disk emission originates (in units of stellar radius) and R_{eq} is the model derived value.

For the purposes of this analysis, the value of A_0 was varied until the best correlation was established for the population as a whole. It is unlikely that all Be star disks will form in such a way as to always produce a peak in the emission at precisely the same height (in stellar radii); however, it is not unreasonable to assume that the disks will, on average, be of a similar scale. Consequently, it is interesting to note what if any, common scale factor might exist, or alternatively if no common correlation is observed at all.

Figure 7.4 shows that the bulk of the model $v_{\rm disk}\sin i$ to observations are consistent, within the resolution of the model grid, with a scale factor on the order of $1.6R_{\rm eq}$. With this value of A_0, $\sim$ 75% of the population lie within the grid–resolution guides. Of the remainder, just three disks appear to peak in emission substantially further out ($\sim 4-7$ R_{eq}, with the rest sitting closer in. Obviously, it is also possible that the fundamental parameters derived from the models are simply imprecise. However, to reiterate, the overall successes in matching the key diagnostic lines, matching Hipparcos data, and also correlating with spectral–calibrated temperatures does not support this. Further, the fact that 75% actually do appear to correlate reasonably adds some weight to the overall successes. It should be stressed that no strict statistical test is applied here as there is no expectation that all disks will peak in emission at a common height. However, applying a Spearman rank–test to the Hypothesis that these data are 'not' linearly related results in this hypothesis being rejected. That is to say that these data are reasonably consistent with a linear relation between the model stellar mass and the double peak separation.

7.3 Does the Null Hypothesis survive?

The purpose of this work has been to generate a grid of model Be star spectra that explores the parameter space of the B star regime. The key to this model grid construction has been the assumption that all Be stars rotate at $0.95V_{\rm crit}$. Whilst this value is somewhat arbitrary it is fixed at this value so that the energetics involved in ejecting matter from the stellar surface into orbit are on the order of weak processes within the stars atmospheres. Accounting for Von Zeipels theorem ($g_{\rm eff} \propto T_{\rm eff}^4$), rotational distortion of the stellar surface, limb darkening and viewing angle dependency provides a comprehensive physical description of these stars. Ninety five stars of Chauville et al. (2001) have been compared to each model in turn and, with a χ^2 goodness–of–fit procedure, a best–fit model for each star has been selected. Subsequently, using Hipparcos parallaxes, apparent magnitudes,

calculated extinction values, spectral–derived temperatures as well as the $V_{\rm disk}\sin i$ as independent measures of success, the overall validity of the model fundamental parameters has been assessed. Despite some exceptions to the rule, the model grid, in general, appears to have succeeded in describing these observations particularly well. As a consequence, the primary aim of testing the null hypothesis has succeeded. Whilst this does not, by definition, mean that these stars do rotate at these near critical velocities, it does tell us that we cannot simply exclude this possibility without some, hitherto undiscovered, alternative evidence.

Amongst the few objects which have not produced a satisfactory fit there have been common themes. Apart from the few shell star spectra and the one eclipsing binary, it also appears that the emission line spectra can be problematic. These observations are particularly interesting in that, they do in general fit well into the model grid but often exhibit minor complications which detract slightly from the success of a fit. Specifically, the Mg II is seen on occasion to possess a relatively sharp 'V'–shape line core (whilst remaining broad in the wings) which is not recreated in the model grid (See HD 20336 for a good illustration of this [ref. figures 5.16 and A.8). It is also the case that for some of these spectra a saw–tooth effect is seen across the spectral range which further detracts from the visual impact of the fit, though it should be stressed that the key fitting requirements are unaffected by this. Consequently, whilst these exceptions do not break the rule they are themselves intriguing and certainly deserve further consideration.

Chapter 8

Be stars as differential rotators

As has been repeated throughout much of the discussion in chapter 5, many of the Be spectra that are clearly in emission show well defined 'V' shapes in their absorption lines (in particular in the Mg II line). Those that do also tend to exhibit more complex spectra as a whole, with multiple minor absorption features repeated throughout the wavelength range. The effect of rotation is that the lines become broader and shallower (leading to more bowl–shaped profiles). However, the appearance of deep, sharp, line cores is suggestive of regions with negligible velocity shifts, while the broad wings conflict with this. Since the primary line that displays this v–shape profile is the Mg II line, which is generally stronger toward the equator where $v\sin i$ is at its strongest, a near pole-on view is rejected. How then can this profile be made? One possibility is differential rotation in the form of a slow–down from equator to pole, to generate a profile whose wings are unaltered whilst the line core is formed by the slower–rotating higher latitudes, providing for a much deeper and narrower profile.

8.1 The expanded model grid

The BUSH code, described in chapter 4, allows for an additional parameter which characterises a specific form of differential surface angular rotation for which the centrifugal force is conservative.

$$\omega(\theta) = \omega_e\{1 - S + S[R(\theta)\sin(\theta)/\mathrm{R_e}]^2\}, \quad (8.1)$$

where the subscript 'e' denotes equatorial values. The model grid described thus far is just a special case where $S = 0$; choosing a value for $S > 0$ allows for a slow–down from equator to pole. Consequently, an additional model grid, exploring the same fundamental parameter space as detailed in § 4.3, has been generated, with the S factor varying from 0.05 to 0.65 in steps of 0.05.

8.2 Emission–line Be stars revisited

With the extended model grid generated, the best–fit algorithm, detailed in § 4.4, is employed again against the entire model grid. However, as this grid is so large the degeneracy space, even for very well constrained parameters, is significantly larger than before (i.e. by a factor of 13); thus a full analysis was not possible in the time available for this research. However, it has been possible to review, albeit incompletely, a couple of the emission line Be stars discussed in the previous section.

HD 212076

Figure 8.1 displays the observed spectrum and a differentially–rotating model fit for HD 212076. The previous attempts to fit this observation with a solid–body model were unsuccessful. Whilst the best–fit solid–body model, displayed in figure A.89, is not completely incompatible with observation it does fall short of being convincing, and it fails to produce an absolute magnitude compatible with the Hipparcos data. However, in contrast, this differentially–rotating model not only successfully recreates the observation across the entire waveband, but it also provides an $M(V)$ of -3.80, well within the Hipparcos limits. What is also interesting with this model is that it returns a T_{app} of 20350K (c.f., The MK derived T_{eff} is 21878K) which has all but removed the disparity which highlighted this object for a more detailed investigation in the first place. Essentially, with model parameters of $T_{\mathrm{eff}} = 20000$K, $\log g = 3.90$, $V_{\mathrm{eq}} = 500\mathrm{km\,s^{-1}}$ and an S factor of 0.65, every observational yard stick is well matched.

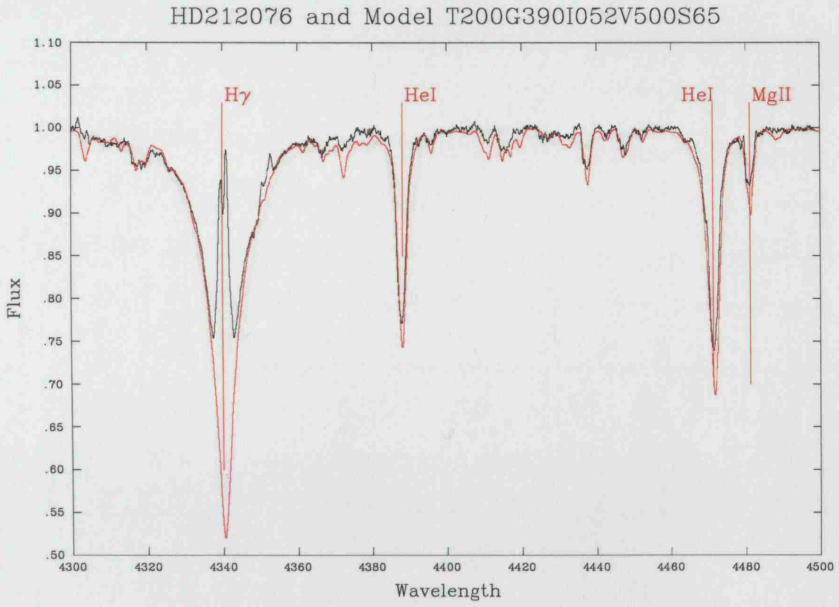

Figure 8.1. The best fit for star HD 212076.

HD 20336

Figure 8.2 displays the differentially–rotating model fit for HD 20336. This model shows an improved correspondence with the minor transitions along the spectrum as well as the obvious success it has in replicating the very pronounced 'V' profile of the Mg II line. This model is a good fit to the observation, though it doesn't replicate the same of level of detailed matching shown in figure 8.1. This model yields $T_{\rm eff} = 20000$K, which at a viewing angle of $i = 60°$ provides a $T_{\rm app}$ of 19930K; which is some 2500K less than the solid–body best–fit model; the BCD–derived temperature is 22182K. The model also significantly improves the polar log$g$ value from 4.80dex down to the more reasonable value of 4.20dex. Finally, $V_{\rm eq} = 500{\rm km\,s^{-1}}$ and $M({\rm V}) = -2.24$, this is consistent with the Hipparcos bounds.

Summary

Though there are only two stars discussed here, the fit improvements, as well as the improved consistency of fundamental parameters with respect to the independently derived values, presents a serious challenge to the assumption of solid–body rotation. Whilst it does appear evident that, on the whole, rigid rotation is an adequate assumption, it also appears that, for at least a few stars, this assumption can be poor when emission lines are

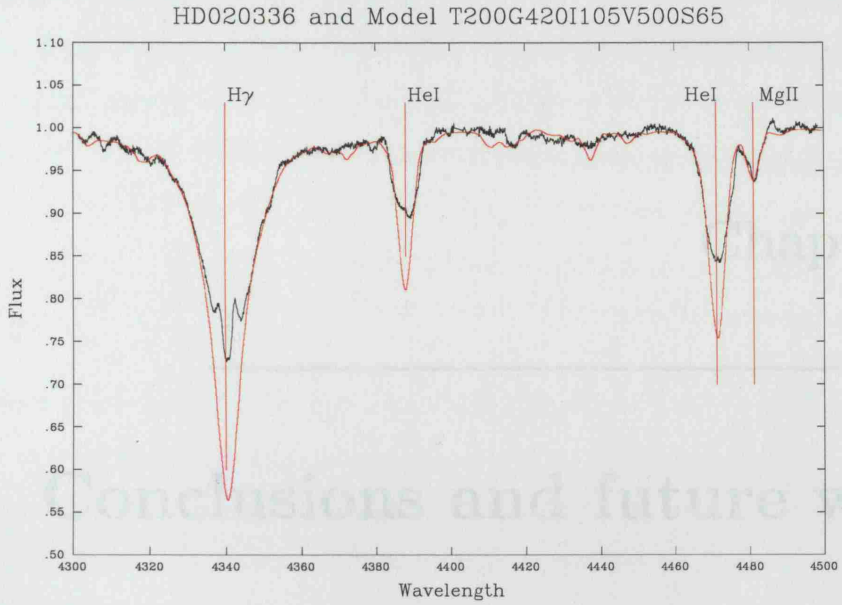

Figure 8.2. The best fit for star HD 20336.

present. In particular, the model spectrum of HD 212076 is quite remarkable in the way it replicates the observation, a level of detail not attainable without allowing for differential rotation. Consequently, this very preliminary glance provides tantalising evidence of a significant shift from solid–body to differential rotation in these stars. It is interesting to consider the physics of this issue and to perhaps theorise as to how such a state–change might occur. The presence of the emission lines perhaps provides a clue. For instance, one of the implications of Von Zeipel's theorem is the driving of meridional circulation. These circulatory currents could perhaps not only provide the momentum transport from core to surface that acts to spin up the surface, but may also, as a consequence, act like a glue ensuring the surface does rotate rigidly. Consequently, at the point where matter starts to break out from the equator these meridional circulations, locally at least, would be disrupted. It is then feasible to think that such a mass loss event might spark a temporary breaking of the glue which could very quickly result in a slow-down of the rotation toward the poles.

In any event, these two objects, whether special cases or just observations taken at just the right moment, do provide evidence for the differential rotation of the surface of Be stars and as such should be investigated further.

Chapter 9

Conclusions and future work

9.1 Conclusions – The Null Hypothesis

This research has focused on the inclusion of *all* of Stoeckley's requisites and has resulted in the construct of a grid of synthetic spectra spanning the B star fundamental parameter space. This grid, built on the assumption that these stars are indeed *near–critical* rotators, has provided substantial evidence to suggest that a simple measure of the Doppler broadening of absorption–line widths is an inadequate approach to establishing a rotational velocity. Indeed, the ability of this grid to represent by far the majority of Chauville et al. (2001) spectra whilst simultaneously satisfying independent constraints, such as the Hipparcos distance measure, ensures this evidence is quite compelling. Though the model grid has been seen to lack the most appropriate resolution, in particular in $\log g$, the overall success supersedes this. Further to this, as a by–product of this research, evidence has been presented that these stars surfaces, throughout the decretion events, cease to rotate as solid bodies and temporarily slow toward the poles and exhibit differential rotation.

Whilst this slow–down has not yet been observed, the implications should not be underestimated. The momentum transport which must surely be involved in spinning up a star to a near–critical velocity is enormous. The effects of periodically switching this mechanism on and off must have a profound effect upon metal enrichment of the stellar atmosphere which, in turn, has a direct, and dramatic, impact upon the mass loss events associated with hot stars. The wider implications of enrichment of the ISM as well as

main sequence life for a massive star clearly impinge upon much of the work that modern astrophysics and astronomy currently undertakes. Whilst the Be and Oe star populations, at a glance, might appear to be a relatively obscure facet of stellar evolution they are potentially no less than a distinct evolutionary phase that all massive stars go through and as such must be understood.

9.2 Future Work

Whilst the work presented here provides significant support for the near–critical rotation scenario it does lack a full non–local thermal equilibrium (nLTE) treatment of the photosphere. Essentially, time, computing and feasibility constraints precluded such a thorough approach at the outset. However, with the preliminary success of using the Local Thermal Equilibrium (LTE) assumption and with imminent access to the forthcoming UCL super–computer, a full nLTE treatment is now feasible and clearly warranted. Also, within this current work, no attempt was made to synthesise the spectra of the decretion disks themselves. Thus this research clearly requires expansion. Consequently any future work should concentrate on three projects:

- Construct of a complete nLTE based model grid of rapidly rotating stars for OB stars
- Develop and construct a grid of decretion disk intensity spectra.
- Increase the number of stars for which there is the relevant spectroscopic data spanning a decretion event (i.e., before, during and after).

1. nLTE Based model grid

Whilst there exist standard nLTE B–star model–atmosphere grids in the literature, the log$g$ resolution as well as effective–temperature ($T_{\rm eff}$) range does not provide the basic input required. Hence as a first step to constructing a nLTE Be star grid one would need to generate the nLTE static star grid using, for example, the TLUSTY stellar atmosphere program of Lanz and Hubeny (1995). Then using the spectrum synthesis program SYNSPEC, a grid of intensity spectra can be generated from the full nLTE stellar atmosphere grid. Finally, as within this work, using the Roche approximation for a rotationally distorted star, the synthetic spectra are generated. This process is then repeated for several

different values of a differential rotation factor which can be included for within the Roche approximation, as detailed in § 8.1.

With a complete nLTE based model grid in place, a systematic analysis of all available Be star spectra against this comprehensive model grid can be undertaken. The caveat here is that all stellar spectra used for comparison *must not* exhibit any Balmer emission. The reason for this is two–fold. Firstly, the differential rotation apparent in many spectra appears to correlate with the decretion (emission) event, hence treating the emission and non-emission populations as distinct should provide a more comprehensive and compelling statistic as to whether the *apparent* differential rotation is *real*. Secondly, though, the emission itself is obviously blended with the stellar components and hence one needs to accommodate this emission also.

2. Modelling Decretion Disks

Modelling of disk spectra is not a new technique. Indeed, the TLUSTY nLTE code has been used successfully to model accretion disks of QSOs (Hubeny et al, 2000), cataclysmic variables (Wade & Hubeny, 1998) and X-ray binaries (Davis & Hubeny, 2006). Whilst these are notionally distinct from *decretion* disks, relevant to this study, physically these systems are to be likely very similar. Hence, the TLUSTY code could again be the start point, at least, from which to begin the modelling of these spectra. Similarly, TLUSTY output provides the structural input to SYNSPEC which would subsequently be used to provide the angle–dependent intensity spectra which can be integrated with the stellar spectra.

Finally, and neatly, utilising the spectra of Be stars which straddle the decretion event will allow the fundamental parameters of these stars to be obtained independently, without having to simultaneously establish fundamental parameters of the disk, thus enabling an independent method for testing the success of the disk modelling. Clearly, this test would be ideal for all Be stars and consequently, as an addendum, any future work should seek to increase this statistic.

3. A need for time-dependent observations

As noted above, in conjunction with the modelling and analysis, there is a need to obtain spectra for those objects which pass through the phase change of a decretion event. Ideally

one would hope to observe periodically before during and after such an event, however the current lack of predictability of these episodes would indicate this to be an unlikely scenario. It is the case, though, that any objects currently in emission are prime targets for systematic repeat observations, as the transient nature of the disk episodes will end. This consequently would allow one to question whether or not the differential rotation scenario occurs as the disk dissipates. Evidencing this could well lead to an additional deduction as to whether the disks ultimately fall back onto the stellar surface or are blown away via stellar winds.

Appendix A

Best Fit Plots

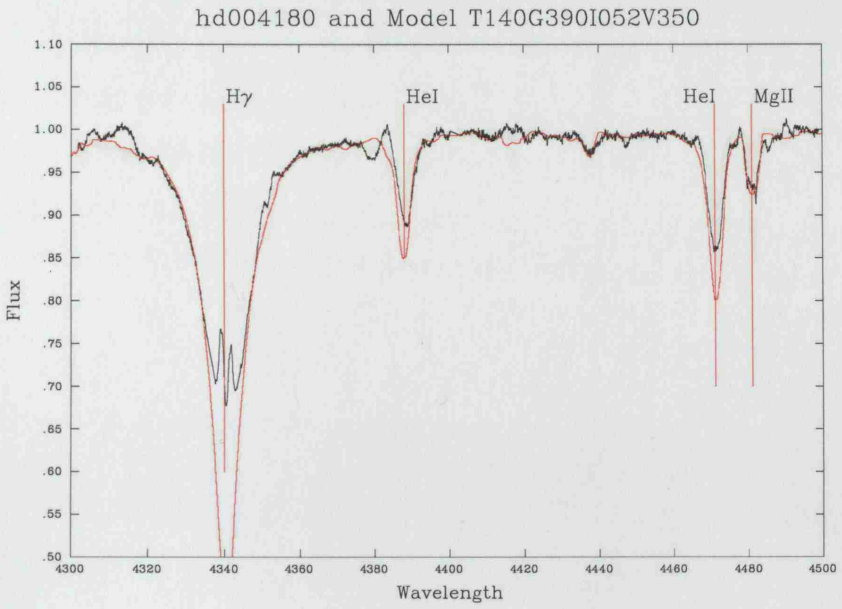

Figure A.1. Plot of the best–fit model versus observation for HD 4180. Observation = black line; Model = red line.

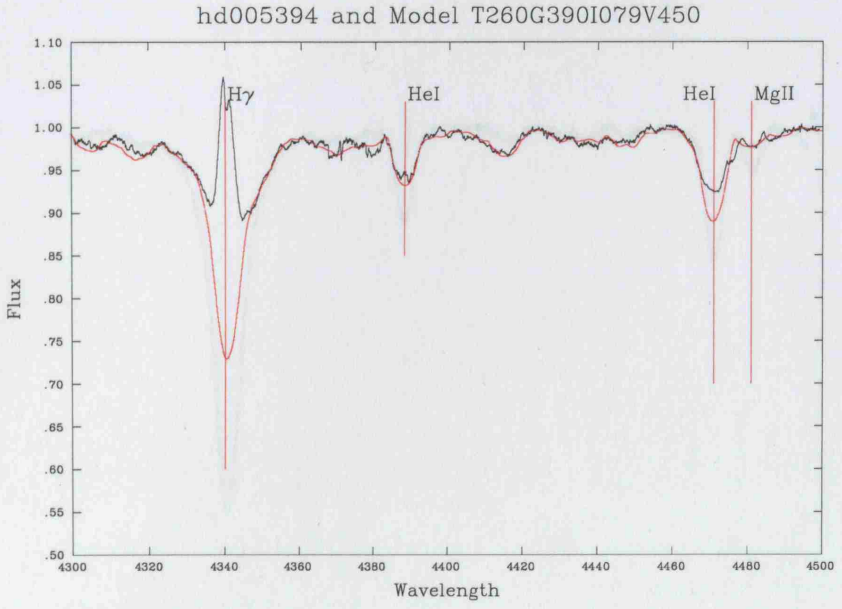

Figure A.2. Plot of the best–fit model versus observation for HD 5394. Observation = black line; Model = red line.

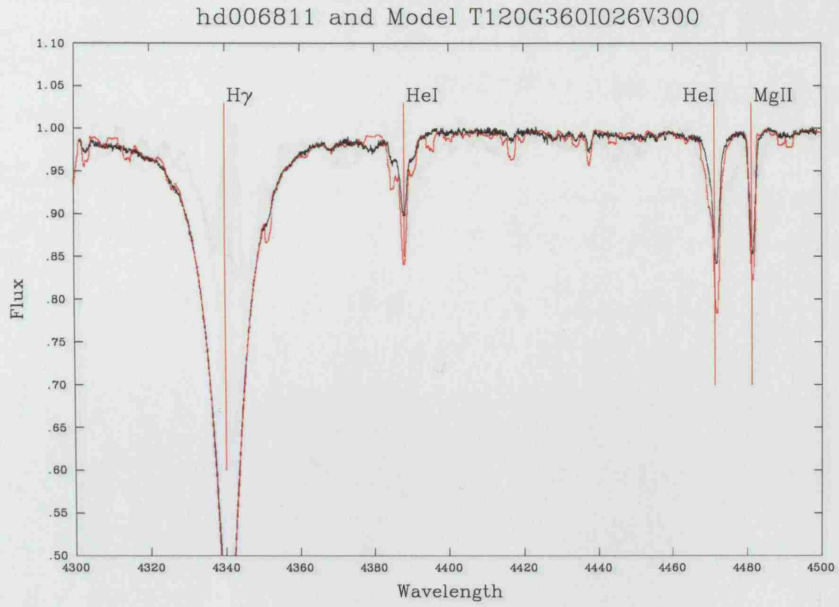

Figure A.3. Plot of the best–fit model versus observation for HD 6811. Observation = black line; Model = red line.

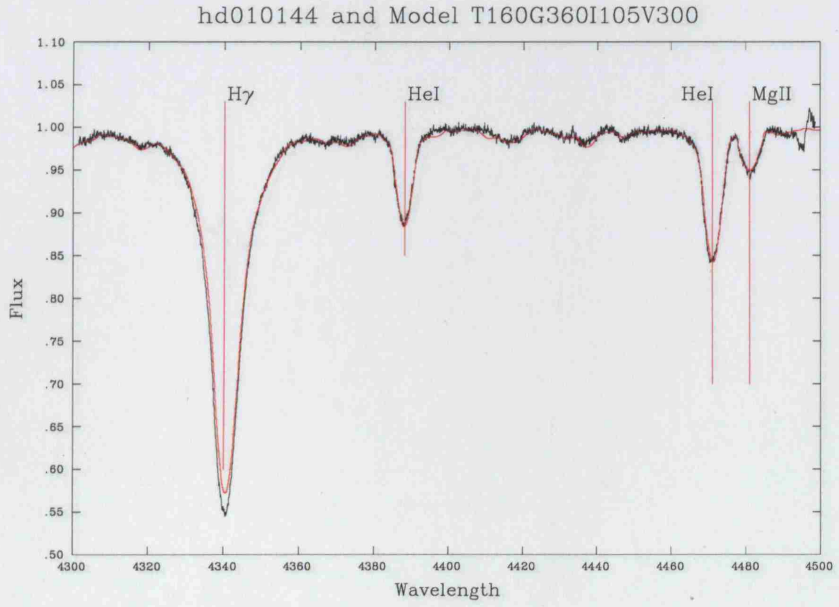

Figure A.4. Plot of the best–fit model versus observation for HD 10144. Observation = black line; Model = red line.

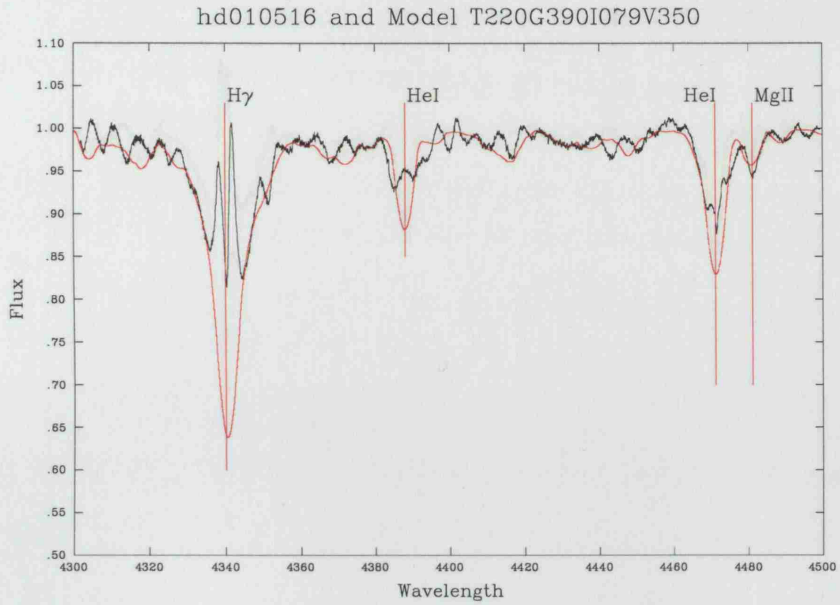

Figure A.5. Plot of the best–fit model versus observation for HD 10516. Observation = black line; Model = red line.

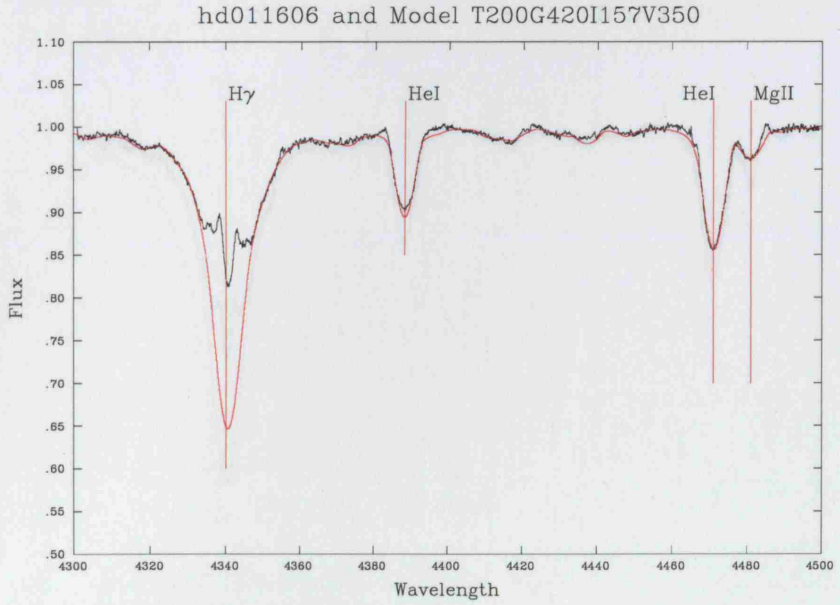

Figure A.6. Plot of the best–fit model versus observation for HD 11606. Observation = black line; Model = red line.

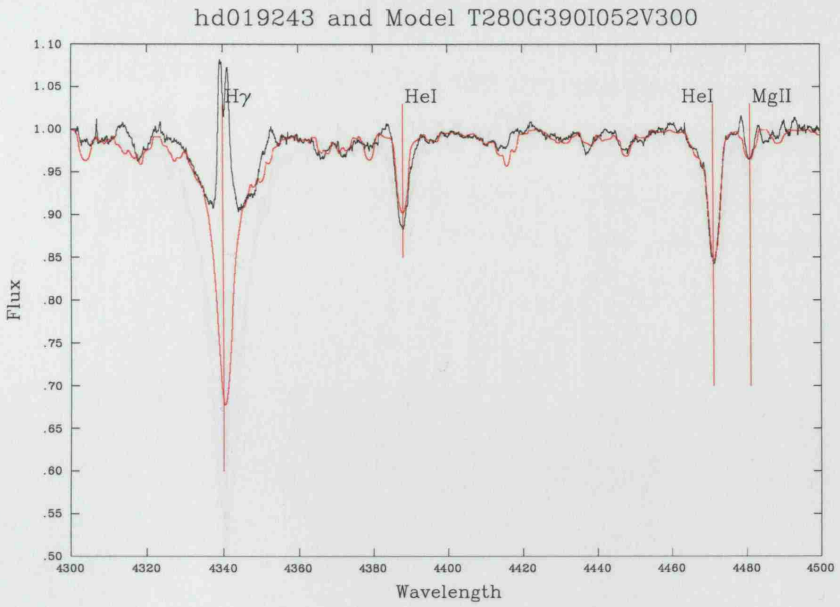

Figure A.7. Plot of the best–fit model versus observation for HD 19243. Observation = black line; Model = red line.

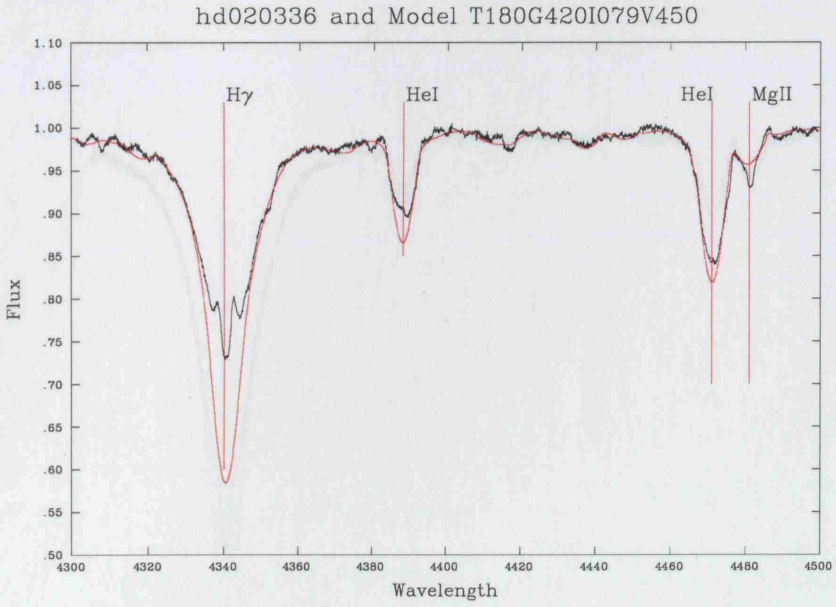

Figure A.8. Plot of the best–fit model versus observation for HD 20336. Observation = black line; Model = red line.

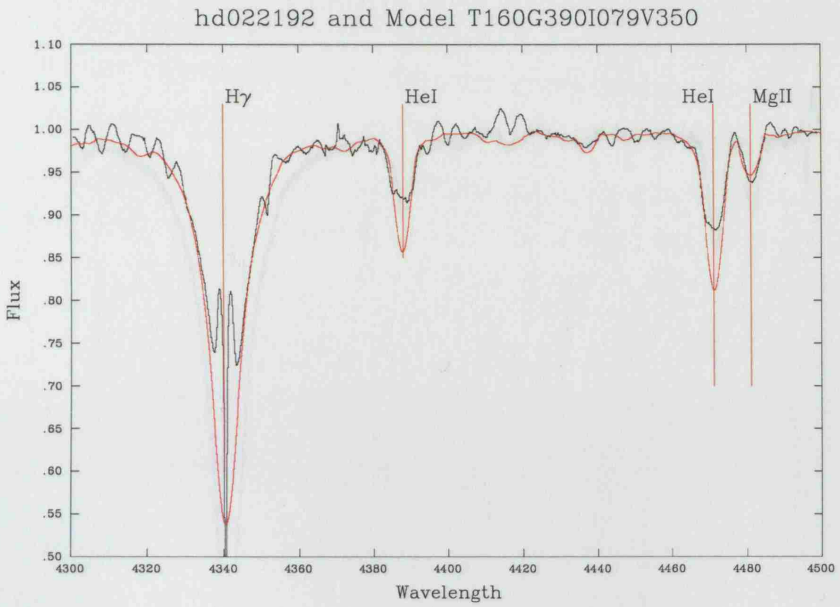

Figure A.9. Plot of the best–fit model versus observation for HD 22192. Observation = black line; Model = red line.

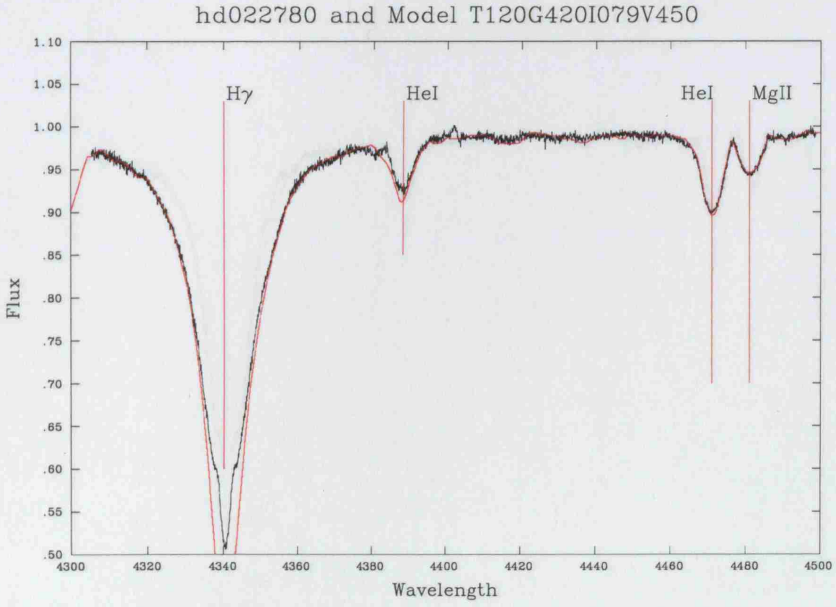

Figure A.10. Plot of the best–fit model versus observation for HD 22780. Observation = black line; Model = red line.

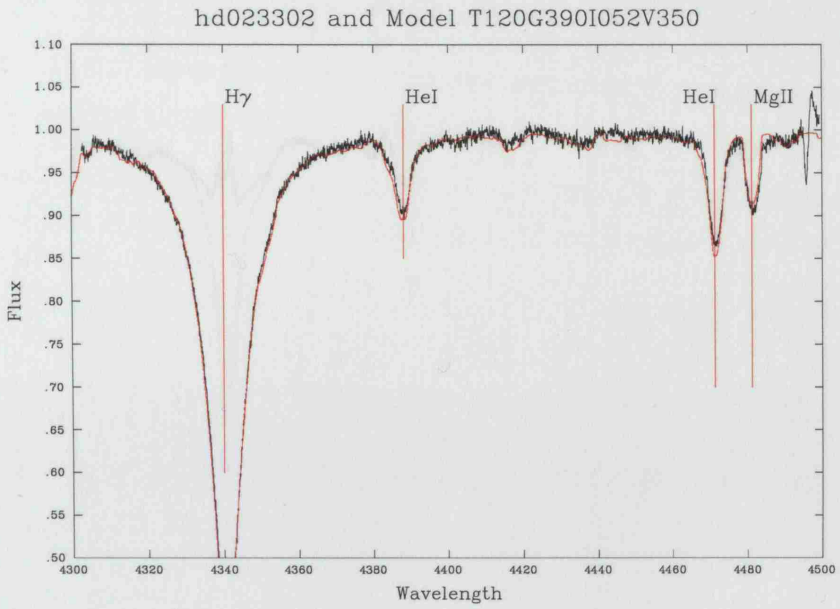

Figure A.11. Plot of the best–fit model versus observation for HD 23302. Observation = black line; Model = red line.

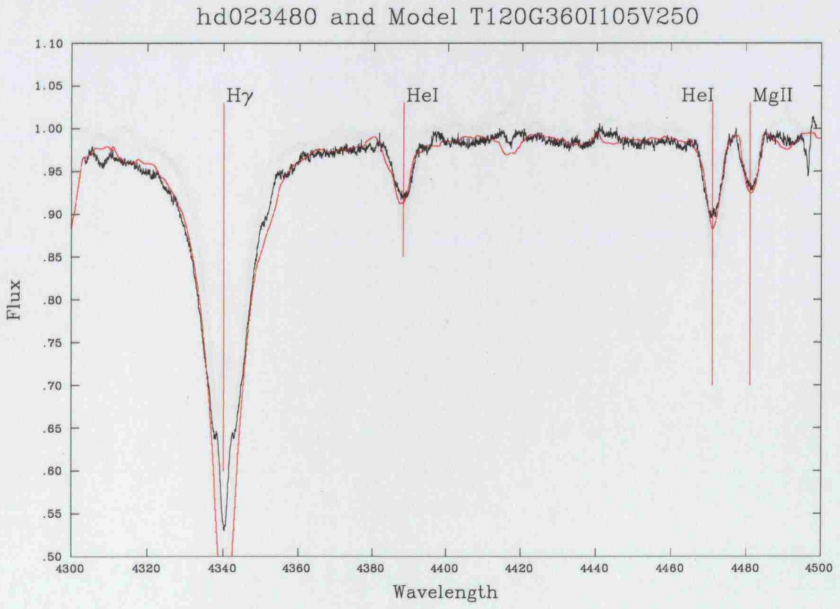

Figure A.12. Plot of the best–fit model versus observation for HD 23480. Observation = black line; Model = red line.

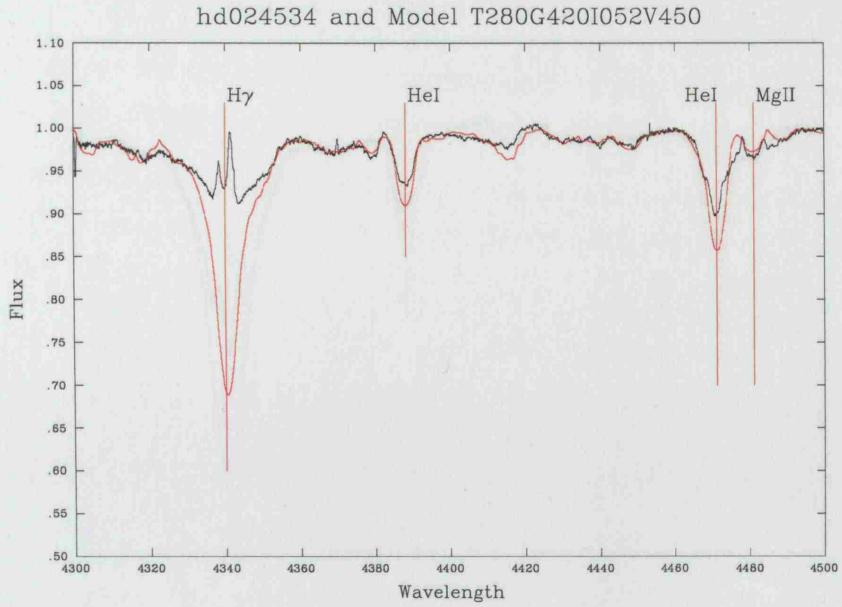

Figure A.13. Plot of the best–fit model versus observation for HD 24534. Observation = black line; Model = red line.

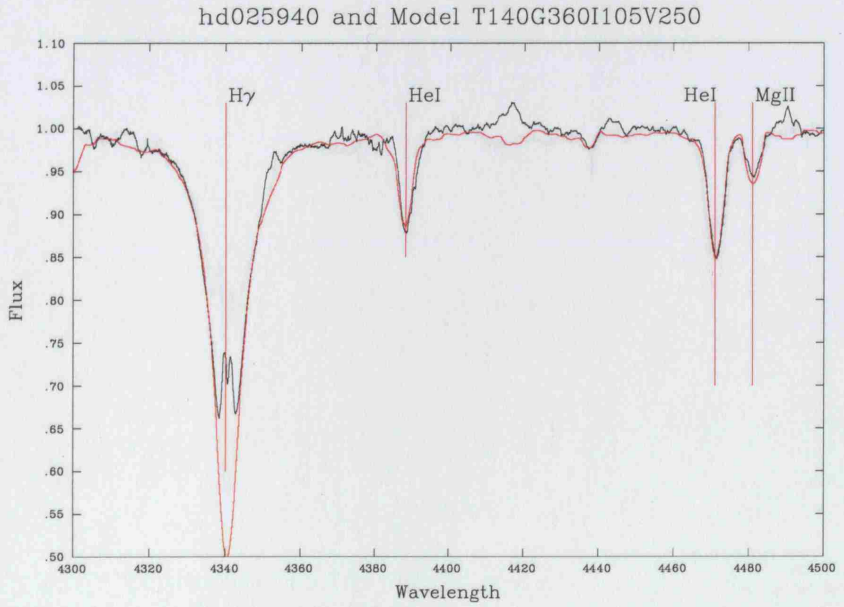

Figure A.14. Plot of the best–fit model versus observation for HD 25940. Observation = black line; Model = red line.

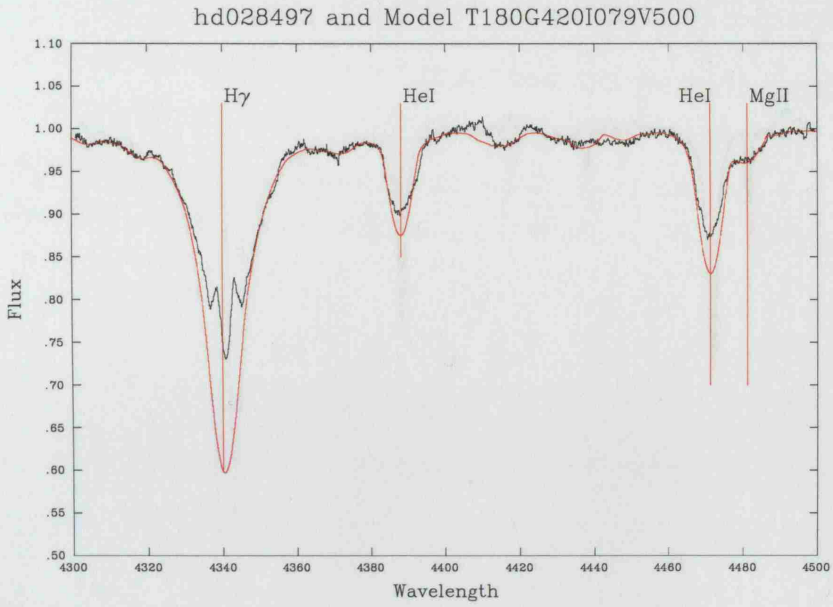

Figure A.15. Plot of the best–fit model versus observation for HD 28497. Observation = black line; Model = red line.

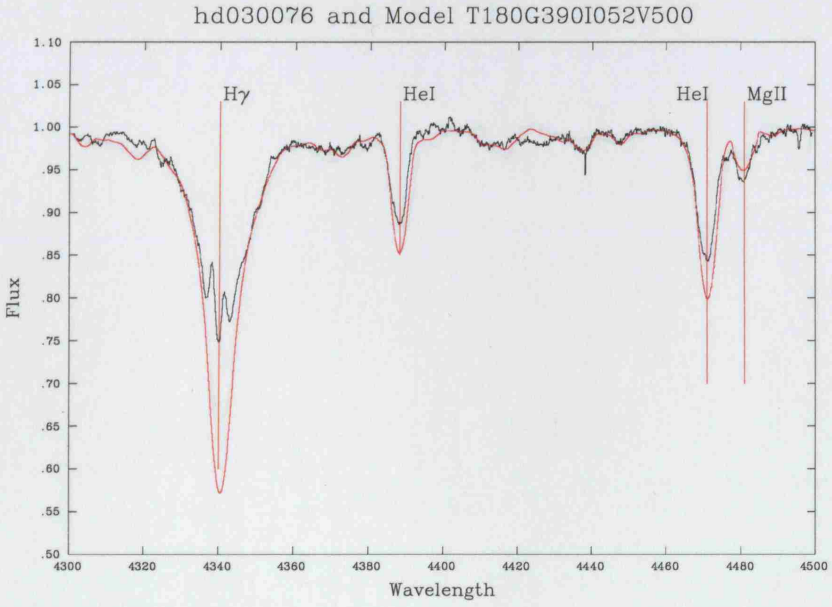

Figure A.16. Plot of the best–fit model versus observation for HD 30076. Observation = black line; Model = red line.

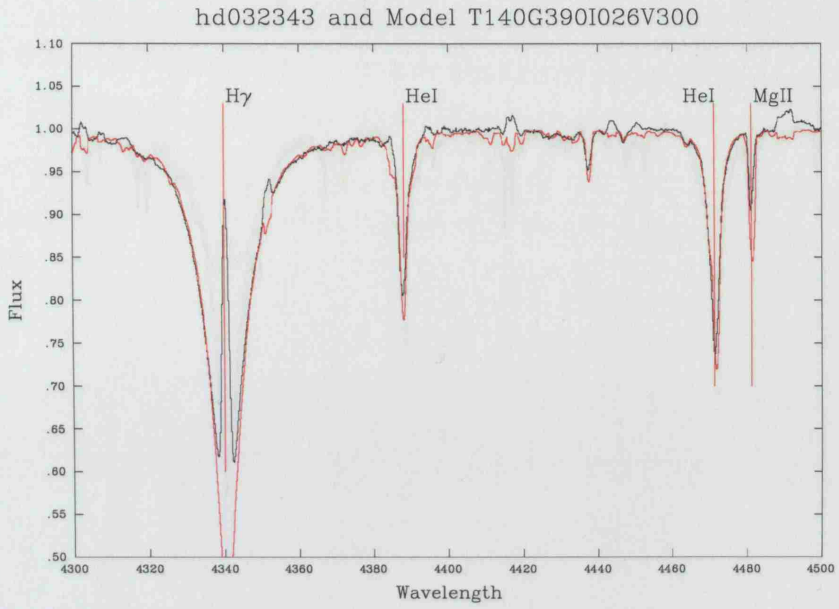

Figure A.17. Plot of the best–fit model versus observation for HD 32343. Observation = black line; Model = red line.

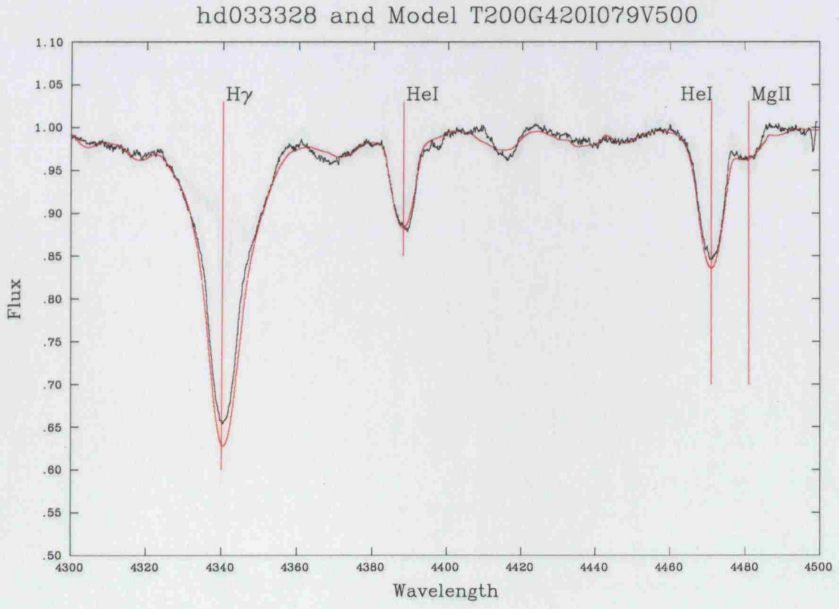

Figure A.18. Plot of the best–fit model versus observation for HD 33328. Observation = black line; Model = red line.

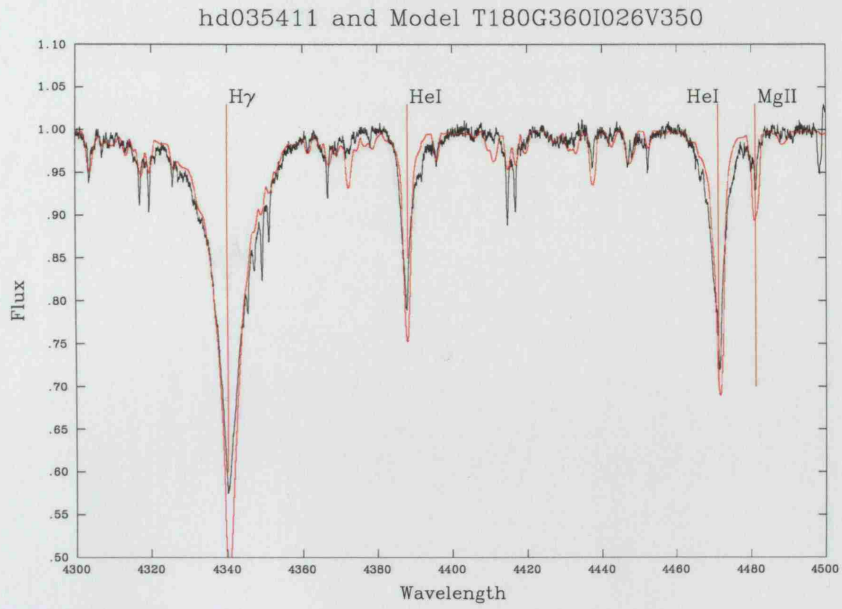

Figure A.19. Plot of the best–fit model versus observation for HD 35411. Observation = black line; Model = red line.

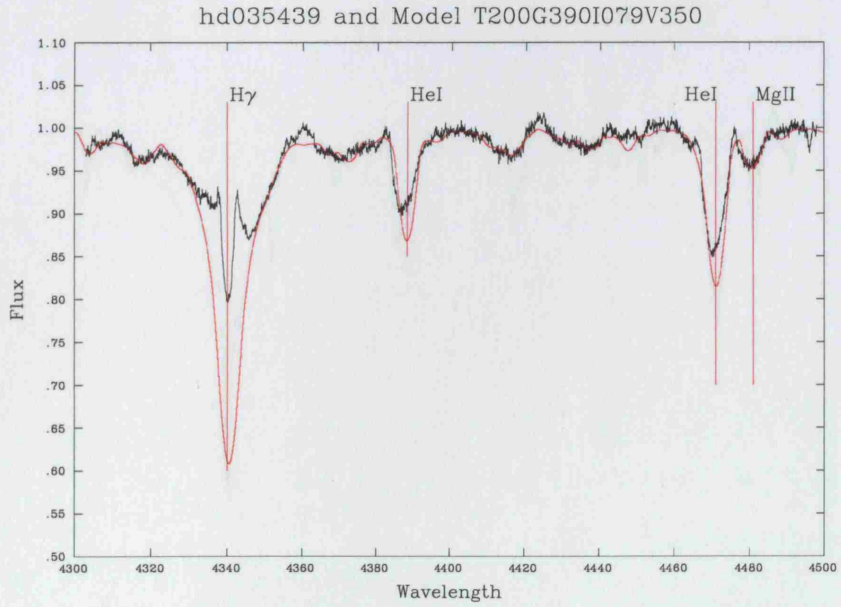

Figure A.20. Plot of the best–fit model versus observation for HD 35439. Observation = black line; Model = red line.

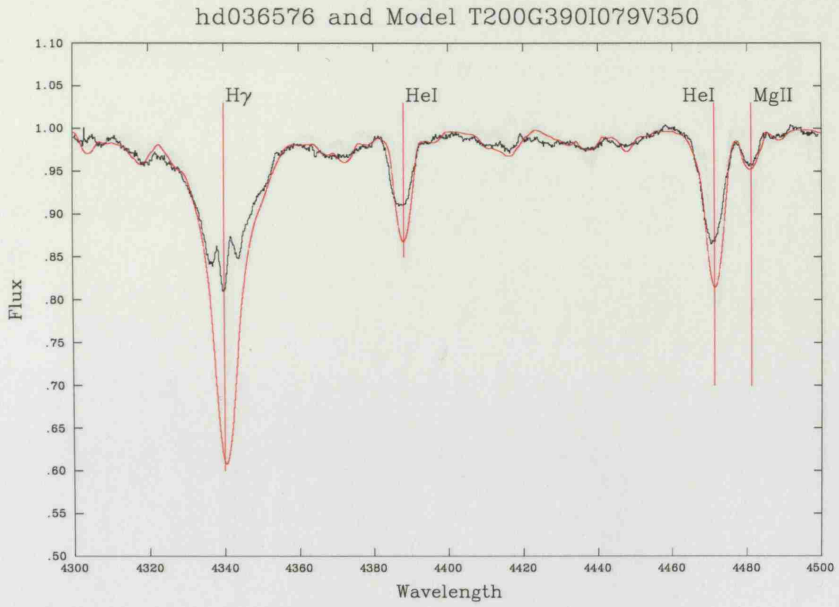

Figure A.21. Plot of the best–fit model versus observation for HD 36576. Observation = black line; Model = red line.

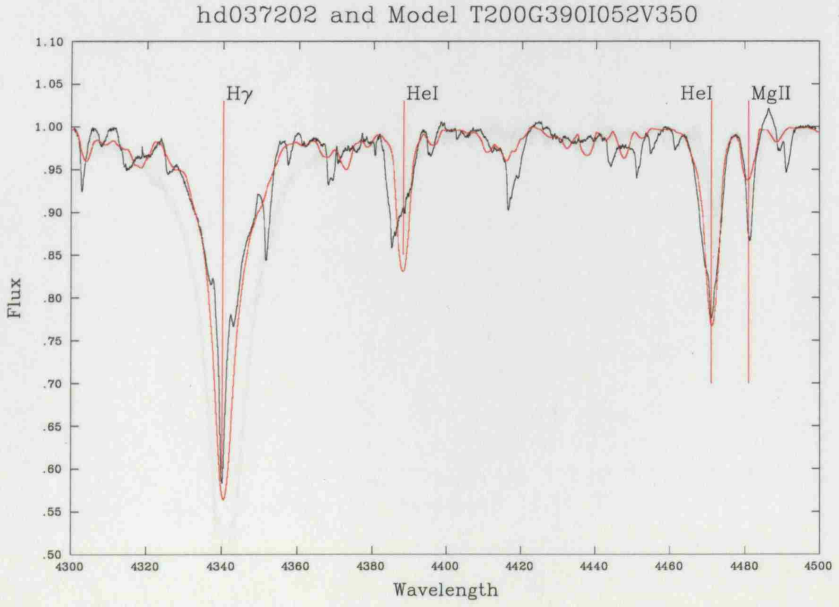

Figure A.22. Plot of the best–fit model versus observation for HD 37202. Observation = black line; Model = red line.

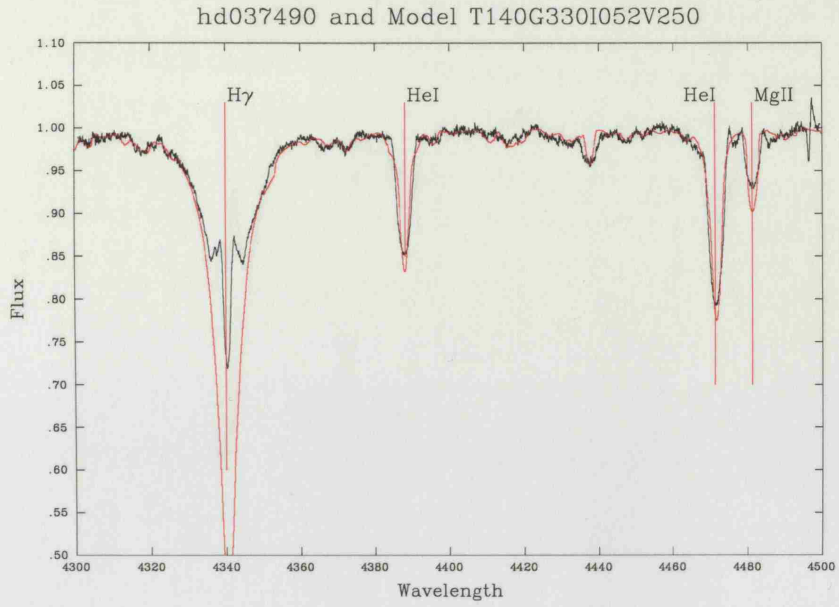

Figure A.23. Plot of the best–fit model versus observation for HD 37490. Observation = black line; Model = red line.

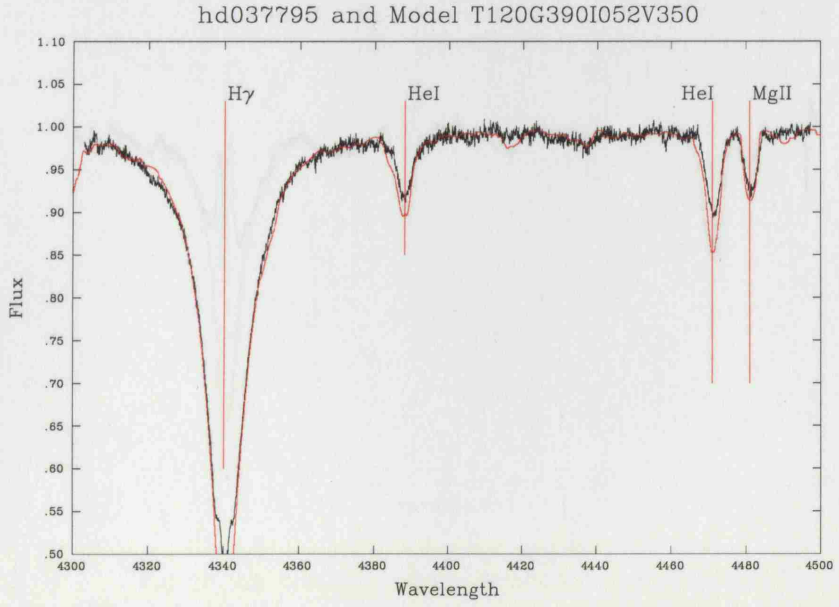

Figure A.24. Plot of the best–fit model versus observation for HD 37795. Observation = black line; Model = red line.

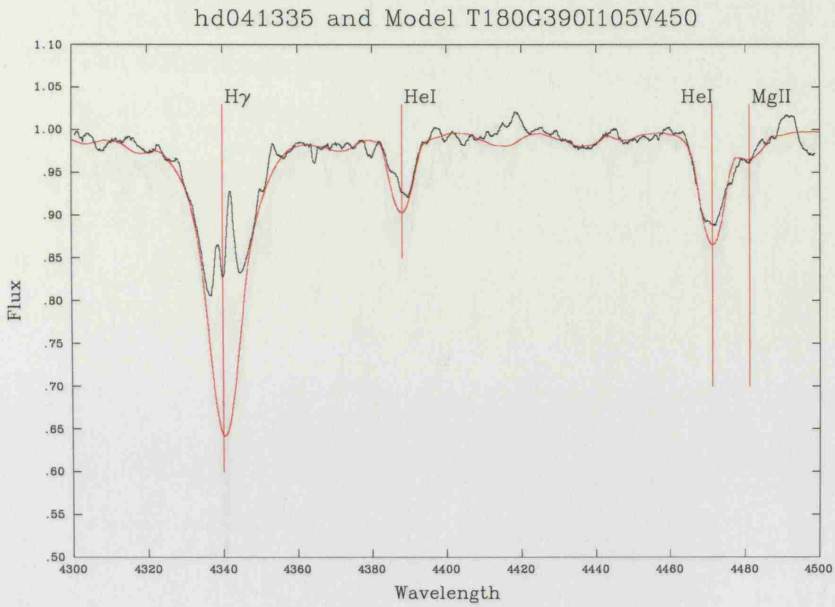

Figure A.25. Plot of the best–fit model versus observation for HD 41335. Observation = black line; Model = red line.

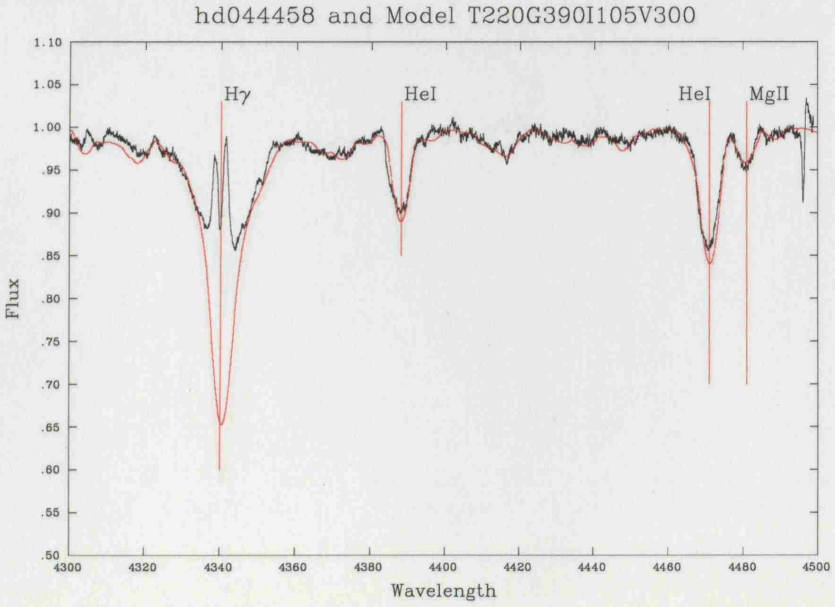

Figure A.26. Plot of the best–fit model versus observation for HD 44458. Observation = black line; Model = red line.

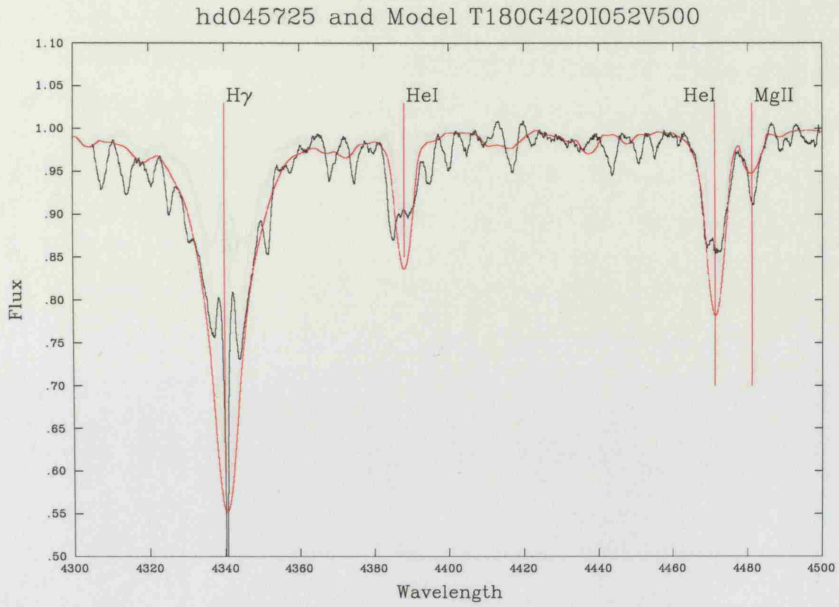

Figure A.27. Plot of the best–fit model versus observation for HD 45725. Observation = black line; Model = red line.

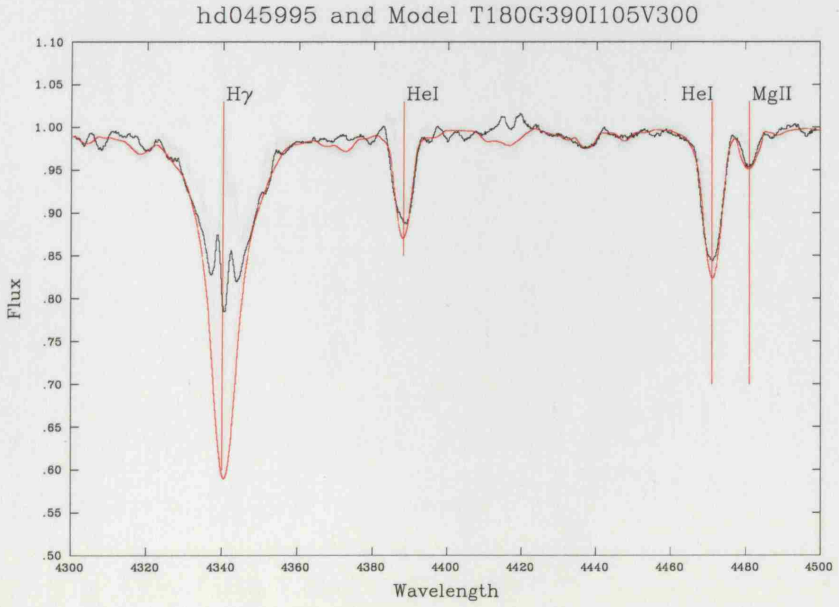

Figure A.28. Plot of the best–fit model versus observation for HD 45995. Observation = black line; Model = red line.

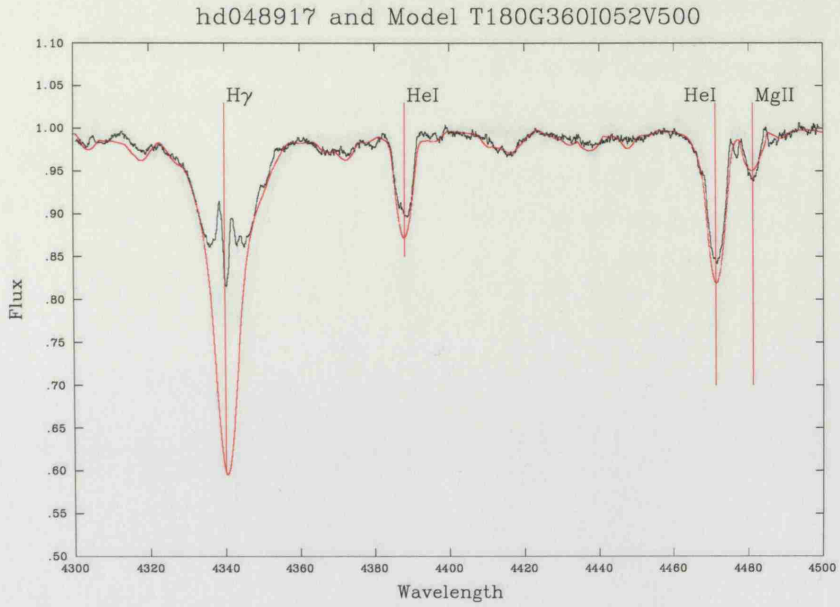

Figure A.29. Plot of the best–fit model versus observation for HD 48917. Observation = black line; Model = red line.

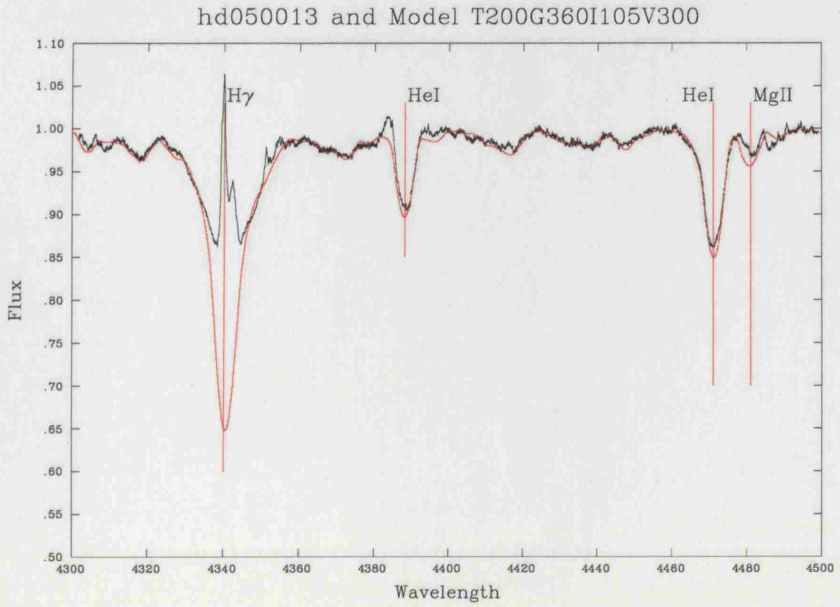

Figure A.30. Plot of the best–fit model versus observation for HD 50013. Observation = black line; Model = red line.

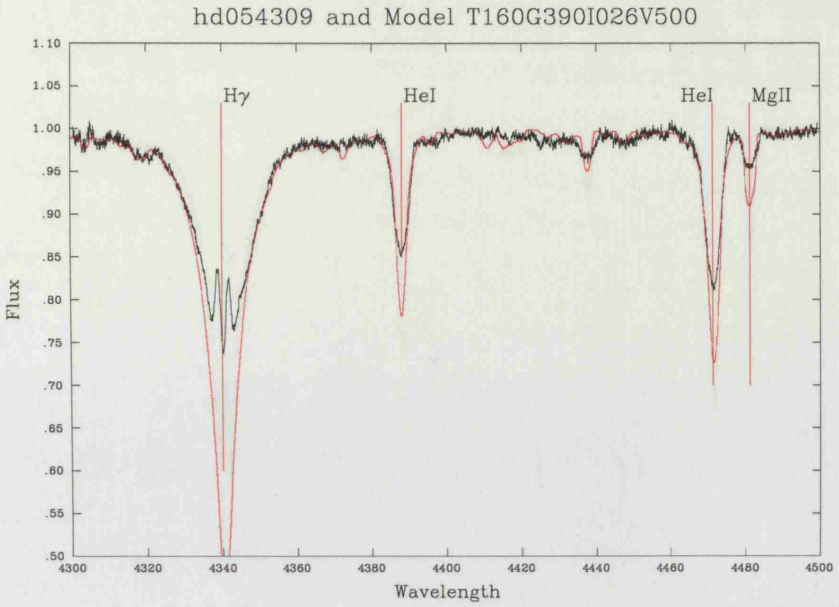

Figure A.31. Plot of the best–fit model versus observation for HD 54309. Observation = black line; Model = red line.

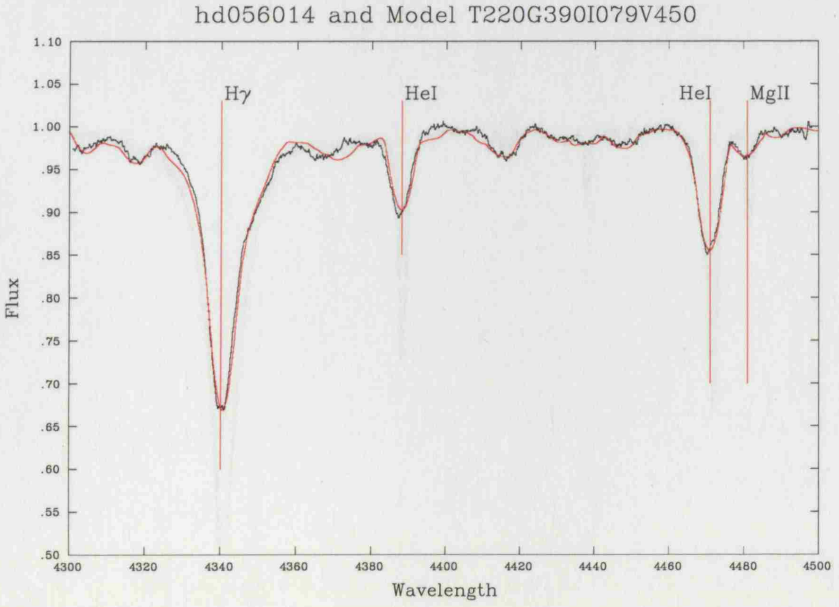

Figure A.32. Plot of the best–fit model versus observation for HD 56014. Observation = black line; Model = red line.

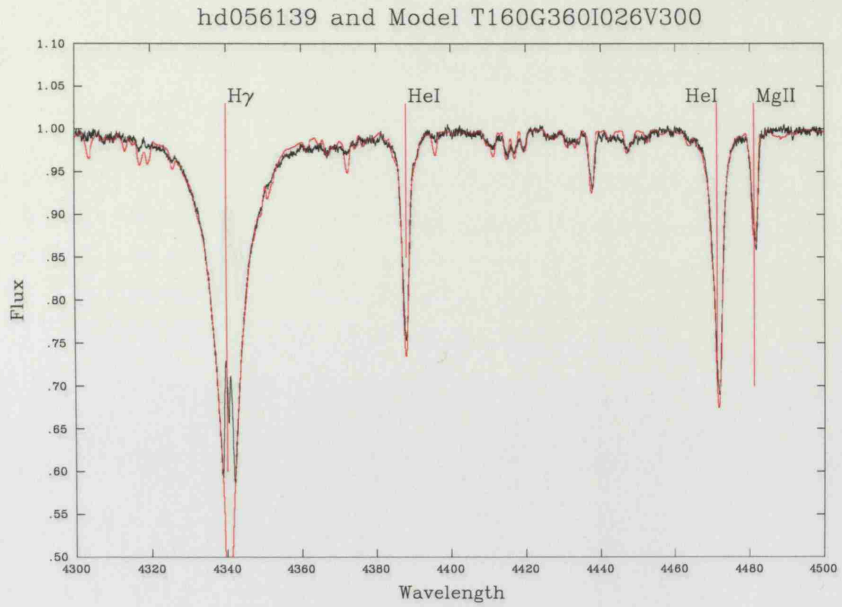

Figure A.33. Plot of the best–fit model versus observation for HD 56139. Observation = black line; Model = red line.

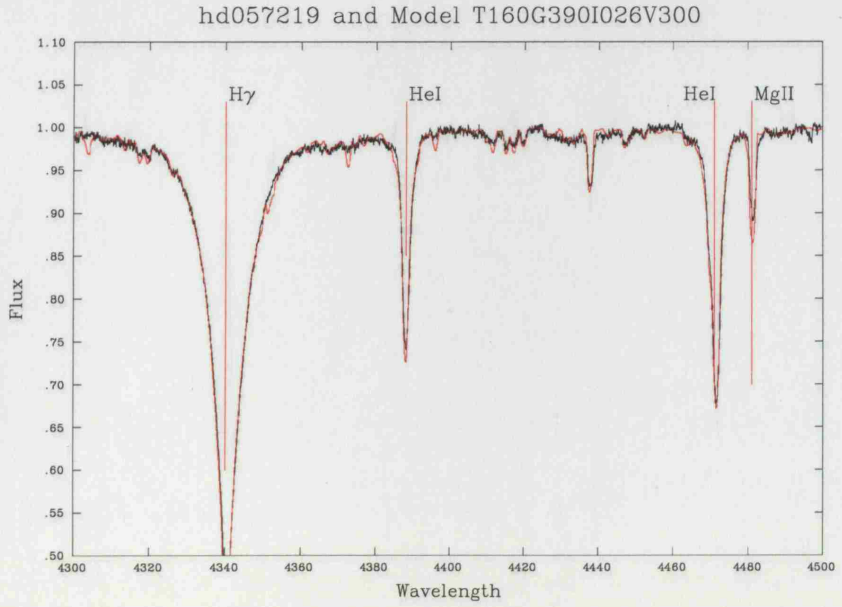

Figure A.34. Plot of the best–fit model versus observation for HD 57219. Observation = black line; Model = red line.

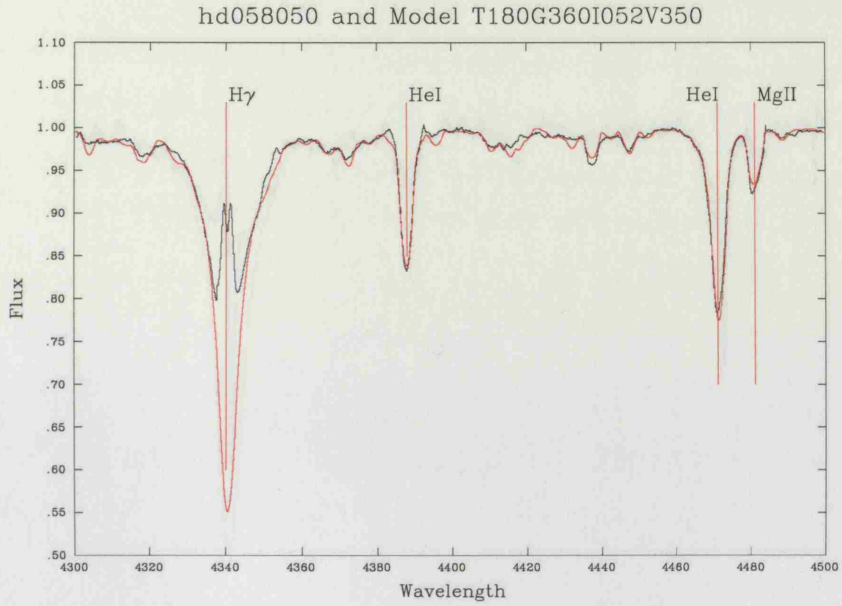

Figure A.35. Plot of the best–fit model versus observation for HD 58050. Observation = black line; Model = red line.

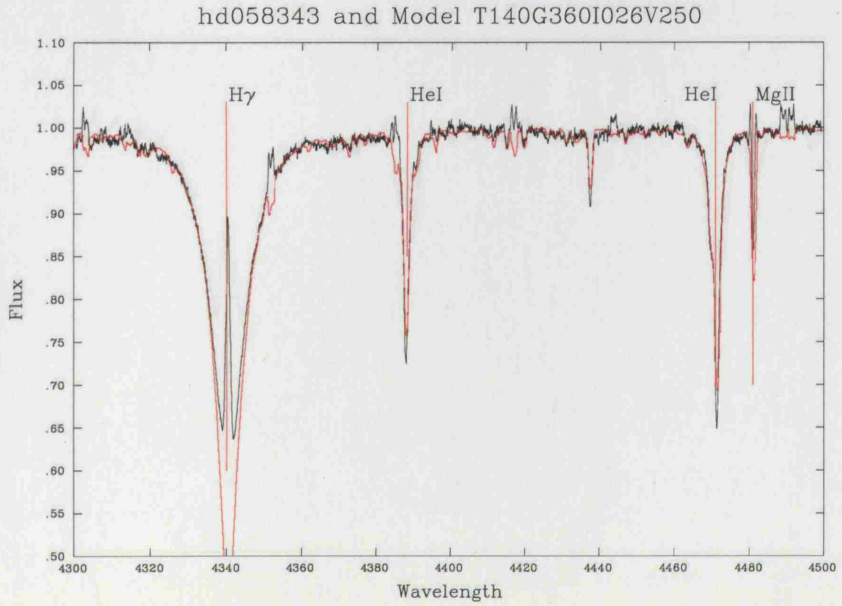

Figure A.36. Plot of the best–fit model versus observation for HD 58343. Observation = black line; Model = red line.

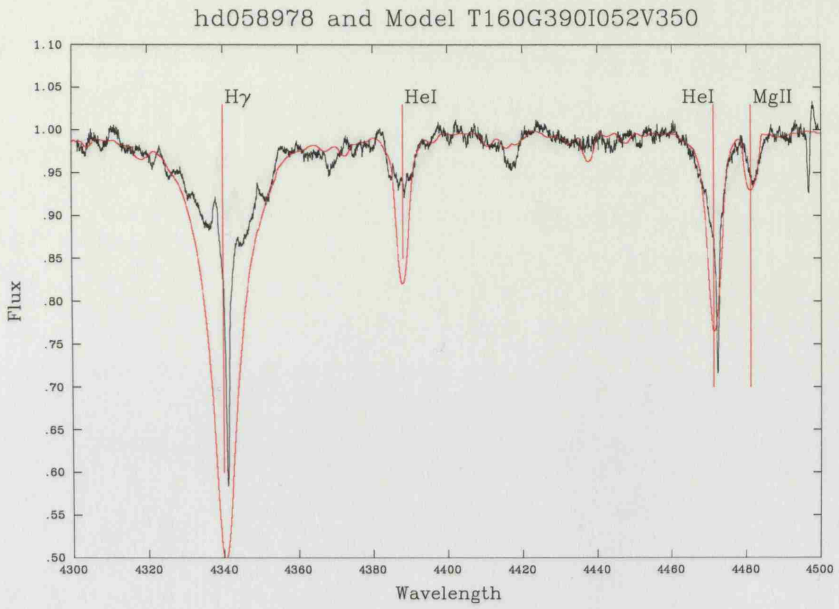

Figure A.37. Plot of the best–fit model versus observation for HD 58978. Observation = black line; Model = red line.

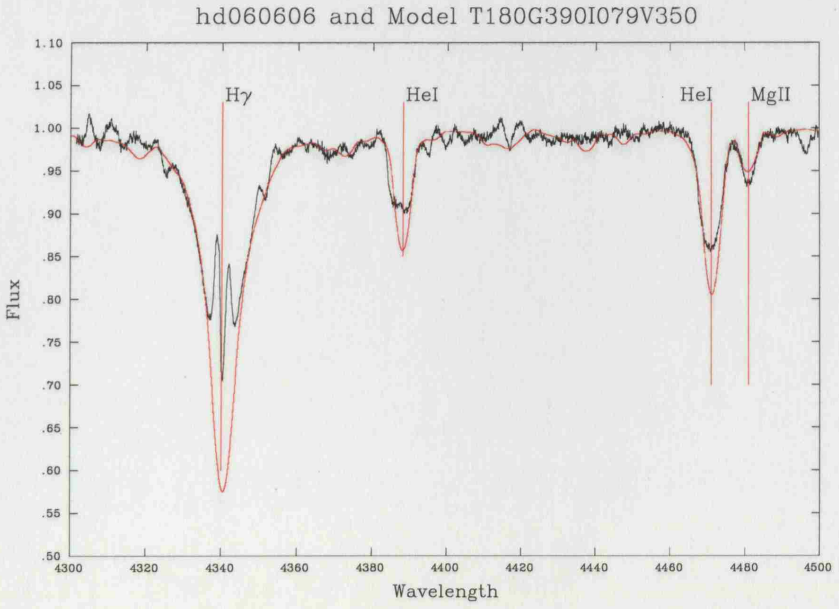

Figure A.38. Plot of the best–fit model versus observation for HD 60606. Observation = black line; Model = red line.

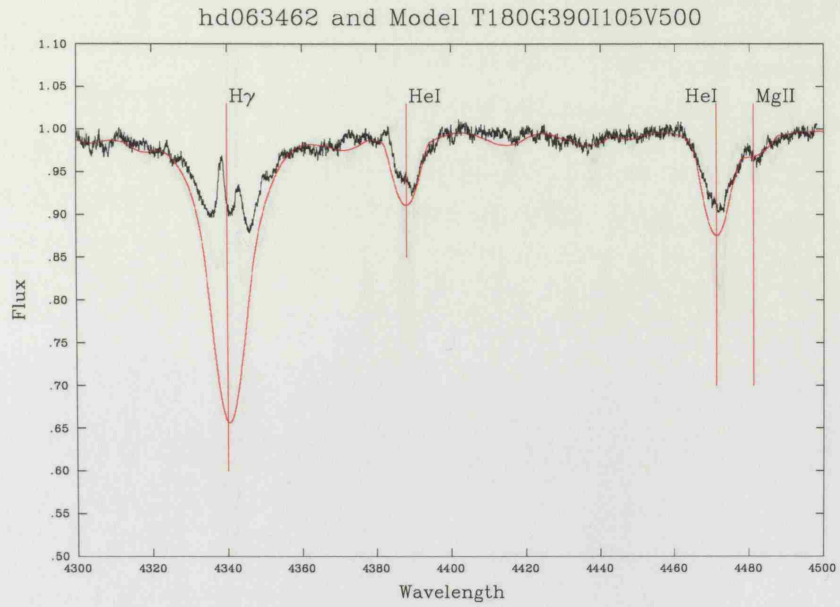

Figure A.39. Plot of the best–fit model versus observation for HD 63462. Observation = black line; Model = red line.

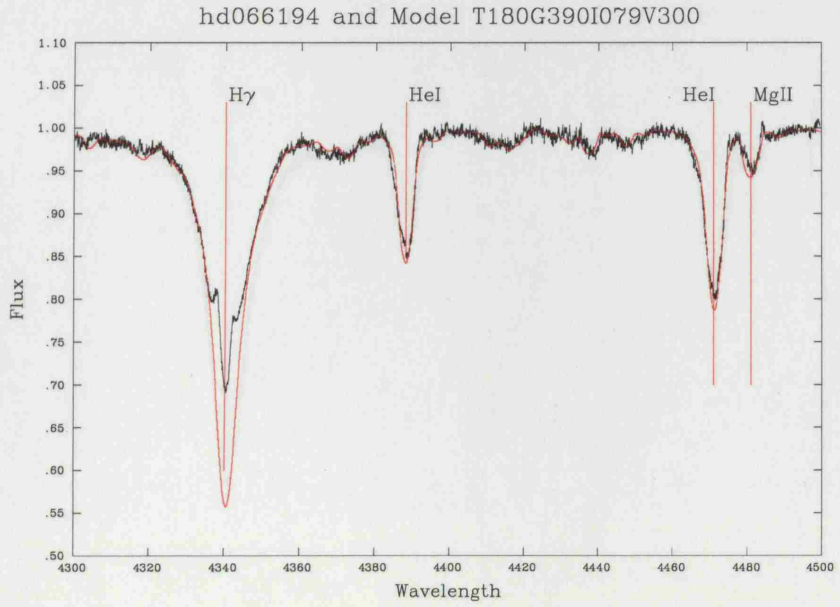

Figure A.40. Plot of the best–fit model versus observation for HD 66194. Observation = black line; Model = red line.

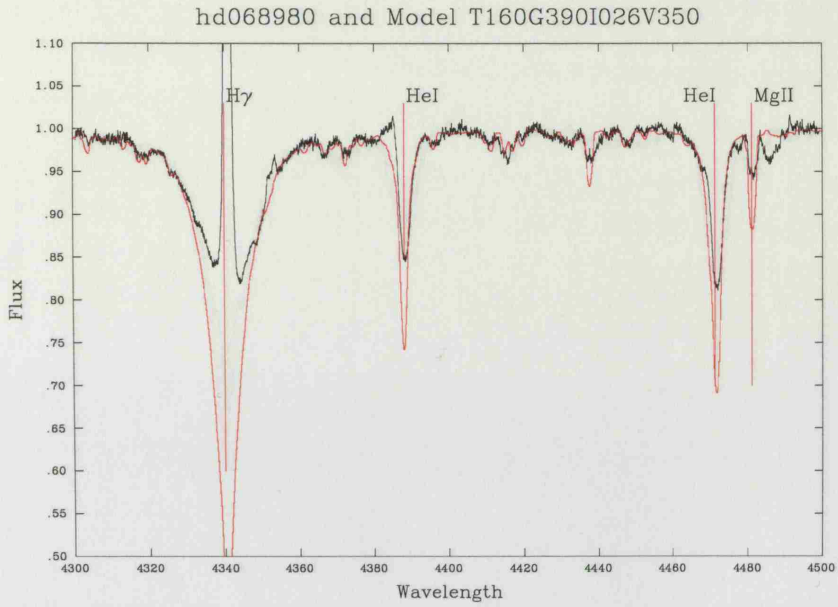

Figure A.41. Plot of the best–fit model versus observation for HD 68980. Observation = black line; Model = red line.

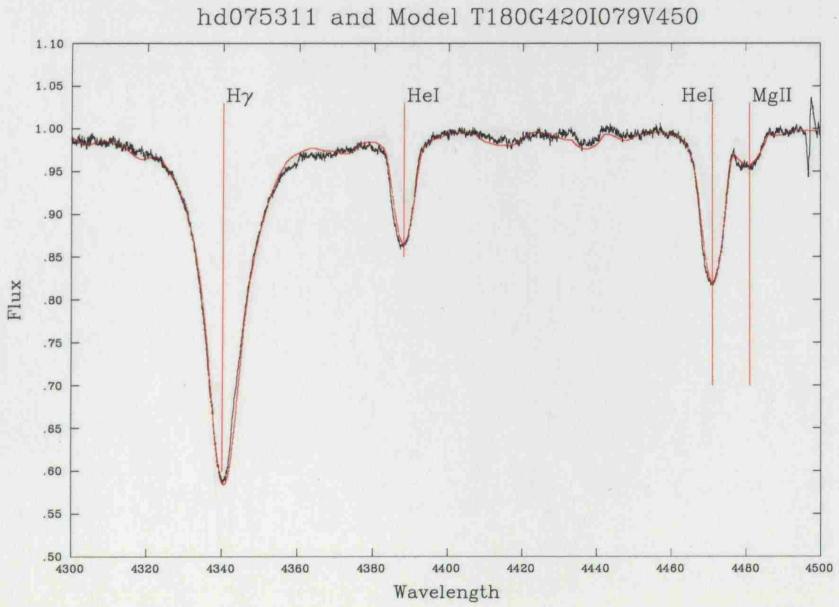

Figure A.42. Plot of the best–fit model versus observation for HD 75311. Observation = black line; Model = red line.

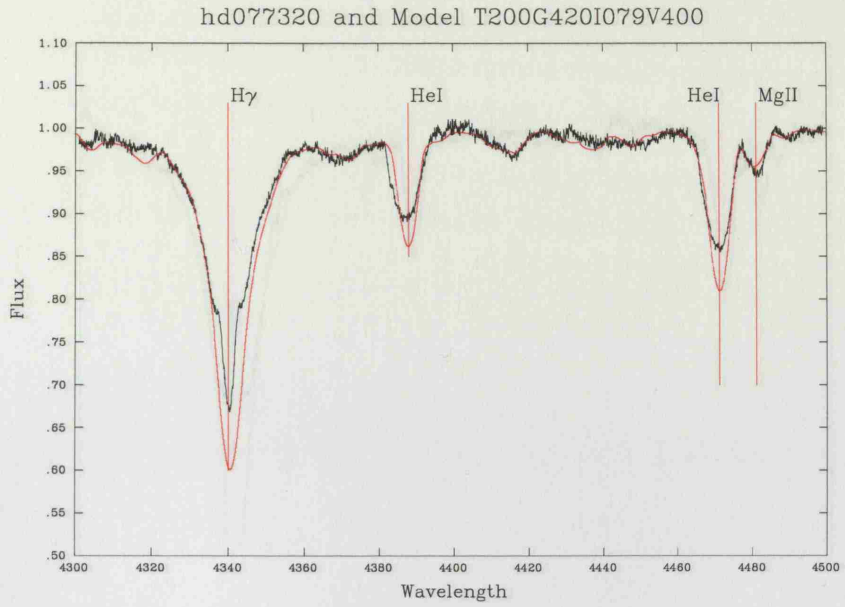

Figure A.43. Plot of the best–fit model versus observation for HD 77320. Observation = black line; Model = red line.

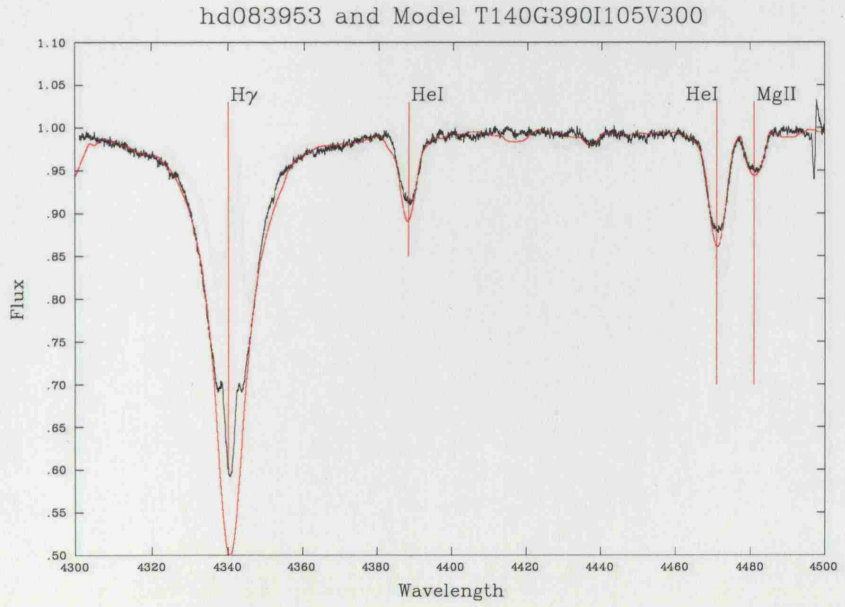

Figure A.44. Plot of the best–fit model versus observation for HD 83953. Observation = black line; Model = red line.

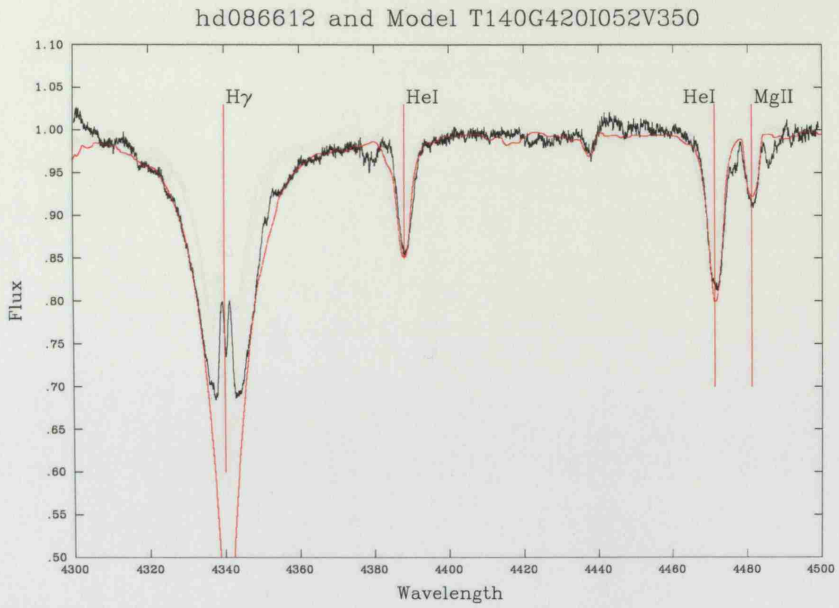

Figure A.45. Plot of the best–fit model versus observation for HD 86612. Observation = black line; Model = red line.

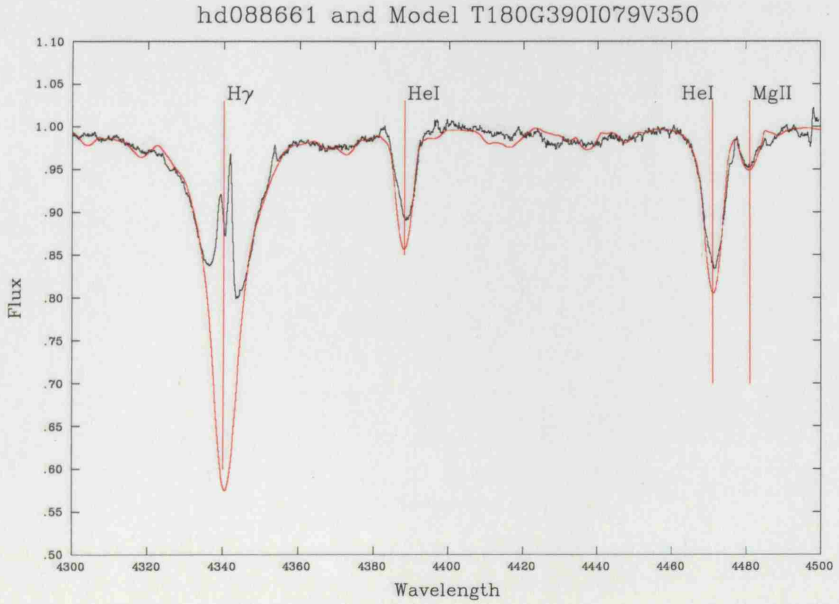

Figure A.46. Plot of the best–fit model versus observation for HD 88661. Observation = black line; Model = red line.

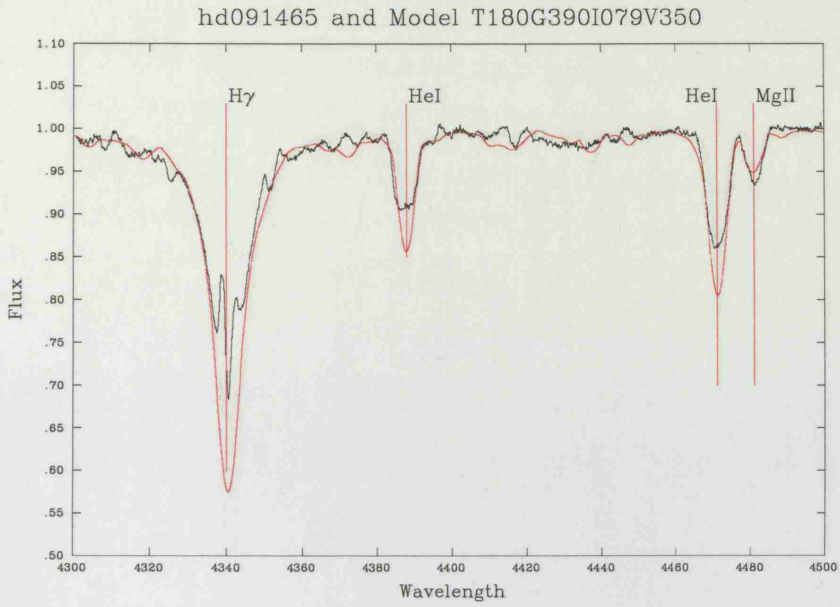

Figure A.47. Plot of the best–fit model versus observation for HD 91465. Observation = black line; Model = red line.

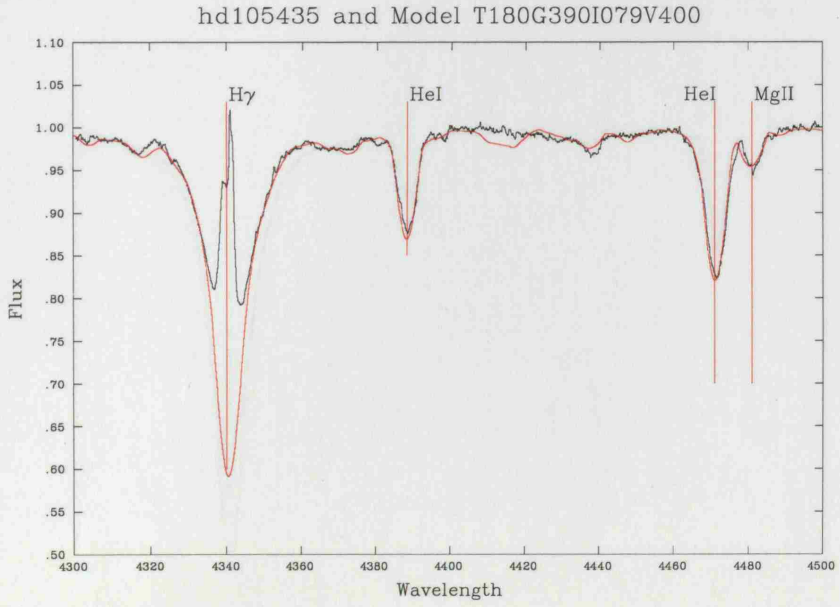

Figure A.48. Plot of the best–fit model versus observation for HD 105435. Observation = black line; Model = red line.

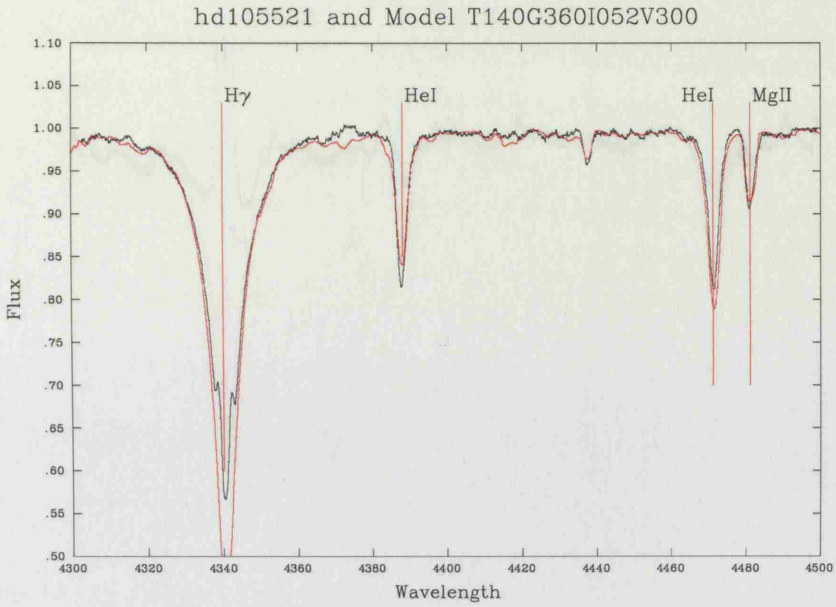

Figure A.49. Plot of the best–fit model versus observation for HD 105521. Observation = black line; Model = red line.

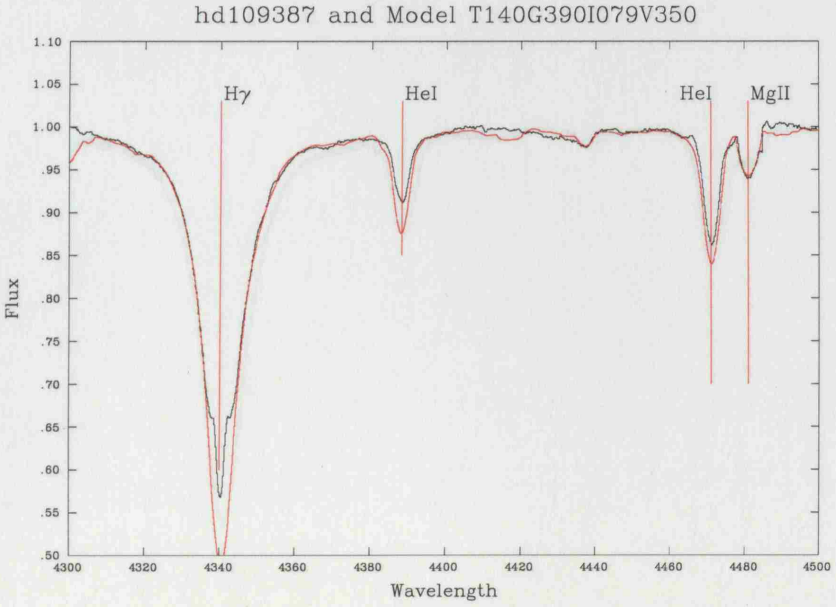

Figure A.50. Plot of the best–fit model versus observation for HD 109387. Observation = black line; Model = red line.

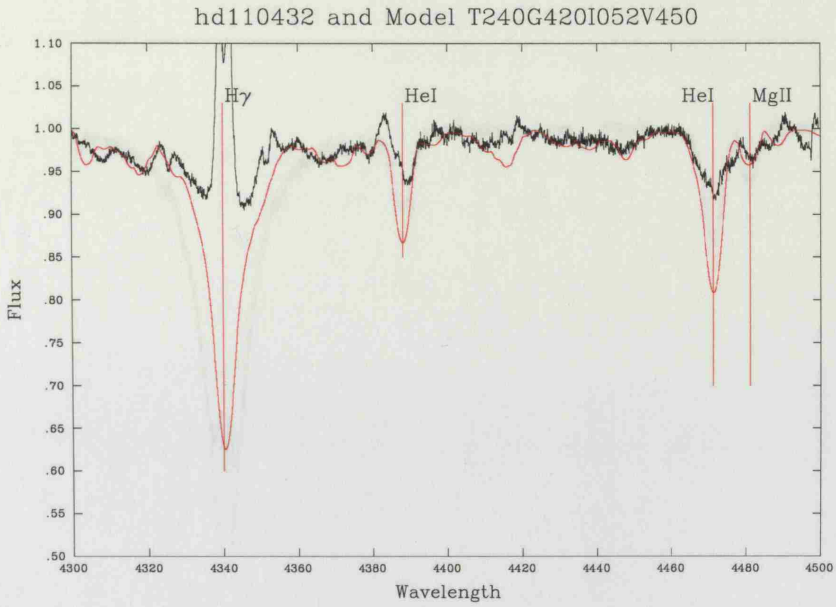

Figure A.51. Plot of the best–fit model versus observation for HD 110432. Observation = black line; Model = red line.

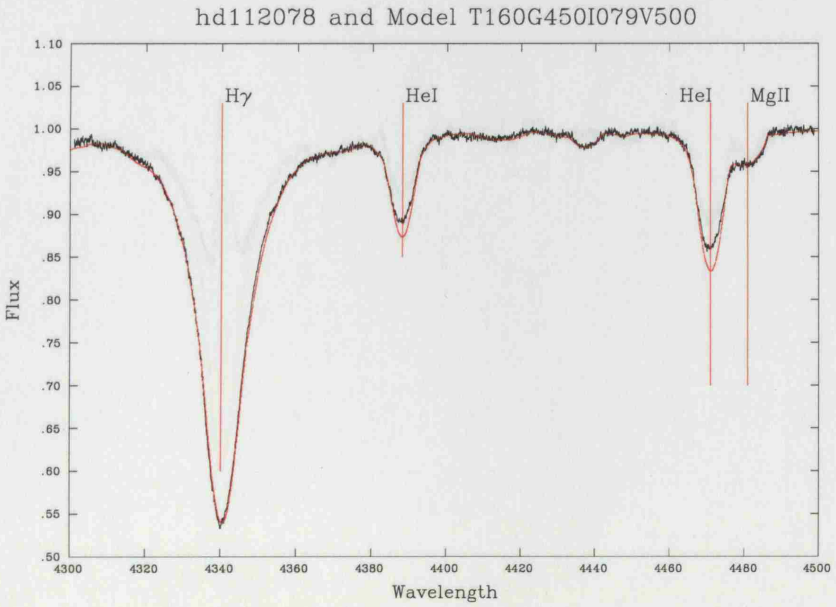

Figure A.52. Plot of the best–fit model versus observation for HD 112078. Observation = black line; Model = red line.

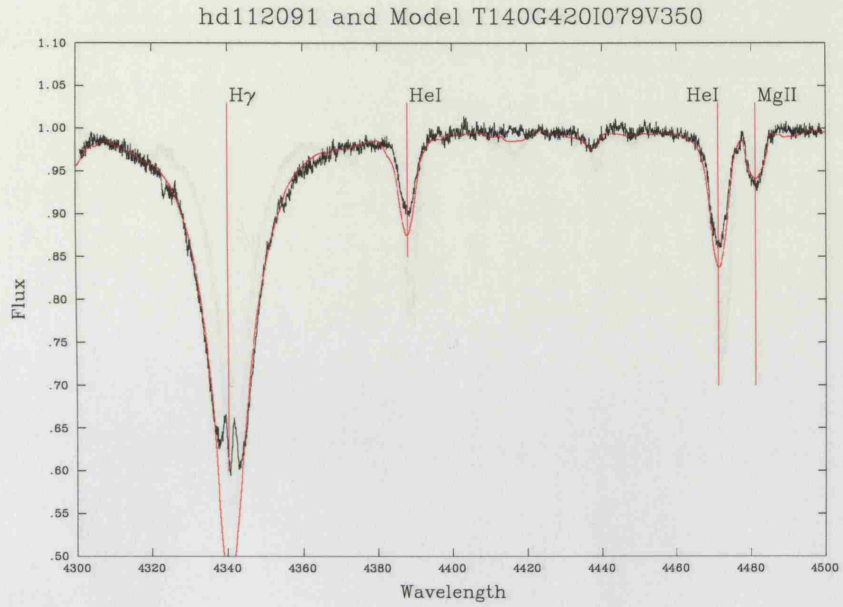

Figure A.53. Plot of the best–fit model versus observation for HD 112091. Observation = black line; Model = red line.

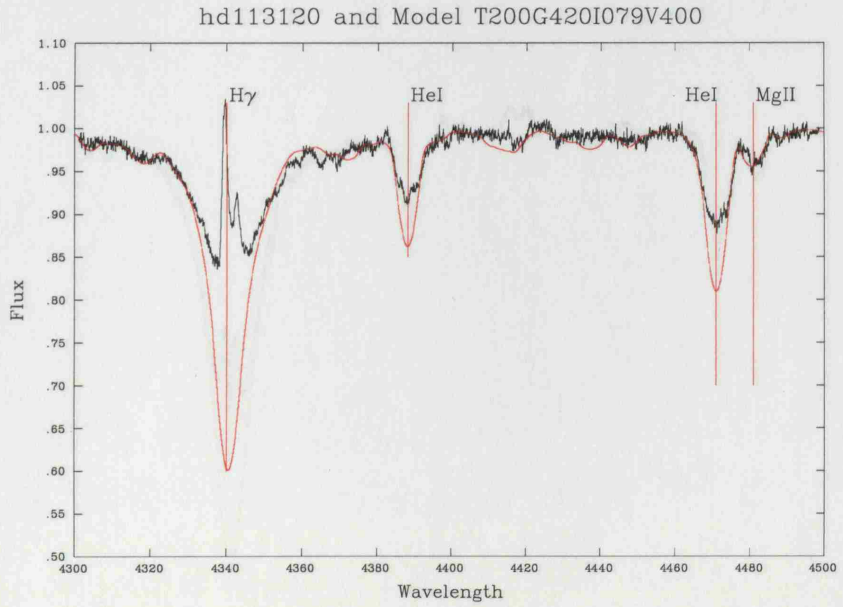

Figure A.54. Plot of the best–fit model versus observation for HD 113120. Observation = black line; Model = red line.

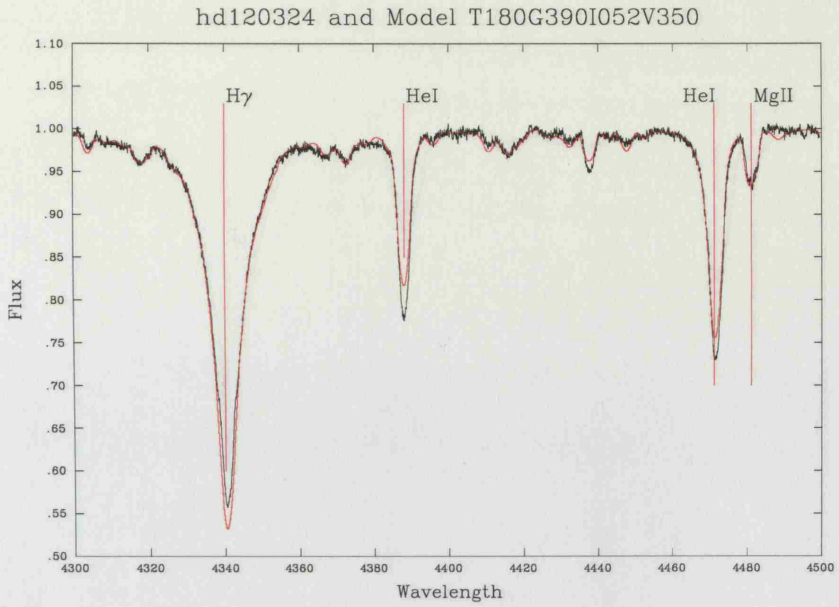

Figure A.55. Plot of the best–fit model versus observation for HD 120324. Observation = black line; Model = red line.

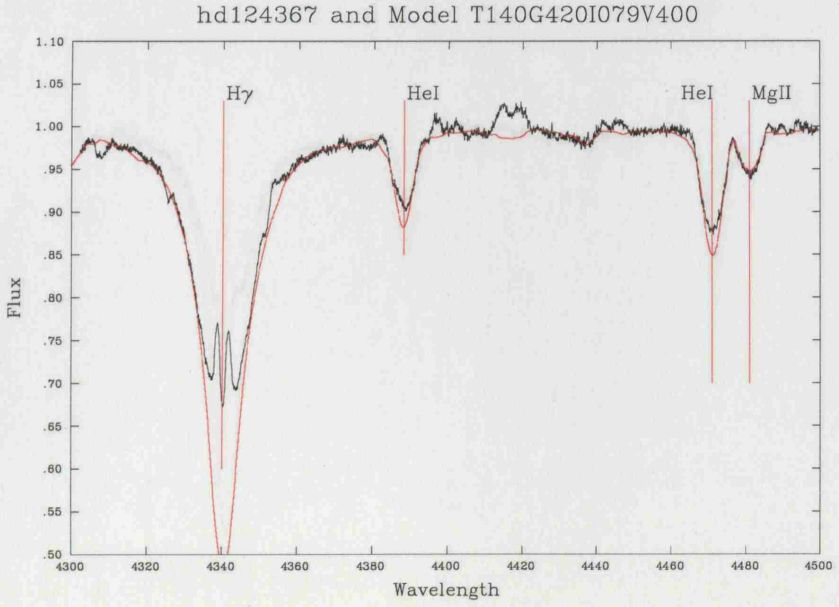

Figure A.56. Plot of the best–fit model versus observation for HD 124367. Observation = black line; Model = red line.

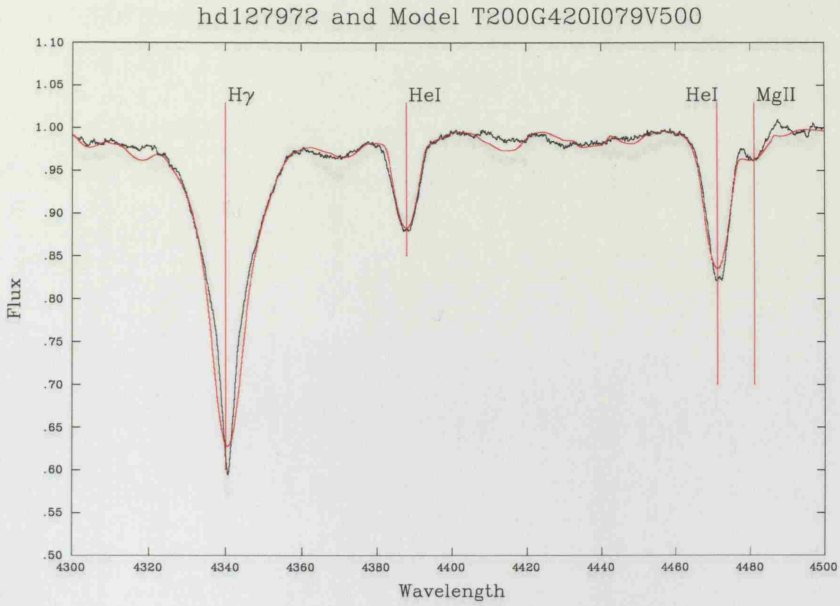

Figure A.57. Plot of the best–fit model versus observation for HD 127972. Observation = black line; Model = red line.

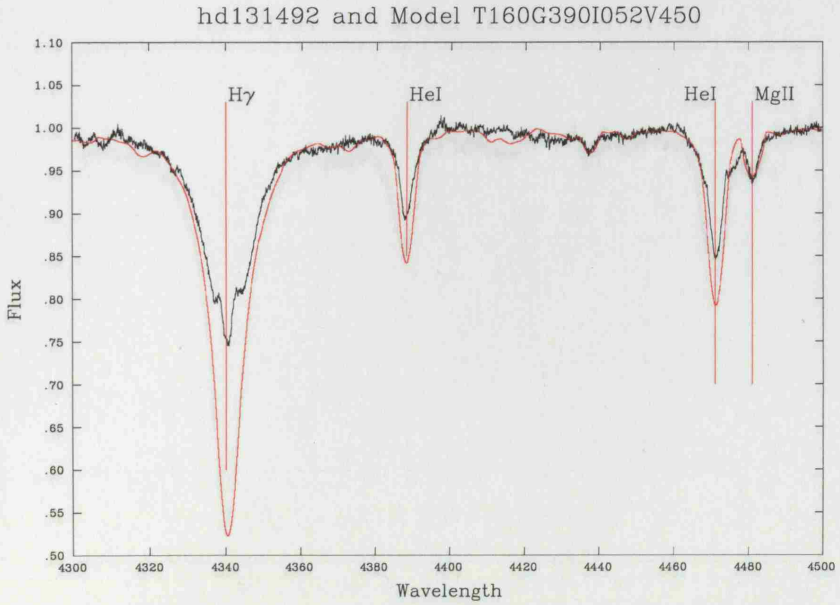

Figure A.58. Plot of the best–fit model versus observation for HD 131492. Observation = black line; Model = red line.

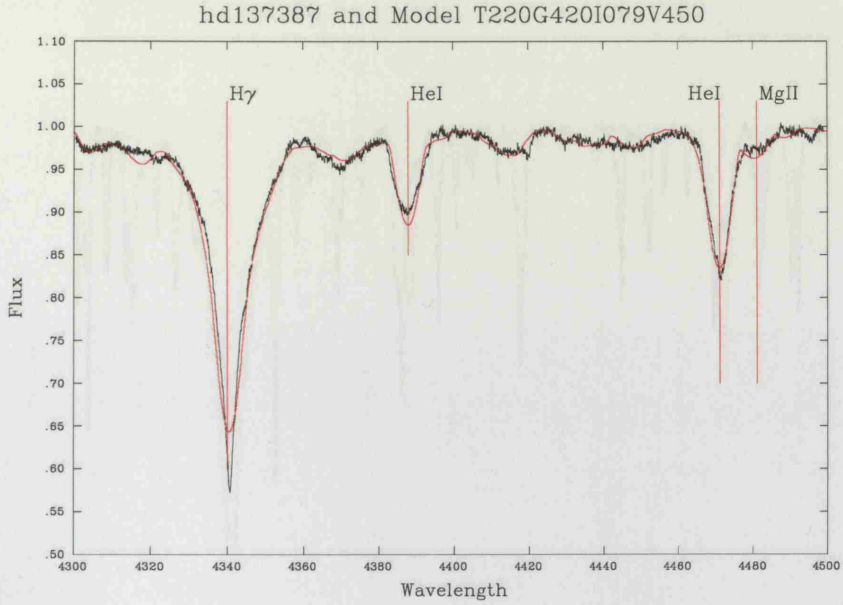

Figure A.59. Plot of the best–fit model versus observation for HD 137387. Observation = black line; Model = red line.

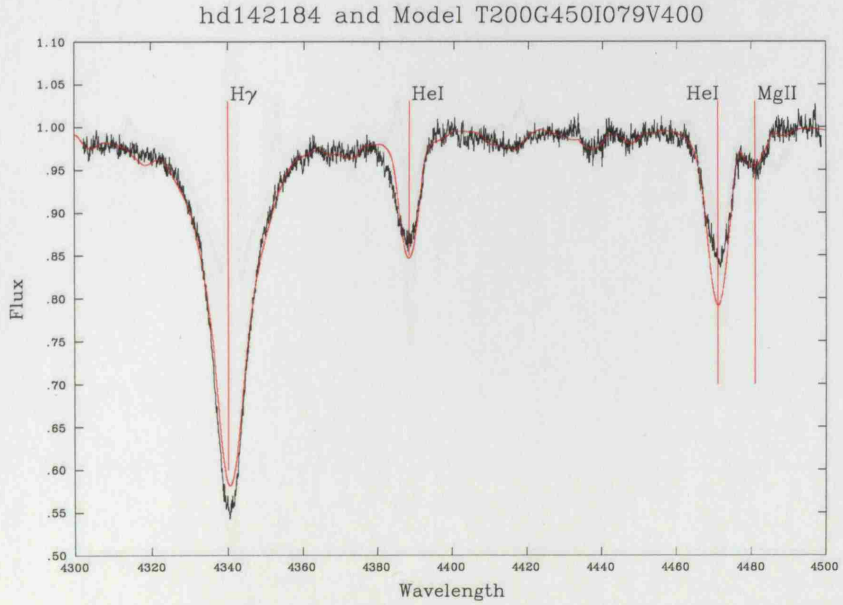

Figure A.60. Plot of the best–fit model versus observation for HD 142184. Observation = black line; Model = red line.

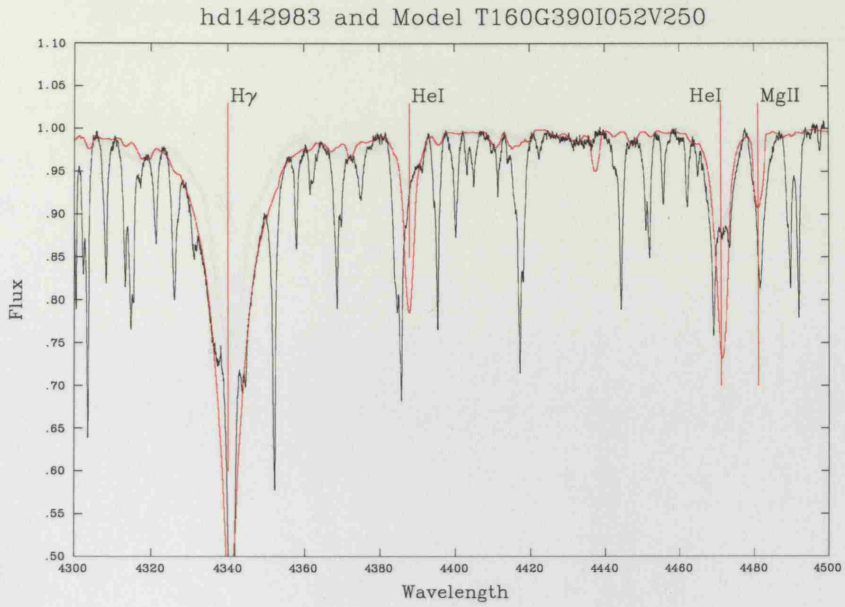

Figure A.61. Plot of the best–fit model versus observation for HD 142983. Observation = black line; Model = red line.

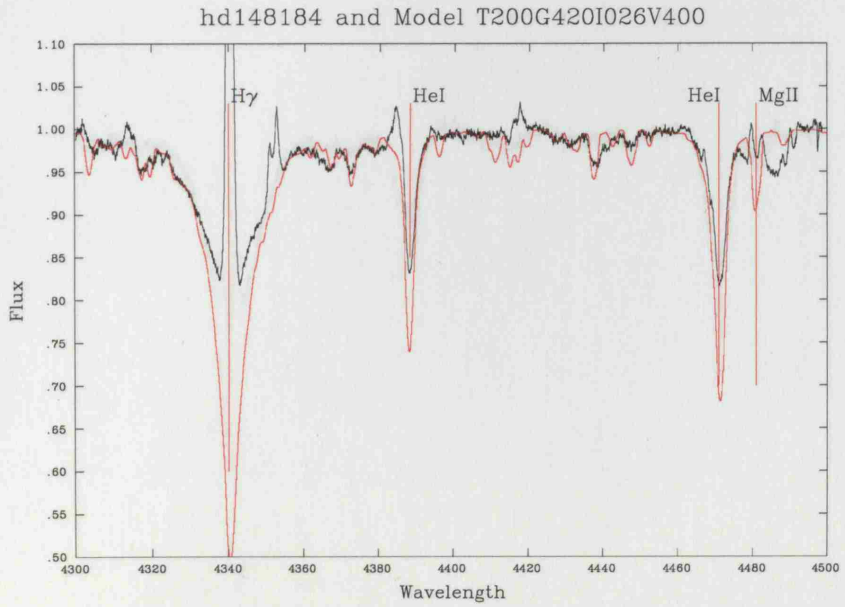

Figure A.62. Plot of the best–fit model versus observation for HD 148184. Observation = black line; Model = red line.

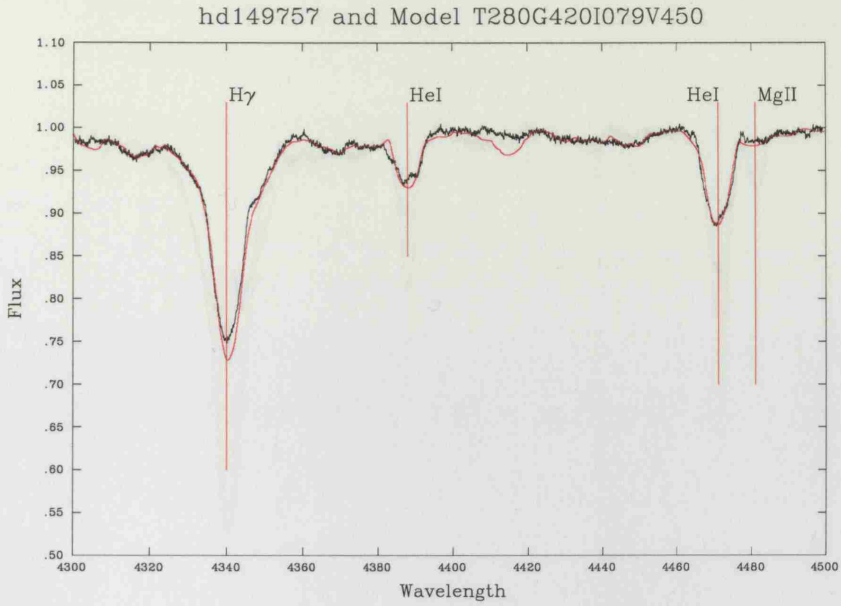

Figure A.63. Plot of the best–fit model versus observation for HD 149757. Observation = black line; Model = red line.

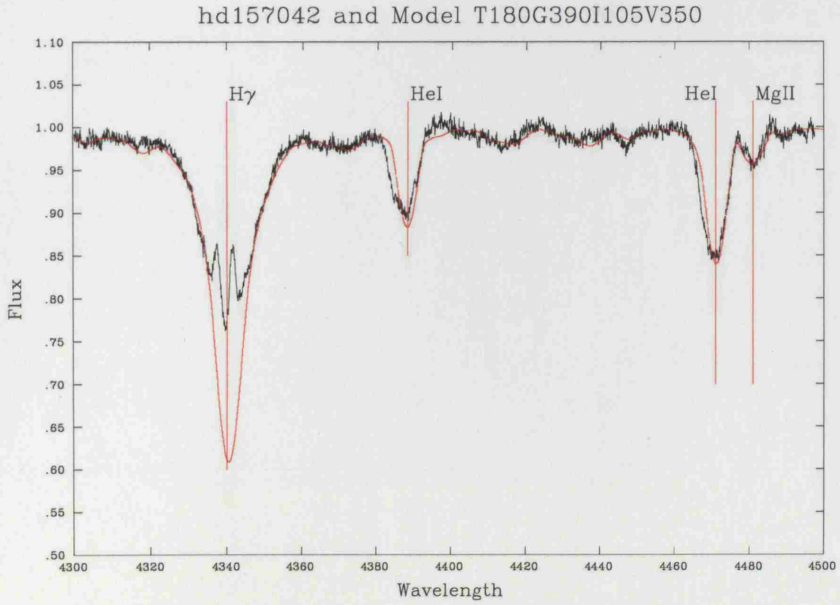

Figure A.64. Plot of the best–fit model versus observation for HD 157042. Observation = black line; Model = red line.

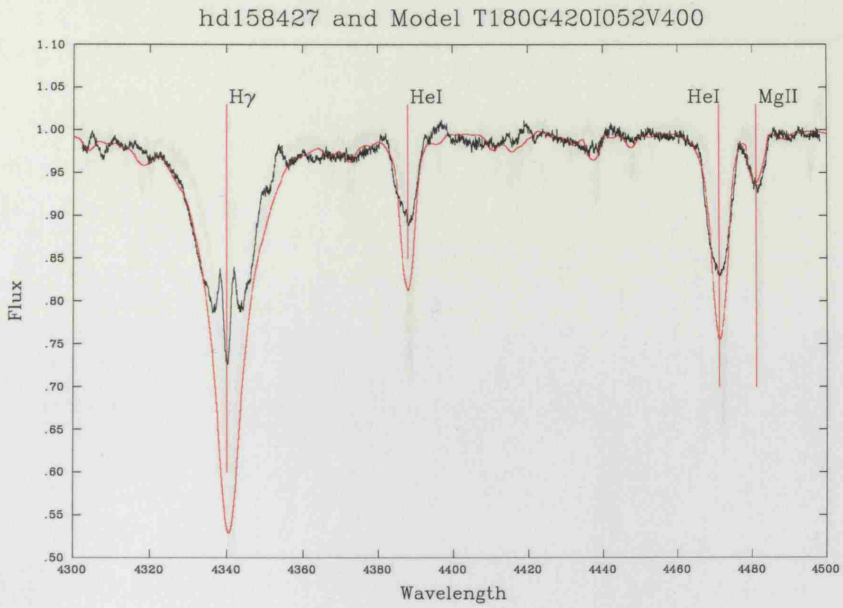

Figure A.65. Plot of the best–fit model versus observation for HD 158427. Observation = black line; Model = red line.

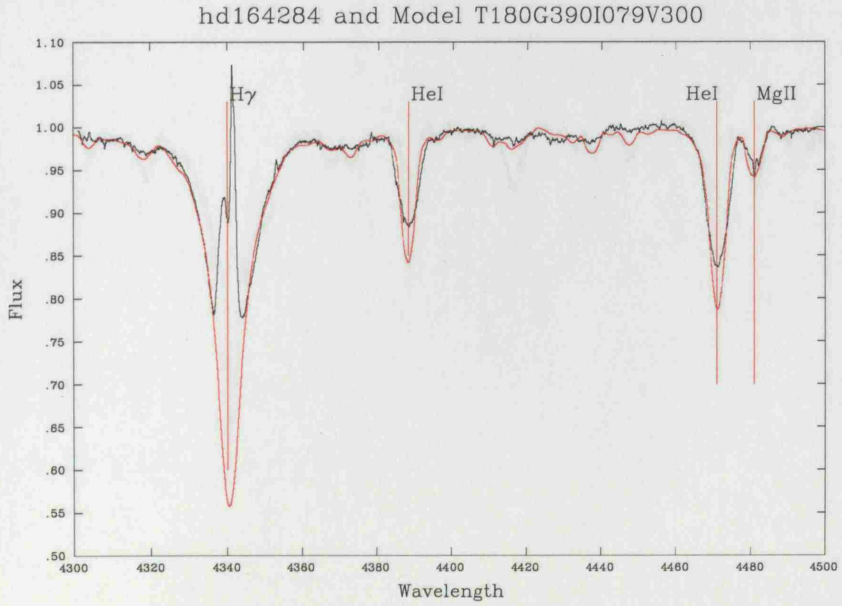

Figure A.66. Plot of the best–fit model versus observation for HD 164284. Observation = black line; Model = red line.

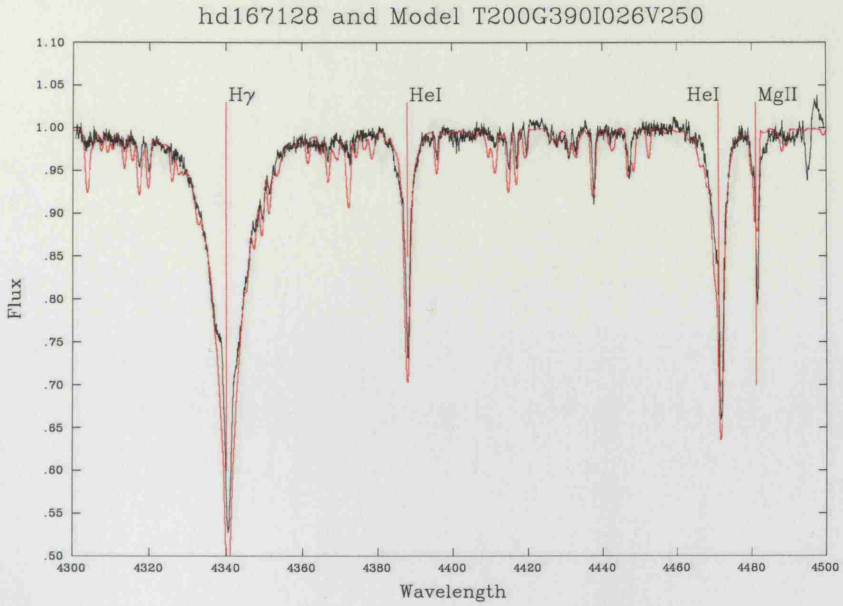

Figure A.67. Plot of the best–fit model versus observation for HD 167128. Observation = black line; Model = red line.

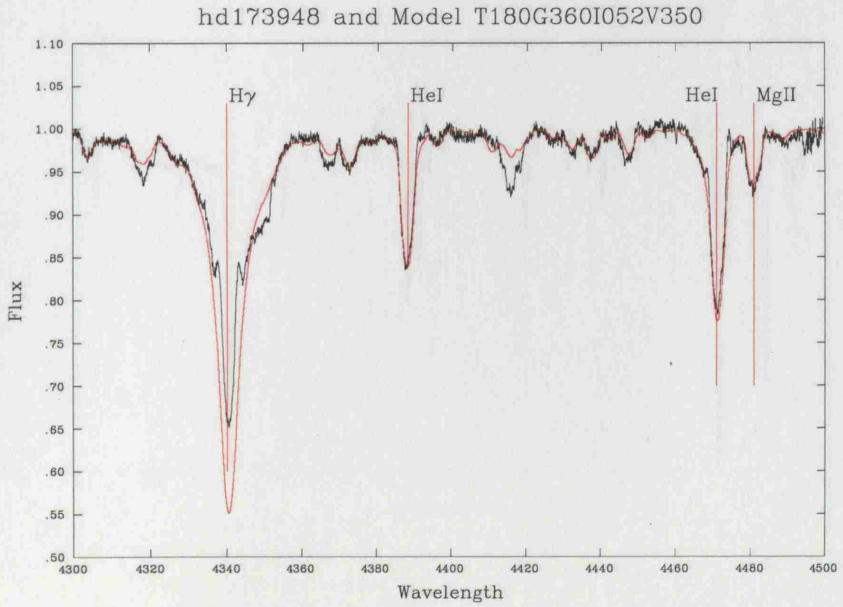

Figure A.68. Plot of the best–fit model versus observation for HD 173948. Observation = black line; Model = red line.

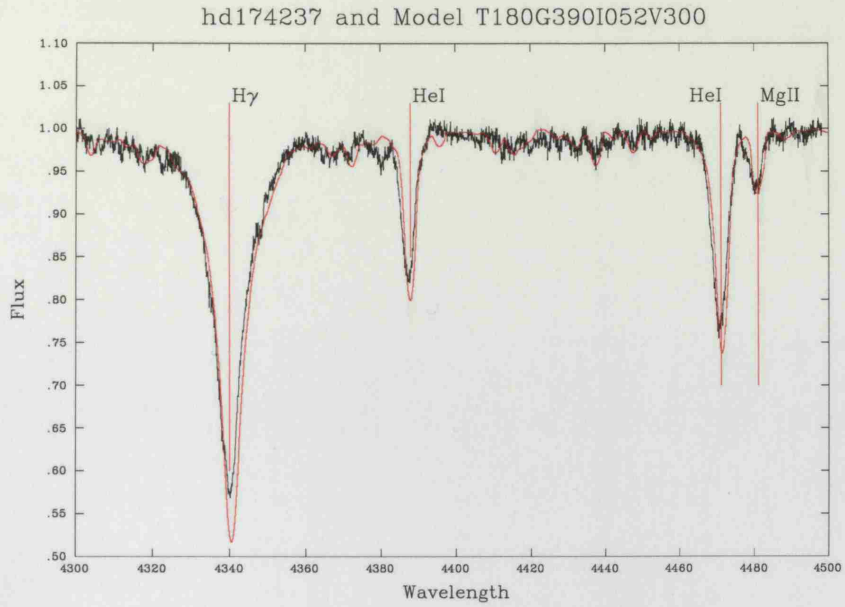

Figure A.69. Plot of the best–fit model versus observation for HD 174237. Observation = black line; Model = red line.

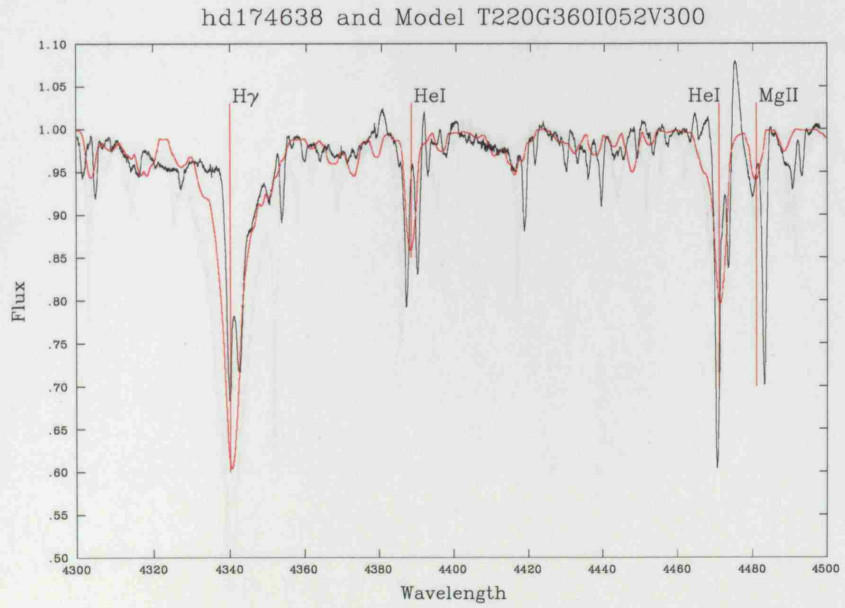

Figure A.70. Plot of the best–fit model versus observation for HD 174638. Observation = black line; Model = red line.

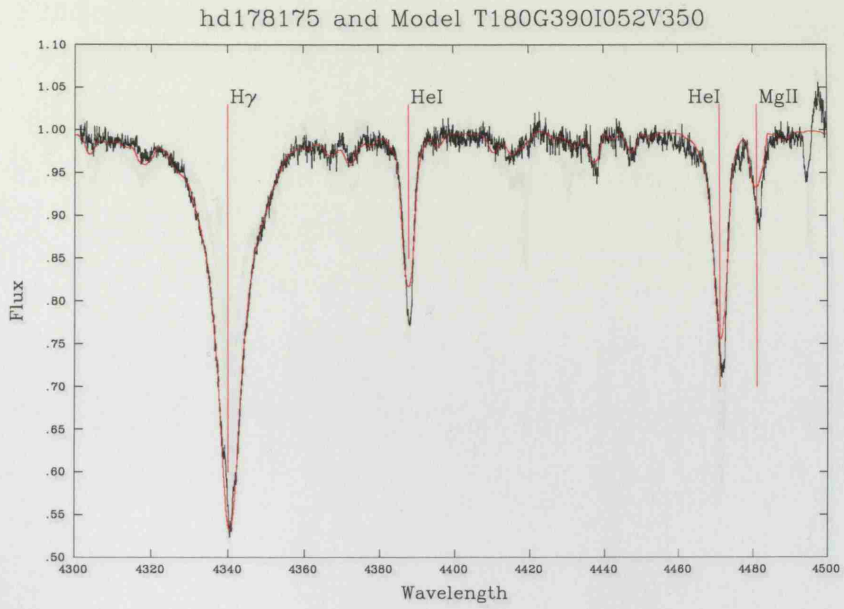

Figure A.71. Plot of the best–fit model versus observation for HD 178175. Observation = black line; Model = red line.

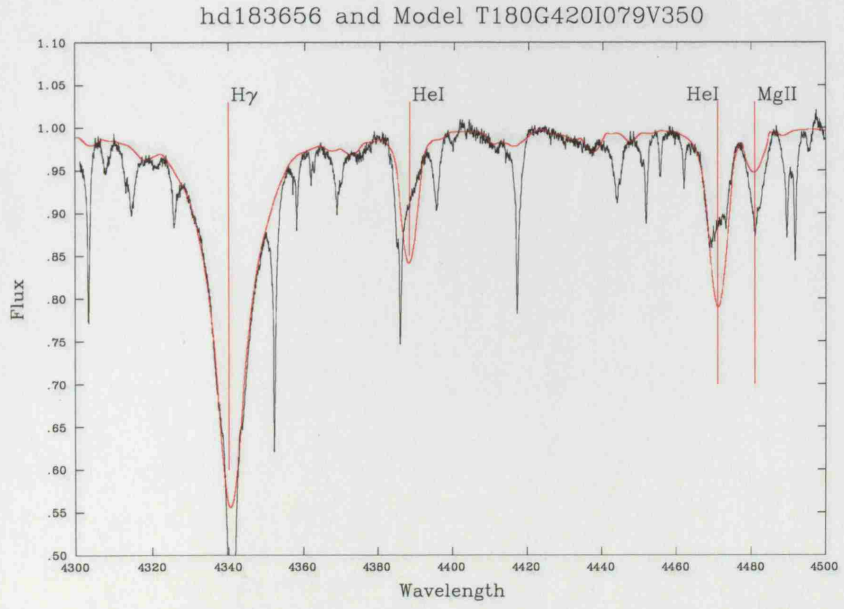

Figure A.72. Plot of the best–fit model versus observation for HD 183656. Observation = black line; Model = red line.

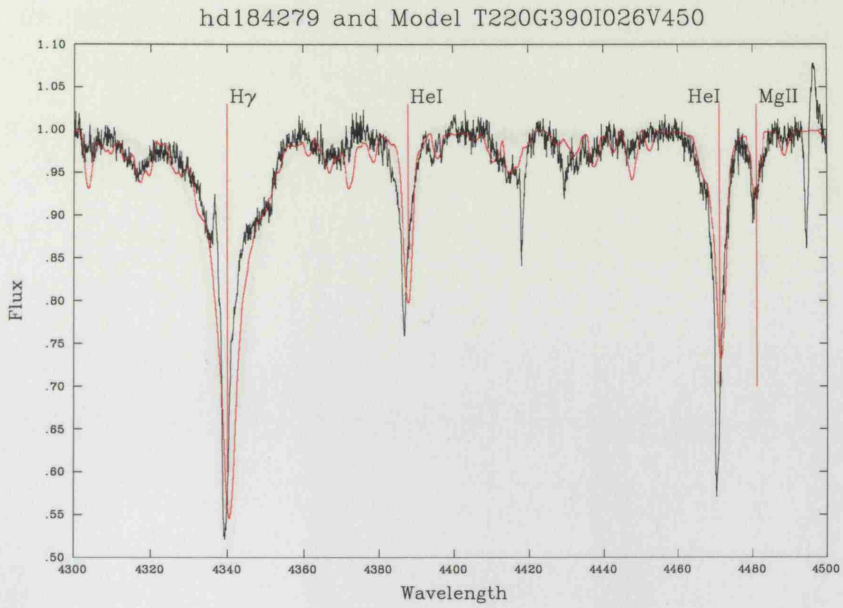

Figure A.73. Plot of the best–fit model versus observation for HD 184279. Observation = black line; Model = red line.

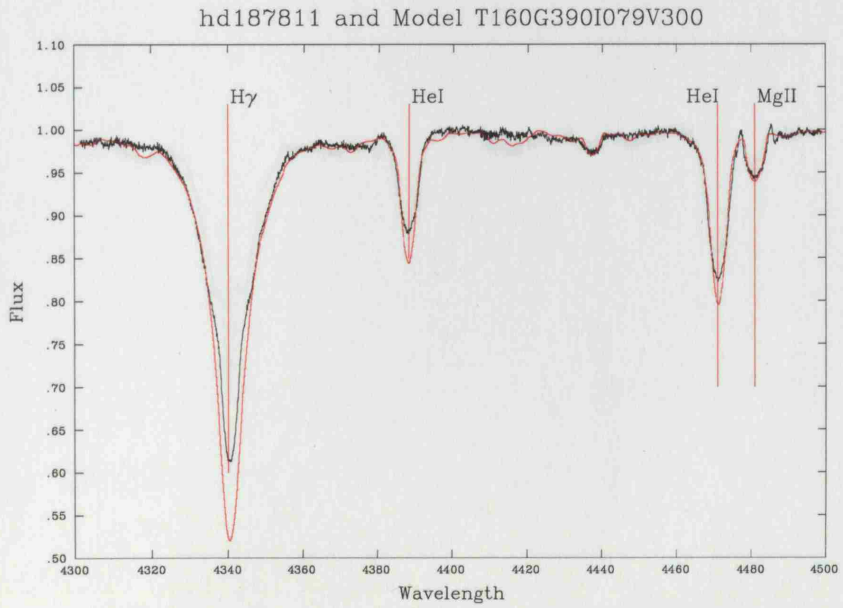

Figure A.74. Plot of the best–fit model versus observation for HD 187811. Observation = black line; Model = red line.

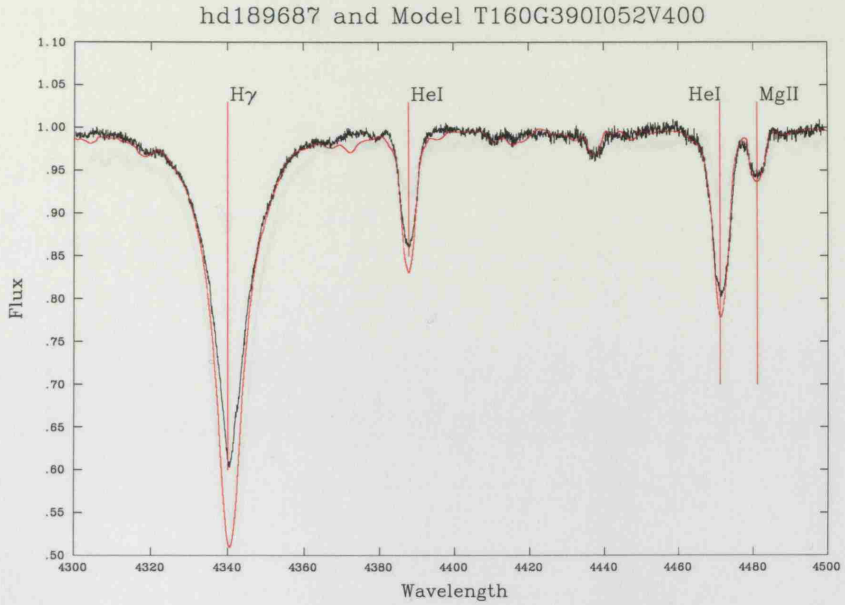

Figure A.75. Plot of the best–fit model versus observation for HD 189687. Observation = black line; Model = red line.

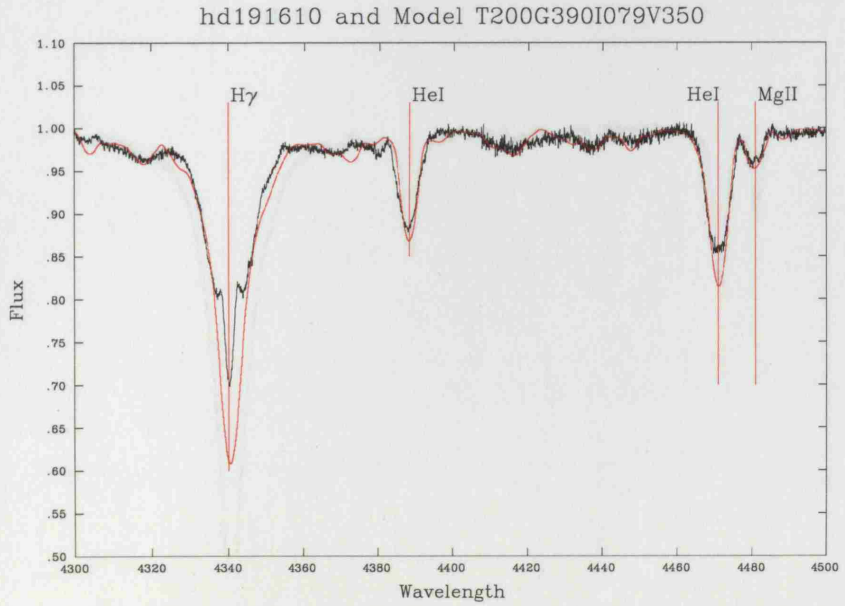

Figure A.76. Plot of the best–fit model versus observation for HD 191610. Observation = black line; Model = red line.

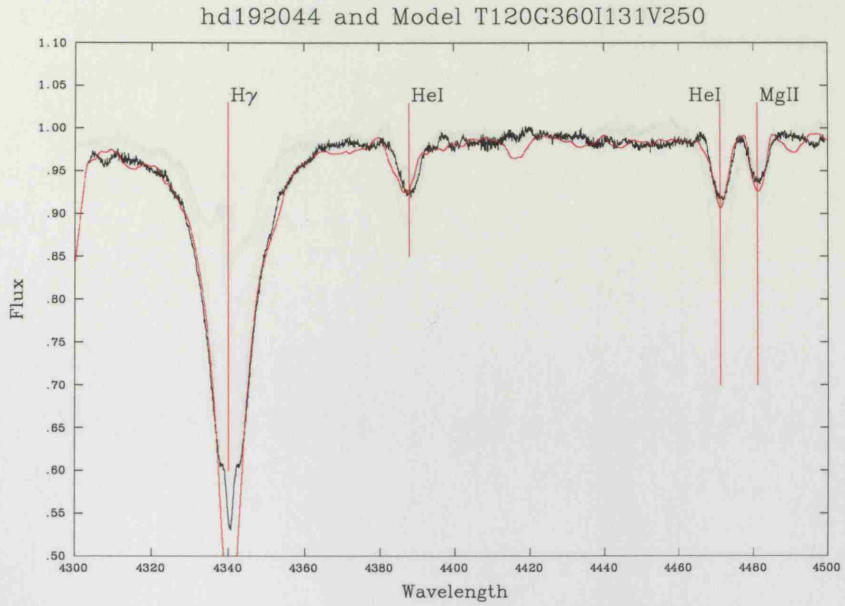

Figure A.77. Plot of the best–fit model versus observation for HD 192044. Observation = black line; Model = red line.

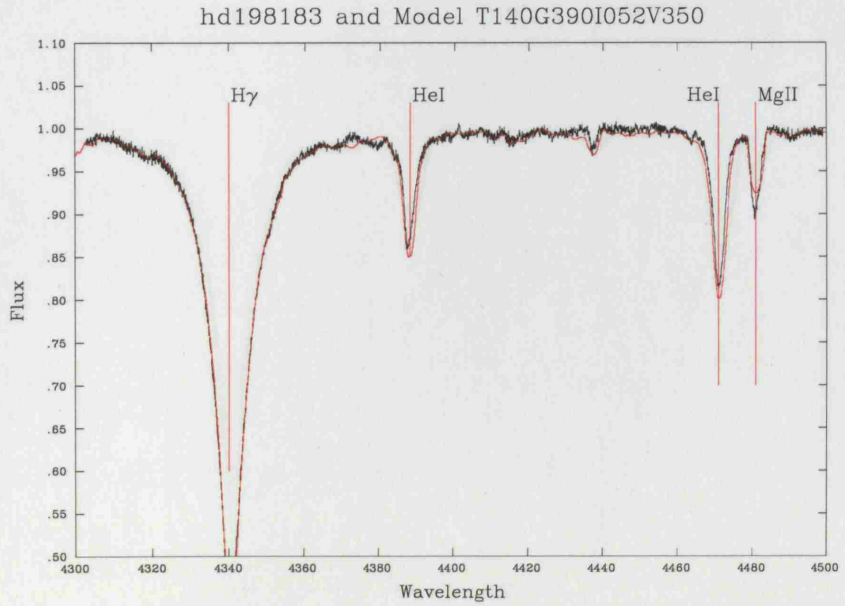

Figure A.78. Plot of the best–fit model versus observation for HD 198183. Observation = black line; Model = red line.

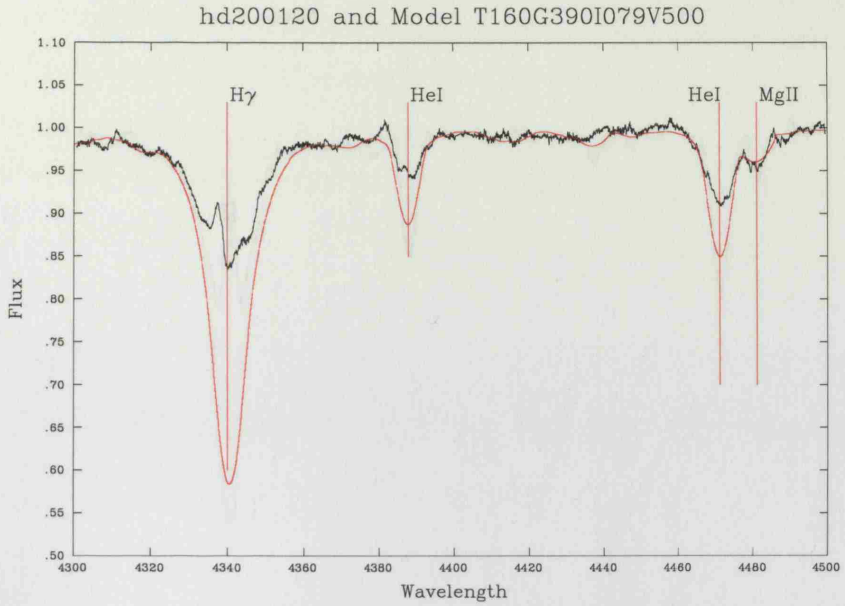

Figure A.79. Plot of the best–fit model versus observation for HD 200120. Observation = black line; Model = red line.

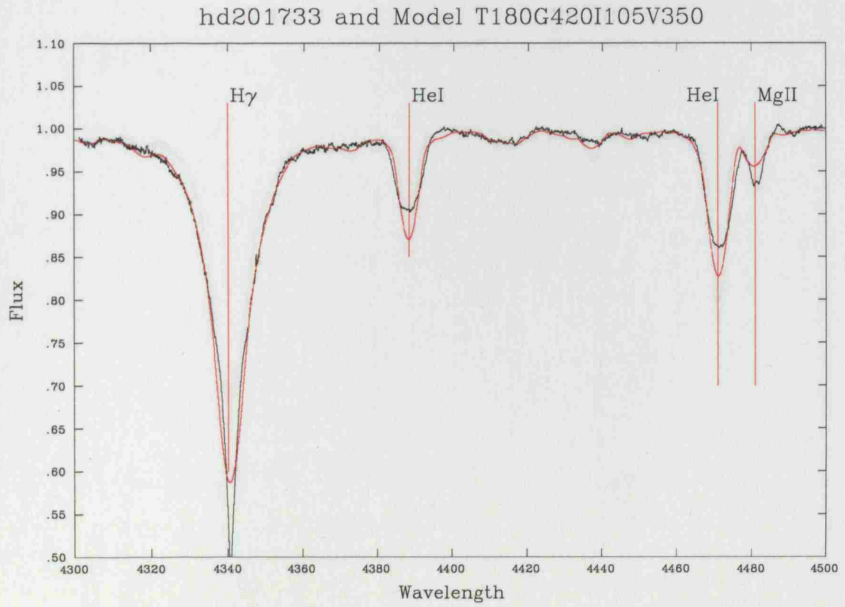

Figure A.80. Plot of the best–fit model versus observation for HD 201733. Observation = black line; Model = red line.

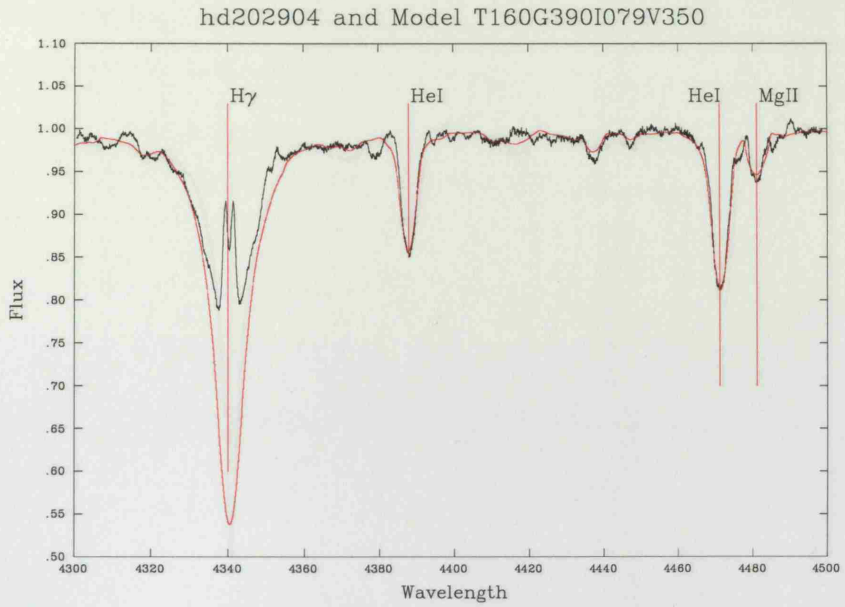

Figure A.81. Plot of the best–fit model versus observation for HD 202904. Observation = black line; Model = red line.

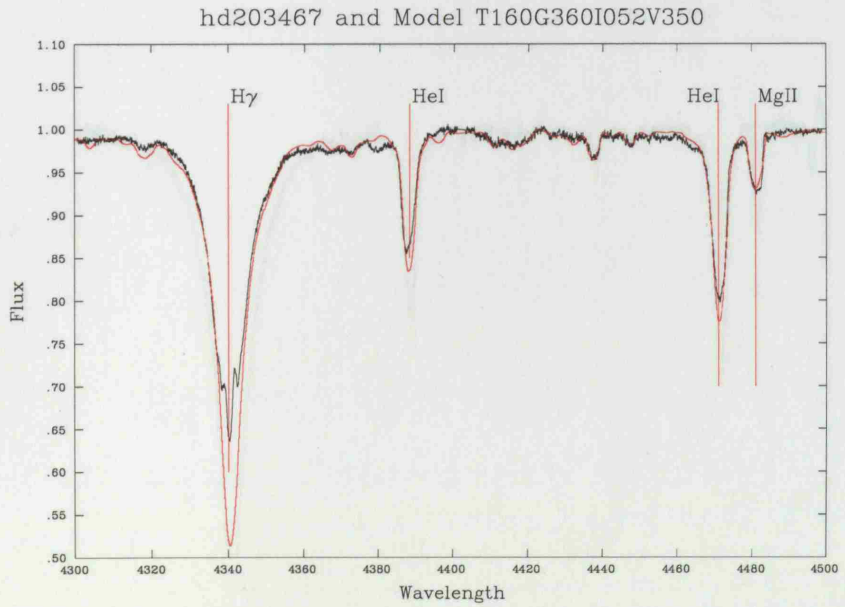

Figure A.82. Plot of the best–fit model versus observation for HD 203467. Observation = black line; Model = red line.

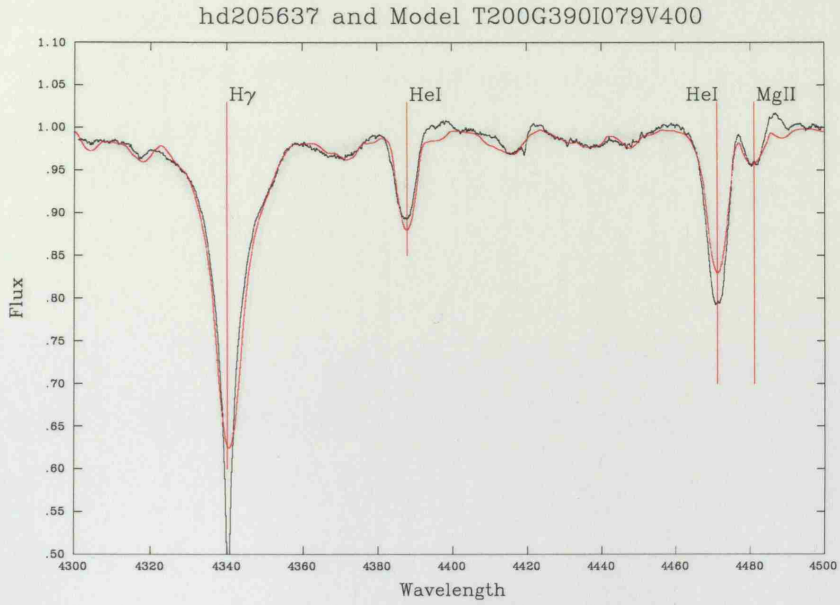

Figure A.83. Plot of the best–fit model versus observation for HD 205637. Observation = black line; Model = red line.

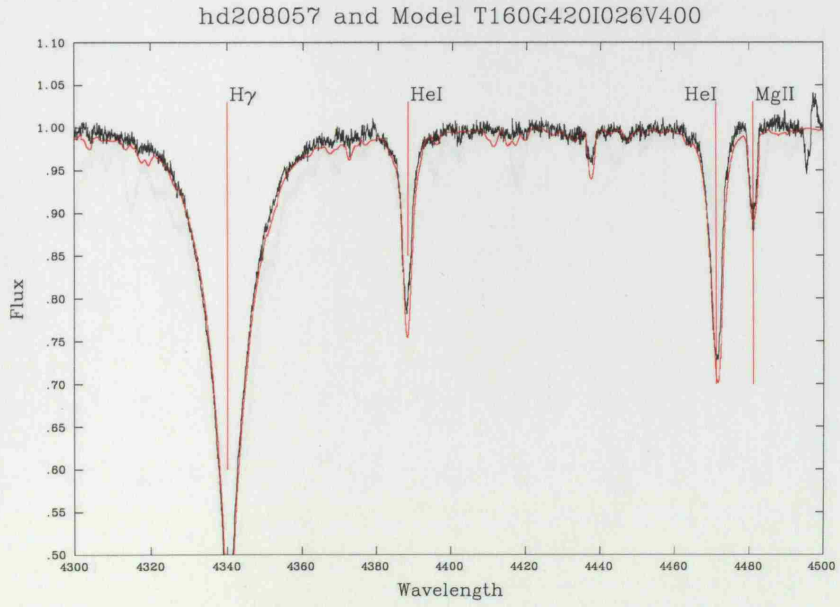

Figure A.84. Plot of the best–fit model versus observation for HD 208057. Observation = black line; Model = red line.

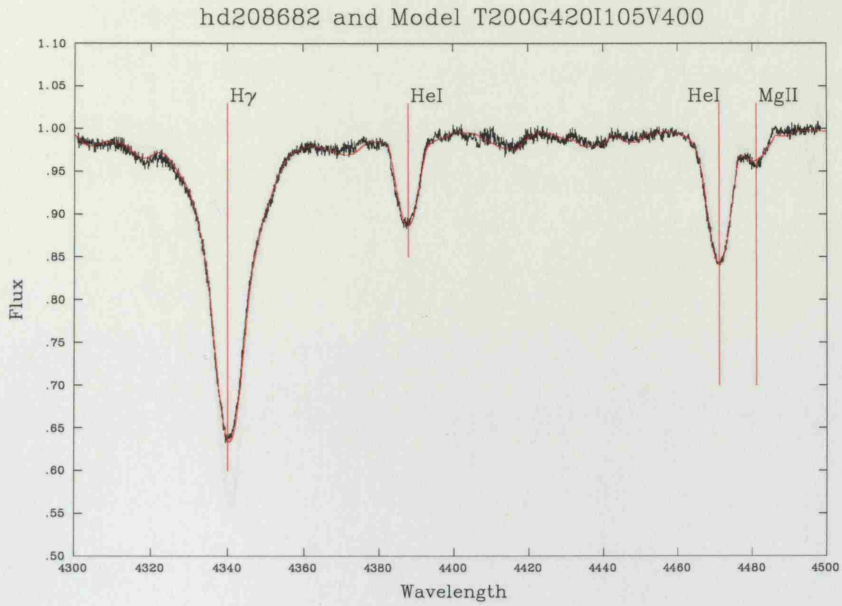

Figure A.85. Plot of the best–fit model versus observation for HD 208682. Observation = black line; Model = red line.

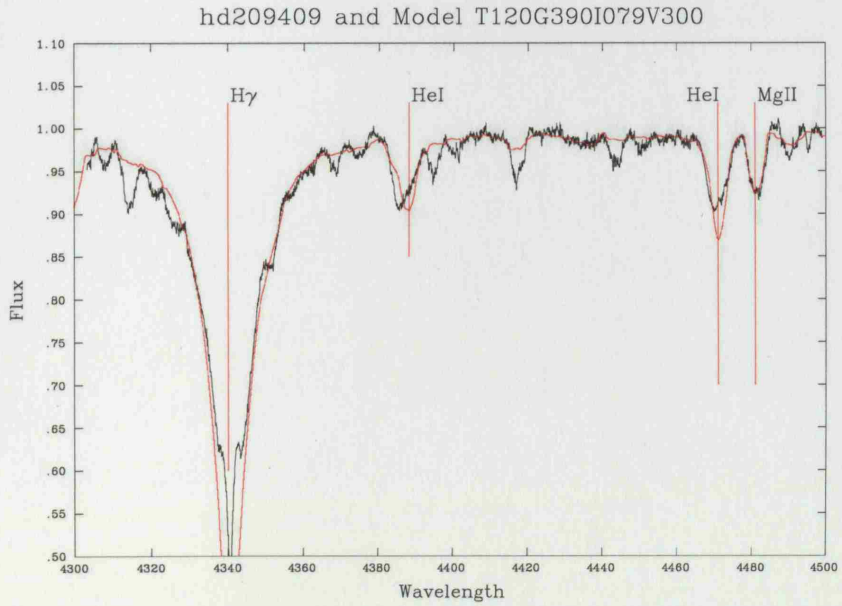

Figure A.86. Plot of the best–fit model versus observation for HD 209409. Observation = black line; Model = red line.

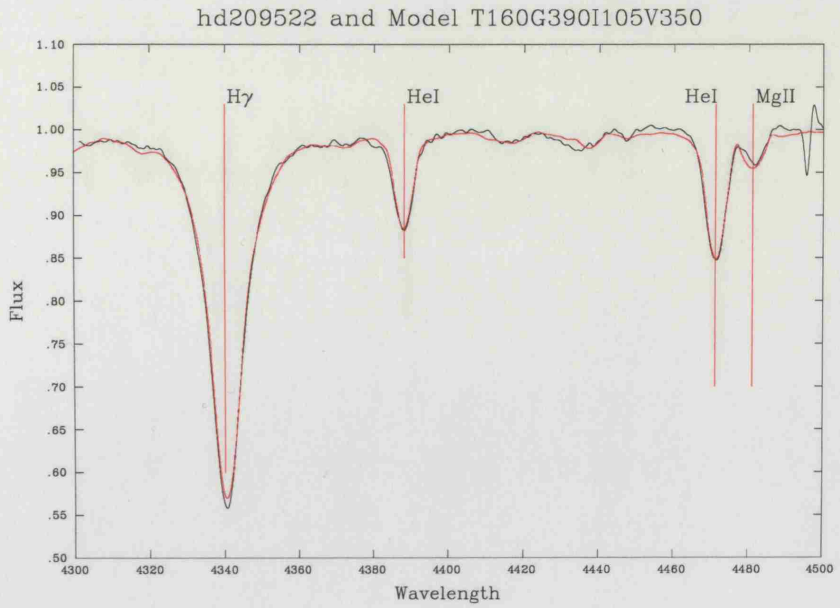

Figure A.87. Plot of the best–fit model versus observation for HD 209522. Observation = black line; Model = red line.

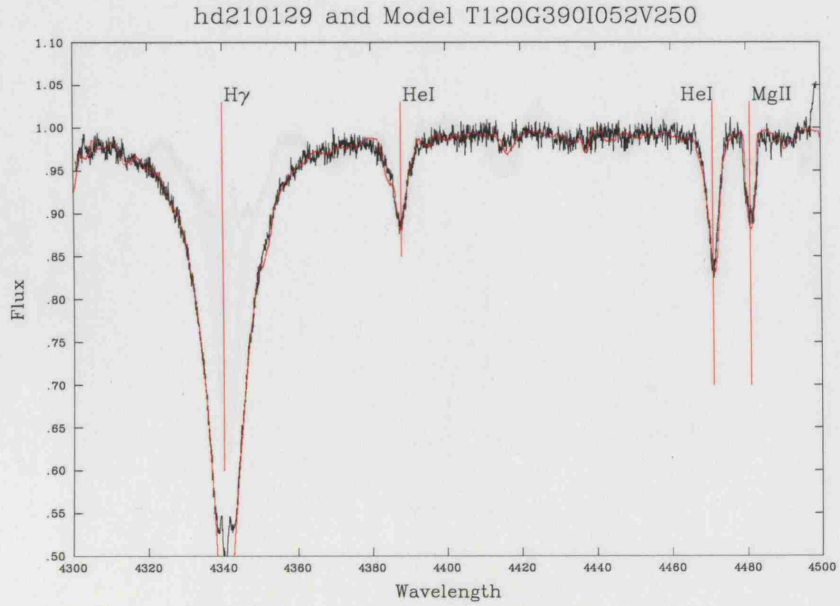

Figure A.88. Plot of the best–fit model versus observation for HD 210129. Observation = black line; Model = red line.

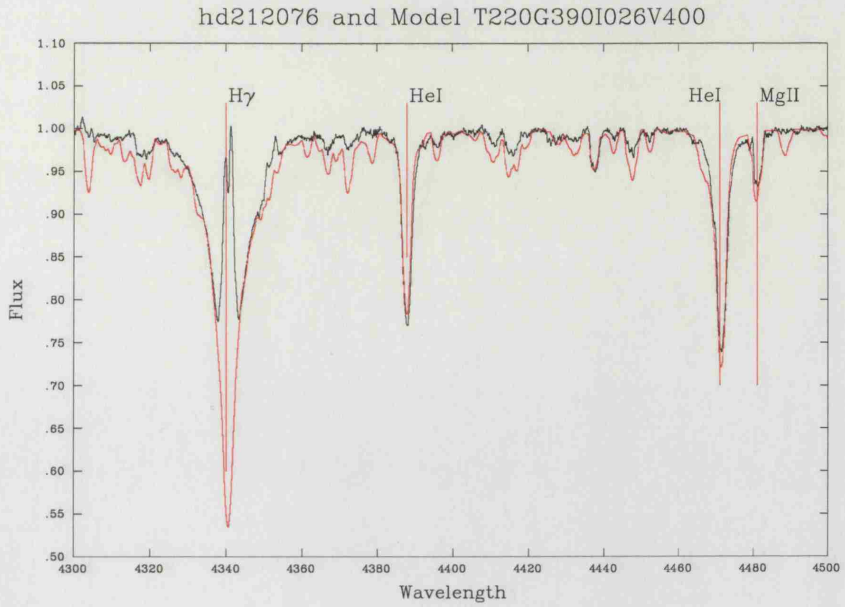

Figure A.89. Plot of the best–fit model versus observation for HD 212076. Observation = black line; Model = red line.

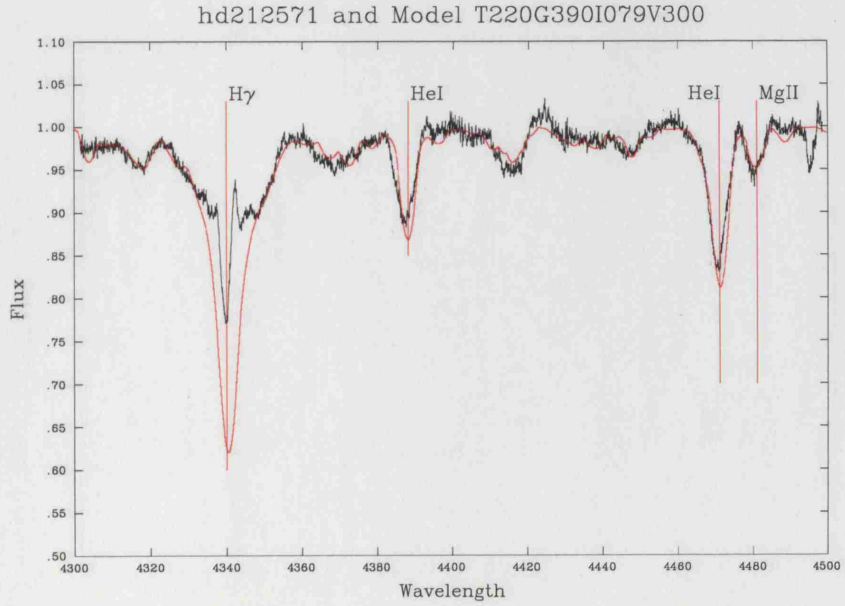

Figure A.90. Plot of the best–fit model versus observation for HD 212571. Observation = black line; Model = red line.

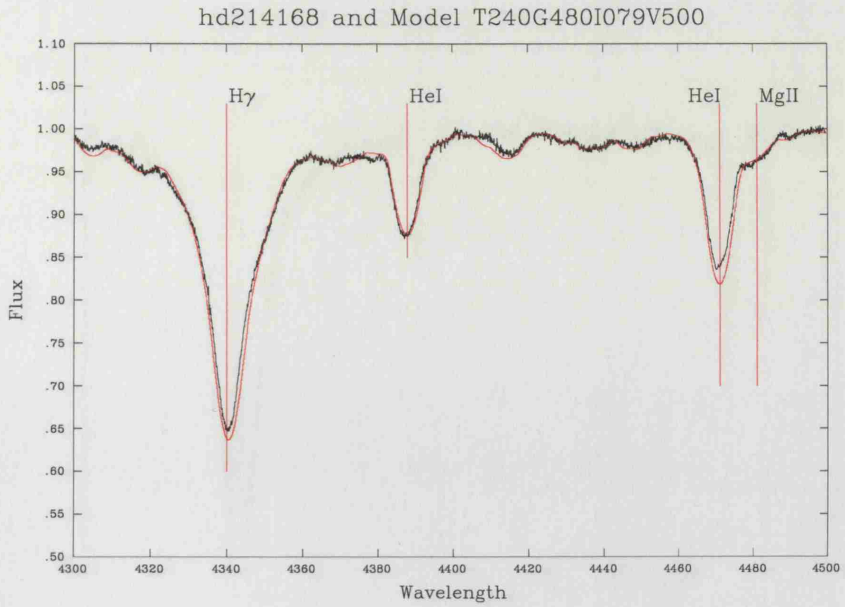

Figure A.91. Plot of the best–fit model versus observation for HD 214168. Observation = black line; Model = red line.

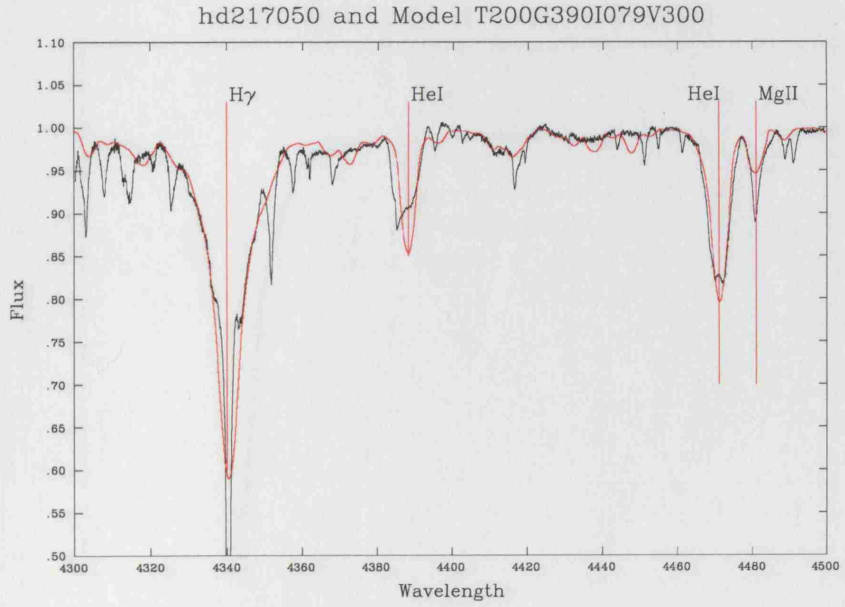

Figure A.92. Plot of the best–fit model versus observation for HD 217050. Observation = black line; Model = red line.

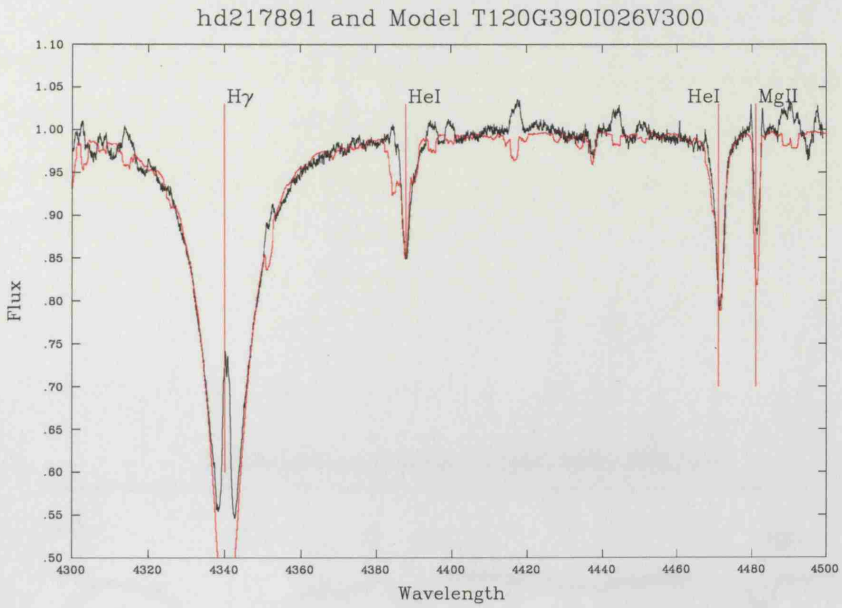

Figure A.93. Plot of the best–fit model versus observation for HD 217891. Observation = black line; Model = red line.

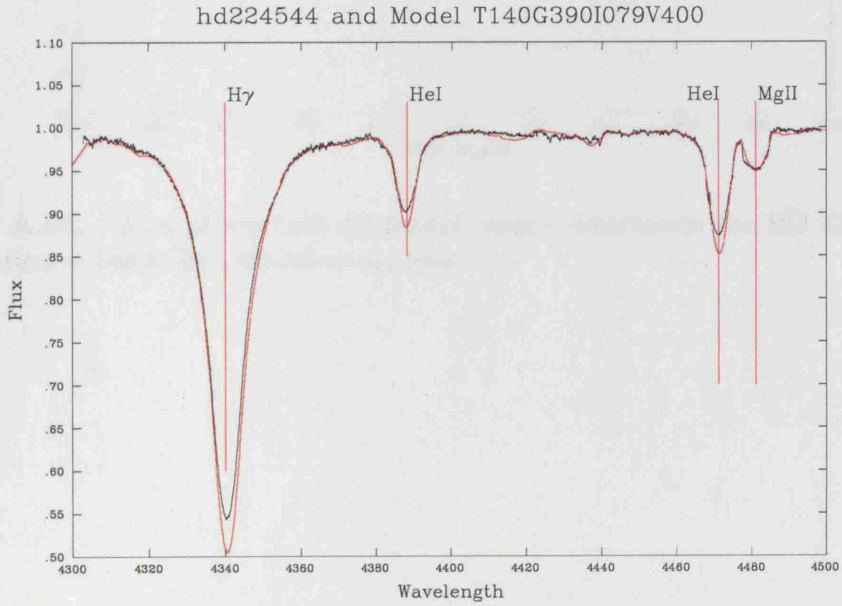

Figure A.94. Plot of the best–fit model versus observation for HD 224544. Observation = black line; Model = red line.

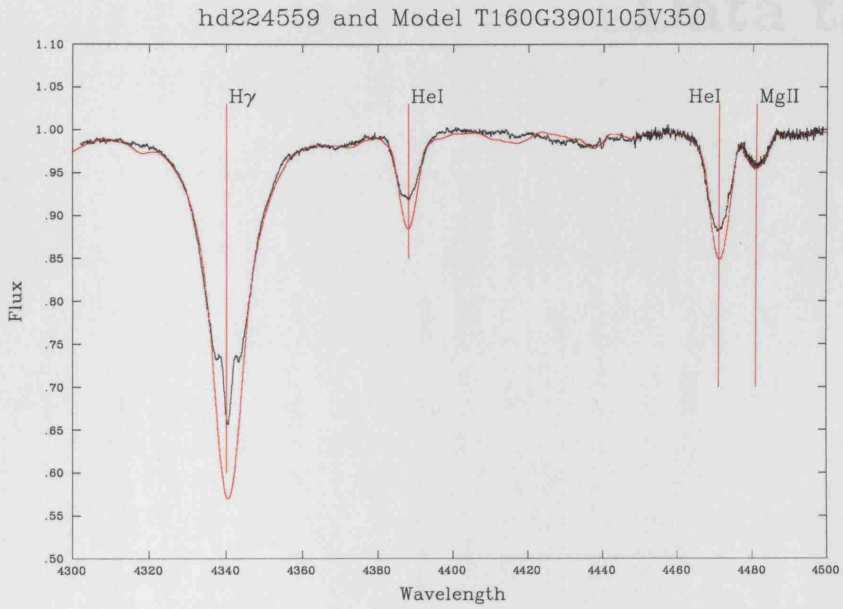

Figure A.95. Plot of the best–fit model versus observation for HD 224559. Observation = black line; Model = red line.

Appendix B

Data table

Table B.1:

Star HD..	Chauville et al (2001) $m(v)$	$T_{\rm eff}$ (kK)	log$g$	Spectral type	Model fit data Best–fit model	$T_{\rm app}$	$T_{\rm pole}$ (kK)	$T_{\rm eq}$	log$g_{\rm pole}$	log$g_{\rm eq}$	$R_{\rm pole}$ $(R_\odot)$	$R_{\rm eq}$	Mass $(M_\odot)$	$v\sin i$ (km/s)	$v_{\rm radial}$	$M(V)$	Hipparcos low	Hi.
4180	4.54	13.74	3.43	B5-6IIIe[a]	T140G390I052V350	14.83	17.32	8.85	3.90	2.73	3.68	5.27	3.93	174	0	-2.2	-2	-2.5
5394	2.47	33.04	3.88	O9Ve[a]	T260G390I079V450	26.86	32.17	16.44	3.90	2.73	6.09	8.71	10.75	320	0	-4.3	-4.3	-4.6
6811	4.25	12.56	4.01	B7Ve[b]	T120G360I026V300	12.86	14.84	7.59	3.60	2.43	5.40	7.72	4.24	77	0	-2.9	-2.2	-2.9
10144	0.46	19.01	4.00	B3Vpe[b]	T160G360I105V300	15.78	19.79	10.11	3.60	2.43	5.40	7.72	4.24	260	2	-2.8	-2.6	-2.8
10516	4.07	28.05	3.82	B0.5IVe[a]	T220G390I079V350	22.73	27.22	13.91	3.90	2.73	3.68	5.27	3.93	249	0	-2.8	-2.7	-3
11606	7.02	22.18	3.98	B2Vne[b]	T200G420I157V350	18.24	24.75	12.64	4.20	3.03	1.85	2.64	1.97	350	0	-0.6	0	-1
19243	6.62	26.67	3.95	B1Ve[b]	T280G390I052V300	29.67	34.65	17.70	3.90	2.73	2.71	3.87	2.12	149	0	-2.9	-2.4	-5.3
20336	4.84	22.18	3.98	B2Ve[a]	T180G420I079V450	18.59	22.27	11.38	4.20	3.03	3.05	4.36	5.39	320	0	-2	-2	-2.6
22192	4.23	16.22	3.63	B4III-IVe[a]	T160G390I079V350	16.53	19.79	10.11	3.90	2.73	3.68	5.27	3.93	249	0	-2.2	-1.9	-2.2
22780	5.57	12.56	4.01	B7Vne[b]	T120G420I079V450	12.39	14.84	7.59	4.20	3.03	3.05	4.36	5.39	320	10	-1.3	-1.3	-1.7
23302	3.70	13.03	3.41	B6IIIe[b]	T120G390I052V350	12.71	14.84	7.59	3.90	2.73	3.68	5.27	3.93	174	0	-1.9	-1.7	-1.9
23480	4.18	13.03	3.83	B6IVe[a]	T120G360I105V250	11.83	14.84	7.59	3.60	2.43	3.75	5.36	2.04	217	20	-1.4	-1.1	-1.4
24534	6.10	33.19	3.96	O9IVe[a]	T300G420I157V400	27.36	37.12	18.97	4.20	3.03	2.41	3.45	3.36	400	0	-2	-1.4	-2.9
25940	4.04	16.37	3.81	B4IVe[a]	T140G360I105V250	13.81	17.32	8.85	3.60	2.43	3.75	5.36	2.04	217	0	-1.8	-1.8	-2
28497	5.60	24.43	3.97	B1.5Vne[a]	T180G420I079V500	18.59	22.27	11.38	4.20	3.03	3.77	5.39	8.21	355	0	-2.5	-2.5	-3.3
30076	5.90	24.43	3.97	B1.5Ve[a]	T180G390I052V500	19.07	22.27	11.38	3.90	2.73	7.52	10.75	16.38	248	0	-4.2	-3.7	-12.9
32343	5.08	16.94	4.01	B4Ve[a]	T140G390I026V300	15.01	17.32	8.85	3.90	2.73	2.71	3.87	2.12	77	0	-1.7	-1.3	-1.8
33328	4.27	21.33	3.70	B2III-IVne[a]	T200G420I079V500	20.66	24.75	12.64	4.20	3.03	3.77	5.39	8.21	355	10	-2.7	-2.7	-3
35411	3.36	26.67	3.95	B1V+B2e[b]	T180G360I026V350	19.29	22.27	11.38	3.60	2.43	7.35	10.51	7.85	90	0	-4.3	-3.5	-5
35439	4.95	23.55	3.72	B1.5III-IVpe[a]	T200G390I079V350	20.66	24.75	12.64	3.90	2.73	3.68	5.27	3.93	249	20	-2.7	-2.1	-3.4

Where: * indicates a spectrum with emission; [a] indicates BCD classified; [b] indicates MK classified.

cont. on next page

cont. from previous page

Star HD..	Chauville et al (2001) $m(v)$	$T_{\rm eff}$ (kK)	log$g$	Spectral type	Model fit data Best–fit model	$T_{\rm app}$	$T_{\rm pole}$ (kK)	$T_{\rm eq}$	log$g_{\rm pole}$	log$g_{\rm eq}$	$R_{\rm pole}$ $(R_\odot)$	$R_{\rm eq}$	Mass $(M_\odot)$	$v$sin$i$ (km/s)	Radial v	$M(V)$	Hipparcos low	Hi.
36576	5.69	26.06	3.82	B1IVe[a]	T200G390I079V350	20.66	24.75	12.64	3.90	2.73	3.68	5.27	3.93	249	30	-2.7	-2.6	-3.3
37202	3.00	21.09	3.57	B2IIIpe[a]	T200G390I052V350	21.19	24.75	12.64	3.90	2.73	3.68	5.27	3.93	174	0	-2.9	-2.5	-3.2
37490	4.57	19.5	3.55	B2-3IIIe[a]	T140G330I052V250	14.83	17.32	8.85	3.30	2.13	7.48	10.70	4.08	124	0	-3.7	-3.5	-4.1
37795	2.64	13.03	3.83	B6IVe[a]	T120G390I052V350	12.71	14.84	7.59	3.90	2.73	3.68	5.27	3.93	174	30	-1.9	-1.8	-2
41335	5.21	23.28	3.62	B1.5IIIen[a]	T180G390I105V450	17.75	22.27	11.38	3.90	2.73	6.09	8.71	10.75	390	10	-3.3	-2.3	-3.8
44458	5.64	28.51	3.94	B0.5Vpe[a]	T220G390I105V300	21.70	27.22	13.91	3.90	2.73	2.71	3.87	2.12	260	30	-1.9	-1.6	-3.3
45725	4.60	20.28	3.91	B2.5IV-Ve[a]	T180G420I052V500	19.07	22.27	11.38	4.20	3.03	3.77	5.39	8.21	248	0	-2.7	-2.4	-3.5
45995	6.14	23.82	3.82	B1.5IVnne[a]	T180G390I105V300	17.75	22.27	11.38	3.90	2.73	2.71	3.87	2.12	260	10	-1.5	-0.8	-2.2
48917	5.20	21.33	3.70	B2III-IVe[a]	T180G360I052V500	19.07	22.27	11.38	3.60	2.43	15.00	21.45	32.69	248	30	-5.7	-4.2	-6.7
50013	3.96	23.82	3.82	B1.5IVne[a]	T200G360I105V300	19.73	24.75	12.64	3.60	2.43	5.40	7.72	4.24	260	0	-3.3	-3.1	-3.4
54309	5.71	21.53	3.81	B2IVe[a]	T160G390I026V500	17.15	19.79	10.11	3.90	2.73	7.52	10.75	16.38	129	0	-4.1	-4.1	-0.1
56014	4.66	17.91	3.54	B3IIIe[a]	T220G390I079V450	22.73	27.22	13.91	3.90	2.73	6.09	8.71	10.75	320	10	-3.9	-3.9	-4.7
56139	3.85	21.53	3.81	B2IVe[a]	T160G360I026V300	17.15	19.79	10.11	3.60	2.43	5.40	7.72	4.24	77	30	-3.4	-3.1	-3.4
57219	5.11	21.53	3.81	B2IVne[a]	T160G390I026V300	17.15	19.79	10.11	3.90	2.73	2.71	3.87	2.12	77	0	-1.9	-1.6	-2
58050	6.41	22.18	3.98	B2Ve[a]	T180G360I052V350	19.07	22.27	11.38	3.60	2.43	7.35	10.51	7.85	174	0	-4.2	-2.7	-4.8
58343	5.33	16.37	3.81	B4IVe[a]	T140G360I026V250	15.01	17.32	8.85	3.60	2.43	3.75	5.36	2.04	64	0	-2.4	-1.8	-2.7
58978	5.61	30.41	3.92	B0Vpe[a]	T160G390I052V350	16.95	19.79	10.11	3.90	2.73	3.68	5.27	3.93	174	0	-2.4	-2.2	-2.8
60606	5.54	19.01	4.00	B3Vne[a]	T180G390I079V350	18.59	22.27	11.38	3.90	2.73	3.68	5.27	3.93	249	20	-2.4	-2.3	-2.7
63462	4.50	30.41	3.92	B0Ve[a]	T180G390I105V500	17.75	22.27	11.38	3.90	2.73	7.52	10.75	16.38	434	0	-3.8	-3.7	-4.2
66194	5.81	19.95	3.82	B2.5IVe[b]	T180G390I079V300	18.59	22.27	11.38	3.90	2.73	2.71	3.87	2.12	213	10	-1.8	-1.7	-2.1
68980	4.78	28.31	3.88	B0.5IV-Ve[a]	T160G390I026V350	17.15	19.79	10.11	3.90	2.73	3.68	5.27	3.93	90	0	-2.6	-2.5	-2.8

Where: * indicates a spectrum with emission; [a] indicates BCD classified; [b] indicates MK classified.

cont. on next page

cont. from previous page

Star HD..	Chauville et al (2001) $m(v)$	$T_{\rm eff}$ (kK)	log$g$	Spectral type	Best-fit model	Model fit data $T_{\rm app}$	$T_{\rm pole}$ (kK)	$T_{\rm eq}$	log$g_{\rm pole}$	log$g_{\rm eq}$	$R_{\rm pole}$ $(R_\odot)$	$R_{\rm eq}$	Mass $(M_\odot)$	$v\sin i$ (km/s)	Radial v	$M(V)$	Hipparcos low	Hi.
75311	4.49	19.95	3.82	B2.5IVne[a]	T180G420I079V450	18.59	22.27	11.38	4.20	3.03	3.05	4.36	5.39	320	20	-2	-1.8	-2
77320	6.07	19.01	4.00	B3Vne[a]	T200G420I079V400	20.66	24.75	12.64	4.20	3.03	2.41	3.45	3.36	284	20	-1.7	-1.3	-1.8
83953	4.77	14.62	3.63	B5IV-Ve[a]	T140G390I105V300	13.81	17.32	8.85	3.90	2.73	2.71	3.87	2.12	260	0	-1.1	-1.1	-1.4
86612	6.21	16.94	4.01	B4Ve[a]	T140G420I052V350	14.83	17.32	8.85	4.20	3.03	1.85	2.64	1.97	174	0	-0.7	-0.5	-1.2
88661	5.72	21.53	3.81	B2IVpne[a]	T180G390I079V350	18.59	22.27	11.38	3.90	2.73	3.68	5.27	3.93	249	15	-2.4	-2	-2.7
91465	3.32	17.91	3.54	B3IIIne[a]	T180G390I079V350	18.59	22.27	11.38	3.90	2.73	3.68	5.27	3.93	249	20	-2.4	-2.4	-2.8
105435	2.60	21.53	3.81	B2IVne[a]	T180G390I079V400	18.59	22.27	11.38	3.90	2.73	4.81	6.88	6.71	284	0	-3	-2.9	-3.4
105521	5.48	18.41	3.82	B3IVe[b]	T140G360I052V300	14.83	17.32	8.85	3.60	2.43	5.40	7.72	4.24	149	0	-3	-2.7	-3.3
109387	3.87	13.9	3.84	B5-6IVpe[a]	T140G390I079V350	14.46	17.32	8.85	3.90	2.73	3.68	5.27	3.93	249	0	-2	-1.9	-2.2
110432	5.31	23.82	3.82	B1.5IVe[a]	T240G420I052V450	25.43	29.70	15.17	4.20	3.03	3.05	4.36	5.39	224	0	-2.8	-2.9	-3.6
112078	4.62	16.94	4.01	B4Vne[a]	T160G450I079V500	16.53	19.79	10.11	4.50	3.33	1.89	2.70	4.12	355	10	-0.8	-0.7	-0.9
112091	5.17	15.31	4.02	B5Vne[a]	T140G420I079V350	14.46	17.32	8.85	4.20	3.03	1.85	2.64	1.97	249	20	-0.5	-0.3	-0.5
113120	6.03	21.09	3.57	B2IIIne[a]	T200G420I079V400	20.66	24.75	12.64	4.20	3.03	2.41	3.45	3.36	284	0	-1.7	-1.3	-2.2
120324	3.04	21.53	3.81	B2IVe[a]	T180G390I052V350	19.07	22.27	11.38	3.90	2.73	3.68	5.27	3.93	174	0	-2.7	-2.5	-2.7
124367	5.07	16.37	3.81	B4IVne[a]	T140G420I079V400	14.46	17.32	8.85	4.20	3.03	2.41	3.45	3.36	284	15	-1	-0.8	-1
127972	2.31	21.88	3.90	B2IV-Vne[a]	T200G420I079V500	20.66	24.75	12.64	4.20	3.03	3.77	5.39	8.21	355	0	-2.7	-2.5	-2.7
131492	5.11	19.01	4.00	B3Vnpe[a]	T160G390I052V450	16.95	19.79	10.11	3.90	2.73	6.09	8.71	10.75	224	0	-3.5	-3.1	-3.8
137387	5.49	26.67	3.95	B1pne[b]	T220G420I079V450	22.73	27.22	13.91	4.20	3.03	3.05	4.36	5.39	320	0	-2.4	-2.4	-2.9
142184	5.42	20.61	3.99	B2.5Vne[b]	T200G450I079V400	20.66	24.75	12.64	4.50	3.33	1.21	1.73	1.69	284	0	-0.2	-0.3	-0.7
142983	4.88	17.18	3.67	B3-4III-IVpe[a]	T160G390I052V250	16.95	19.79	10.11	3.90	2.73	1.88	2.69	1.02	124	0	-1	-0.8	-1
148184	4.42	28.51	3.94	B0.5Vpe[a]	T200G420I026V400	21.44	24.75	12.64	4.20	3.03	2.41	3.45	3.36	103	0	-2.1	-2.5	-2.8

Where: * indicates a spectrum with emission; [a] indicates BCD classified; [b] indicates MK classified.

cont. on next page

cont. from previous page

Star HD..	Chauville et al (2001) $m(v)$	$T_{\rm eff}$ (kK)	log$g$	Spectral type	Best–fit model	$T_{\rm app}$	$T_{\rm pole}$ (kK)	$T_{\rm eq}$	log$g_{\rm pole}$	log$g_{\rm eq}$	$R_{\rm pole}$ $(R_\odot)$	$R_{\rm eq}$	Mass $(M_\odot)$	$v$sin$i$ (km/s)	Radial v	$M(V)$	Hipparcos low	Hi.
149757	2.56	33.04	4.00	O9Vn[a]	T280G420I079V450	28.93	34.65	17.70	4.20	3.03	3.05	4.36	5.39	320	20	-2.9	-3.1	-3.4
157042	5.25	19.95	3.82O	B2IVe[a]	T180G390I105V350	17.75	22.27	11.38	3.90	2.73	3.68	5.27	3.93	304	20	-2.2	-2	-2.4
158427	2.95	19.01	4.00	B3Vne[a]	T180G420I052V400	19.07	22.27	11.38	4.20	3.03	2.41	3.45	3.36	199	15	-1.7	-1.6	-2
164284	4.64	26.67	3.95	B1Ve[a]	T180G390I079V300	18.59	22.27	11.38	3.90	2.73	2.71	3.87	2.12	213	-10	-1.8	-1.7	-2
167128	5.33	17.91	3.54	B3IIIep[b]	T200G390I026V250	21.44	24.75	12.64	3.90	2.73	1.88	2.69	1.02	64	0	-1.5	-1.4	-2
173948	4.22	23.28	3.62	B1.5IIIe[a]	T180G360I052V350	19.07	22.27	11.38	3.60	2.43	7.35	10.51	7.85	174	10	-4.2	-3.9	-4.3
174237	5.88	19.01	4.00	B3Ve[a]	T180G390I052V300	19.07	22.27	11.38	3.90	2.73	2.71	3.87	2.12	149	35	-2	-1.9	-2.5
174638	3.45	12.56	4.01	B7Ve+A8p[b]	T220G360I052V300	23.31	27.22	13.91	3.60	2.43	5.40	7.72	4.24	149	0	-3.9	-3.7	-4
178175	5.54	22.18	3.98	B2Ve[b]	T180G390I052V350	19.07	22.27	11.38	3.90	2.73	3.68	5.27	3.93	174	-10	-2.7	-2.3	-2.9
183656	6.05	13.77	4.03	B6VeShell[b]	T180G420I079V350	18.59	22.27	11.38	4.20	3.03	1.85	2.64	1.97	249	-20	-0.9	-0.7	-1.2
184279	6.82	30.41	3.92	B0Ve[b]	T220G390I026V450	23.59	27.22	13.91	3.90	2.73	6.09	8.71	10.75	116	70	-4.3	-1.9	-4.3
187811	4.95	20.61	3.99	B2.5Ve[b]	T160G390I079V300	16.53	19.79	10.11	3.90	2.73	2.71	3.87	2.12	213	10	-1.6	-1.4	-1.7
189687	5.19	18.41	3.82	B3IVe[b]	T160G390I052V400	16.95	19.79	10.11	3.90	2.73	4.81	6.88	6.71	199	0	-3	-2.7	-3.2
191610	4.93	18.41	3.82	B3IVe[b]	T200G390I079V350	20.66	24.75	12.64	3.90	2.73	3.68	5.27	3.93	249	-20	-2.7	-2.4	-2.9
192044	5.92	12.56	4.01	B7Ve[b]	T120G360I131V250	11.22	14.84	7.59	3.60	2.43	3.75	5.36	2.04	242	-20	-1.2	-0.9	-1.3
198183	4.53	15.31	4.02	B5Ve[b]	T140G390I052V350	14.83	17.32	8.85	3.90	2.73	3.68	5.27	3.93	174	0	-2.2	-2.1	-2.7
200120	4.74	24.43	3.97	B1.5Vne[a]	T160G390I079V500	16.53	19.79	10.11	3.90	2.73	7.52	10.75	16.38	355	20	-3.8	-3.2	-4.1
201733	6.63	16.37	3.81	B4IVpe[b]	T180G420I105V350	17.75	22.27	11.38	4.20	3.03	1.85	2.64	1.97	304	0	-0.7	-0.4	-0.9
202904	4.43	19.01	4.00	B3Vne[a]	T160G390I079V350	16.53	19.79	10.11	3.90	2.73	3.68	5.27	3.93	249	0	-2.2	-1.9	-2.5
203467	5.18	18.41	3.82	B3IVe[b]	T160G360I052V350	16.95	19.79	10.11	3.60	2.43	7.35	10.51	7.85	174	0	-3.9	-3.6	-4.1
205637	4.68	17.3	3.73	B3II-IIIpe[a]	T200G390I079V400	20.66	24.75	12.64	3.90	2.73	4.81	6.88	6.71	284	0	-3.2	-2.9	-3.3

Where: * indicates a spectrum with emission; [a] indicates BCD classified; [b] indicates MK classified.

cont. on next page

cont. from previous page

Star HD..	Chauville et al (2001) $m(v)$	$T_{\rm eff}$ (kK)	log$g$	Spectral type	Model fit data Best–fit model	$T_{\rm app}$	$T_{\rm pole}$ (kK)	$T_{\rm eq}$	log$g_{\rm pole}$	log$g_{\rm eq}$	$R_{\rm pole}$ $(R_\odot)$	$R_{\rm eq}$	Mass $(M_\odot)$	$v$sin$i$ (km/s)	Radial v	$M(V)$	Hipparcos low	Hi.
208057	5.08	19.01	4.00	B3Ve[b]	T160G420I026V400	17.15	19.79	10.11	4.20	3.03	2.41	3.45	3.36	103	0	-1.6	-1.3	-1.7
208682	5.86	20.61	3.99	B2.5Ve[b]	T200G420I105V400	19.73	24.75	12.64	4.20	3.03	2.41	3.45	3.36	347	0	-1.5	-1.4	-2.1
209409	4.69	14.29	3.83	B6IVe[a]	T120G390I079V300	12.39	14.84	7.59	3.90	2.73	2.71	3.87	2.12	213	0	-1	-0.8	-1.1
209522	5.96	16.37	3.81	B4IVne[b]	T160G390I105V350	15.78	19.79	10.11	3.90	2.73	3.68	5.27	3.93	304	-5	-2	-1.7	-2.3
210129	5.78	13.18	4.02	B6-7Vne[b]	T120G390I052V250	12.71	14.84	7.59	3.90	2.73	1.88	2.69	1.02	124	0	-0.4	-0.4	-0.8
212076	5.01	21.88	3.90	B2IV-Ve[b]	T220G390I026V400	23.59	27.22	13.91	3.90	2.73	4.81	6.88	6.71	103	0	-3.8	-3.4	-4.1
212571	4.66	26.67	3.95	B1Ve[a]	T220G390I079V300	22.73	27.22	13.91	3.90	2.73	2.71	3.87	2.12	213	10	-2.2	-2	-2.4
214168	5.73	22.18	3.98	B2Ve[b]	T240G480I079V500	24.79	29.70	15.17	4.80	3.63	0.95	1.35	2.06	355	0	0	3.1	-0.8
217050	5.43	17.91	3.54	B3IIIeshell[a]	T200G390I079V300	20.66	24.75	12.64	3.90	2.73	2.71	3.87	2.12	213	0	-2	-1.6	-2
217891	4.53	14.22	3.93	B5-6IV-Ve[a]	T120G390I026V300	12.86	14.84	7.59	3.90	2.73	2.71	3.87	2.12	77	0	-1.4	-0.9	-1.3
224544	6.52	13.03	3.83	B6IVe[b]	T140G390I079V400	14.46	17.32	8.85	3.90	2.73	4.81	6.88	6.71	284	0	-2.6	-1.9	-3.1
224559	6.54	16.94	4.01	B4Ven[b]	T160G390I105V350	15.78	19.79	10.11	3.90	2.73	3.68	5.27	3.93	304	0	-2	-1.3	-2.2

Where: * indicates a spectrum with emission; [a] indicates BCD classified; [b] indicates MK classified.

Appendix C

Best Fit Plots – cool stars

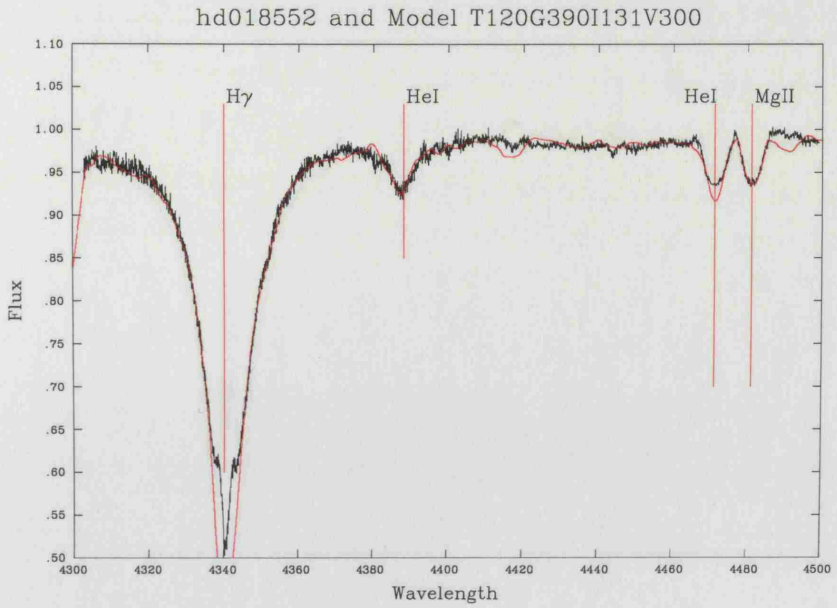

Figure C.1. Plot of the best–fit model versus observation for HD 18552. Observation = black line; Model = red line.

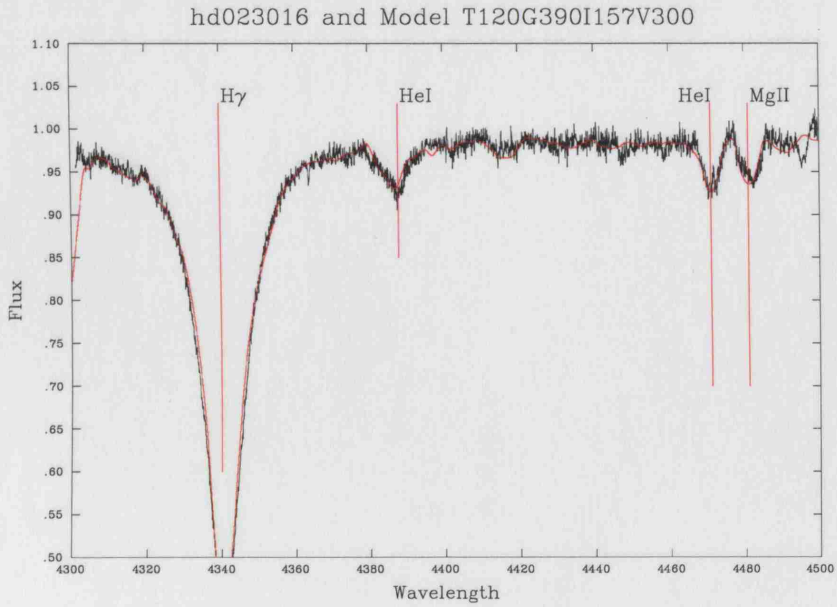

Figure C.2. Plot of the best–fit model versus observation for HD 23016. Observation = black line; Model = red line.

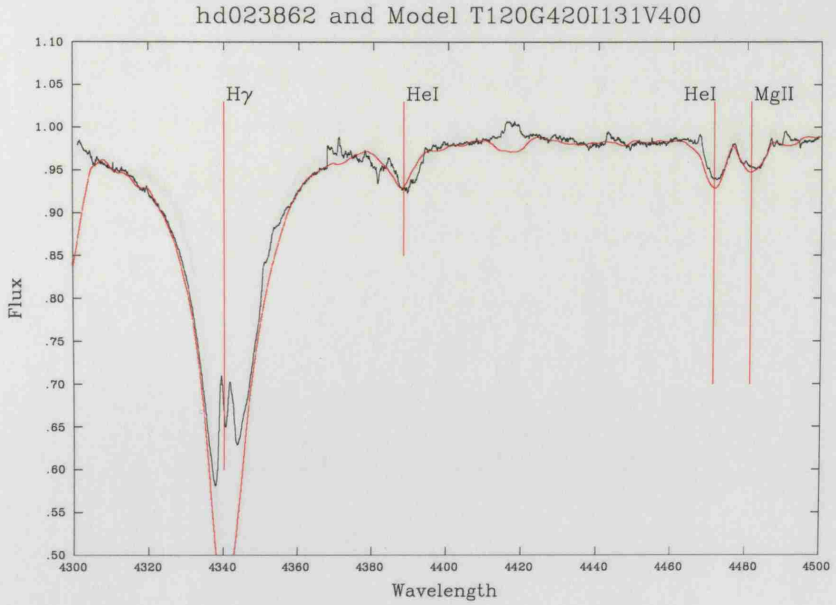

Figure C.3. Plot of the best–fit model versus observation for HD 23862. Observation = black line; Model = red line.

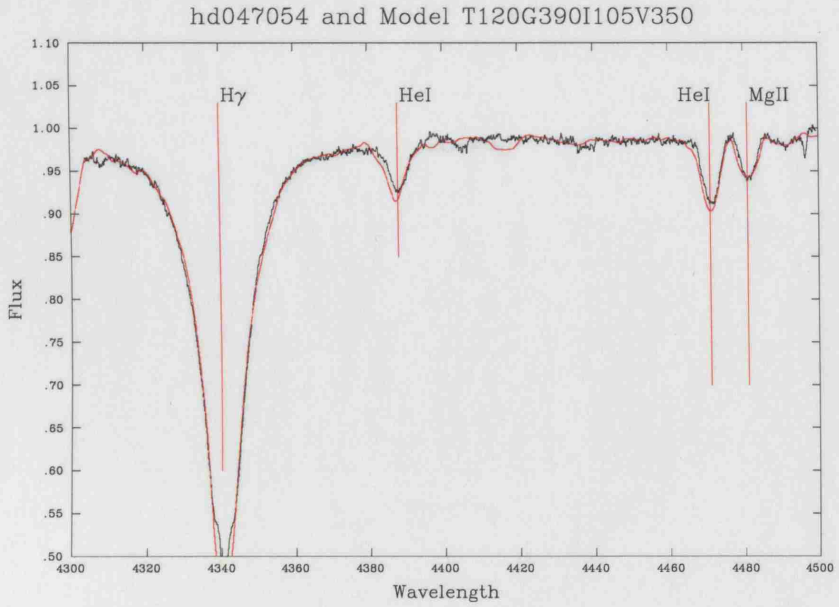

Figure C.4. Plot of the best–fit model versus observation for HD 47054. Observation = black line; Model = red line.

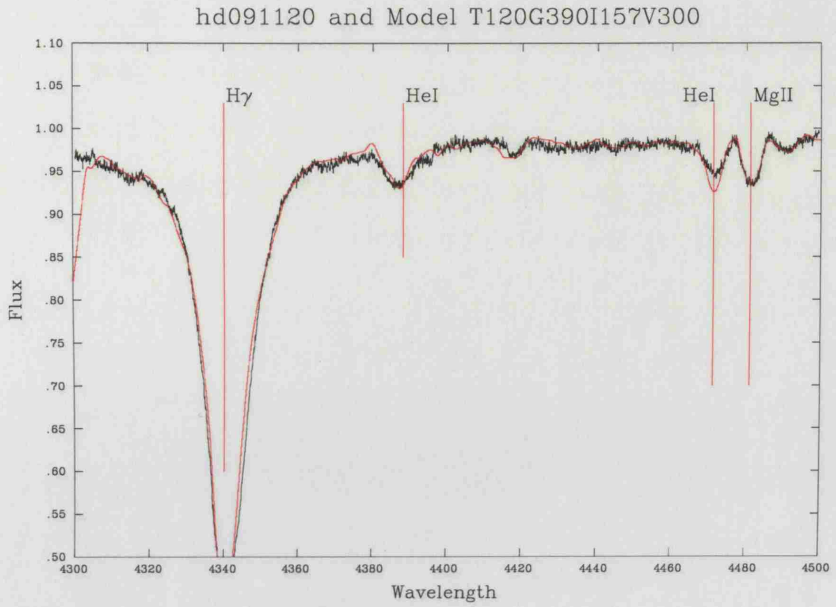

Figure C.5. Plot of the best–fit model versus observation for HD 91120. Observation = black line; Model = red line.

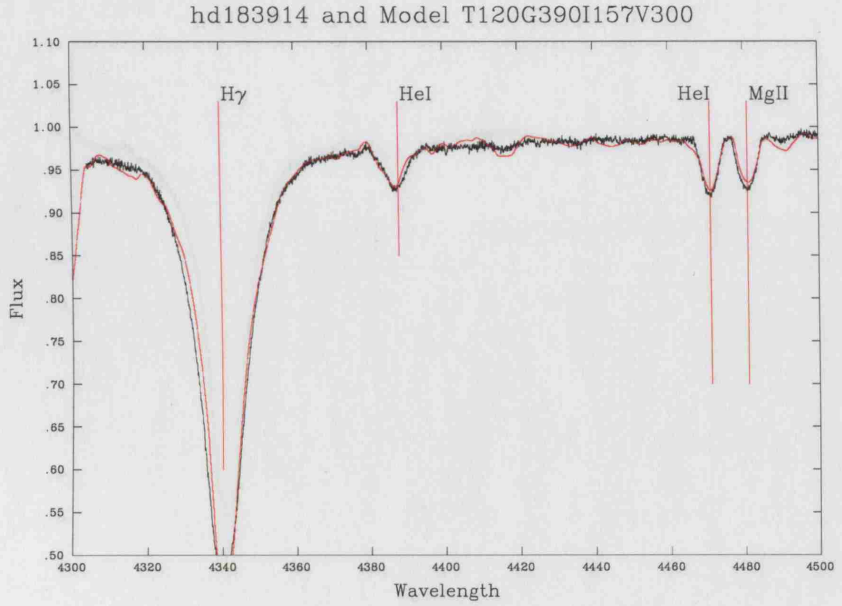

Figure C.6. Plot of the best–fit model versus observation for HD 183914. Observation = black line; Model = red line.

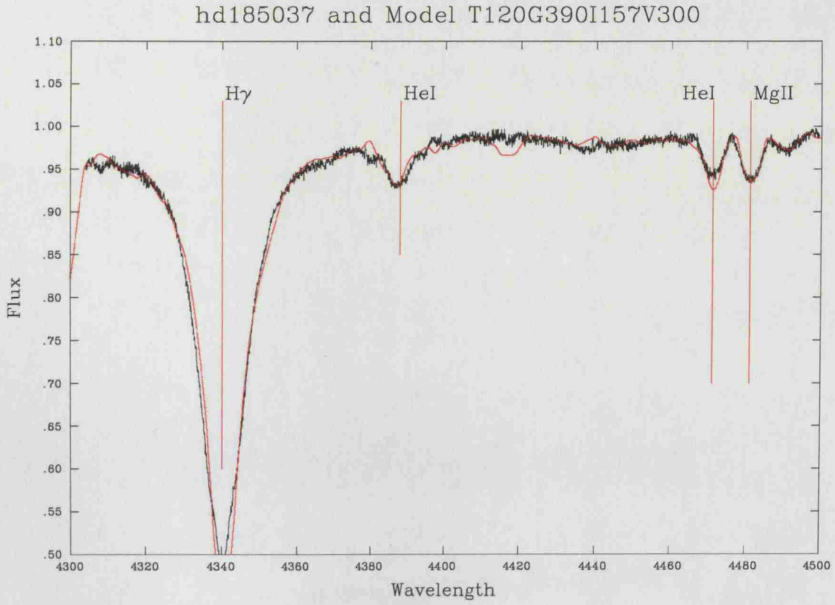

Figure C.7. Plot of the best–fit model versus observation for HD 185037. Observation = black line; Model = red line.

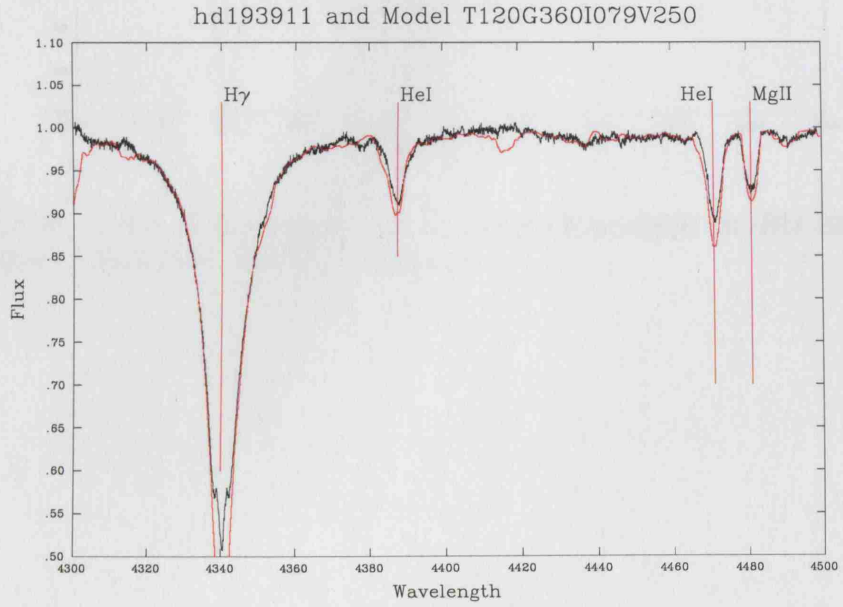

Figure C.8. Plot of the best–fit model versus observation for HD 193911. Observation = black line; Model = red line.

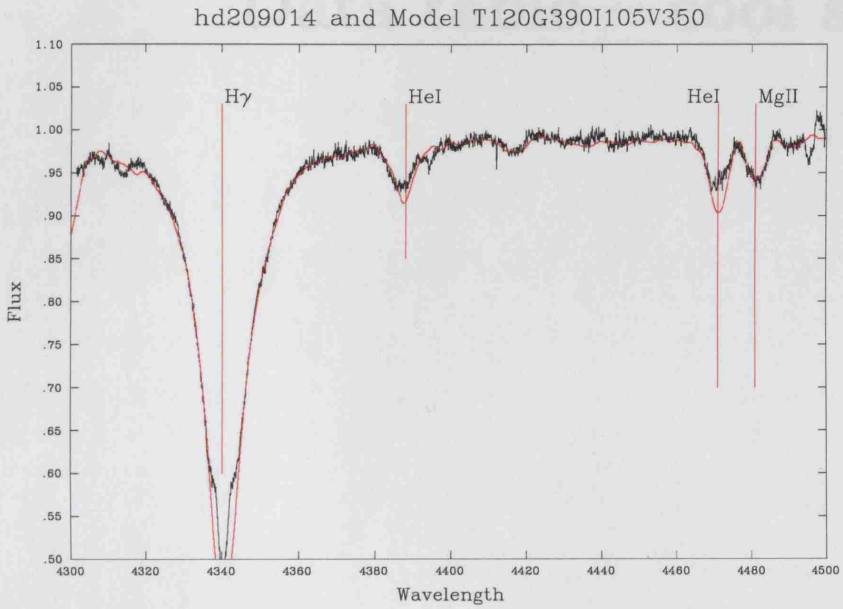

Figure C.9. Plot of the best–fit model versus observation for HD 209014. Observation = black line; Model = red line.

Appendix D

Data table – cool stars

Star HD..	Chauville et al (2001) $m(v)$	$T_{\rm eff}$ (kK)	log$g$	Spectral type	Best–fit model	Model fit data $T_{\rm app}$	$T_{\rm pole}$ (kK)	$T_{\rm eq}$	log$g_{\rm pole}$	log$g_{\rm eq}$	$R_{\rm pole}$ $(R_\odot)$	$R_{\rm eq}$	Mass $(M_\odot)$	$v\sin i$ (km/s)	$v_{\rm radial}$	$M(V)$	Hipparcos low	Hi.
18552	6.11	11.83	3.99	B8Vne[b]	T120G390I131V300	11.22	14.84	7.59	3.90	2.73	2.71	3.87	2.12	290	0	-0.5	-0.2	-0.7
23016	5.69	11.14	4.04	B9Vne[b]	T120G390I157V300	10.94	14.84	7.59	3.90	2.73	2.71	3.87	2.12	300	0	-0.4	-0.2	-0.6
23862	5.09	11.67	3.93	B8IV-Ve[a]	T120G420I131V400	11.22	14.84	7.59	4.20	3.03	2.41	3.45	3.36	386	0	-0.3	-0.2	-0.4
47054	5.52	11.67	3.93	B8IV-Ve[b]	T120G390I105V350	11.83	14.84	7.59	3.90	2.73	3.68	5.27	3.93	304	20	-1.4	-1	-1.5
91120	5.58	11.04	3.88	B9IVne[a]	T120G390I157V300	10.94	14.84	7.59	3.90	2.73	2.71	3.87	2.12	300	0	-0.4	-0.3	-0.6
183914	5.11	11.83	3.99	B8Ve[b]	T120G390I157V300	10.94	14.84	7.59	3.90	2.73	2.71	3.87	2.12	300	0	-0.4	-0.2	-0.4
185037	6.05	11.83	3.99	B8Vne[b]	T120G390I157V300	10.94	14.84	7.59	3.90	2.73	2.71	3.87	2.12	300	0	-0.4	-0.1	-0.5
193911	5.54	11.38	3.38	B8IIIne[b]	T120G360I079V250	12.39	14.84	7.59	3.60	2.43	3.75	5.36	2.04	178	0	-1.7	-1.6	-2.3
209014	5.42	11.83	3.99	B8Ve[b]	T120G390I105V350	11.83	14.84	7.59	3.90	2.73	3.68	5.27	3.93	304	0	-1.4	-1.3	-1.9

Where: * indicates a spectrum with emission; [a] indicates BCD classified; [b] indicates MK classified.

Bibliography

Ballereau, D., Chauville, J. & Zorec, J., 1995, *A&AS*, **111**, 423

Bjorkman, J. E. & Cassinelli, J. P., 1993, *ApJ*, **409**, 429

Cassinelli, J. P., Brown, J. C., Maheswaran, M., Miller, N. A. & Telfer, D. C., 2002, *ApJ*, **578**, 951

Castor, J. I., Abbott, D. C. & Klein, R. I., 1975, *ApJ*, **195**, 157

Chalonge, D. & Divan, L., 1952, *Annales d'Astrophysique*, **15**, 201

Chauville, J., Zorec, J., Ballereau, D., Morrell, N., Cidale, L. & Garcia, A., 2001, *A&A*, **378**, 861

Chen, H.-Q. & Huang, L., 1987, *Chinese Astronomy and Astrophysics*, 11, 10

Cranmer, S. R. & Owocki, S. P., 1995, *ApJ*, **440**, 308

Curé, M., 2004, *ApJ*, **614**, 929

Friend, D. B. & Abbott, D. C., 1986, *ApJ*, **311**, 701

Friend, D. B. & MacGregor, K. B., 1984, *ApJ*, **282**, 591

Harmanec, P. & Scholz, G., 1993, *A&A*, **279**, 131

Hirata, R., 1995, *PASJ*, **47**, 195

Howarth, I. D. & Smith, K. C., 2001, *MNRAS*, **327**, 353

Howells, L., Steele, I. A., Porter, J. M. & Etherton, J., 2001, *A&A*, **369**, 99

Hubeny, I., Stefl, S. & Harmanec, P., 1985, *Bulletin of the Astronomical Institutes of Czechoslovakia*, **36**, 214

Ignace, R. & Gayley, K. G. (eds.), 2005, *The Nature and Evolution of Disks Around Hot Stars*, volume 337 of *Astronomical Society of the Pacific Conference Series*

Jaschek, C. & Jaschek, M., 1990, *The Classification of Stars* (The Classification of Stars, by Carlos Jaschek and Mercedes Jaschek, pp. 427. ISBN 0521389968. Cambridge, UK: Cambridge University Press, July 1990.)

Jeans, J. H., 1928, *Astronomy and cosmogony* (Cambridge [Eng.] The University press, 1928.)

Kurucz, R., 1993, *ATLAS9 Stellar Atmosphere Programs and 2 km/s grid. Kurucz CD-ROM No. 13. Cambridge, Mass.: Smithsonian Astrophysical Observatory, 1993.*, **13**

Lanz, T. & Hubeny, I., 2007, *ApJSS*, **169**, 83

Lee, U., Osaki, Y. & Saio, H., 1991, *MNRAS*, **250**, 432

Madura, T. I., Owocki, S. P. & Feldmeier, A., 2007, *ApJ*, **660**, 687

Meilland, A., Stee, P., Vannier, M., Millour, F., Domiciano de Souza, A., Malbet, F., Martayan, C., Paresce, F., Petrov, R. G., Richichi, A. & Spang, A., 2007, *A&A*, **464**, 59

Mihalas, D., 1978, *Stellar atmospheres /2nd edition/* (San Francisco, W. H. Freeman and Co., 1978. 650 p.)

Moujtahid, A., Zorec, J., Hubert, A. M., Garcia, A. & Burki, G., 1998, *A&AS*, **129**, 289

Owocki, S. P., Cranmer, S. R. & Gayley, K. G., 1996, *ApJL*, **472**, L115+

Pauldrach, A., Puls, J. & Kudritzki, R. P., 1986, *A&A*, **164**, 86

Poe, C. H. & Friend, D. B., 1986, *ApJ*, **311**, 317

Porter, J. M., 1996, *MNRAS*, **280**, L31

Porter, J. M. & Rivinius, T., 2003, *PASP*, **115**, 1153

Quirrenbach, A., Bjorkman, K. S., Bjorkman, J. E., Hummel, C. A., Buscher, D. F., Armstrong, J. T., Mozurkewich, D., Elias, II, N. M. & Babler, B. L., 1997, *ApJ*, **479**, 477

Secchi, A., 1867, *Astronomische Nachrichten*, **68**, 63

Slettebak, A., 1949, *ApJ*, **110**, 498

Slettebak, A., 1979, *Space Science Reviews*, **23**, 541

Slettebak, A., 1988, *PASP*, **100**, 770

Slettebak, A. & Kusma, T. J., 1979, in M. F. McCarthy, A. G. D. Philip & G. V. Coyne (eds.), *IAU Colloq. 47: Spectral Classification of the Future*, volume 9 of *Ricerche Astronomiche*, pp. 87–93

Slettebak, A., Kuzma, T. J. & Collins, II, G. W., 1980, *ApJ*, **242**, 171

Stoeckley, T. R., 1968, *MNRAS*, **140**, 121

Struve, O., 1931, *ApJ*, **73**, 94

Townsend, R. H. D., Owocki, S. P. & Howarth, I. D., 2004, *MNRAS*, **350**, 189

Underhill, A. & Doazan, V., 1982, *B Stars with and without emission lines, parts 1 and 2* (NASA monograph series)

van Leeuwen, F., 2007, *A&A*, **474**, 653

von Zeipel, H., 1924, *MNRAS*, **84**, 665

Weber, E. J. & Davis, L. J., 1967, *ApJ*, **148**, 217

Zorec, J. & Briot, D., 1991, *A&A*, **245**, 150